THE UNIVERSITY
of LIVERPOOL

Fabrication of Functionally Graded Structures by Direct Metal Laser Remelting

Thesis submitted in accordance with the requirements for the degree of Doctor in Philosophy

Simon Richard Pogson

July 2008

Fabrication of Functionally Graded Structures by Direct Metal Laser Remelting by Simon R Pogson

Abstract

Investigations have been conducted into the production of Functionally Graded Structures (FGS) with varying composition and porosity using Direct Metal Laser Remelting (DMLR), a Rapid Prototyping (RP) technology. Following a series of experiments on a number of metal systems and analyses conducted using a series of metallographic and spectrographic techniques (SEM-EDS, XRD), it has been possible to assess the viability of a processing system to produce tailored structures.

The creation of FGS is a developing field that has important implications for manufacturing and design. Investigations have been conducted to determine how graded structures could be produced using the laser-melting of metal powders. Initial work developed the process to allow the production of dense, homogeneous structures from H13 tool steel. After overcoming processing difficulties, a study of processing parameters, scanning strategies and processing environments allowed the optimal processing conditions to be defined (a maximum laser scanning speed of 500mms^{-1} in conjunction with a specially derived scanning pattern).

Work conducted to ascertain what would happen within a graded region in a compositionally graded structure considered the types of material mixtures that may be used in FGS. Examination of the behaviour of mixtures of H13 and copper when producing three-dimensional structures, materials with an important application in the production of casting dies, found that their markedly different properties made production of such structures difficult to control. Microstructural analysis from this work showed that the presence of certain alloying elements within the H13, namely carbon and silicon, resulted in the production of two immiscible liquids in the melt pool. Investigations found that increasing the laser scanning speed and varying the powder size minimised the metallurgical interactions but did not eradicate them. This work concluded that similar problems were likely to be evident if other material systems were used, thus requiring each to be investigated in a similar way.

Structures with graded porosity, applicable in the production of bio-implants, were produced to specifications provided by an industrial sponsor. Presently, the main cause of failure of bio-implants is the use of bone cement for implant fixation; it would be desirable to produce a porous surface on the implant that would allow bone to grow directly into the implant, thereby providing a direct mechanical fixation. By varying DMLR processing parameters, such as laser scanning speed and scan-line spacing, during the construction of a part, it was found that material with controlled porosity could be produced. Grading of the porosity would allow a porous surface to be produced with a dense inner core, so as not to compromise the structural integrity and mechanical strength of the part. It was not only possible to produce parts with a tailored morphology, but also to produce such parts from a combination of dissimilar metals, utilising an intermediate material (tantalum) to provide a barrier that prevented the materials (titanium and cobalt-chrome) from interacting whilst molten.

Both the compositional and porosity investigations found that the production of such parts is highly process dependent. For example, the formation, size and shape of the meltpool, controlled by the size, shape, speed and energy density of the heat source as well as the absorptivity of the laser radiation, influenced the structural and compositional gradation obtained. The limitations of the laser system used here (the maximum laser scanning speed and laser power available constrained the investigations) and the inability to control the processing environment successfully meant that further technological advancement and understanding of metallurgical interactions are required before such technology becomes a feasible proposition in manufacturing.

Acknowledgments

I would like to thank: my supervisor, Dr Peter Fox, for his invaluable support and guidance during my research; Dr Chris Sutcliffe, Dr Eric Jones and Stryker Howmedica Osteonics for arranging, commissioning and sponsoring the graded porosity work; the EPSRC for sponsoring the graded composition work.

I also wish to pass on my gratitude to Dr Justin Ritherdon and the staff and technicians within the Dept. of Engineering at The University of Liverpool for the support they gave me during the course of my project.

I would also like to thank my current employers, NUKEM Limited for their support and use of their facilities.

On a personal note, I also wish to thank my family, girlfriend and friends for their support and for putting up with me during this intense period in my life.

List of Tables

Table 3.1	Table showing the First Pulse Suppression parameters used; these were used in conjunction with a laser power of 82W CW and a 0% beam overlap	54
Table 4.1	Composition of H13 tool steel	60
Table 4.2	Parameter ranges used for single track, multi-layer copper/H13 experiments	60
Table 4.3	Parameter ranges used for multi-track, multi-layer copper/H13 experiments	61
Table 4.4	Table showing results of copper/H13 experiments micro-hardness measurements	79
Table 5.1	Stryker specifications for porosity of structured components	98
Table 5.2	Composition of Co212-e cobalt-chrome alloy	99
Table 5.3	Composition of CP titanium powder	99
Table 5.4	Complete parameter set for initial process work on porous structures	102
Table 5.5	Initial scan strategy for production of structured coatings	106
Table 5.6	Laser parameters used for 'random scan' experiments	110
Table 5.7	Variations in coating thickness, expressed as a proportion of total build height, relative to laser scanning speed	124
Table 5.8	First series of titanium on titanium tensile test results	137
Table 5.9	Laser parameters of Samples 1 to 5 in Table 5.8	137
Table 5.10	Second series of titanium coated titanium tensile test results	139
Table 5.11	Laser parameters of samples 6 to 10 in Table 5.10	139
Table 5.12	Tensile testing results of coated cobalt-chrome substrates	141
Table 5.13	Laser parameters of samples 1 to 9 in Table 5.12	141

List of Figures

Figure 2.1	The SLS process *(reproduced courtesy of www.arptech.com.au)*	10
Figure 3.1	Sectioned view of DMLR build chamber *(R Morgan)*	48
Figure 3.2	Photograph showing build platform focal length gauge	50
Figure 3.3	Focal characteristics of DMLR equipment	51
Figure 3.4	Photograph showing the lattice structure of the waffle food compared with a structured titanium coating from the work described in Chapter 5.0	52
Figure 3.5	Photographs showing variation in first pulse suppression settings	55
Figure 4.1	Schematic diagram of a mould tool cavity	58
Figure 4.2	Relationship between laser frequency and laser power for single-track, multi-layer H13 structures	64
Figure 4.3	3 x 3 Array of H13 structures produced using relatively high energy parameters with laser scanning speed varying incrementally in steps of 30mm.s-1 from 30mm.s^{-1} to 90mm.s^{-1} and a laser frequency varying incrementally in steps of 10 kHz from 10kHz to 30kHz	65
Figure 4.4	Images showing successfully fused H13 structures	68
Figure 4.5	Photographs showing the effects of melt bead balling on the surface morphology	70
Figure 4.6	Digital photograph and SEM micrograph of a sectioned H13 build	71
Figure 4.7	Optical micrograph showing cast microstructure within DMLR processed H13 at 240mm.s^{-1}	72
Figure 4.8	First array of dissimilar metal coupons showing the relationship between laser power and laser scan speed; this experiment used a fixed Ø100μm laser spot and a beam overlap of 25%	73
Figure 4.9	SEM micrographs showing the surfaces of six selected copper/H13 coupons	74
Figure 4.10	SEM micrographs showing sections of the selected copper/H13 coupons	76
Figure 4.11	Optical micrograph showing iron-rich region on a coupon	77
Figure 4.12	Plot showing ratio of kα peak heights (Fe:Cu and Fe:Cr) with distance from sample upper surface	78

Figure 4.13	Plot showing variation in microhardness, for the six coupons listed in Table 4.4, at the upper surface (VHN values mean of 10 readings)	79
Figure 4.14	Optical images showing section views of copper/H13 samples produced with a laser scanning speed of 175mm.s^{-1}	81
Figure 4.15	Optical images showing section views of copper/H13 samples produced with a laser scanning speed of 400mm.s^{-1}	82
Figure 4.16	Optical images showing appearance of cracks in the structure produced with a 25% Cu/ 75% H13 composition and a scanning speed of 175mm.s^{-1}	83
Figure 4.17	Higher magnification optical images showing section views of copper/H13 samples produced with a laser scanning speed of 175mm.s^{-1}	84
Figure 4.18	Plot of the XRD data for DMLR processed H13 and 50%H13/50%Cu	85
Figure 4.19	Higher magnification optical images showing section views of copper/H13 samples produced with a laser scanning speed of 400mm.s^{-1}	86
Figure 4.20	Optical image of sample produced with 25% 212μm Cu/ 75 % 22μm H13 with a laser scanning speed of 250mm.s^{-1}	87
Figure 4.21	CCT diagram for H13 Tool Steel austenised at 1020°C (Jacques, P. and Doyle, E.D., 1997)	92
Figure 5.1	SEM micrographs showing: a) spherical 'solid' titanium powder; b) irregular 'sponge' titanium powder	100
Figure 5.2	3 x 3 Array of 1.6mm thick cobalt-chrome coupons on stainless steel substrate	101
Figure 5.3	Uncoated cobalt-chrome and titanium alloy substrates	105
Figure 5.4	Tensile test assembly	107
Figure 5.5	Porous titanium structure produced using sintering	109
Figure 5.6	Diagram showing use of: a) Unidirectional and b) Bidirectional hatch lines used by graphics-based laser-marking software	111
Figure 5.7	Graphical representations of initial "random" scans	111
Figure 5.8	Graphical representations of revised random scan patterns	112
Figure 5.9	Further revised random scan patterns used to enable more even distribution of scan-lines	113
Figure 5.10	SEM micrographs of the surface structure of cobalt-chrome on titanium alloy substrate	115

Figure 5.11	SEM micrographs of the surface structure of niobium on titanium alloy substrate produced with a laser power of 82W CW, -40% beam overlap at scanning speeds varying from 160mm.s^{-1} to 240mm.s^{-1}	116
Figure 5.12	SEM micrographs of the surface structure of tantalum on titanium alloy substrate produced with a laser power of 82W CW, -40% beam overlap and laser scanning speeds varying from 160mm.s^{-1} to 240mm.s^{-1}	117
Figure 5.13	SEM micrographs of the surface structure of titanium on titanium alloy substrate produced with a laser power of 82W CW, -40% beam overlap and scanning speeds varying from 160mm.s^{-1} to 240mm.s^{-1}	118
Figure 5.14	SEM micrographs of the surface structure of titanium on cobalt-chrome substrate produced with a laser power of 82W CW, -40% beam overlap and laser scanning speeds varying from 160mm.s^{-1} to 240mm.s^{-1}	119
Figure 5.15	SEM micrographs showing titanium builds on titanium alloy substrates produced with a "waffle" scanning format, scanning speed of 160mm.s^{-1}, laser power of 72W CW and beam overlaps varying from -400% to-600%	120
Figure 5.16	SEM surface micrograph of porous structure made from sintered titanium sponge	121
Figure 5.17	Failed samples produced using titanium sponge coating on Ø20mm titanium alloy substrates (samples produced using v = 120mm.s^{-1}, P = 82W, Qs = 30kHz and BO = 0% for the first three layers followed by v = 200mm.s^{-1}, P = 82W CW and BO = -1000% for the hatched layers)	122
Figure 5.18	Photograph showing Z-growth during a 15 layer build where the resultant coating measured 2mm thick	123
Figure 5.19	Plot of degree of excess vertical growth ("Z-growth"), for titanium powder on titanium substrates, relative to variation in scanning speed	124
Figure 5.20	Photographs showing evidence of Z-growth and curvature on top surface	125
Figure 5.21	Optical micrographs showing the interface interaction of a titanium structure and titanium alloy substrate produced with a laser scanning speed of 180mm.s^{-1} laser power of 82W CW and beam overlap of –40%	126
Figure 5.22	Failed samples produced using titanium sponge coating on cobalt-chrome substrates (samples produced using parameters v = 120mm.s^{-1}, P = 82W, Qs = 30kHz and BO = 0%)	127
Figure 5.23	SEM micrographs of fractured titanium on cobalt-chrome interface produced with parameters v = 180mm.s^{-1}, P = 82W CW and BO = –40%	128
Figure 5.24	Optical images showing micro-fractures along cobalt-chrome substrate/ titanium coating interface produced with parameters v = 220mm.s-1 (left image and 230mm.s-1 (right image),P = 82W CW and BO = –40%	128

Figure 5.25	Optical micrographs of sectioned Ti/CoCr interface (v = 220mm.s^{-1}, P = 82W CW and BO = –40%). Etchants: 5g NH_4FHF 100ml Distilled H_20, + 5ml HCl (titanium coating); 5% Nital solution (interface); 50% vol. HCl, 50% H_20 heated to 80°C: (cobalt-chrome alloy)	129
Figure 5.26	SEM micrographs of sectioned titanium/cobalt-chrome samples produced with parameters v = 190mm.s^{-1}, P = 82W CW and BO = –40%	130
Figure 5.27	EDS spectra of sectioned titanium/cobalt-chrome sample showing variation in molybdenum content between phases	131
Figure 5.28	XRD spectra of titanium/cobalt-chrome interface	132
Figure 5.29	EDS spectra of the cracked layer within a titanium/cobalt-chrome alloy interface	132
Figure 5.30	Optical micrograph of tantalum/cobalt-chrome interface	133
Figure 5.31	EDS spectra obtained across the interface of a tantalum bond-coated titanium on cobalt-chrome sample	134
Figure 5.32	XRD analysis through the tantalum/cobalt-chrome substrate interface	135
Figure 5.33	First series of tensile test failures, produced with laser parameters shown in Table 5.9	138
Figure 5.34	Second series of tensile test failures, produced with laser parameters shown in Table 5.11	140
Figure 5.35	Coated cobalt-chrome tensile test pieces after fracture for the results shown on Table 5.12, produced with the laser processing parameters shown in Table 5.13	142
Figure 5.36	Pore size characteristics for typical layer thicknesses for solid titanium coated titanium samples with parameters v = 180mm.s^{-1} and P = 82W CW	143
Figure 5.37	Clockwise from top left, array of three samples, solid titanium on titanium waffle structure at increasing magnification, showing the regular pore size achievable by DMLR processing; these samples were produced with parameters v = 180mm.s^{-1}, P = 82W CW and BO = –500%	144
Figure 5.38	Photograph showing 32 line and 54 line manually drawn interpretations of random scan used during the production of solid titanium on titanium samples, produced with the parameters shown in Table 5.6	146
Figure 5.39	Photograph showing solid titanium on titanium structures produced using a 50 line and a 100 line scan, using revised computer generated data, and the parameters shown in Table 5.6	146
Figure 5.40	Photograph showing solid titanium on titanium structures produced using random scans with scan pattern based on a varying number of scan lines whose start and end-points met on the perimeter of a varying number of	147

	circles (Figure 5.9). The laser parameters used are shown in Table 5.6	
Figure 5.41	Optical micrographs of solid titanium on titanium specimen produced with 50 line random scan and laser parameters shown in Table 5.6	147
Figure 5.42	Optical micrographs of the sectioned sample shown in Figure 5.41	148
Figure A2.1	Theoretical temperature profile from surface of powder bed derived using analytical solution provided by Steen, 1998	175
Figure A3.1	Cu-Fe binary phase diagram *(reproduced courtesy of Hansen, 1958)*	176
Figure A 3.2	Mo-Co binary phase diagram *(reproduced courtesy of ASM International)*	177
Figure A3.3	Mo-Cr binary phase diagram *(reproduced courtesy of ASM International)*	177
Figure A3.4	Ti-Co binary phase diagram *(reproduced courtesy of ASM International)*	178
Figure A3.5	Ti-Cr binary phase diagram *(reproduced courtesy of ASM International)*	178
Figure A3.6	Ti-Mo binary phase diagram *(reproduced courtesy of ASM International)*	179
Figure A3.7	A 1050°C partial isothermal section of Co-Cr-Ti system with the FCC γ phase boundary at 950°C shown by a dashed line and at 750°C by a dash-dot line *(reproduced courtesy of Gupta, 2001)*	179
Figure A 3.8	A 1000°C partial isothermal section of Co-Cr-Ti system *(reproduced courtesy of Gupta, 2001)*	180
Figure A3.9	A 20°C partial isothermal section of Co-Cr-Ti system *(reproduced courtesy of Gupta, 2001)*	180
Figure A3.10	A liquidus projection at the Co corner of Co-Cr-Ti system showing liquidus isotherms and three binary eutectic reactions (e) and three ternary eutectic reactions (E). *(reproduced courtesy of Gupta, 2001)*	181
Figure A3.11	A solidus projection at the Co corner of Co-Cr-Ti system showing solidus isotherms *(reproduced courtesy of Gupta, 2001)*	181

Abbreviations

BO	Beam Overlap
CP	Commercially Pure
CW	Continuous Wave
CVD	Chemical Vapour Deposition
CVI	Chemical Vapour Infiltration
DF	Direct Fabrication
DLS	Direct Laser Sintering
DMLR	Direct Metal Laser Remelting
DMLS	Direct Metal Laser Sintering
EBM	Electron Beam Melting
EDS	Energy Dispersive Spectroscopy
EOS	Electro Optic Systems
FDM	Fused Deposition Modelling
FGM	Functionally Graded Material
FGS	Functionally Graded Structure
FPS	First Pulse Suppression
HAP	Hydroxyapatite
HAZ	Heat Affected Zone
HIP	Hot Isostatic Pressing
Hv	Vickers Hardness
LENS	Laser Engineering Net Shaping
LOM	Laminated Object Manufacturing
LPS	Liquid Phase Sintering
LSA	Laser Surface Alloying
M_s	Martensite Start Temperature
Nd:YAG	Neodymium: Yttrium Aluminium Garnet
OFHC	Oxygen-Free High Conductivity
OM	Optical Microscopy
RM	Rapid Manufacturing
RP	Rapid Prototyping
RS	Rofin-Sinar
RT	Rapid Tooling
SDM	Shape Deposition Manufacturing
SEM	Scanning Electron Microscope

SFF	Solid Freeform Fabrication
SIMS	Secondary Ion Mass Spectrometry
SLPS	Supersolidus Liquid Phase Sintering
SLM	Selective Laser Melting
SLS	Selective Laser Sintering
UHMWPE	Ultra-High Molecular Weight Polyethylene
XPS	X-ray Photoelectron Spectroscopy
XRD	X-Ray Diffraction

Nomenclature

α	Thermal Diffusivity ($m^2.s^{-1}$)
α_{min}	Minimum Estimate of Absorptivity (%)
δ	Unit Impulse Function
ρ	Density ($kg.m^{-3}$)
λ	Wavelength of Laser in a Vacuum (m)
λ^{I}	Wavelength of the Instability (m)
ϖ_0	Effective Beam Radius (m)
Ø	Diameter (m)
c	Speed of Light in a Vacuum ($m.s^{-1}$)
g	Thickness of Metal Plate (m)
h_{eff}	Total Heat Transfer Coefficient due to Convection and Radiation ($W.(m^2.K)^{-1}$)
k	Thermal Conductivity of the Material ($W.(m.K)^{-1}$)
q	Heat Flux ($W.m^{-2}$)
m	Track Mass per Unit Length ($kg.m^{-1}$)
n	Pulse Width (ns)
r	Particle Radius (m)
t	Time (s)
t_0	Interaction Time between Heat Source and Powder Bed (s)
v	Laser Scan Speed ($m.s^{-1}$)
z	Distance from Surface of Powder Bed (m)
A^{I}	Absorptivity of Metals (%)
A	Surface Area of the Element (m^2)
A_n	Andrew Number ($J.m^{-2}$)
B.O	Beam Overlap (%)
C_p	Heat Capacity ($J.(kg.K)^{-1}$)
D	Initial Diameter of Cylinder (m)
E_d	Specific Energy Density ($J.m^{-2}$)
H	Specific Enthalpy ($kJ.kg^{-1}$)
L	Latent Heat ($kJ.kg^{-1}$)
LCU	Lamp Current (A)
LS	Scan Line-spacing (m)

N	Unit Surface Vector Normal to Surface
P	Laser Power (W)
P_n	Nominal Laser Power (W)
P_{peak}	Peak Laser Power (W)
Q_s	Pulse Repetition Rate (Hz)
Q_{sink}	Surface Heat Loss due to Convection and Radiation (kJ)
Q_{source}	Heat Input (kJ)
T	Temperature (K)
T_O	Initial Temperature (K)
T_m	Melting Temperature (K)
T_b	Boiling Temperature (K)
T_L	Liquidus Temperature (K)
T_S	Solidus Temperature (K)
ΔT	Temperature Range (K)
T_∞	Ambient Temperature (K)

CONTENTS

Acknowlegements i

List of Tables ii

List of Figures iii

Abbreviations viii

Nomenclature x

CONTENTS xii

1.0 Introduction 1

2.0 Literature Review 5

2.1 Introduction to Literature Review 5

2.2 FGS Fabrication State-of-the-Art 6

2.2.1 Manufacturing Techniques 6

2.2.1.1 3D Printing 6

2.2.1.2 Laser Surface Alloying (LSA) 7

2.2.1.3 Laser Engineered Net-Shaping (LENS) 8

2.2.1.4 Shape Deposition Manufacturing (SDM) 8

2.2.1.5 Selective Laser Sintering (SLS) 9

2.2.1.6 Direct Metal Laser Sintering (DMLS) 11

2.2.1.7 Direct Laser Sintering (DLS) 11

2.2.1.8 Selective Laser Melting (SLM) 11

2.2.1.9 Electron Beam Melting (EBM) 13

2.2.1.10 Hybrid (LENS and Spray-forming) 14

2.2.1.11 Direct Metal Laser Remelting (DMLR) 16

2.2.2 Mechanism for Build 16

2.2.2.1 Solid Phase Sintering 16

2.2.2.2 Liquid Phase Sintering 17

2.2.2.3 Supersolidus Liquid Phase Sintering (SLPS) 18

2.2.2.4 Laser Melting 18
2.2.3 Lasing Strategies 19
2.2.3.1 Pulsed CO_2 19
2.2.3.2 Continuous Wave CO_2 20
2.2.3.3 Pulsed Nd:YAG 20
2.2.3.4 Continuous Wave Nd:YAG 21
2.2.4 Build Technique 21
2.2.4.1 Pre-Placed Powder Bed 21
2.2.4.2 Roller/Platform 22
2.2.4.3 Wiper/Blade 22
2.2.4.4 Blown Powder 23
2.2.4.5 Intermixed Powder Feed 24
2.2.4.6 3D Printing/Ink-Jet Printing 24
2.3 Characterising the DMLR Process 25
2.3.1 Introduction 25
2.3.2 Modelling the Process 27
2.4 Laser Processing of Composition Gradients 34
2.4.1 Laser Processing of Copper 35
2.4.2 Laser Processing of Tool Steel 35
2.4.3 Laser Processing of Iron and Copper 38
2.4.4 Processing of H13 Tool Steel and Copper 39
2.5 Laser Processing of Materials with Controlled Porosity 40
2.5.1 Laser Processing of Bio-Materials 40
2.5.2 Production of Porous Structured Surfaces 42
2.6 Summary 46
3.0 Experimental Arrangement 47
3.1 Direct Metal Laser Remelting 47
3.2 Analytical Tools Used 56
4.0 Investigation into the Production of Structures with a Controlled Variation in Composition 57

4.1 Experimental Procedure 59
4.1.1 Experiments to Produce Homogeneous H13 Builds 59
4.1.2 Cu/H13 Pre-placed Powder Bed (Single Layer Coupons) 61
4.1.3 Cu/H13 Multi-Layer Coupons 62
4.1.4 Cu/H13 Optimised Processing Conditions 62
4.2 Results 63
4.2.1 Experiments to Produce Homogeneous H13 Builds 63
4.2.2 Cu/H13 Pre-placed Powder Bed (Single Layer Coupons) 72
4.2.3 Cu/H13 Multi-Layer Coupons 80
4.2.4 Cu/H13 Optimised Processing Parameters 81
4.3 Discussion 88
4.5 Summary 96

5.0 Investigation into the Production of Structures with a Controlled Variation in Porosity 97

5.1 Experimental Procedure 98
5.1.1 Initial Process Characterisation 98
5.1.1.1 Z-Growth Investigations 103
5.1.1.2 Substrate Preparation and Optimised Cleaning Procedure 104
5.1.2 Development of Titanium Coatings 104
5.1.3 Titanium Coated Cobalt-Chrome Alloy Substrates 106
5.1.4 Mechanical Testing of Porous Titanium Coatings 107
5.1.4.1 Pore Size Optimisation 108
5.1.4.2 Random Scan Generation 108
5.2 Results 114
5.2.1 Initial Process Characterisation 114
5.2.1.1 Z-Growth Investigations 123
5.2.2 Titanium Coated Titanium Substrates 126
5.2.3 Titanium Coated Cobalt-Chrome Substrates 127
5.2.3.1 Application of Intermediate Tantalum Coating 133
5.2.4 Mechanical Testing of Porous Titanium Coatings 135
5.2.4.1 Mechanical Testing of Coated Titanium Substrates 135

5.2.4.2 Mechanical Testing of Coated Cobalt-Chrome Substrates 140
5.2.5 Pore Size Optimisation 143
5.3 Discussion 148
5.3.1 Titanium on Cobalt-Chrome 148
5.3.2 Tantalum on Cobalt-Chrome 151
5.3.3 Pore Size 152
5.3.4 Random Patterns 153
5.3.5 Tensile Tests 153
5.3.6 Laser System 154
5.3.7 Processing Chamber 155
5.4 Summary 156
6.0 Conclusions 157
6.1 Production of Structures with Graded Composition 157
6.2 Production of Structures with Graded Porosity 158
6.3 General 159
7.0 Future Work 161
7.1 Basic Process Metallurgy 161
7.2 Porous Materials 161
7.3 Powder Placement for Composition Gradients 162
7.4 Automatic Control of Laser Parameters 162
7.5 Composition Gradients 163
References 164
Appendix 1.0 Example Calculation of Peak Power from a Pulsed Laser Beam 173
Appendix 2.0 Theoretical Temperature Profile from Surface of Powder Bed 174
Appendix 3.0 Referenced Phase Diagrams 176

1.0 Introduction

A Functionally Graded Structure (FGS) is one that demonstrates spatially varying macro and/or microstructure so as to exhibit a range of properties in a single body with the properties being optimised to suit a particular purpose. Two examples of such components include:

- A die for metal casting or injection moulding, with a hard, wear-resistant material for the internal cavity and a material with a high thermal conductivity for the cooling channels.
- Bio-implants or bone grafts, where the ideal structure may consist of a fully dense core for impact resistance and load bearing, while the outer structure is porous to allow bone ingrowth for implant stabilisation thereby replacing bone cement fixation, presently the most common cause of implant failure (Oliveira *et al*, 2002).

There are many factors that limit the complexity of FGS that can currently be produced. For example, it is possible to sinter powder onto bio-implants to produce a simple functional porosity gradient; however, more complex and controlled structural variations within a single component are difficult to produce using conventional manufacturing techniques.

Manufacturing technologies do, however, continue to develop and new techniques lead to new methods of part production, including those that were originally only conceived as methods of producing prototypes. Some of these techniques, which were originally designed to allow the rapid production of one-off components for demonstration or prototyping purposes have been, and continue to be, adapted to allow the production of short runs of high value components. They bring to manufacturing the advantage of process flexibility, which is defined by the degree of control that the operator has over the manufacturing process and the ability to reproduce many different types of features. However, this flexibility may be at the expense of increased production time and costs. More importantly, these techniques hold the potential to produce components with structures that cannot be created by existing, more conventional, processes. One such rapid prototyping technique is Direct Metal Laser Remelting (DMLR), a tool-less Solid

Freeform Fabrication (SFF) Rapid Prototyping (RP) process that produces parts on a layer-by-layer basis. DMLR works by creating a thin, pre-placed, powder layer across an underlying metal substrate, which is scanned using a laser to fuse together the regions that are to form the component. Successive layers are added to the build surface and fused to produce a three-dimensional part.

There are a number of different ways of locally changing the properties of a material (e.g. composition, residual stresses, porosity, microstructure). The work described in this thesis has focussed on investigating the metallurgical and processing issues associated with the production of two types of such structure; those with either spatially varying composition or porosity. To investigate the first of these, work was carried out that looked at the metallurgical interactions that would take place within a region with compositional variation, for example, in or near an interface where there may be a gradual change in composition, or where the component materials are able to mix and interact with each other. To investigate the second type of structure, parts were produced that utilised structural gradation to achieve a variation in porosity. The examples considered have relevance to two possible applications, one related to mould tools, part of a larger research project that investigated creating a mould tool with conformal copper cooling channels, and the other to the medical industry where porous materials are of interest.

Chapter 2.0 reviews the literature relevant to both the materials and technology used, including techniques that are closely related to DMLR. It also considers the differences between processes that rely on sintering (Selective Laser Sintering [SLS]) and those where the powders fully melt and form a melt pool (Selective laser Melting [SLM] & DMLR) as these terms (SLS and SLM) are often confused in publications. Work that has been conducted on graded structures by other researchers is included, identifying the increased difficulty faced in producing heterogeneous structures compared to the relative ease of producing homogeneous structures with uniform morphology.

Following the description in Chapter 3.0 of the experimental apparatus and analytical tools used for this work, Chapter 4.0 then presents the experimental techniques that have been applied to investigate the production of structures with a graded composition. This includes the experiments on single and mixed powder systems, which identified the relationships

between the processing conditions and the final components. These experiments describe an investigation into the production of parts using a powder bed consisting of more than one metal. Although the ultimate intention of this investigation was to produce compositional FGS using copper and H13 tool steel, no means of locally modifying the powder bed composition was available and therefore the metallurgical interactions that would occur at different places in the FGS were modelled using different powder mixtures. To achieve this, mixed powder beds were produced and then laser processed using DMLR. The parts produced were analysed using a series of metallographic techniques and the results used to provide an understanding of the problems that would occur within a mixed material region within a compositional functionally graded structure. With a specific application in mind (the production of a mould tool), microstructural and processing constraints have been identified that limit the use of such processing technology in the production of parts with a controlled compositional variation. Solutions have then been investigated to attempt to address these problems.

Chapter 5.0 describes research into the production of parts with graded porosity. With an application in the manufacture of bio-implants with spatially varying morphology, the limits of the processing system were investigated to produce parts to specifications provided by an industrial sponsor. Initial research considered parts with a spatially varying porosity in a single material system, while later research in this section considered the production of tailored implants using more complex material systems utilising compositional variation as well as porosity gradation. This work provided detailed information into the processing difficulties that would be encountered if both composition and porosity were varied at the same time within the same part. Solutions to detrimental materials interactions and processing problems were identified so as to maximise the overall structural mechanical performance.

This thesis is concluded with a summary of the most important factors affecting the production of functionally graded parts. Suggestions are made for ways that this work can be continued and brought to a satisfactory conclusion, where parts with a functional micro/macrostructure can be produced using a single-step manufacturing process.

The production of FGS using rapid prototyping technology would have important benefits to industry; it would allow complex parts with relatively high dimensional accuracy and spatially varying properties to be produced in a single manufacturing operation that otherwise would require additional post-process activities such as the machining of complex internal cavities or adhesive bonding of porous coatings. This thesis aims to increase understanding of the process/material interactions involved so as to allow the production of such tailored structures to enter real-world applications.

2.0 Literature Review

2.1 Introduction to Literature Review

A major factor that has, in the past, limited the ability to produce functionally graded components has been the lack of suitable manufacturing routes. This changed during the mid 1980s with the development and commercial exploitation of Selected Laser Sintering (SLS; Williams and Deckard, 1998) and other Solid Freeform Fabrication (SFF) processes. These processes construct the parts in an additive manner; adding material where it is required rather than removing it from where it is not. This opened up the possibility of selectively controlling the material deposited in different parts of the component to optimise the overall structure. Initially, these SFF techniques only worked with low strength materials or produced structures that were porous and required subsequent post-process infiltration. Since this time, technological advances have allowed structures to be produced with reasonably high final part densities (Morgan *et al*, 2001), which has led to development of commercial systems that can produce functional parts from materials such as stainless steels, some low carbon steels and titanium.

The research work discussed in this thesis has used an SFF process to produce structures with either a controlled composition or porosity that could suit a particular application. Therefore, the first part of the literature review is a study of the state-of-the art; this includes a review of related techniques that have been, or could be, used for a similar purpose. It is intended to inform the reader of the state of advancement of technology in providing a process that can produce a structure with a functional gradient. Section 2.2 will begin with a discussion of different Rapid Prototyping (RP) or Rapid Manufacturing (RM) processes, relate the aspects that make the individual processes unique and then consider and compare the manufacturing processes and different aspects of Functionally Graded Structures (FGS). Section 2.2.2 will look at the build mechanisms, comparing the various forms of sintering employed by other processes, with complete melting as used by DMLR. The final part of Section 2.2 will consider work on advancing the design of powder deposition platforms; as using highly complex scanning strategies and the latest laser systems is irrelevant unless the powder delivery system is flexible enough to deliver controlled, level powder beds with the ability to deposit single or multiple powders.

Section 2.3 in this review will look at work characterising the DMLR process and at solving fundamental processing issues using numerical and analytical techniques. This section aims to describe the many constraints encountered when melting and solidifying a powder bed in a track-by-track, layer-by-layer manner. Sections 2.4 and 2.5 will review work directly relevant to the research undertaken for this thesis, presenting work both on producing parts with varying composition and varying porosity. Here, published work on the primary metallurgical and processing constraints that had to be overcome during the experimental work in this thesis will be presented.

2.2 FGS Fabrication State-of-the-Art

2.2.1 Manufacturing Techniques

SFF technologies are material additive processes, where numerical control data for part production is usually extracted directly from 3-dimensional CAD models. Although not an exhaustive list, the processes referred to by the cited authors either represent radically different technologies (e.g. 3D Printing, Electron Beam Melting [EBM] and Spray-Forming or simply a development of an existing process (e.g. Direct Metal Laser Sintering [DMLS], Direct Laser Sintering [DLS] and Direct Metal Laser Remelting [DMLR] are all based on Selective Laser Sintering [SLS]). All the cited research works, however, describe studies that have been undertaken to advance the application of RP and RM techniques into the production of tailored structures.

2.2.1.1 3D Printing

3D printing is a non-laser based SFF process that produces parts on a layer-by-layer basis by depositing a layer of powder over the surface of the build chamber, followed by the selective deposition of a binding component (Jackson *et al*, 1999). By the use of a print-head with several jets, with each depositing different materials or binders, a controlled variation in composition can be achieved. Thus, the component is constructed as a series of layers; each new layer being formed by lowering the bed and component, and then spreading and binding a new thin layer of powder. The composition control resolution with

this process is similar to the binder droplet size (approximately 100μm). The authors of this work claim that a composition gradient could be achieved in a similar manner to that by which an inkjet printer is able to reproduce multiple colours.

The use of 3D Printing is constrained by the limited range of materials that can be used and the required use of a binder. This limits the material properties that can be obtained and so any functionally graded materials that are produced will also have only a limited range of properties. This technique does, however, show the basic mechanisms that underlie many RP processes; that the accuracy of the final part is controlled by the minimum layer thickness, and that the numerical data from the CAD model allows complex shapes to be produced and modifications to the geometry to be made without the need for alternative tooling.

2.2.1.2 Laser Surface Alloying (LSA)

The LSA process uses a scanning laser beam to produce a moving melt pool on the surface of a component into which is fed alloying additions, producing a surface composition different to the bulk (Majumdar and Manna, 1999a and 1999b). An example of how this technique can be used was described by the authors, who produced an alloyed surface on a primary metal component by electroplating the alloying element onto the original surface before melting it with a 2kW CO_2 laser, operating in Continuous Wave (CW) mode with a 1mm spot size. In this case, the objective was to add chromium to the surface to improve the wear resistance of the primary copper. Although the original chromium layer was only 20μm thick, the alloyed region was 0.85mm deep. This research work shows that although the LSA process can be used to produce functional gradients, these changes are limited to near the surface, and also that the melting process leads to a fairly coarse, cast, microstructure, even though the heating and cooling rates are reasonably rapid. The main limitation of LSA technology is that in this form it is not a RP or RM process, as to build a component, solid material must be continuously fed into the melt pool. It does, however, illustrate how laser melting technology can be used to locally produce variations in composition and so improve overall functionality.

2.2.1.3 Laser Engineered Net-Shaping (LENS)

Developed at Sandia National Laboratories, LENS technology addresses a major limitation of LSA; that of supplying metal to the melt pool. With this technique a high powered laser is used (760W Nd:YAG used by Collins *et al*, 2003 and 1.8kW Nd:YAG used by Maziasz *et al*, 1998) to produce a melt pool on the surface. The sample is then moved, while the laser remains stationary, with powders being injected into the melt pool from a feed system allowing material to be added to the surface. Brooks *et al*, 1999, developed a model that predicted the properties of materials produced by LENS technology, given the thermal history of the part. The major problems with components manufactured by this technique are due to the large melt pool and high heat input, which produces fairly coarse, cast structures and high internal thermal stresses.

A further refinement of LENS introduced a multiple hopper powder delivery system to feed a blend of powders to produce a graded structure (Collins *et al*, 2003). The authors used titanium-vanadium and titanium-molybdenum alloy builds to show how the multi-hopper system could produce controlled microstructure and composition. They concluded that this technology had the potential to manufacture near-net shapes with a graded composition for use in aerospace and biomedical applications. However, for most applications it would be necessary to heat treat the components after manufacture to replace the cast microstructure with a more suitable microstructure and to remove residual stresses. One of the most significant problems with this system is due to the component moving rather than the laser beam, as the inertia of the build system limits the maximum scanning speed possible ($<10 mm.s^{-1}$; Brooks *et al*, 1999). A further problem is that feeding the powder into the melt pool means the melt pool tends to be large.

2.2.1.4 Shape Deposition Manufacturing (SDM)

SDM is closely related to LENS in that a number of powders are fed into a melt pool produced by a high powered (2.4kW) Nd:YAG laser. However, unlike LENS, the substrate is fixed, while the deposition system traverses above the surface by means of a robotic manipulator (Fessler *et al*, 1997). As with LENS, the powder feeders are under computer control and the composition can be varied, creating parts with a graded structure. One possibility proposed by the authors of this work on SDM was to mix stainless steel

powders of varying hardness to create a structure that exhibited a 'smooth' variation in hardness. Also claimed was that with the appropriate mixing of these powders, parts more resilient to failure by fatigue could be produced. It is difficult to see how these claims can be justified as fluid movements within the melt pool will remove any composition variations within each layer. This will result in a stepped composition gradient throughout the bulk, with each layer having a different composition. Another example given by Fessler et al, 1997 was the combination of Invar and stainless steel to produce a structure with the low thermal expansion coefficient of the former and the corrosion resistance of the latter.

2.2.1.5 Selective Laser Sintering (SLS)

Invented in the mid 1980s at The University of Texas (Williams and Deckard, 1998) and commercialised by the DTM Corporation (USA), SLS was one of the first SFF processes to be commercialised. The SLS process is another layer-by-layer RP process, where powder is stored in a piston chamber before being spread by a roller or scraper to produce a thin layer. In this case the binding of the powder is achieved by heating the relevant regions with a laser. As each new layer is applied the component is lowered, maintaining the top of the sample at the same height. Initial designs usually used a CO_2 laser, because of the good coupling efficiency with a wide-range of materials, to selectively fuse successive layers of special material powder; suitable powders include metal, plastic and ceramic materials (Bourell *et al*, 1992). Special metal and ceramic powders are normally required because they must contain a polymer binder that can be melted by the laser to bond the powders together. The subsequent green parts must then be post-processed to attain densities greater than 48% and develop reasonable strength. The parts are built-up on a layer-by-layer basis where each layer corresponds to numerically defined cross-sectional geometry (Williams and Deckard, 1998); this information usually being derived from a 3D CAD model. The quality of SLS builds therefore relies on the repeated deposition of a uniform layer of powder across the metal substrate using a platform/roller mechanism. A diagram, provided courtesy of *www.arptech.com.au*, shows the layout of this apparatus (Figure 2.1).

Subsequent developments in SLS have included the use of post-processing techniques, including liquid phase metal infiltration to fill the voids, producing part densities up to 82%

(Carter and Jones, 1993) and the use of other types of lasers. If the CO_2 laser is replaced by a Nd:YAG laser (Fischer *et al*, 2003), to take advantage of the latter's improved absorptivity with metals (Xie *et al*, 1997), it is possible to avoid using polymer binders by using a mixture of low and high melting temperature metals (also known as DMLS). Some of the main advantages of the SLS process are that support structures are not required whilst building is under way and unsintered powder can be reused. The ability to use ceramic and plastic powders as well as those with a primary metal component make this process more flexible than those, such as DMLR, designed to work exclusively with single component metal powders. However, when a key objective to using rapid prototyping technology is to allow the user to carry out a detailed assessment of a design, densification with a secondary material that possesses inferior mechanical properties will affect the performance of the part, reducing the functionality of the process and thus limit its uses. Since commercialisation, several derivatives of the SLS process have been developed, but these changes have been fairly minor involving varying the type and size of the laser and changes to the powder spreading system.

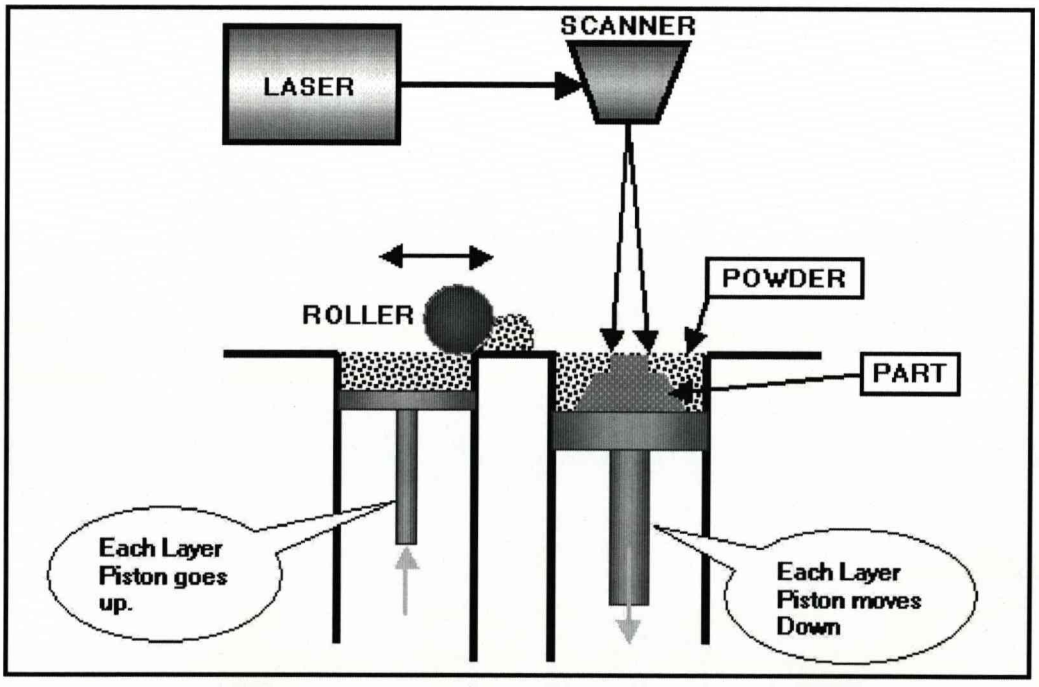

Figure 2.1 The SLS process *(reproduced courtesy of www.arptech.com.au)*

2.2.1.6 Direct Metal Laser Sintering (DMLS)

Developed by Electro Optic Systems (EOS) of Germany, DMLS uses a higher powered (215W) CO_2 laser (Simchi & Pohl, 2003) than SLS to directly melt the metal powders, usually consisting of a primary metal and a low melting point alloy. The system also uses a wiper/platform build chamber rather than the roller/platform system used by SLS, which requires the powder to be carefully sieved before building to attain a higher dry powder fluidity. Although a low melting point alloy is normally used so as to obtain near full density (Simchi & Pohl, 2003), it is possible to produce parts from cast iron powder, which has a wide freezing range, although the resultant parts are porous.

Although DMLS contains certain process advantages over SLS (e.g. higher powered laser and use of alloy rather than thermoplastic binding components), it still shares one of the key weaknesses of the earlier process in that the densification mechanism is sintering, rather than full melting, which must affect the mechanical properties of the final parts and the consequent functionality of the process.

2.2.1.7 Direct Laser Sintering (DLS)

Direct Laser Sintering is basically SLS with the CO_2 laser replaced by a 50W continuous wave Nd:YAG laser (Carter and Jones, 1993). The shorter wavelength light (1.064μm) produced by the Nd:YAG laser couples more efficiently with metals, compared to the 10.64μm CO_2 laser (Xie *et al*, 1997), and the powders are sintered together by partially melting, thus avoiding the use of binding agents. A fully dense component can then be produced by post-processing operations such as hot isostatic pressing (HIP). Also referred to as DLS is work conducted that uses a 200W CO_2 laser system (Zhu *et al*, 2003). This laser was claimed to produce parts with lower porosity than that seen with the Nd:YAG laser. This work was based the use of Fe-Cu alloys, which has direct relevance to the research presented in this thesis and will be discussed later.

2.2.1.8 Selective Laser Melting (SLM)

Selective Laser Melting is a similar technology to SLS but in this case, the powder particles are not sintered together, instead they are fully melted to produce a melt pool.

SLM is in many ways the same process as DMLR (described in Section 2.2.1.11) with the complete melting of the powders offering the possibility of 100% dense components and removing the need for binders or low melting point phases. A possible application was the production of bio-implants from commercially pure titanium (powder particle size <45μm; Abe *et al*, 2000). This work showed that good mechanical properties could be obtained, with the parts having a tensile strength of 120% of the value quoted for solid pure titanium. This increase was probably due either to the oxygen content of the alloy or the small grain size produced. This work was carried out using an SLM system with a 50W Nd:YAG laser, a scanning galvo-head and a moving X-Y table, allowing greater flexibility during the build process. However, this system produced a relatively large, 0.8mm, beam diameter, which limited the feature sizes that could be produced, such as wall thickness and part tolerances. A second effect of the large beam diameter and the low power of the laser was that the maximum laser scan speed was approximately 16mm.s^{-1} which increased build times and led to a coarse microstructure.

Abe *et al*, 2000 concluded that SLM could successfully produce 3-dimensional parts from a titanium powder bed and that the tensile strength was comparable with solid titanium. Unfortunately, the fatigue strength was only 10 per cent of that for wrought titanium, due to porosity and partially fused powder within the build. This problem could be reduced by careful control of the processing conditions (scan pattern and laser scanning parameters), but it was thought by Abe *et al* that suitable fatigue strength would only be achieved after a post-process densification procedure, such as HIP. This would, however, negate the advantages in fusing single component powder beds by directly melting. Although SLM is still a development of SLS, the ability to fully melt the powders together rather than sinter them means that theoretically fully dense, functional, parts can be produced from a single primary material, which is a significant process advantage. The inferior mechanical properties identified by the authors of this work may be addressed if the researchers looked at using a more advanced laser system (e.g. with higher power, smaller spot diameter and increased scanning speeds) that would enable structures with reduced porosity, improved surface finish and improved microstructural control to be produced.

2.2.1.9 Electron Beam Melting (EBM)

Cormier *et al*, 2004 present work looking at EBM, an RP process capable of operating with incredibly high scanning speeds that can, effectively, reduce the total manufacturing time. Commercialised by Arcam, EBM is a layer-by-layer manufacturing technique that uses a 4kW electron beam to melt a powder layer of 0.1mm nominal thickness. This process uses the electron beam to initially preheat the substrate and lightly sinter the powder layer to hold it in place, prior to a main scan which then melts the metal powder. This technique differs from the other melt processing techniques in that an electron gun, rather than a laser, is used, and the heat source and processing is carried out under vacuum rather than a protective gas.

To process H13 tool steel, Cormier *et al*, 2004 used ten preheating scans per layer (with a scan speed of 10,000 $mm.s^{-1}$, each scan with increased power) followed by a high power scan at a reduced scan speed of $500mm.s^{-1}$, the intention being to gradually raise the temperature of the powder bed and so reduce the temperature gradient between the melted layer and the rest of the part. Further, rather than scan the whole area in one pass, each layer was divided up into contours and squares, the former of these representing the build profile and the latter subdividing the interior of the layer into smaller sections. These squares were then melted in a random order that varied between each layer to enable the heat generated to be more evenly distributed across the part and reduce thermal distortion. Analysis of the subsequently formed structures showed a non-homogenous microstructure, of constant chemical composition, that probably resulted from the use of this unusual scanning arrangement. Cormier *et al*, 2004 also found that the resultant microstructures showed "virtually no porosity" with good inter-layer bonding and possessed a martensitic microstructure. Cracking was evident throughout the structure which the authors said was due to shrinkage on cooling.

EBM is a unique process within this review, as the electron beam can scan at extremely high speeds, which can allow preheating scans to take a matter of seconds, rather than minutes (Cormier *et al*, 2004). These preheating scans in turn allow the temperature of the powder bed to be raised relatively slowly, preventing it from experiencing sudden thermal shock. However, this does not seem to stop the component cracking as the cracks appear to form on cooling. As the authors stated, this investigation was initial work on a system

that had yet to be optimised and no beam power or energy data was presented, making direct comparisons with alternative processes difficult. The need to bead blast the final structures to remove partially melted powder attached to the surface and the tendency for the final structure to be cracked does suggest that either too large a melt pool was being formed or that the metal is being overheated.

Besides the claimed energy efficiency of this process, other benefits include the capability of the electron beam to process highly reflective materials such as aluminium and copper. Further, processing the materials under vacuum rather than under a protective atmosphere produced a degree of material purification; the authors reasoned that this was due to the removal of gasses that often cause porosity in metal castings. As with SLM, the ability of EBM to fully melt single component powder beds (i.e. no binding component with inferior mechanical properties) means fully dense, functional, parts could be produced without the requirement for further heat treatment. Whereas SLS has been continually developed by many research establishments over the past twenty years (many research works have been written to attempt to fully characterise the process and many proprietary developments have taken place and been recorded), EBM is a relatively new technology (ARCAM was founded in 1997; www.arcam.com), which is radically different to any other SFF process. Further development by universities and other research groups may allow the process weaknesses to be resolved and a full comparison of the respective benefits of EBM with other technologies to be made.

2.2.1.10 Hybrid (LENS and Spray-forming)

Maziasz *et al*, 1998 presented work on dies produced from H13 tool steel by spray-forming the bulk of the die, with the fine detail being produced using LENS. The authors claimed that by combining the two Direct Fabrication (DF) processes, the use of conventional normalising and tempering heat treatments, that can result in part distortion, could be avoided.

Maziasz *et al*, 1998 produced an H13 steel block by induction melting the H13 in a nitrogen atmosphere before pressure feeding it into a converging/diverging spray nozzle so it was sprayed onto a steel substrate. The material was deposited at a rate of 200kg/hr.

LENS was then used to build up further deposits on this underlying structure by streaming H13 powder into a focussed 280W CW Nd:YAG laser beam. Characterising the resultant microstructure, the authors of this work found that the spray forming process produced a fine-grained bainitic microstructure with some retained austenite at the grain boundaries and a 98% density. The rapid heating and cooling rates of the LENS process produced a finer, more uniform, martensitic microstructure with possibly some retained austenite. A harder H13 structure was reported to be formed by the Spray-forming process (659Hv compared to 564Hv for LENS), with additional post-process tempering effectively normalising the microstructure and hardness values.

Further investigations looked at using LENS to deposit H13 onto either mechanically-polished or alternatively "as-received" Spray-formed surfaces. Here, higher normal stresses were observed when a polished substrate was processed compared to the unmodified surface. The polished surface was also found to show a thicker "processing zone" – a region below the surface that was affected by the LENS process. Examination of material deposited by the LENS process detected no residual stresses, the authors concluding that this was due to the stress-relieving nature of the LENS process. This analysis also showed that the microstructure of the Spray-formed material varied with distance from the surface, unlike the more uniform LENS structure.

The hybrid LENS and Spray-forming process is included in this review as it shows how RP technology (i.e. LENS) can be combined with other processes to increase their functionality. Maziasz *et al*, 1998 found that the coupling of the two processes allowed parts with superior, tailored, mechanical properties to be obtained. Spray-forming was used to manufacture the bulk of the final parts, the areas where the mechanical properties were less critical, whilst LENS produced the surface details where a more uniform and predictable microstructure would be required. In this respect, as well as detailing the dissimilarity in microstructural formation between the two processes, this work demonstrated a solution that would avoid the need for potentially damaging heat treatments.

2.2.1.11 Direct Metal Laser Remelting (DMLR)

As stated previously, DMLR and SLM are essentially the same process and there is some interchangeability in the use of the terms. However, DMLR has been the preferred term for the version of the process that uses a higher power (90W) Nd:YAG laser with a finer spot size (100μm) to directly melt the metal powder (Morgan *et al*, 2001 and Pogson *et al*, 2003). As with SLM, the process involves the movement of a melt pool across a pre-laid, thin layer of powder to build the component, with specially derived scanning strategies being used to improve densification. The process requires no additional binder or low melting point phase but uses the increased absorptivity of the Nd:YAG laser radiation with metal powders (when compared with CO_2 laser radiation; Xie *et al,* 1997) to directly melt the powders. This allows near fully dense parts to be produced from a primary metal.

The fine spot size and higher power allows the use of rapid scan speeds (up to 500mm.s^{-1}), increasing process rates and allowing finer features to be formed (wall thicknesses of the order of 100μm can easily be produced). A secondary effect of the rapid laser scanning speed is an increased cooling rate that produces a finer microstructure. A more detailed description of this process is included in the next chapter (3.0).

2.2.2 Mechanism for Build

2.2.2.1 Solid Phase Sintering

A strict definition of sintering (German, 1996) is of "a thermal treatment for bonding particles together into a coherent, predominantly solid structure via mass transport events that occur largely at atomic level", locally fusing adjacent particles together. For this definition to apply to laser sintering, the laser must only heat the powder bed to just below the solidus temperature of the powder so that all the material remains in the solid phase. The bonding together of the powder would then occur by solid state diffusion forming necks between adjacent powder particles (Amon *et al*, 1993), the driving force being the reduction in particle surface free energy. As this process occurs in the solid state, it will be very slow and unsuited to the types of rapid processing described in this review. With solid phase sintering, densification can be assisted by using particles of varying size with the smaller particles filling in the voids between the larger particles, increasing the maximum

packing density (German, 1996). In general, the principal mechanisms of solid phase sintering are vapour transport (where constituent components migrate through liquid metal in the vapour phase), grain boundary, surface and volume diffusion (Tolochko *et al*, 2003). As all of these processes are slow, they probably do not significantly occur in most laser-based rapid processing systems.

A more likely process for the rapid fusing of particles occurs if the powders melt over a range of temperatures, for example with alloys (between the liquidus and solidus) and mixed powders with different melting points. When there are two powders with different melting points the liquid phase can occupy the voids between the higher melting point particles to form a dense material even though the powder bed has not fully melted. However the need for a lower melting point metal restricts the systems that can be used and tends to produce weaker components.

2.2.2.2 Liquid Phase Sintering

Many products are processed by liquid phase sintering such as dental porcelains, cemented carbide cutting tools, automotive connecting rods and refractory ceramics (German, 1996). With Selective Laser Sintering, liquid-phase sintering is used with multi-component powder beds, with one or more of the powders melting to form the liquid phase (Tolochko *et al*, 2003). Densification is achieved by the low melting point material forming a binder between the higher melting point components. German, 1996 stated that full density could be reached if enough liquid phase was formed within the system during processing. If the particles were initially spherical and of one size, then a theoretical packing density of 74% can be reached and this would require a minimum liquid content of 26 vol. % to fully fill the voids. Even with powder systems that melt at one temperature, liquid phase sintering is still theoretically possible if the processing conditions can be adjusted so that the powder nearest the heat source melts but that the particles further away do not. Tolochko *et al*, 2003 proposed that this could only occur with thin layers, as the only temperature at which, for a pure metal, solid and liquid phases could exist in equilibrium is at the melting temperature. This is, of course, not true for alloy powders.

Simchi *et al*, 2001, when discussing Direct Metal Laser Sintering, identified sintering as occurring by the liquid phase (the primary metal powder being pre-alloyed with a lower melting point powder that melts under the laser). As this liquid phase flows and wets the solid particles, rapid densification occurs by the rearrangement of the solid particles. The authors reported that single element metal systems could not be processed by Direct Metal Laser Sintering as pure metals melt at one temperature and, therefore, there is no liquid flow to aid densification, even at temperatures approaching the melting point of the powder.

2.2.2.3 Supersolidus Liquid Phase Sintering (SLPS)

SLPS has been considered by several authors (Simchi *et al*, 2001 and German, 2003) as being an important mechanism by which laser sintering occurs. The term refers to the sintering of materials at temperatures between the liquidus and solidus, in what Simchi *et al* referred to as the 'mushy zone'. Within this range, which varies from alloy to alloy, both liquid and solid can coexist and sufficient liquid may be formed to aid densification. This mechanism is different from true liquid phase sintering because the liquid phase is formed within individual particles (German, 2003); with the liquid spreading to form pendular bonds at the particle contacts. Densification occurs because of capillary forces between the wetted, weakened, semi-solid particles. Careful control of the temperature is important with SLPS processing, especially with alloys with a narrow semi-solid temperature range as small temperature changes can lead to either full melting or not melting at all, completely changing the process (Simchi *et al*, 2001).

2.2.2.4 Laser Melting

With laser melting, sufficient energy is supplied to fully melt the powder bed (Amon *et al*, 1993). Two major advantages of melting over sintering are that the process is rapid as the particles melt and fuse together, and the formation of a melt pool should make it possible to produce 100% dense material. Two disadvantages are that molten metal tends to be harder to control and that whatever component is formed will have a cast structure. Thus, copper can be processed by laser melting to produce a high thermal conductivity

component, while sintering would produce worse thermal properties due to the inclusion of a low melting point alloy or a thermoplastic.

Complete melting of the powder bed means that densification is controlled by the temperature of the powder bed, the fluidity of the metal in its molten state and the wetting characteristics of the metal concerned (Su *et al*, 2002, Morgan *et al*, 2001 and Pogson *et al*, 2003). Changes to the process parameters and subsequent heating/cooling rates will modify the cast structure, producing either finer or coarser microstructure. However, it has been found that if the heating and cooling rates are too high, then thermal stresses can form as the material freezes (Morgan *et al*, 2001 and Pogson *et al*, 2003). If insufficient energy is supplied by the power source to the powder bed, solid or liquid phase sintering may occur instead, producing only weakly bonded material.

2.2.3 Lasing Strategies

In Selective Laser Sintering and its derivatives, CO_2 and Nd:YAG lasers are most commonly used due to their price, commercial availability and suitability with the materials commonly processed, (LIA Handbook of Laser Materials Processing, 2001). This section will focus on these two types of laser and the key laser processing strategies that can be employed.

2.2.3.1 Pulsed CO_2

The CO_2 laser used to be the most popular choice for SLS applications due to its good coupling efficiency with most materials and its low price per Watt (Amon *et al*, 1993). It also allowed ceramics, thermoplastics and metals to be processed using the same heat source. Pulsed mode means that the amplitude of the laser power varies with a given frequency (pulse repetition rate). When the laser is operated in this mode the average beam power is decreased and less energy is fed into the material (Eurolaser Academy, 1998), the energy being supplied as a series of discrete pulses. The majority of CO_2 lasers can be operated in pulsed or continuous wave (CW) mode.

2.2.3.2 Continuous Wave CO_2

When a laser is operated in CW mode the power is continuous and of constant amplitude. CO_2 lasers are normally operated in this mode (Eurolaser Academy, 1998). Although the selection criteria for using pulsed or CW mode has been published for Nd:YAG lasers (Morgan *et al*, 2001) similar work has not been published for CO_2 lasers. However, in work undertaken using a 200W CW CO_2 on iron/copper powder beds (Zhu *et al*, 2003), continuous power delivery was considered important because it made it easier to compare the interactions between process conditions and the materials produced.

2.2.3.3 Pulsed Nd:YAG

The Nd:YAG laser is usually operated in pulsed mode (Laser Institute of America, 2001). Carter and Jones, 1993, state how the shorter wavelength of the Nd:YAG (1.06μm) transfers heat in to metals more efficiently than the longer wavelength (10.6μm) CO_2 laser. The Hagen Ruben relationship described by Xie *et al*, 1997 shows that the absorptivity of metals is 3.16 times greater with an Nd:YAG laser than with a CO_2 laser. Consequently, a reduced quantity of optical energy is lost.

As with pulsed CO_2 lasers, the aim of using a pulsed Nd:YAG laser beam is to introduce a near instantaneous pulse of energy into the powder bed. Peak laser power resulting from this pulsing far exceeds the nominal laser power resulting from operation of the laser in CW (Continuous Wave) mode. An example calculation of this is shown in Appendix 1.0.

Nd:YAG lasers are often used in pulsed mode when processing powders with a relatively high melting point. These materials require higher laser powers to melt the powders where these powers may not be possible in CW mode, without replacing the laser with a more powerful and expensive unit. In such a case the high peak powers exist only for a short time but the pulse is sufficient to melt the powder. The use of an Nd:YAG laser in pulsed mode can be disadvantageous as shock waves can develop in the powder bed, displacing the powder (Morgan, 2003). Morgan *et al*, 2001 also reported that high energy pulses were responsible for generating thermal stresses within the build, producing features such as tears or curling.

2.2.3.4 Continuous Wave Nd:YAG

Although Nd:YAG lasers are not normally operated in CW mode (Eurolaser Academy, 1998), the ability to operate in this mode combined with improved absorptivity by metals (Xie *et al*, 1997) gives Nd:YAG lasers an advantage over CO_2 lasers as the power being absorbed by the powder bed is greater and consequently a lower powered laser is required. Laser light with a wavelength less than 1.2μm has a reflectivity of between 85 and 95% with polished metals, whilst CO_2 laser light with a longer wavelength has a reflectivity approaching 99% (Laser Institute of America, 2001). The use of the Nd:YAG laser in CW mode also produces a higher average power than that possible in pulsed mode; although the peak power available is lower (Eurolaser Academy, 1998). Therefore, if an Nd:YAG laser capable of operating in both pulsed and CW mode is selected, a larger range of processing parameters is available for the production of satisfactory parts. As with other processing parameters, the most satisfactory regime may be largely material dependant with the laser being switched from CW to pulsed mode when the material changes.

2.2.4 Build Technique

This section describes the different methods used to place the powders before laser processing can take place and how the choice of method affects the flexibility of the manufacturing/prototyping process used.

2.2.4.1 Pre-Placed Powder Bed

A pre-placed powder bed is one where the powder is manually placed into a well in a container and levelled off to produce a single flat, thick, uniform layer. The entire unit is then placed into the build chamber prior to laser processing. Although this technique allows simple metallographic and microstructural analysis (Morgan *et al*, 2001 and Pogson *et al*, 2003), multi-layer parts are difficult to produce as the deposition of subsequent uniform layers is not trivial.

2.2.4.2 Roller/Platform

This technique, used in SLS and its derivatives (see Figure 2.1), is based on a powder storage platform that displaces upwards to provide powder. A second platform, upon which the build substrate is located, displaces down by an equal distance. The roller then distributes the powder across the build platform to produce a uniform layer, which is then laser scanned. The major advantages of this technique are that it is quick and that the spreading of the powder by the roller increases the pre-scanning dry powder packing density. There are difficulties in controlling layer thickness, unless the system is well designed, which tends to be worse with mixed powder layers as each powder may have a different packing density. The major disadvantage, however, is when trying to produce composition variation, as even with multiple powder sources only uniform compositions can be produced within each layer.

The characteristics of the powder bed before (SLS) sintering are reported (Karapatis *et al*, 1999) to significantly affect the quality of the finished component. More specifically, it was reported that the relative density of the bed directly influenced the density of the sintered body, the large voids in a coarse powder bed making a fully dense structure harder to achieve. However, if a mixture of fine and coarse powders were used, the fine powder would fill the voids producing the highest possible layer density before sintering. The significance of powder bed density in DMLR is more difficult to ascertain as the powder entering a melt pool would remove any voids between the particles.

2.2.4.3 Wiper/Blade

Used in DMLS, the wiper/blade levels the powder and produces the correct layer thickness, after a powder container has deposited an approximate amount of powder onto the surface. The laser beam then scans the resultant layer to produce the component (Yevko *et al*, 1998). The use of a wiper system requires that the dry powder has satisfactory fluidity to allow it to be spread evenly across the substrate. For this, the powder must be sieved prior to use, the humidity controlled and the optimal powder particle shape and size distribution used (spherical powders of a narrow size distribution) to allow the particles to roll over each other. Again, there is difficulty in depositing more than one powder within the same build and achieving a controlled composition. As with the

roller/platform system, multiple powders would require separate powder containment systems prior to being spread over the substrate, but it would be difficult to keep these separate during this procedure. Similarly, as with the roller system, the wiper would not be able to have sufficient control over the powder distribution to allow specific powders to be placed in pre-determined locations.

2.2.4.4 Blown Powder

Blown powders are used with laser cladding where a high-powered laser forms a melt-pool on the surface of the substrate and powder is blown into it. The powder is stored in a hopper and is fed into the melt pool by means of a flow of argon. This powder feed along with the laser traverses across the surface of the substrate until the layer has been completed (Steen, 1998). The advantage of this deposition method is that when it is combined with a high powered laser (e.g. 3kW Nd:YAG with a ∅3.34mm spot; Pei and Hosson, 2002), a fully dense part is readily achievable. However with this work, the size of the laser spot limits the size of the smallest dimension that can be produced, which restricts the parts that can be created.

Laser Melt Injection uses a similar powder delivery system to Laser Cladding, but with the former, reactions between the injected materials and the melt pool tend to be minimised. Pei *et al*, 2002 described work injecting silicon carbide particles into a melt pool so as to form a composite layer on a surface of a metallic substrate. To minimise reactions between the metal and ceramic, the injection point was behind the traversing laser beam rather than into it, with the powder stream being positioned close to the beam, but without touching it. The focal spot of the beam was maintained 9mm above the substrate and this produced a ∅3mm laser spot. This illustrates well one of the major problems when using melt pools, the rapid reactions between materials. Also, the use of blown powders feeding into a melt pool makes the control of the melt pool more difficult compared to when powders are deposited prior to scanning, as careful control is required to produce a flat surface and a melt bead of a controlled height.

2.2.4.5 Intermixed Powder Feed

In this example, used in Shape Deposition Manufacturing (Section 2.2.1.4), a number of powder feeds are fed into a single powder delivery nozzle and by altering the supply of the different powders the material's composition and properties can be varied (Fessler *et al*, 1997). The combination of this powder feed mechanism and accurate laser control should allow both structural and chemical gradation, with the variation occurring with position in a layer as well as between layers, allowing the production of material with continuously varying properties. Fessler *et al* coupled this powder deposition method with a high powered (2.4kW) Nd:YAG system with the specific intention of fully melting the powder to produce fully dense parts, which was reported to improve the material functionality. However, the use of a powder feed that traverses the substrate restricts the minimum size of feature that can be produced, as the feature size is controlled by the size of the melt pool, rather than the laser spot size. The melt pool tends to be relatively large as the deposition system can only move reasonably slowly over the surface.

A micro-intermixed powder system has been produced (Yang and Evans, *private communication, 2003)* that uses a number of nozzles to deposit individual powders from vibrating hoppers, numerical data being used to control the vibration, which in turn controls the powder flow so that powder is deposited in pre-defined areas. An earlier micro-LENS version of this system was tested where a carrier gas delivered the powder, but this system still had most of the problems associated with LENS technology and, therefore, a system that avoided blowing the powder was developed. By carefully controlling which powders were deposited in which locations, a graded powder bed layer could be laid-up prior to laser melting. This technique avoids the increased melt pool size associated with slow scanning, by separating the layer deposition and laser scanning cycles, allowing the laser to be scanned rapidly.

2.2.4.6 3D Printing/Ink-Jet Printing

With this technique the powder is deposited by means of one or more 'print-heads' that traverse the powder bed; multiple print heads allowing the deposition of several different powders in a single build (Jackson *et al.* 1999). As such, this powder deposition technology should be able to produce FGS, if it is coupled with a suitable laser system.

The print-heads could, theoretically, integrate both the powder feed and laser scanning galvanometers providing a flexible system of reduced size. Ink-jet deposition systems have been developed to produce ceramic structures (Mott and Evans, 1999 and Mohebi and Evans, 2001) and this work at Queen Mary, University of London has being developed further for the Ink-Jet printing of metal powders (Yang and Evans, *private communication, 2003*). Development of the metal ink systems requires the use of fine powders (<5μm) as the powders have to be kept in suspension. Even with these fine particle sizes, both constant agitation of the 'inks' and the use of an organic additive to aid suspension are required to prevent the powder from settling out within the ink jetting system and blocking it. The requirement for small particles sizes restricts the use of this system, as only a limited range of powders are available in these small sizes. A second problem is that the solvent and organic additive must be removed from the powder before laser melting, if the build is not to be contaminated.

2.3 Characterising the DMLR Process

2.3.1 Introduction

For the DMLR process to be characterised, the interactions between a large number of process variables must be understood. This is especially important when comparing results from different systems. For example, DMLR work at Liverpool used a lower powered Nd:YAG laser (90W), with a small spot size (Ø0.1mm) and fine powders (<22μm), while work at Loughborough, funded as part of the same research project, used a high power Nd:YAG laser (550W), a large spot size (Ø1mm) and a large powder size (<212μm), (Su *et al*, 2003). If any meaningful comparison of the results from these systems is to be made then it must be possible to determine process variables, such as, heating and cooling rates and the size of the melt pool.

Williams and Deckard, 1998, produced a simple relationship between three of the key laser processing parameters used during SLS (Eqn. (1)). The *Andrew Number*, which is a measure of specific energy density applied to a powder bed, is reasonably useful for helping to understand the interactions between processing parameters but its application

is limited as it considers neither the size of the heat source (laser spot size) or the loss of energy from the melt pool, which is important in determining the behaviour of the system.

The *Andrew Number* ($J.mm^{-2}$) is defined as:

$$A_n = \frac{P}{v \times d} \quad (1)$$

Where P is laser power (W), v is laser scanning speed ($mm.s^{-1}$) and d is the scan spacing (mm).

The relationship above is limited because it does not consider the effects of varying the powder particle size or variations in absorptivity of the laser energy between the melt pool, powder bed and solid metal.

The effect of powder particle size can best be described by considering that the application of laser energy will raise the temperature of the powder particles beneath the laser beam. An increase in particle radius (r) would result in an r squared increase in particle surface area ($4\pi r^2$) and an r cubed increase in particle volume ($4/3\pi r^3$). As the particle surface area increases (and thus the particle's area which couples with the laser radiation increases also), its volume will increase rapidly. Therefore, the ratio of surface area to volume will decrease accordingly as the particle radius increases. So for a given laser intensity the larger the particle the lower the power to volume ratio so the longer it takes to heat. Inversely, as the surface area to volume ratio is increased, the particle should be easier to heat up and should melt more readily. From this, if all other properties remain constant a smaller particle will have more energy falling on its surface for a given volume than a larger particle. This is important when considering the behaviour of a powder bed, as it predicts that larger particles are more difficult to melt for a given laser power. However, as mentioned above, the absorptivity of the powder bed is an important consideration when modelling the DMLR process. Hauser *et al*, 2004 reported that the unmelted powder had an absorptivity for laser radiation approaching that of a black body, whilst the molten metal has a far higher reflectivity.

2.3.2 Modelling the Process

Models based on numerical and analytical data are used to develop an understanding of manufacturing processes in a way not possible using simple experimentation. Recent advances in computer technology have made it possible to carry out many calculations per second. This allows complex 'finite element' type simulations to be developed, allowing understanding of the overall process to be refined. This section of the review describes the published modelling work on DMLR and related processes, to provide the reader with an understanding of the issues and process constraints when producing graded structures by this method.

The modelling of the laser melting of powders is complex and models were initially developed from work considering conventional manufacturing processes, such as welding (Kou, 1981). The author described a model based on two-dimensional steady state heat flow during the welding of plates. As the heat and mass transfer mechanisms are similar, an insight into the behaviour of a localised heat source transferring heat to and subsequently melting the metal is possible. To further enhance the model, the author considered more variables in his calculations, including heat conduction in the welding direction, the latent heat of fusion, the size and distribution of the heat source, the temperature dependence of thermal properties and the surface heat loss due to both convection and radiation. This work also described a molten weld pool controlled by a moving heat source, such as a tungsten electrode, electron beam or laser beam that traversed across the surface. Due to the difficulty in modelling heat transfer due to convection, Kou used an effective thermal conductivity allowing the formulation of an energy balance equation for the melt pool.

Due to the nature of the two-dimensional heat flow, Kou took Q_{source} to be a line heat source of strength qA/g, located at (x_{source}, y_{source}) and Q_{sink} to be a line heat sink of strength $h_{eff}A(T-T_{\infty})/g$ located at (x_{sink}, y_{sink}).

The quantity of heat put into the welded plate (kJ) can be defined as:

$$Q_{source} = (qA/g)\delta(x - x_{source})\delta(y - y_{source}) \qquad (2)$$

Where q is the heat flux ($W.m^{-2}$), A is the surface area of element subjected to heat input or heat loss (mm^2), g is the thickness of the plate (mm) and δ is a unit impulse function.

The surface heat loss due to convection and radiation (kJ) can be defined as:

$$Q_{\sin k} = \left[h_{eff} A(T - T_\infty)/g\right] \qquad (3)$$

Where T_∞ is the ambient temperature (K) and h_{eff} is the total heat transfer coefficient due to convection and radiation ($W.(m^2.K)^{-1}$).

Kou, 1981 then suggested that for a track of sufficient length the temperature distribution would attain a steady state (with respect to a coordinate system moving with the heat source), except for the initial and final stages of a weld track. The time dependant function in Eqn. (2), therefore, becomes zero and the process is reduced to a steady state heat flow problem, allowing finite difference equations to be used to calculate the temperature at specific nodes. If the material was solid or liquid the calculation was fairly simple but between the solidus and liquidus the fraction of solid or liquid phase is required for calculating the enthalpy of the mixture. The calculations made several assumptions to simplify the problem. The workpiece was idealised to be symmetrical about the centreline of the welded track. As such, only the temperature distribution in one half of the workpiece needed to be calculated. Far away from the heat source, it was assumed that the workpiece was unaffected by the heat flux and the temperature remained unchanged. As the workpiece was thin, the heat loss at the sides of the plate was assumed to be negligible compared to that from the top and bottom surfaces.

To use this model a grid of varying spacing was applied to the top surface of the computer model, a denser mesh being used nearer to the heat source with an increasing mesh spacing further away. The temperature distribution was then calculated and compared with empirical data from tests carried out using an automatic tungsten arc welding apparatus under varying welding conditions. Good agreement was found between the results and the model.

Kou, 1981's work is of interest as it proposes solutions to the dissipation of heat from the localised heat source as well as considering material properties and latent heat of fusion. However, several features must be considered before applying this model to the construction of a multi-layer part using the laser melting of metal powders. The 6mm effective radius (∅12mm) of the heat source is much larger than the ∅100μm spot size used by most DMLR and the speed of the weld (4mm.s^{-1} to 5mm.s^{-1}) is markedly slower than that for most DMLR experiments (up to 500mm.s^{-1}). This results in not only a much larger melt pool than with DMLR but also means that the effects of heat transfer by convection and radiation become insignificant compared to those by conduction. However, the welding system is similar to laser melting in that the heat transfer at the boundaries is similar. Kou assumed that because the plates were of thin-section the heat transfer at the edges would be negligible. Similarly, because the layers that are being processed by laser melting are surrounded by unmelted powder, who's thermal conductivity is much less than for the solid material (Hauser *et al*, 2003), heat transfer at the edges is also negligible.

The simplification of Kou, 1981's model by making it symmetrical about the centreline, although reasonable when considering the welding of thin section plates, limits the application of the model to DMLR as it is not possible to model the effects of previously scanned tracks and their effects on the thermal history of the work piece. This may not only alter the volume of material within the previously welded area but would also affect the boundary condition that the material is at ambient temperature away from the heat source. Therefore, although this model is initially accurate, as the build continues and heat builds up within the component, the model becomes increasingly inaccurate and, therefore, more complex models are required to model DMLR.

Complimenting Kou, 1981's work, Steen, 1998 and Carslaw and Jaeger, 1959 provide analytical solutions to the flow of heat through the workpiece rather than the temperature profile across the surface. Within their text, Steen describes an analytical solution which expresses the temperature as a function of time and distance from the surface. The temperature (K) is defined as:

$$T(z,t) = T_0 + \frac{2.P.A^{\prime}}{\pi.\omega_0^{\,2}.k}\left[(\alpha t)^{\frac{1}{2}}.ierfc\left(\frac{z}{2\sqrt{\alpha t}}\right)\right] \qquad (4)$$

Where α is the thermal diffusivity ($m^2.s^{-1}$), ϖ_0 is the effective beam radius (m), k is the thermal conductivity ($W.(m.K)^{-1}$), t is time (s), t_0 is the interaction time between beam and powder bed (s), A^l is the absorptivity (%; = 1 – Reflectivity), P is the laser power (W), temperature (K), T_O is the initial temperature of the powder bed (K) and z is the distance from the surface of the powder bed (m).

The integral of the complimentary error function, *ierfc*, is:

$$ierfc(x) = \frac{e^{-x^2}}{\sqrt{\pi}} - x.(1 - erf(x)) \qquad (5)$$

And the complimentary error function is:

$$erfc(x) = \frac{2}{\sqrt{\pi}} \int_0^x e^{-t^2} dt \qquad (6)$$

A prediction of the temperature profile for the work described in Section 4.1.1 has been calculated using the above formulae, in conjunction with physical data for a tool steel and the processing conditions used in this thesis. This is shown in Appendix 2.0. In this example, it was assumed that the melted block was fully dense and that the laser beam was used in continuous wave mode rather than pulse mode (as the high instantaneous power surges associated with pulsing the beam, and the cooling that occurs between pulses, cannot be modelled by this equation).

Peng *et al*, 2001 also looked at deriving numerical solutions for the melting of solids, this time providing a more general case that could, the authors say, be applied to the laser melting of solids. By initially calculating the critical time for heat conduction in the molten pool, the authors predicted the size and dynamics of the melt pool and assessed its effect on subsequent melt pool development. Investigating the effects of Marangoni flow (convection initiated by surface tension gradients), natural thermal convection and thermal conduction, this work determined the times and dimensions that, above which, heat transfer by thermal conduction was no longer the dominant mechanism controlling the size of the melt pool. Describing the system in terms of two-dimensional heat transfer, Peng *et al*, 2002 used a derivation of suitable boundary conditions to model the melting process.

The authors noted that for their theoretical and analytical estimation to begin, information on the initial molten pool was required. By predicting the formation of this pool, they found good agreement between their predictions and experimental results, up to a certain point. Below a critical time and pool thickness (a critical time of 5.4 seconds, and a pool thickness of 0.37mm were suggested), the melt pool growth was found to be controlled entirely by conduction. Above this time and pool thickness the calculations predicted that heat transfer would also be affected by Marangoni forces resulting in convection within the melt pool, consequently affecting melt pool growth.

Peng *et al*, 2001's work appears to indicate that Marangoni forces should be negligible during DMLR processing as at a laser scanning speed of 300mm.s^{-1}, the melt pool traverses a distance of 100μm (the diameter of the laser spot) in 0.003 sec, much less than the critical time Peng *et al* found for the onset of Marangoni forces. However there is an important difference between this work and DMLR in that the melt pool in Peng et al's work was stationary and that temperature gradients were shallow (1-10K). However, Yilbas and Aleem, 1999 calculated that for laser surface melting the cooling rate for 321 stainless steel was in excess of 10^6 Ks^{-1} implying that cooling from 2000°C to ambient takes less than 1/100th of a second. Hofmeister *et al*, 1999 measured the cooling rate of Laser Engineered Net Shaping (LENS), using a thermal imaging camera, to be in the range 100 to 1000Ks^{-1} for a laser scanning speed of 7.62mm.s^{1}. The high scanning rates and rapid cooling in DMLR lead to very steep temperature gradients which greatly increase the variation in surface tension that drives the Marangoni forces. This makes it likely that the minimum melt pool thickness in which flow occurs under Marangoni forces will be much thinner for DMLR than the case considered in the model. Other authors consider Marangoni forces to be important in SLS processed metals in that they lead to the generation of thermal stresses within solidifying melt pools (Simchi *et al*, 2001).

For some years, researchers at Leeds University have been developing a computer based model to accurately simulate the Direct Metal Selective Laser Melting of powders. Hauser *et al*, 2004 reported on further developments to this model to include the variation in powder bed properties as it is heated to in excess of the liquidus temperature. Unlike other authors' work, this paper considers how the thermal properties of the bed change from those of unmelted powder to those of solid metal, including how the material absorptivity of

the laser radiation varies. Using experimental data obtained from a CO_2 laser system operating at up to 200W and scanning speeds from 0.5 to 500mm.s^{-1}, the authors processed both single tracks and single layers, using M2 or H13 tool steel or 314S stainless steel, to test the validity of their model and thus explain the formation and morphology of these tracks. The simulation was developed to consider the effects of powder bed densification as the temperature is raised from T_S to T_L. Hauser *et al* used the model to predict the temperature distribution and the mass per unit length of the melt tracks, and these results were then compared with experimental data for the same conditions. Using the thermo-physical properties of the three different alloys, it was possible to estimate the length, depth and width of the melt pool. Additionally the authors used the following relationship to calculate the changes in laser absorptivity during processing. The minimum estimate of laser absorptivity (%) is defined as:

$$\alpha_{\min}(P/v) = m\{C_P(T_L - T_o) + L\} \qquad (7)$$

Where v is the laser scanning speed (m.s^{-1}), P is the laser power (W), C_p is the heat capacity (J.(kg.K)$^{-1}$), m is the track mass per unit length (kg.m^{-1}) and L is the latent heat (kJ.kg^{-1}).

The experiments showed that a variation in laser absorptivity occurred between the melted and unmelted powder; the absorptivity changing with the degree of melting, (the absorptivity of the unmelted powder bed approaching one, i.e. the same as a black body). The total cross-sectional area and subsequent mass per unit length were calculated assuming the tracks were cylindrical. This data was then compared with the experimental results to assess how the physical properties of the tracks varied as the processing parameters were changed. As with most models, to simplify the process and prevent overly long calculations, several assumptions were made, including assuming that the tracks were cylindrical. This model does, however, use empirical data to revise the simulation improving the overall accuracy. The simulations described by Hauser *et al*, 2004 are still being developed and continually improved software should increase the overall reliability of the data and make the work more complete. Hauser *et al* also considered Rayleigh instability and the break up of scan tracks into short sections during processing. This concept is used by a number of authors to explain the breaking up of

cylindrical scan tracks into short sections. Niu and Chang, 1999, describe how sinusoidal fluctuations in a cylinder of water cause it to become unstable when the wavelength, λ, is greater than the cylinder circumference; the cylinder breaking up into short sections reducing the surface area and energy. The driving force for this behaviour is the same for water and molten metal and so it is possible to predict when Rayleigh instability will occur.

Rather than using empirical data and modelling to develop a computer simulation of the processing of metals, Shen *et al*, 2001 proposed a more fundamental mathematical model of laser heating of solids. This work used purely analytical solutions to assess the temperature distribution before and after melting, the discontinuity in the thermal gradient giving an indication of the effect of the latent heat of fusion on the cycle. Unlike Hauser *et al*, 2004's model, which assumed that the material properties (thermal conductivity and heat capacity) varied linearly with temperature, Shen *et al*, 2001 assumed that the physical properties of the material remained constant with temperature (i.e. they did not consider the variation in physical properties from unmelted powders to molten metal).

Shen *et al*, 2001 used analytical solutions to calculate the melt depth at incremental time periods from the initial radiation of the workpiece using a stationary light source. The thermal predictions were then compared with earlier published experimental work to test the validity of the model. The calculations showed that the melt depth increased rapidly to begin with but then slowed, as Hauser *et al*, 2004 predicted. This is probably due to the variation in laser radiation absorptivity with temperature. Good agreement was observed between the theoretical and experimental results when $t < 3s$. At greater times, Shen *et al*, 2001 considered that the formation of plasma above the meltpool would absorb some of the laser energy and partially block the incident laser light. The formation of plasma above the powder bed surface has also been reported by other authors to affect processing when using a laser with low pulse repetition rates where there are high instantaneous power surges (Morgan *et al*, 2001).

Shen *et al*, 2001 noted a rapid decrease in temperature within the melt pool from the surface to the base (which was at the melting point of the alloy). Following a discontinuity in the temperature gradient at the solid/liquid interface, there was a gradual decrease in temperature within the solid until ambient temperature was reached. The authors adjudged

this discontinuity to be a consequence of the latent heat of fusion and the higher thermal conductivity of the solid. The model was used to compare the behaviour of four metals, and to determine the variation in melt depth for different incident power densities, noting that copper and silver, with their high thermal conductivities and low absorptivity, are more difficult to process at lower power densities. Furthermore, more energy was conducted through the solid/liquid interface for silver and copper, requiring greater laser energy to achieve melting. However, the model showed that at higher power densities, the behaviour was reversed and the melt depth for copper and silver would exceed that of aluminium and titanium. As a method of providing analytical solutions to the temperature profiles of different materials and using these to explain the difficulties in processing certain materials, Shen *et al*'s work is valid. However, assuming that the laser heating and melting is a linear process and that the physical properties of these materials are independent of temperature contradicts the findings of Hauser *et al*, 2004.

2.4 Laser Processing of Composition Gradients

The work presented in Chapter 4.0 examines the modelling of compositional functional gradients using mixed powder beds of fixed composition consisting of copper and H13. This section of this literature review considers work that has been conducted on the processing of copper and iron-based alloys.

To understand the laser processing of a multi-component system, specifically, a powder-bed consisting of copper and H13 tool steel, the relevant binary and ternary phase diagrams must be reviewed (American Society of Materials, 1997). As no phase diagram could be found for H13 tool steel, the binary diagram for copper and iron, as well as the ternary iron, copper and carbon diagram was studied. However, because of the presence of additional elements within tool steel that affect phase formation and the high cooling rates with DMLR, the phase diagrams are limited in predicting the solid phases that will form. A detailed literature study was therefore required to provide a more comprehensive understanding of the metallurgical interactions.

2.4.1 Laser Processing of Copper

Prior to undertaking the research work discussed in this thesis, an MSc project was undertaken by the author looking at the manufacture of micro heat exchangers using DMLR (Pogson *et al*, 2003). In this instance, parts were constructed using single component powder beds consisting of 80%<22μm OFHC copper powder. Using a wide selection of processing parameters, revised scanning strategies and repeated experiments, a process window was defined, within which the most satisfactory parts were produced, i.e. that had reasonable strength and has fused together sufficiently so that further analysis could be undertaken. Pogson *et al*, 2003 describes how the optimal copper parts were produced with a laser scanning speed of 100mm.s^{-1} and a laser power of 82W continuous wave (the maximum achievable with the Nd:YAG laser used for this work and the work described in this thesis). Under these conditions it was also necessary to have four laser passes per layer so that a high enough temperature was reached to melt the copper. Although this work described how a laser system and a layer-by-layer manufacturing technology could be used to produce coherent 3-dimensional copper parts, it did not consider the processing of copper in a multi-component powder bed.

Other work on copper has tended to consider copper-based alloy systems (Zhu *et al*, 2003(b)). The authors pre-alloyed a SCuP binding component with a 40μm copper powder to aid densification. Phosphorous within the secondary component provided a flux to prevent the copper from oxidising as well as improving the wetting characteristics of the system. This flux component was also cited by the authors as being able to dissolve and remove oxides from the powder surfaces as well as protecting the metal surfaces from reoxidisation during heating. Zhu *et al*, 2003(b) describe this latter aspect as improving wetting and consequently aiding formation of a good bond. In spite of the use of a fluxing agent, the authors were only able to obtain parts with an approximate density of 65%, with the addition of epoxy resin being required to improve density and surface finish of the final part.

2.4.2 Laser Processing of Tool Steel

When laser processing pure metals, the major problem to be overcome is the production of a solid component. With tool steels, however, the problem is further complicated by the

desire to obtain a suitable morphology so that with further heat treatment the optimum microstructure can be produced. In this section, the laser processing of tool steels will be considered as two distinct types of process: one where only a fraction of the powder melts and the other where the powder fully melts.

Research has been conducted looking at processing a relatively high carbon tool steel (M2) using SLS with a CO_2 laser, power range 6.5 to 25W CW, laser scanning speed 1 to 30mm.s^{-1} and beam diameter 0.5mm (Niu and Chang, 1998); thereby producing parts that were predominantly sintered (where only partial melting took place). The authors considered the principle densification and binding mechanism to be liquid phase sintering and supersolidus liquid phase sintering.

Although full melting did not take place, Niu and Chang, 1998 reported that the M2 tended to 'ball' during the sintering. This balling was attributed to Rayleigh instability which resulted in the cylindrical scan tracks breaking up into a row of spheres when the wave length of the instability $\lambda < \pi D$, where D is the initial diameter of the cylinder. If the wavelength is constant then the behaviour of the scan track is dependent on D (e.g. width of the scan tracks), which is in turn is dependent on the laser power and scanning speed. Accordingly, the authors suggest that a larger D produced with a higher laser power or reduced laser scanning speed will make it more difficult for the cylinder to break up, allowing a smooth and continuous surface to be obtained. In contrast Morgan *et al*, 2001 and Pogson *et al*, 2003 found that higher speeds and lower powers created finer melt beads that were less likely to ball. This difference in observed behaviour may be due to differences in flowability and surface chemical energies between alloys, but is more likely to be due to Niu and Chang scanning thick powder beds, while Morgan *et al* and Pogson *et al* worked on thin powder layers above solid metal substrates where the wetting of the melt pool to the metal substrate would dominate any effects from Rayleigh instabilities.

Continuing from their earlier work on selective laser sintering of M3/2 tool steel (i.e. M3 Class 2; a tungsten-molybdenum high speed tool steel), work was then conducted using a higher powered CO_2 laser (with the power being varied over a larger range from 2.5 to 100W CW, laser scan speed 1 to 30mm.s^{-1} and a laser spot of Ø0.5mm; Niu and Chang, 1999). In these experiments gas atomised powders were used instead of water atomised

as the spherical particles produce higher packing density and allowed the formation of a 'highly dense surface'. The effect of powder size was noted as powders with a mean size greater than 150μm could not be sintered successfully to high density. The reduced density could result from a lower pre-sintered packing density or could be due to difficulty in melting the particles. Niu and Chang, 1999 used a relationship between the incident energy density (a function of laser power), scan speed and line-spacing to help plan their work, this being the same as the *Andrew Number* (Eqn. (1)).

Niu and Chang, 1999 noted that large scan line-spacing required increased power or reduced scanning speed to compensate. If, however, the line-spacing was reduced so that the tracks overlapped, a lower laser power or increased scanning speed could be used, although this led to increased surface roughness. The scan speed was also shown to have an effect on the structures formed, with low scan rates producing coarse but dense melt beads. To prevent this, the laser power was increased above a critical value, while the scan speed was increased to compensate. This produced a finer microstructure with a high surface density and with minimal balling. In a third paper Niu and Chang, 2000 processed M2 tool steel with a higher powered laser (400W) similar to that used in laser cladding and in this case fully melted the powder. This produced a thicker layer but the melting significantly altered the microstructure with a reduced amount of retained austenite being observed, producing a martensitic microstructure but with an increased volume of large carbides.

Su *et al*, 2003 reported the importance of using complex scanning strategies to achieve high densities when melt processing H10 and H13 tool steels. Using a manually laid-up powder bed (average powder size 150μm) and a 550W Nd:YAG laser (0.9mm spot size), a number of different scanning strategies were examined. They reported that scanning successive tracks across the powder layer produced powder splatter and that the reflection of the laser by the previously scanned tracks affected the unmelted powder nearby. This disrupted the powder layer producing an uneven surface which later tracks had difficulty bonding to correctly. By dividing the scan tracks into even numbers and odd numbers and scanning the odd tracks first followed by the even tracks a better structure was produced. The authors also reported that laying powder between the odd and even numbered scans further improved the part density as it replaced power that was lost

during the formation of the previous tracks, this being in agreement with Morgan *et al*, 2001 who came to similar conclusions when working on stainless steel. Su *et al*, 2003 also noted that reduced powder layer thickness improved the build quality. H13 and H10 as used by Su *et al*, 2003 have lower carbon contents than M2 and consequently do not require complex heat treatments to produce suitable tool steel microstructures, which makes it possible to process the materials over a wider range of conditions.

2.4.3 Laser Processing of Iron and Copper

The iron-copper phase diagram is a useful indicator of the phases that may form in a copper-H13 system; although it must be remembered that metastable phases can also exist. At higher temperatures complete liquid solubility is observed for Fe-Cu binary alloys, but as the temperature lowers an iron-rich phase solidifies, this being either δ ferrite or austenite depending on the alloy composition and temperature. Significant copper solubility (≈18wt% Cu at ≈1400°C) is reported in the austenite phase. When the alloy cools further the copper solubility in austenite drops until it reaches 3.1wt%Cu at the eutectoid temperature of 650°C. Below this temperature ferrite is formed and the copper solubility diminishes to near zero by room temperature. On the copper rich side of the diagram freezing of the copper rich phase occurs at 1095°C by a peritectic reaction. The solubility of iron in the copper rich phase again reduces with reduced temperature. There are no intermetallic phases present on the published phase diagram (Hansen, 1958; see Figure A3.1 in Appendix 3.1).

Zhu *et al*, 2003(a) looked at the direct laser sintering of a binary copper and iron system using a relatively high powered 200W CO_2 laser to directly melt the copper powder (and some of the iron), a CO_2 laser being used as the authors had found that materials produced with an Nd:YAG laser were porous and brittle. No mechanism was elaborated on for this difference in behaviour and it is in contrast to Morgan *et al*, 2001 where fully dense parts were produced using an Nd:YAG laser.

Zhu *et al*, 2003(a) aimed to assess the effects of processing conditions and material composition on the final part structure, identifying variations in part distortion, surface roughness and morphology. A relationship was observed between the ratio of iron and

copper and the amount of distortion, with minimum distortion occurring at a Fe:Cu ratio of 70:30 (by weight). Both below and above this ratio the distortion increased. The maximum distortion occurred with a Fe:Cu ratio of 50:50 (by weight). Further, the authors found that higher laser scanning speeds resulted in reduced surface roughness, finer pores, but increased porosity; the pore size reduction being reported to be due to the reduced amount of melting occurring at higher speeds. Also observed was balling of the melt beads, a phenomenon which other researchers described as being one of the complicated problems inhibiting successful single component sintering/melting (Tolochko *et al*, 2003).

Zhu *et al*, 2003(a) identified process parameter control as an important method of avoiding this problem, by preventing the complete melting of the powder. The balling phenomenon, which has also been discussed by other authors (Niu and Chang, 1998 and Simchi *et al*, 2001) was reported to depend on the viscosity of the liquid phase, which should be low enough to surround the solid phase but not too low as this would allow the material to flow into a ball and as such, balling is composition dependent. The viscosity is also affected by the temperature reached by the powder bed under the laser beam, and this may be affected by the composition, as copper has a higher reflectivity than iron. A comparison of processing under an air or nitrogen atmosphere was carried out and showed that samples produced under nitrogen were denser with a smoother surface. The presence of oxygen in the air led to oxide formation that reduced wetting of adjacent melt beads and reduced the build quality of the component. When considering the microstructure, Zhu *et al*, 2003(a) used XRD to identify ferrite and Fe_4Cu_3 intermetallic in their processed materials. It is difficult to confirm their interpretation as no data could be found that refers to the Fe_4Cu_3 phase.

2.4.4 Processing of H13 Tool Steel and Copper

Although the binary copper/iron phase diagram (Hansen, 1958; see Figure A3.1 in Appendix 3.0) shows complete solubility in the liquid phase and limited solubility in the solid phase, this diagram cannot be used when considering H13 tool steel. This alloy contains carbon and silicon that are reported, in the notes that accompany the phase diagram, to reduce the solubility of copper and iron, and this will lead to the formation of two immiscible liquids for some compositions. Although H13-Cu phase diagrams do not

exist, a better understanding of the system can be developed by considering the Cu-C-Fe ternary diagram (Larsson, 1975). The author studied the iron rich section of the diagram and concluded that the presence of carbon did indeed lead to the formation of two immiscible liquids at higher temperatures. While it was concluded that at lower temperatures the addition of copper stabilised austenite and thus retarded the formation of martensite. Also identified was a ternary eutectoid associated with the transformation of austenite to ferrite, the eutectoid temperature lowering as the copper content increased.

Work on processing copper with tool steels is limited to a few works considering lower temperatures that have microstructures very different to those formed by melting copper and tool steel together.

2.5 Laser Processing of Materials with Controlled Porosity

2.5.1 Laser Processing of Bio-Materials

The development of materials with controlled porosity has largely been driven by the needs of the medical industry, although other uses of this technology are being developed. Within the medical industry there are three main metallic materials groups used, (Ward *et al*, 1996) titanium alloys, cobalt-chrome alloys and austenitic stainless steels; these materials being used in load bearing situations such as in hip replacements. Of these, commercially-pure titanium is becoming an important material for bio-structures such as implants and bone-grafts as it possesses excellent corrosion resistance, bio-compatibility and has a high strength to weight ratio (Santos *et al*, 2004). These authors also reported that the major disadvantages of titanium are related to its high reactivity, especially with interstitial elements such as oxygen, carbon, nitrogen and hydrogen. For this reason titanium is processed under a protective atmosphere containing less than 150ppm oxygen (Arcella *et al*, 1998). Although early designs of bio-structures had relatively smooth surfaces and were cemented into the bone, this method of fixating bio-implants has lost favour and other methods of fixation have been pursued. One of these methods is to encourage bone growth into the implant by producing a suitable porous structure. A

number of technologies have been considered for the production of these porous surfaces and one of these is DMLR.

The laser-processing of bio-compatible titanium powders to produce porous structures on solids has the benefit that the composition and macrostructure can be graded in a controlled manner (Abbott and Arcella, 1998). Early work on this process used an Nd:YAG laser as part of a proprietary Selective Laser Melting (SLM) process to investigate the direct production of bio-structures from commercially pure titanium powders (Abe *et al*, 2002). It was reported that optimum structured surfaces could be produced by controlling the hatch-patterns used to scan the powder layers. The authors also reported that the rapid heating and solidification associated with laser melting produced structures stronger than solid pure titanium (a tensile strength 120% of that of a reference material). A similar SLM process was used by (Santos *et al*, 2004) who observed an acicular martensitic microstructure resulting from the rapid cooling. Hot Isostatic Pressing (HIP) of this material produced a near fully dense material with an alpha phase equi-axed microstructure. The authors quoted a Vickers Hardness greater than that of wrought titanium. In this case, the authors attributed the increased hardness to the laser processing increasing the oxygen levels within the titanium.

Another important bio-material is tantalum and, like titanium, it has a strong affinity for interstitial elements such as oxygen, carbon, nitrogen and hydrogen (Cardonne *et al*, 1995). No published data is available on the direct laser melting of tantalum and therefore, only work on conventionally manufactured material is available. The authors of this work commented on how it was suitable as a bio-implant material as it is inert in bodily fluids and has a high corrosion resistance. However, one possible processing problem is tantalum's relatively high melting point (quoted by *Efunda.com* as being 3017°C), which is significantly higher than most materials processed by DMLR and consequently, there could be difficulties in obtaining suitable laser parameters. Ward *et al*, 1996 researched the deposition of tantalum and niobium (another bio-compatible material with a relatively high melting temperature 2477°C) using a Leybold-Hereaus L560 ion-plating machine. This work considered the production of thin (5 – 9μm) films on the surface of existing components to enhance corrosion resistance.

2.5.2 Production of Porous Structured Surfaces

Bio-implants (bone grafts or joint replacements) are, commonly, cast items usually held in place with bone cement (Recum, 1999). Ward *et al*, 1996 described how the failure of this bone cement (poly methyl methacrylate – PMMA) limits the life of the implant to 10 to 12 years, effectively limiting their application so they can only be used for the elderly. Oliveira *et al*, 2002 also reported this method to be the most common reason for implants loosening. To provide an alternative method of bone-implant fixation, several researchers have looked at the application of porous structures to the outer surfaces of the implant allowing bone ingrowth (whereby the bone grows into the implant to provide a direct mechanical fixation) to hold the structure in place. Over the course of the last 30 years, researchers have looked at both the optimal pore size and shape for this bone ingrowth and the latest advances in manufacturing techniques with which to produce them. This part of the Literature Review will discuss some of the work that has been undertaken in this subject area to provide both a comparison and a background to the work that is described in Chapter 5.0.

Researchers presented the results of an early investigation into the application of porous surfaces to bio-implants (Bobyn *et al*, 1980). By using a precursor to modern manufacturing techniques they sintered, under an inert atmosphere, a cobalt-base alloy powder onto a cast cobalt base alloy to produce a porous coating. A network of interconnected pores was obtained giving a density of 30 to 35%. Four powder size ranges were used, giving four different pore sizes ranging from 20 to 800μm. By adjusting the thickness of the coating and the diameter of the stem used, the final size of the implants could be adjusted and maintained within specification. Rather than exploring the viability of the manufacturing process, it was the main intention of this work to adjudge the optimal pore size for bone ingrowth to take place. After bone ingrowth, the strength of the bone/metal interface was mechanically tested. A maximum shear strength of 17MPa was obtained; this being for a pore density of 30% (a higher pore density achieving a higher contact area with the bone, but with less metal being present to transfer the load). The shear strength of the bone itself was expected to be 60MPa, which the authors say would give a theoretical maximum shear strength of approximately 18MPa (0.3 x 60MPa).

As well as investigating the importance of pore density, Bobyn *et al*, 1980 examined pore size and found that the smallest pore size range of 30 to 50μm was too small for uniform tissue calcification. For this reason, the maximum fixation strength was less than with the other three size ranges tested. To determine the degree of ingrowth achieved at various stages of the process, the implants were tested at varying elapsed time periods from the initial implant into the test subject. It was found that the largest size range used, 400 to 800μm, provided the most variable test data, and consequently pointed to these coatings producing unpredictable results. The optimal size range, which the authors say would give the maximum fixation shear strength of 17MPa for an implant with a porous surface, was found using powders in the 50 to 400μm size range.

Akin *et al*, 2001 suggested that a major cause of long-term failure of osteo-implants was due to bone loss at the bone/cement interface and consequently, a critical aim of their work was to increase the speed at which mature bone is formed at the interface. The authors studied the application of a porous TiO_2 bio-ceramic film on a titanium surface. Aqueous slurries were made up using 39nm TiO_2 powder and polystyrene latex beads of 0.5, 16 or 50μm diameter. An approximately 0.5mm thick film of this material was then applied to the surface of a ∅15mm polished titanium substrate which was subsequently left to dry in air for over a day. The polystyrene beads were then burned off by heating the test pieces to between 450 and 900°C, annealing at 900°C and then leaving to cool in the furnace. The samples were then tested by the ingrowth of human bone-derived cultures. Analysis was undertaken using Scanning Electron Microscopy (SEM), X-Ray Diffraction (XRD) and X-ray Photoelectron Spectroscopy (XPS). After manufacture, the pore sizes were found to be in the range ∅0.3 to ∅36μm for the three polystyrene bead sizes used. The authors also suggested that modifying the polystyrene to TiO_2 weight ratio would provide a more ordered surface morphology. Cracking within the coating was observed in all samples produced, it was proposed that this was a result of TiO_2 material shrinkage. From their work, it is clear that overall control of the surface coating morphology is restricted to altering the size and quantity of the polystyrene beads.

Hacking *et al*, 2000 used chemical vapour deposition/infiltration (CVD/CVI) to deposit commercially pure tantalum onto a porous carbon skeleton to produce a porous structure; tantalum being chosen because of its strength, ductility and high oxidation and corrosion

resistance. The carbon skeleton was produced by heating thermosetting polymer foam in an inert atmosphere so it decomposed to form a low density carbonaceous foam skeleton, which possessed a repeating array of interconnected dodecahedron shaped pores. Onto this structure tantalum was progressively deposited which, in turn, increased the overall structural integrity. A final coating thickness of between 40 and 60μm was deposited. The average pore size obtained by this technique was found to be in the range 400 to 600μm with volume porosity (pore density) between 75 and 80%. By altering the initial polymer foam and varying the thickness of the tantalum coating, the pore size was controlled. The authors reported that these coatings had better attachment strength to the bone compared to those reported by other authors (Bobyn *et al*, 1980); a portion of this improvement being attributed to the greater pore size produced with the CVD/CVI technique. Also thought to be of importance were the pore geometry and high frictional coefficient of the porous tantalum, which was observed to be of significant benefit to soft tissue adhesion. These factors were also thought to be important when considering materials with more disordered/random pore distributions. The authors further state that the high inherent porosity of the porous tantalum was of benefit as it allowed more tissue to develop at the bone/implant interface and consequently enabled a more secure implant fixation.

Pompe *et al*, 2003 noted that functional gradation is a characteristic feature of living tissue and proposed that the ideal form of a bio-implant would possess a similar morphology. The authors described how bone gradually changes from one structure to another, from a dense, stiff external structure (cortical bone) to a porous internal one (cancellous bone) and they proposed that the ideal morphology of a bio-implant would utilise a similar structural gradient. Graded structures produced by various processes and materials are considered in the paper and a study of how implants can be improved by utilising gradient material manufacturing is presented.

Using animal test subjects and more conventional mechanical testing (abrasion testing), the performance of implants produced using novel manufacturing techniques has been contrasted with those produced more conventionally (Pompe *et al*, 2003). To provide as large a data set as possible, implants produced using a range of materials were included; including a graded composition of ultra-high molecular weight polyethylene (UHMWPE) fibre reinforced high-density polyethylene combined with a surface of UHMWPE. Further,

the authors describe how the ingrowth behaviour of hard tissue into titanium implants was improved by depositing a graded biopolymer coating. Finally, the authors included a functionally graded porous hydroxyapatite (HAP) structure, manufactured by the sintering of HAP tapes filled with polymer spheres, to provide as diverse a range of manufacturing routes as was possible. As this was preliminary work when published, it was not possible to identify the ultimate structural/material implant configuration. Focussing solely on hard tissue replacement, the only valid conclusions that were drawn by the authors were that the direct mechanical contact between an implant, possessing a graded morphology, and a bone would provide an improved mating face than the presently used technique of implant and bone cement. This is what has been reported as being the major cause of implant loosening (Recum, 1999).

Although a number of alternative materials and structures have been considered in the literature, the production of the implant and the coating at the same time using one technology (e.g. laser melting) has not been examined. This is why the work described in Chapter 5.0 is important.

2.6 Summary

This literature review describes a number of different processes and techniques that have been researched to allow for the production of graded structures. There is no doubt that parts that have had their composition and/or morphology tailored to suit an application will have greater functionality and fitness for purpose than those that have been produced using more conventional means. However, none is sufficiently developed to provide a real-world manufacturing route. The work on bio-implants and structured surfaces is an example of this. Investigations have been made to determine the possibility of producing such structures but none is capable of producing an implant with a graded porosity in a single manufacturing application. However, laser-melting based rapid prototyping processes such as DMLR have the potential to do so.

It is clear from the literature that the manufacture of graded structures is neither solely a manufacturing issue nor a metallurgical issue but a combination of both, and consideration of the development of particular technologies, such as DMLR, for producing graded composition and porosity structures is required. The limitations of such processes also need to be evaluated.

DMLR has many benefits to manufacturing. It is capable of directly melting metal powders to produce parts with up to 100% density (R, Morgan *et al*, 2001). Its relatively small beam diameter (100μm) and build chamber resolution (50μm) mean that parts can be produced with an accuracy of a similar order. Its use of computer-generated data to accurately control the laser scanning and layer control means highly complex parts can be reliably and repeatedly produced. Producing complex parts in a single manufacturing operation would be an important benefit to manufacturing, and the production of structures with either a graded composition or porosity is therefore an area that requires further work.

3.0 Experimental Arrangement

A complete description of the design and construction of the DMLR rig used for this work is given in the thesis of Morgan, 2003, and so full details of its development will not be reproduced here. Instead, a brief description of the system and the developments that were specific to problems encountered during this work are discussed. The rig consists of two reasonably independent systems - the laser-optics and the powder deposition system, and these will be considered separately. The final section of this chapter will give a brief summary of the analytical methods used throughout the course of this PhD. As the research was conducted in two distinct sections and particular experimental details tended to be relevant to only one section of work, these specific experimental details are discussed in the appropriate section

3.1 Direct Metal Laser Remelting

The laser used was a Rofin-Sinar (RS) krypton flash-lamp pumped Nd:YAG (λ=1.064μm) industrial laser-marker capable of producing a maximum power output of 90W CW (continuous wave). The laser can also be operated in pulsed mode when it produces pulses of 80-120ns duration within a frequency range of 5 – 60kHz. When the laser is used in pulsed mode, the energy inputted between pulses is stored within the laser cavity, allowing the pulses to have high instantaneous peak powers (up to 20kW). This is useful when processing metals with a high melting point or high thermal conductivity but can also produce shock waves within the powder, blasting powder from the bed. When used in CW mode, these problems are avoided but the maximum power available is much lower. The laser beam was scanned using an RSG1014 analogue galvanometer scanning head integrated into the laser system, giving a maximum scanning speed of 500mm.s^{-1}.

The beam was directed through a suitable glass aperture into an atmospherically controlled processing chamber (Figure 3.1). Inside the build chamber were two computer controlled platforms; one rising to deliver the powder, the other, to which the build substrate was secured, dropping to control the powder layer thickness. Both platforms consisted of Ø110mm aluminium pistons attached to linear actuators controlled by stepper

motors so the movement of the platforms could be controlled to an accuracy of 5μm. On top of the build piston was an adjustable platform allowing the platform to be aligned with the powder spreading roller. The uniform powder layer was produced by raising the powder delivery piston to supply a measured quantity of powder. A counter-rotating roller then spread the powder over the build platform. After scanning the laser over the newly spread powder layer, the build platform was lowered and the process repeated.

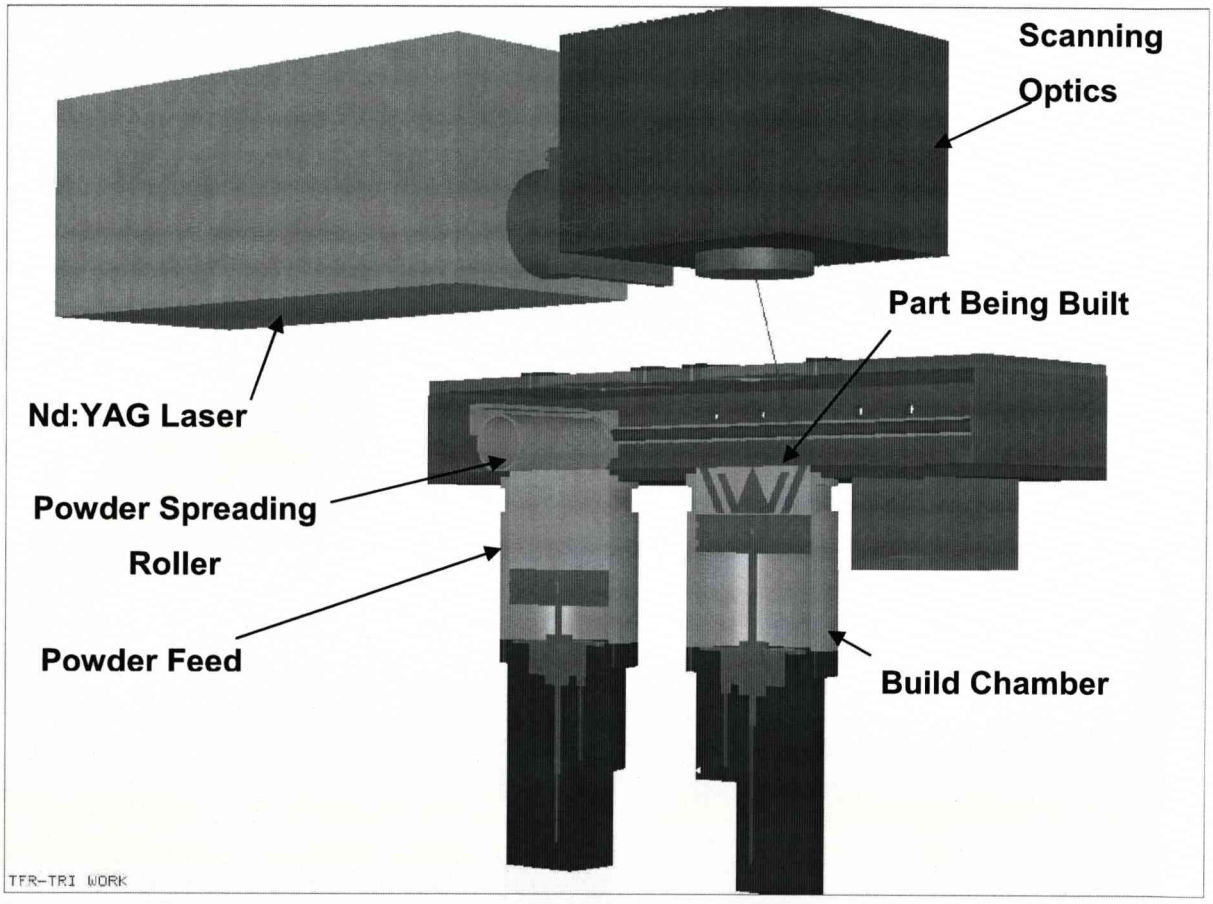

Figure 3.1 Sectioned view of DMLR build chamber *(drawing provided courtesy of R Morgan)*

The experiments carried out during this work used powders that oxidised easily and therefore careful control of the atmosphere above the powder bed was required. To allow for the removal of oxygen from the system, which contained many partially sealed off sections that could trap air, the chamber was pumped using a rotary vacuum pump before being back-filled with either an inert or a reducing gas. The gas used was dependent on the metal being processed. Pure nitrogen or a hydrogen/nitrogen mix was used when

processing steels and copper, whilst argon was used with more reactive metals like titanium where nitride and hydride formation had to be avoided.

To understand the effect of varying the key DMLR laser processing parameters, a relationship was developed to calculate the specific energy density that could be applied to the powder bed. The specific energy density ($J.m^{-2}$) can be defined as:

$$E_d = \frac{P}{v.s \times \left(1 - \left(\frac{B.O}{100}\right)\right)} \quad (8)$$

Where P is the laser power (W), v is the laser scanning speed ($m.s^{-1}$), s is the beam spot size (m) and $B.O$ is the beam overlap (%).

This formula predicts how the energy density put into the powder bed will vary as the laser spot size and other key process parameters are modified. This is a development of the formula for the '*Andrew Number*', A_n, (Eqn. (1); Williams and Deckard, 1998) which shows a more basic processing parameter relationship that doesn't consider the laser spot size and instead specifies the distance between adjacent scan tracks.

The layer thickness normally used was 100μm but this could be reduced to allow thinner powder layers to be deposited, although this would be constrained by both the minimum step size (5μm) of the powder platforms or the size of the powder particles used (e.g. 22μm). The major difficulty was in producing a uniform powder layer thickness across the bed, which was limited by the accuracy that could be achieved using feeler gauges to measure the gap between the roller and the substrate. A maximum accuracy of ±5μm was possible using this technique. It was also important that the build substrate was aligned accurately with the optics and so a system was devised to allow the substrate surface to be aligned to a total combined tolerance of ±25μm. This system consists of an accurately machined gauge that can be positioned flush with the aperture of the laser galvanometer (Figure 3.2). The height of the gauge is then calibrated using a Vernier height gauge to ensure the correct 'working distance' (the distance between the galvanometer optic and the surface of the build substrate.

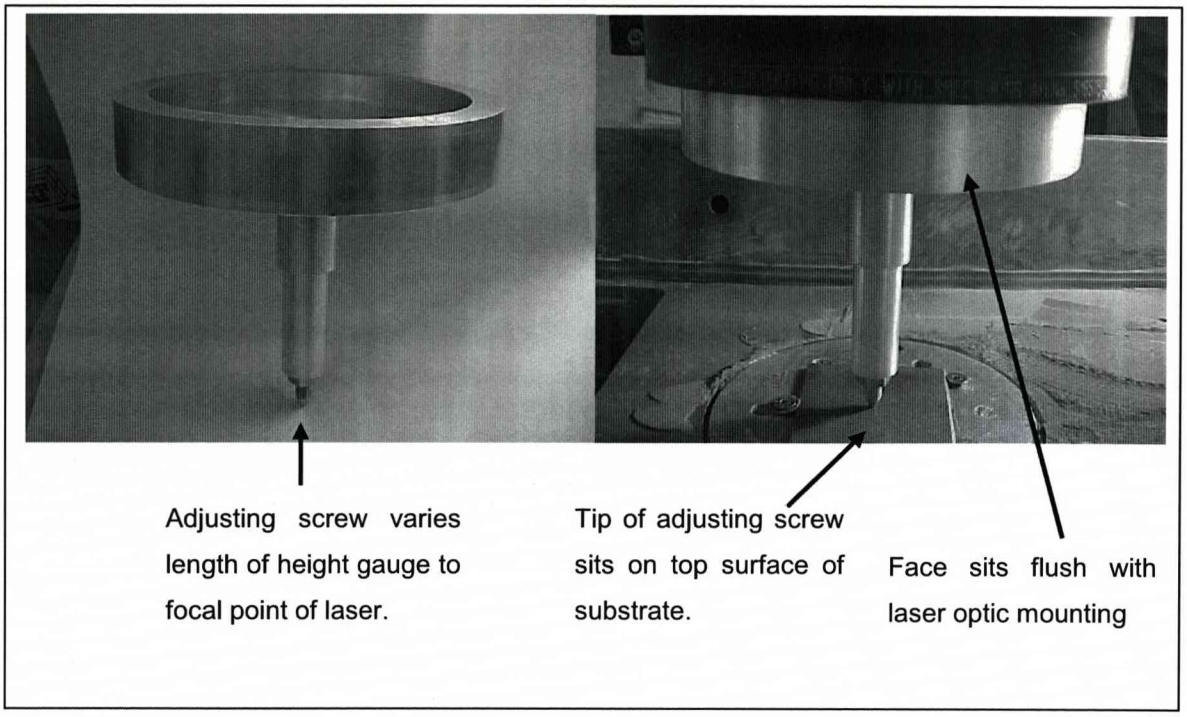

Figure 3.2 Photograph showing build platform focal length gauge

The relationship between the working distance and the spot size was determined by scanning the laser over a flat surface covered with laser marking tape (3M Code 7847) at various distances about the quoted 112mm focal length. The widths of the resultant marks were measured using a travelling microscope (Carl Zeiss D-7082). It was determined that the actual focal length was 109mm (Figure 3.3) and that at focus the spot size was approximately 100μm diameter.

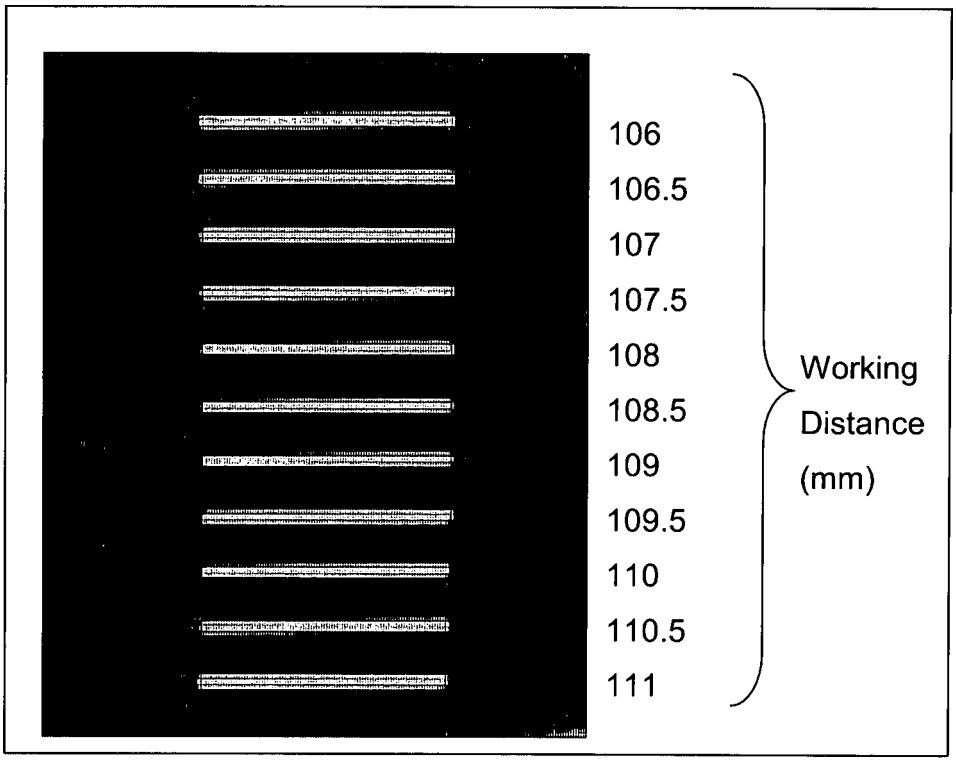

Figure 3.3 Focal characteristics of DMLR equipment

Although the working distance of the laser will affect the spot size and the intensity of the beam (the beam diameter is at its smallest and most intense at the focal point), thus affecting the ability to melt the powder and the substrate, the system is tolerant to a few millimetres (a deviation of up to 2mm from the focal point had a negligible effect on the beam diameter). If this were not the case, the area that could be scanned without the laser going out of focus would be limited. Even so, in order to maintain repeatability between builds and minimise any sources of error, it was important to use the height gauge to retain the same working distance.

The laser used in these experiments was turned on and off at the beginning and end of each line by Q-switching the laser. This feature also allowed the beam to be pulsed during scanning by 'shuttering' the laser cavity to allow the energy to build up and be stored during the off period between pulses. This excess energy is also released when the Q-switch is opened at the start of each scan, causing a high energy pulse to be delivered to the powder bed. If this happens when the laser is scanning the powder bed, the high peak powers associated with these first pulses blast away powder from the substrate leaving a

powder-free region. The RS laser has a facility for eliminating these unwanted pulses (First Pulse Suppression) and therefore a series of experiments was carried out to optimise this feature.

To set the First Pulse Suppression (FPS), there are two parameters that have to be defined. These are:

Upper Limit: Proportion of laser power that is suppressed with the first pulse.

Step: Quantity for the gradual removal of pulse suppression with each further pulse (the number of pulses after the first pulse before the laser power returns to 100% of that defined in the scanning program.

Initial experiments showed that for producing simple cubic structures with H13 tool steel, changing the FPS parameters had little effect and therefore the laser was left with its default settings. However, with the more complex 'waffle' (the waffle term being used here due to the similarity of the structure of the food type with the structured titanium coating used in the porosity work; Figure 3.4) structure (with a circular profile on a circular substrate), produced whilst processing titanium structures, selection of the correct FPS settings became significant. It was also found that the optimum settings were affected by the laser scanning speed.

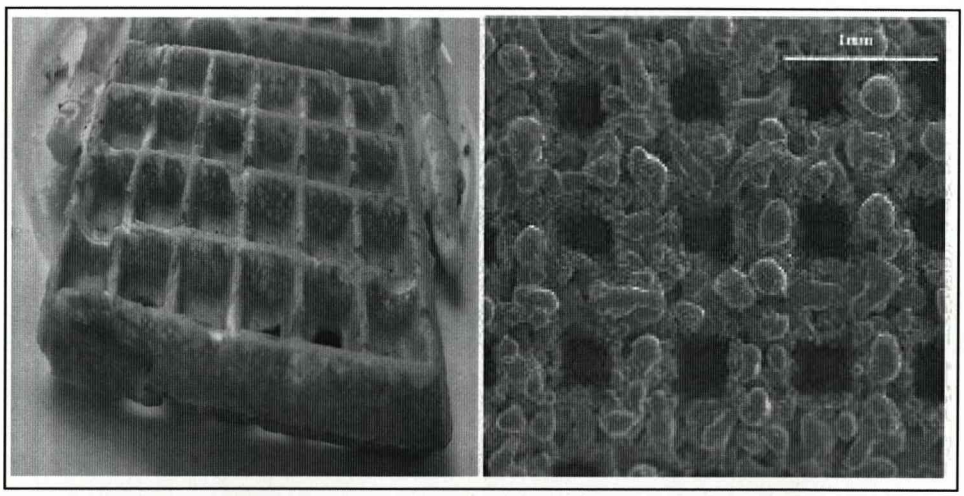

Figure 3.4 Photograph showing the lattice structure of the waffle food *(image reproduced courtesy of Wikepedia.com)* compared with a structured titanium coating from the work described in Chapter 5.0

A number of experiments were conducted scanning a pattern of parallel Y-direction scan lines within a circular profile, onto a newly spread powder layer upon a circular substrate (the scanning of which appeared most affected by the First Pulse problem). Following the laser scanning, it was observed that regions around the perimeter of the scan were depleted of powder, the solidified material was elliptical rather than circular in profile and areas around the edges of the scan were devoid of material (the powder had been blasted from the powder bed as a result of a shock wave being generated due to the instantaneous pulse of energy being applied to the powder bed).

It was also noticed that the surface of the processed material, rather than being flat, uniform and level with the surface of the surrounding powder bed, as is expected following this type of layer-by-layer laser processing, was curved. That is, the material at the centre of the scan was of an increased distance in the Z-direction (above the surface of the powder bed) than the material at the edges of the scan.

One of the findings of these experiments was that the optimisation of the FPS settings only reduced the effects of the First Pulse problem rather than removing it completely. These effects were only eliminated when a 1mm thick profile scan was introduced prior to the main scan. This allowed the perimeter to be melted and sufficiently fused to the substrate to prevent the powder from being blasted away. Table 3.1 shows a tabulated summary of these experiments.

Experiment No.	Upper Limit (%)	Step	Scanning Speed ($mm.s^{-1}$)	Results
1	70	2	160	Depleted region around scan perimeter, elliptical melt region
2	100	5	160	Depleted region. Rounder melt region
3	100	7	180	As above
4	100	3	200	Smaller depleted region. Building above powder bed
5	100	5	220	As above
6	100	3	240	As above
7	100	3	260	Flatter melt region. More uniform build (bidirectional scan used)
8	100	3	260	As above but with single direction scan. Powder depletion and building above the powder bed at one end of scan
9	100	3	300	Not building as high.
10	100	3	300	Used in combination with 1mm profile scan prior to main scan. This produced best results

Table 3.1 Table showing the First Pulse Suppression parameters used; these were used in conjunction with a laser power of 82W CW and a 0% beam overlap

To demonstrate the effect of the use of First Pulse Suppression, photographs were taken of a selection of these builds. These are shown in Figure 3.5.

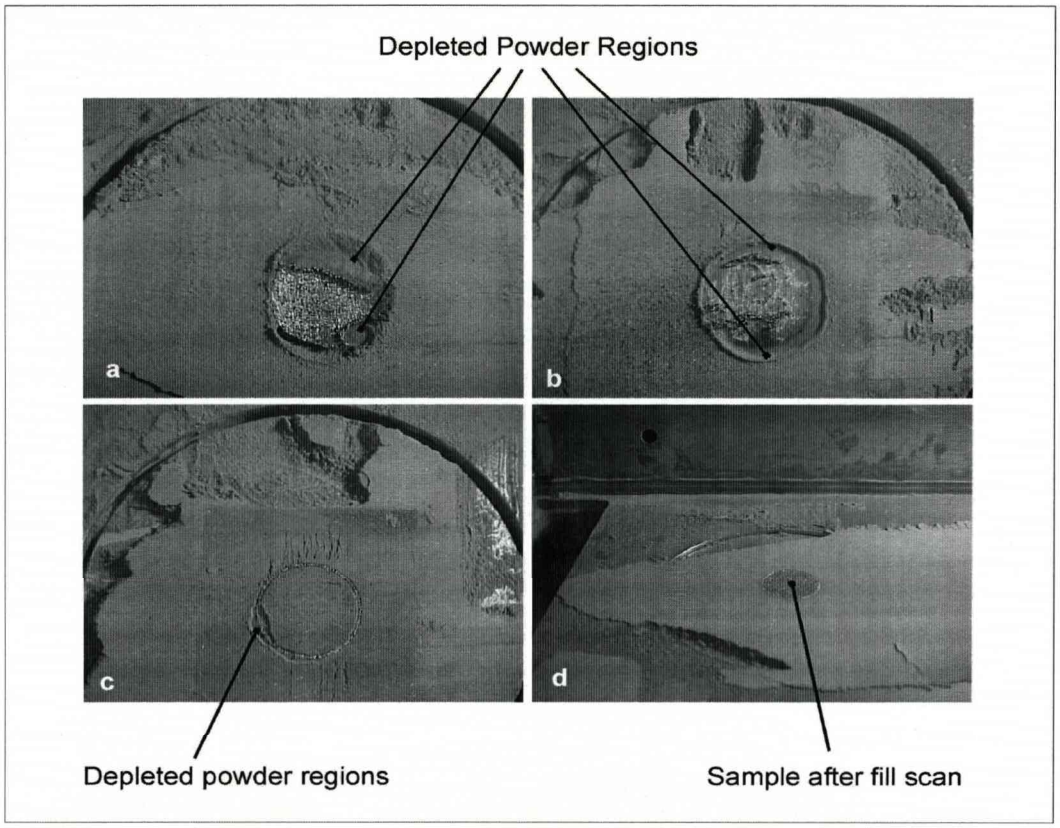

Figure 3.5 Photographs showing variation in first pulse suppression settings. Referring to the data in Table 3.1, this figure shows samples produced from experiments: a) Experiment 1, b) Experiment 2, c) and d) Experiment 10

The photographs shown in Figure 3.5 show the effects of varying the first pulse settings. Figure 3.5a shows the laser-marking software default settings of: Upper Limit 70%, Step 2. These parameters were used with a laser scanning speed of 160mm.s^{-1}. Figure 3.5b shows a photograph of a build produced with values of 100% limit and Step size of 3. An increased scanning speed of 260mm.s^{-1} was used. Figure 3.5c shows a photograph of the build produced after a 1mm thick profile had been scanned prior to the main scan. First pulse suppression was not used in this instance; consequently, a depleted powder region is still seen but was visibly reduced compared to the use of first pulse suppression on its own. Figure 3.5d shows the layer shown in Figure 3.5c after the main scan had followed the profile scan.

This investigation attempted to devise the optimal first pulse suppression settings available with this laser-marking software. A more reliable solution was found to be the use of a

perimeter scan, i.e. prior to scanning the powder layer, a series of high-speed, overlapped, perimeter scans (in this case concentric circles) were run before the main filling scan.

3.2 Analytical Tools Used

Most of the optical microscopy was performed using a Leitz Metalloplan, which had objective lenses in the range 8 to 160X. The numerical aperture for the 160X objective was 0.95 giving a resolution limit of 0.5μm (manufacturer's specification). Macroscopic examination was carried out using a Wild M8, which had an optical zoom from 6 to 25X and 10X eyepieces.

Scanning Electron Microscopy (SEM) was undertaken using a Hitachi S-2460N SEM, with an acceleration voltage of up to 25kV, giving 6nm resolution (manufacturer's specification) and a working distance of 6mm. The Energy Dispersive Spectroscopy (EDS) system used an ultra-thin beryllium window to allow the detection of light elements, the detection limit for heavier elements being approximately 0.5 to 1wt%. A Robinson ETP-SEM RA detector was used to obtain back-scattered electron (BSE) images.

A Rigaku Miniflex diffractometer with a copper tube (kα λ = 1.64 angstroms, accelerating voltage 30kV, current 15mA) was used to obtain the X-Ray Diffraction (XRD) spectra. The goniometer (radius 150mm) allowed a 2θ range of 0 – 150° with scanning speeds between 0.01 and 100°/min (step angle >0.01°). Although there are problems with x-ray fluorescence when a copper tube is used with iron based samples, the copper tube was the only one available and reasonable results were obtained.

4.0 Investigation into the Production of Structures with a Controlled Variation in Composition

The aim of the project, of which the work in this section was a part, was to produce a mould that contained a composition gradient. The optimal design for a mould tool would take advantage of the physical properties of different materials, for example, a wear resistant material for the internal surface of the mould cavity (to resist scratching and other surface defects that may form during use, which would affect the surface finish of the final part) and a material with a high thermal conductivity for the cooling channels. A simple design could possibly be made by casting the main part and then machining a space for insertion of the cooling channels. If, however, the design was more complex with, for example, the mould cavity requiring a curved profile in more than one plane and cooling channels that conform to this profile, as suggested in Figure 4.1, then the use of a solid freeform fabrication material additive process such as DMLR would be a possible solution. With this application in mind, the production of parts using copper and H13 tool steel was investigated; H13 tool steel was chosen as a possible material for the bulk of the mould tool including the lining of the mould cavity because of its relatively high wear resistance and copper because of its high thermal conductivity.

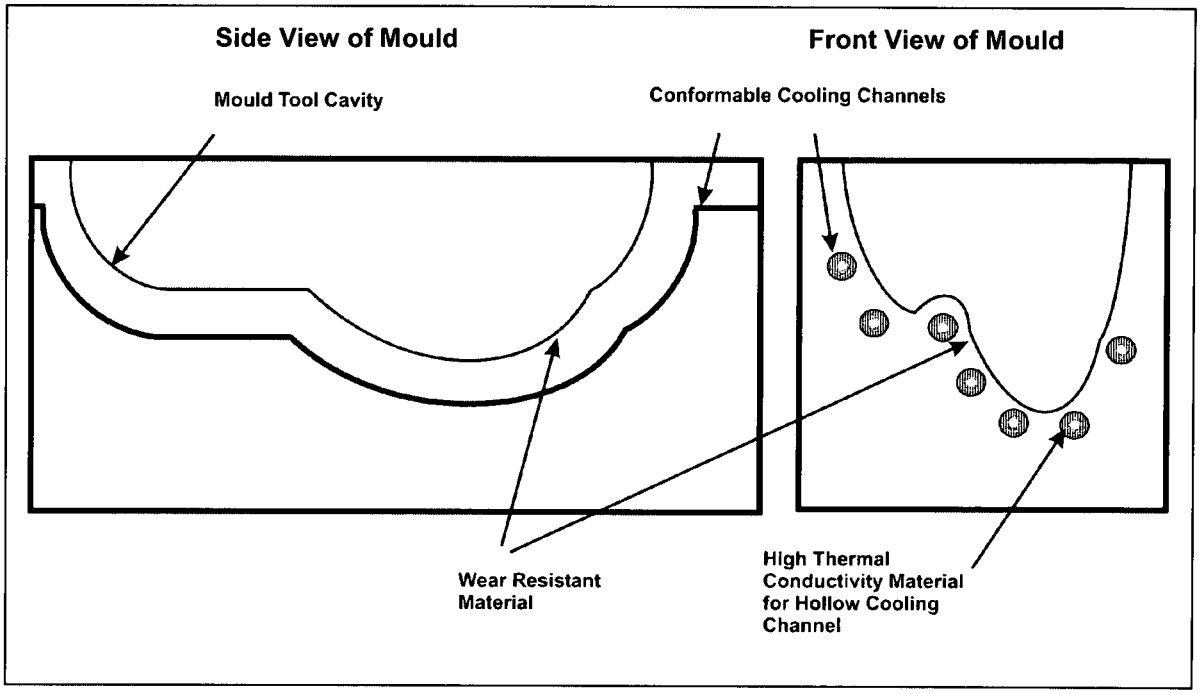

Figure 4.1 Schematic diagram of a mould tool cavity

At the end of the project, this objective was not achieved as the powder delivery system, being developed elsewhere, was not available. This section therefore concentrates on more fundamental work investigating the behaviour of single powder and mixed powder beds and their interactions with the laser beam.

Initial process characterisation was carried out using H13 single component powder beds to develop further understanding of the DMLR process. Later experiments looked at the interactions between copper and H13 tool steel when both materials were processed at the same time, so as to model what happens near to the interface between the copper and H13 regions. Whilst the ultimate intention of this work was to process multi-component powder beds, where both powders were selectively deposited with local composition control, no means of achieving this was available. The build platform was to be developed at Queen Mary University of London but was not completed by the end of the project. Instead, mixed powder beds were produced and scanned with the laser to assess the resultant metallurgical interactions. The first part of this work looked at producing single layer coupons from mixed (H13 and copper), pre-placed, powder beds. The data from these experiments was then used to build cubes on steel substrates using multiple, thin (75μm), layers of the mixed powder compositions. The final series of experiments looked

at optimising the processing parameters and conditions in order to produce the most suitable microstructures for use in a FGS such as a mould tool.

Creating a functional structure with a compositional gradient would require careful tailoring of the material properties at both a macro and microstructural level. To understand the interactions between the different components of the powder bed requires not just an understanding of the fundamental material science issues but also of the empirical data. As metallurgical phase diagrams are based on equilibrium heating and cooling and DMLR involves relatively fast heating and cooling rates, these diagrams can only be used to provide a general indication of the material interactions. This section therefore describes a range of experiments that were devised and conducted to identify the issues involved in this procedure.

4.1 Experimental Procedure

The parts considered in the section were etched using either ferric chloride or 2%-nital (or a combination of both for samples that contained both copper and H13) to allow the microstructure formed to be determined.

4.1.1 Experiments to Produce Homogeneous H13 Builds

Although the optimal DMLR processing conditions for copper (Osprey Metals OFHC 99.99% copper; 80%<22μm) were already known (Pogson *et al*, 2003), no work had previously been conducted on H13. Thus, it was necessary to characterise the production of parts using H13 tool steel.

The H13 (a chromium-molybdenum hot working steel; composition Table 4.1) powder used for these experiments was obtained from Osprey Metals and had a particle size distribution of 80%<22μm (80% of the typical powder is less than 22μm in size, mean size 12μm).

Element:	Fe	C	Cr	V	Mo	Si	Mn	Ni
Nominal Composition: (Wt %)	Bal	0.4	5.2	1.0	1.5	1.0	0.4	0.3

Table 4.1 Composition of H13 tool steel

Characterisation of the DMLR-processed H13 started with initial analysis of single-track, multi-layer 'walls' fused onto steel substrates, processed under a 99.9% N_2 atmosphere using the parameters shown in Table 4.2.

Frequency (kHz)	Laser Power (W)	Laser Scanning Speed ($mm.s^{-1}$)
5 –50	52 – 82	10 - 30

Table 4.2 Parameter ranges used for single-track, multi-layer experiments

3-Dimensional multi-track, multi-layer structures were then produced so that process windows/maps could be developed from melt-depth and track width data. For the multi-track experiments, a simple scanning strategy consisting of a series of parallel X-direction lines, with a beam overlap of 50%, was used. The multi-track samples were processed as 3 x 3 arrays of 10mm x 10mm structures. Following initial experiments looking at using similar scanning speeds to the single-track experiments, it was found that speeds at the lower end of the range caused excessive energy to be delivered to the powder bed, which resulted in over-melting of the powders, i.e. in some cases this caused overheating of the meltpool, which resulted in excessive balling of the molten material. This prevented flat, uniform material tracks from being formed and fusing with the substrate; in other cases, the excessive energy blasted the powder from the underlying surface. Consequently, following the initial work, the multi-track experiments focused on looking at higher scanning speeds within the range 300 to $500mm.s^{-1}$. Additional experiments also looked at using modified scanning patterns, supplementing the simple raster-scan format with an additional scan. Also used here was the scanning arrangement proposed by Morgan *et al*, 2001. The parameter ranges used for these builds are shown in Table 4.3.

Frequency (kHz)	Laser Power (W)	Laser Scanning Speed ($mm.s^{-1}$)
5 – 50	75 – 82	10 - 500

Table 4.3 Parameter ranges used for multi-track, multi-layer experiments

The process windows were further refined by building single 20mm x 20mm square section blocks; a single block being produced to avoid any interactions between multiple blocks, such as heat build up in the substrate.

4.1.2 Cu/H13 Pre-placed Powder Bed (Single Layer Coupons)

Process maps were developed for mixed copper and H13 powders as single layer coupons in a thick bed. The mixed powders were produced by adding a measured quantity of each powder (wt %) to a mixing vessel and stirring vigorously for ten minutes. Each powder mixture was poured into an aluminium tray of internal dimensions 70mm x 100mm x 7 mm high and compacted to produce a pre-placed powder bed. In this part of the mixed powder bed work, the main aim was to produce samples that had fused together sufficiently to allow metallographic analysis to take place.

Three different compositions of copper and H13 powders were used for this work. Composition A used 75wt% copper and 25wt% H13, Composition B used 50wt% copper, 50wt% H13 and Composition C used 25wt% copper and 75wt% H13. Pre-placed powder beds were then produced with each of the three different compositions. 5 x 5 arrays of 10mm x 10mm samples were produced, with each having different processing parameters; the laser scanning speed varying from $150mm.s^{-1}$ to $250mm.s^{-1}$ and the laser power varying from 45.8W CW to 68.6W CW. These parameter ranges were chosen as they were an appropriate compromise between the optimum parameters found from processing copper alone (v = 100 to $180mm.s^{-1}$, P = 72W CW to 82W CW; Pogson *et al*, 2001) and the optimum H13 parameters (v = 300 to $500mm.s^{-1}$, P = 82W at 30kHz) found from the experiments described in this chapter. The laser spot size was fixed at Ø100μm and the beam overlap at 25%. After scanning, the coupons were cleaned and visually inspected and samples from two parameter sets were chosen for further analysis; one set with a

laser scanning speed of 175mm.s^{-1} and laser power of 51.5W CW and the second with a laser scanning speed of 250mm.s^{-1} and a laser power of 57.2W CW.

4.1.3 Cu/H13 Multi-Layer Coupons

Parts were next produced by laser melting multiple thin (75μm) layers of the mixed powders onto steel substrates. For these experiments, a simple laser raster scan was used rather than the more complex scans proposed by Morgan *et al*, 2001. Although this simple scan pattern made the thermal history of the material easier to predict, it did lead to increased sample porosity (which subsequently affected their cohesion making it more difficult to prepare suitable metallographic samples). The components were produced as simple (10mm x 10mm) cubes in 3 x 3 arrays (again, the arrays of samples allowed a large range of processing parameters to be investigated). To allow comparison with the previous experiments, the range of processing parameters chosen (beam overlap 25%, laser scanning speed 150mm.s^{-1} to 200mm.s^{-1}, laser power 45.8 to 82W CW) included the values used for the single-layer work. As with the single layer mixed powder beds work, it was the primary intention to produce samples of sufficient strength to allow for further metallographic analysis to take place, allowing the interactions between copper and H13 to be investigated and not to create fully dense, functional, structures.

4.1.4 Cu/H13 Optimised Processing Conditions

The production of multi-layer builds in the previous series of experiments allowed ranges of processing parameters to be investigated, showing the effect of laser scanning speed and laser power on the structures. The final experiments concentrated on the parameter combinations which produced the best results. As it was no longer necessary to experiment with large ranges of parameters, single blocks (10mm x 10mm) were produced on each substrate instead.

Copper and H13 have markedly different melting temperatures, therefore the remaining experiments were intended to reduce the effects the difference in melting temperatures may have. The first of these was designed to minimise the time that any part of the powder

bed is molten by increasing the laser scanning speed to 400mm.s^{-1} (from a previous maximum of 250mm.s^{-1}). Although the increased speed of the heat source would reduce the specific energy density that would be applied to the powder bed, this experiment was designed to give the materials less time to interact in their molten state. The laser power used was 82W CW with a spot size Ø100μm and beam overlap 25%.

The final experiment considered the effect of varying the relative powder sizes, with powder sizes of 212+65μm copper (a minimum powder size of 212μm with an upper limit tolerance of 65μm [Osprey Powders]) and 80%<22μm H13 being used. The intention was to investigate another way to reduce the interaction time (Section 2.3.1 explains why larger particles require longer to melt them). As the particle size of the copper was greater than the nominal layer thickness (75μm) used in the thin multi-layer experiments, these experiments were conducted using thick, 7mm, pre-placed powder beds instead.

4.2 Results

4.2.1 Experiments to Produce Homogeneous H13 Builds

Single-track, multi-layer walls (process parameters Table 4.2) allowed the preliminary process window for H13 to be determined. For the laser system used here, there appeared to be a critical laser power (60W), below which the powder would not fuse (see Figure 4.2). During the multi-track, multi-layer experiments, the powder also appeared not to fuse if lower laser pulse frequencies were used (this is shown in Figure 4.3 where the three samples produced at 10kHz completely failed to fuse). This initially appeared odd, as the lower frequency allows more energy to build up in the laser cavity and should produce the highest peak energies. However, also observed near these specimens was a black powdery residue and it is likely that the high peak energies are vaporising a significant amount of the powder in the layer, generating a strong plasma above the melt pool and generating a shock wave that disturbed the powder bed. The black powder is likely to be a nano-sized metal powder formed as a condensate from the plasma (Perrie *et al*, 2005).

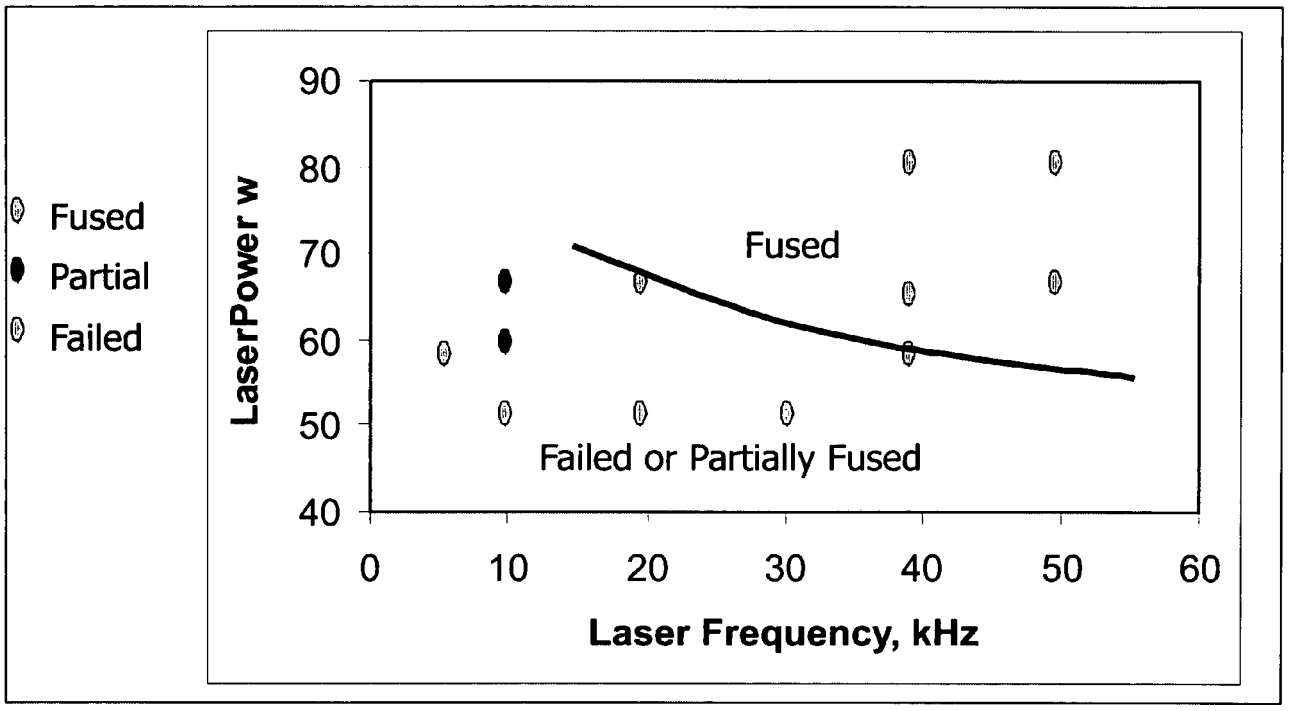

Figure 4.2 Relationship between laser frequency and laser power for single-track, multi-layer H13 structures (data based on samples produced with laser scanning speed of 30mm.s^{-1})

At the other extreme, some samples failed to fuse coherently due to over-melting (denoted as failed samples on Figure 4.2), identified by the melt tracks being torn or by the corners of the coupons lifting or curling. These effects are due to thermal stresses and have been observed in previously published DMLR work (Morgan *et al*, 2001 and Pogson *et al*, 2003) as well as sintering-based work (Zhu *et al*, 2003 and Simchi *et al*, 2001). Another effect observed was the tendency of the melt pool to ball-up (Figure 4.3), producing a round rather than flattened melt bead; an effect that is much stronger with H13 than with copper or stainless steel. The most significant effect of this change of behaviour was the tendency for the processed material to stand proud of the original powder bed surface (referred to as 'Z-growth' or 'overbuilding').

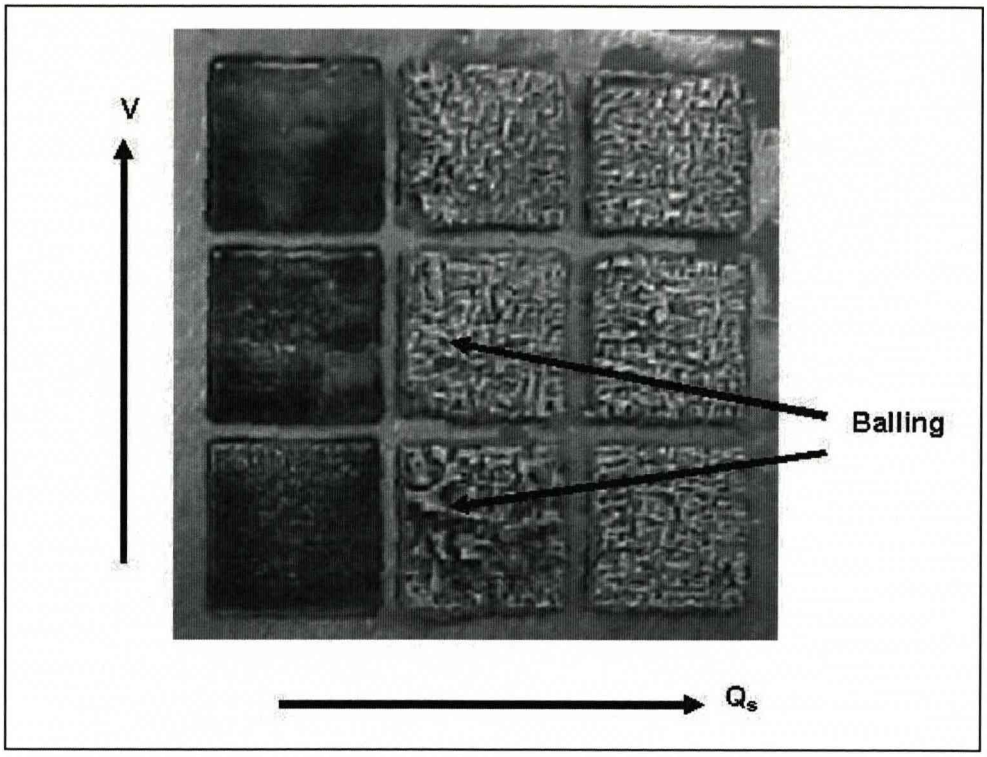

Figure 4.3 3 x 3 Array of H13 structures produced using relatively high energy parameters with laser power of 82W, laser scanning speed varying incrementally in steps of 30mm.s^{-1} from 30mm.s^{-1} (bottom row) to 90mm.s^{-1} (top row) and a laser frequency varying incrementally in steps of 10 kHz from 10kHz (left column) to 30kHz (right column)

With single-track walls, the balling problem was less obvious as the powder spreader could pass over the samples, but with multi-track builds the powder spreader would jam after about thirty layers. If, however, the laser scanning speed was increased from 300 to 500mm.s^{-1}, the maximum number of layers possible increased to about 60 layers; the high scanning rates giving less time for the melt pool to draw in powder from the surrounding areas and ball-up. As it was not possible to increase the scanning speed further (500mm.s^{-1} being the maximum achievable by the scanning galvanometers), an alternative solution had to be found. For DMLR to work, it is imperative that the build never stands proud of the powder bed as it interferes with the powder spreading mechanism, thereby, either creating an uneven powder layer or causing the mechanism to jam.

To alleviate these problems, a series of builds was produced with modified scanning formats. For these, the simple X-direction scan was supplemented with a second, lower

powered, Y-direction scan that smoothed the surface and melted any powder that had been deposited on the surface from surrounding areas due to shock waves (Morgan *et al*, 2001) from the pulsed laser.

As a lack of wetting would stop the molten H13 flattening out on the underlying material, factors that affected surface reactivity had to be considered. Any oxygen within the build chamber would lead to thin oxide surface films, which in turn would reduce the surface reactivity. Therefore a reducing gas (90% N_2, 10% H_2) was used instead of nitrogen. These modifications to the processing conditions were successful and allowed continuous building to take place (which was limited only by the powder feeder being exhausted of powder). The process parameters used were further refined for this modified procedure using 3 x 3 arrays of 10mm x 10mm structures and 20mm x 20mm builds. The parameters that were used for both the successfully fused samples (where the layers are sufficiently bonded together and the surface is flat and uniform) and partially fused, or failed samples (where the layers have failed to fuse and the surface does not possess a flat, uniform, surface), were:

Single-Track, Multi-Layered Builds

Fused Samples:

Laser Power	65 - 82W
Laser Frequency	40 - 50kHz
Laser Scanning Speed	10 - 30mm.s^{-1}

Partially Fused or Failed Samples:

Laser Power	52 - 60W
Laser Frequency	5 - 10kHz
Laser Scanning Speed	≥30mm.s^{-1}

Multi-Track, Multi-Layered Builds

Fused Samples:

Laser Power	75 - 82W
Laser Frequency	30kHz
Laser Scanning Speed	300 - 500mm.s^{-1}

Partially Fused or Failed Samples:

Laser Power	<75kW
Laser Frequency	5 - 20kHz
Laser Scanning Speed	<300mm.s^{-1}

Figure 4.4 shows examples of the successful builds that were produced during these experiments.

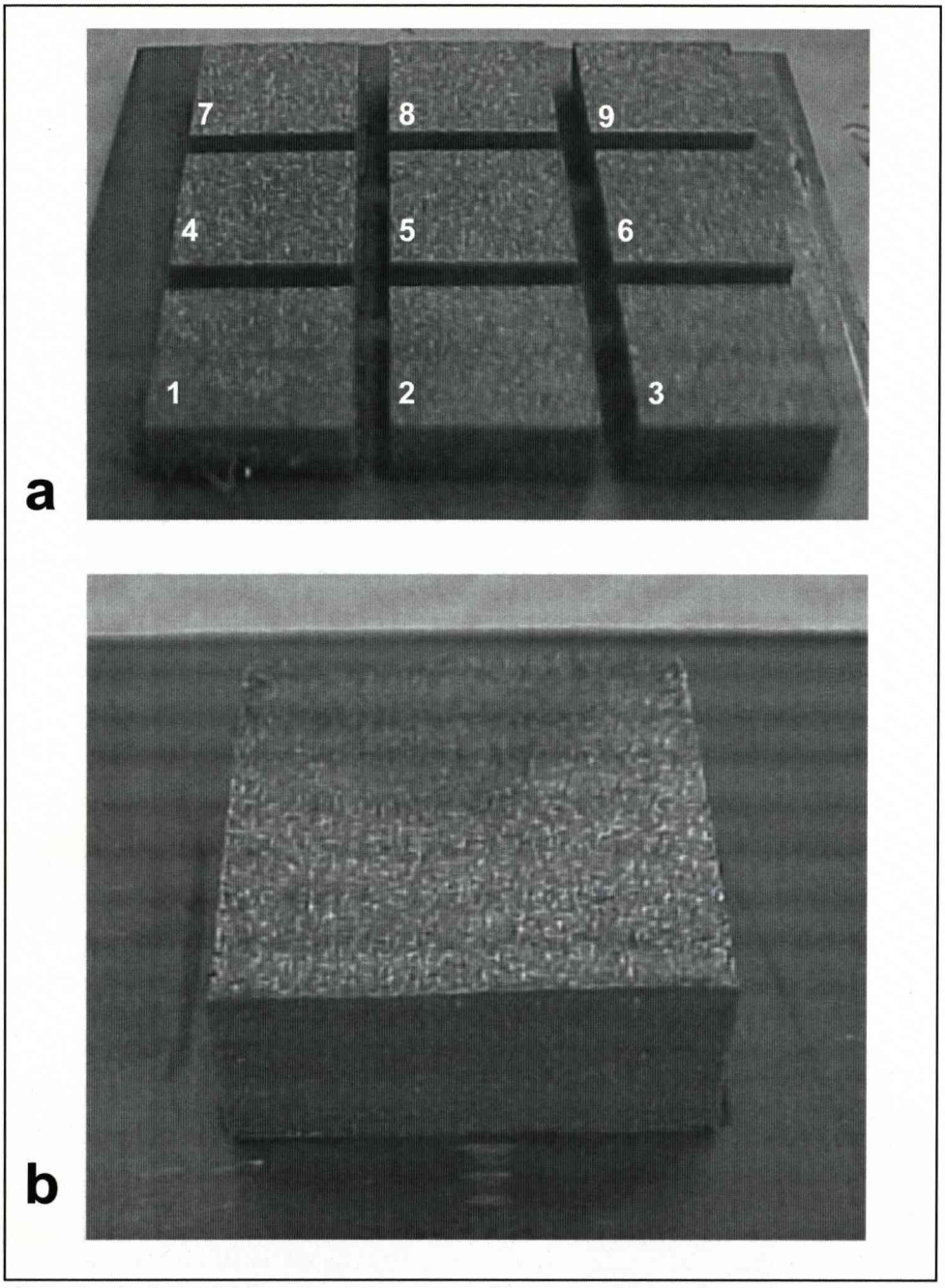

Figure 4.4 Images of successfully fused H13 structures; the builds in the array in Figure 4.4a were produced with a laser power of 82W, a frequency of 30kHz and laser scanning speeds of: 1) 460mm.s^{-1}, 2) 465mm.s^{-1}, 3) 470mm.s^{-1}, 4) 475mm.s^{-1}, 5) 480mm.s^{-1}, 6) 485mm.s^{-1}, 7) 490mm.s^{-1}, 8) 495mm.s^{-1} and 6) 500mm.s^{-1}; the build in Figure 4.4b was produced with a laser scanning speed of 500mm.s^{-1}, a laser power of 82W at a frequency of 30kHz

Also tried during this work was the scanning strategy proposed by Morgan *et al*, 2001 (who used it for stainless steel), which used four different scan patterns, scanned on alternate layers, with a supplementary "cleaning scan". However, it proved unsuccessful when processing H13 as it led to the part building above the bed and the powder spreading roller jamming.

Figure 4.5 shows the improvement possible by fine-tuning the process (Figure 4.5a to 4.5c before optimisation, Figure 4.5d after optimisation). These images not only show the change in surface morphology as the process was modified but also how the balling left a broken, distorted surface. During the spreading of the subsequent layer, the high points would have a very thin powder layer, while any holes would lead to a locally thick layer. If these pockets of powder were deep enough the laser would not be able to melt all the powder, leading to porosity and unmelted powder in the component.

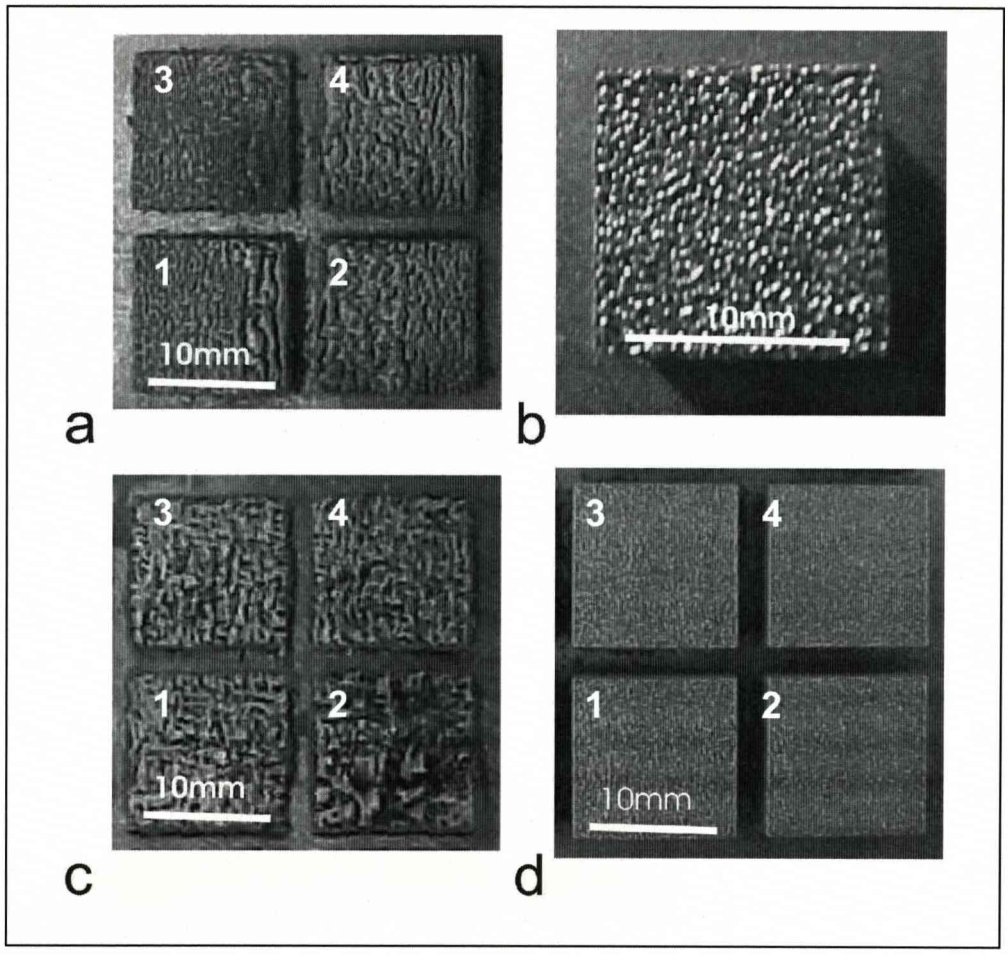

Figure 4.5 Photographs showing the effects of melt bead balling on the surface morphology. The builds in Figure 4.5a were produced with a laser power of 82W at a frequency of 30kHz with scanning speeds of: 1) 225mm.s^{-1}, 2) 250mm.s^{-1}, 3) 275mm.s^{-1} and 4) 300mm.s-1. The build in 4.5b was produced with a laser power of 82W at a frequency of 30kHz and scanning speed of 400mm.s^{-1}. The builds in 4.5c were produced with a laser power of 82W at a frequency of 20kHz and scanning speeds of: 1) 325mm.s^{-1}, 2) 350mm.s^{-1}, 3) 375mm.s^{-1} and 4) 400mm.s^{-1}. The builds in 4.5d were produced with a laser power of 82W at a frequency of 30kHz and scanning speeds of: 1) 450mm.s^{-1}, 2) 465mm.s^{-1}, 3) 480mm.s^{-1} and 4) 495mm.s^{-1}. All were produced with a beam overlap of 50%

A quick measurement of the part density possible for the optimised settings was obtained by measuring the ratio of black to non-black pixels on micrographs, where the contrast had been greatly increased; the black pixels being the pores. This gave an average porosity of

6%. Figure 4.6 shows the macrostructure and microstructure of samples used for this analysis.

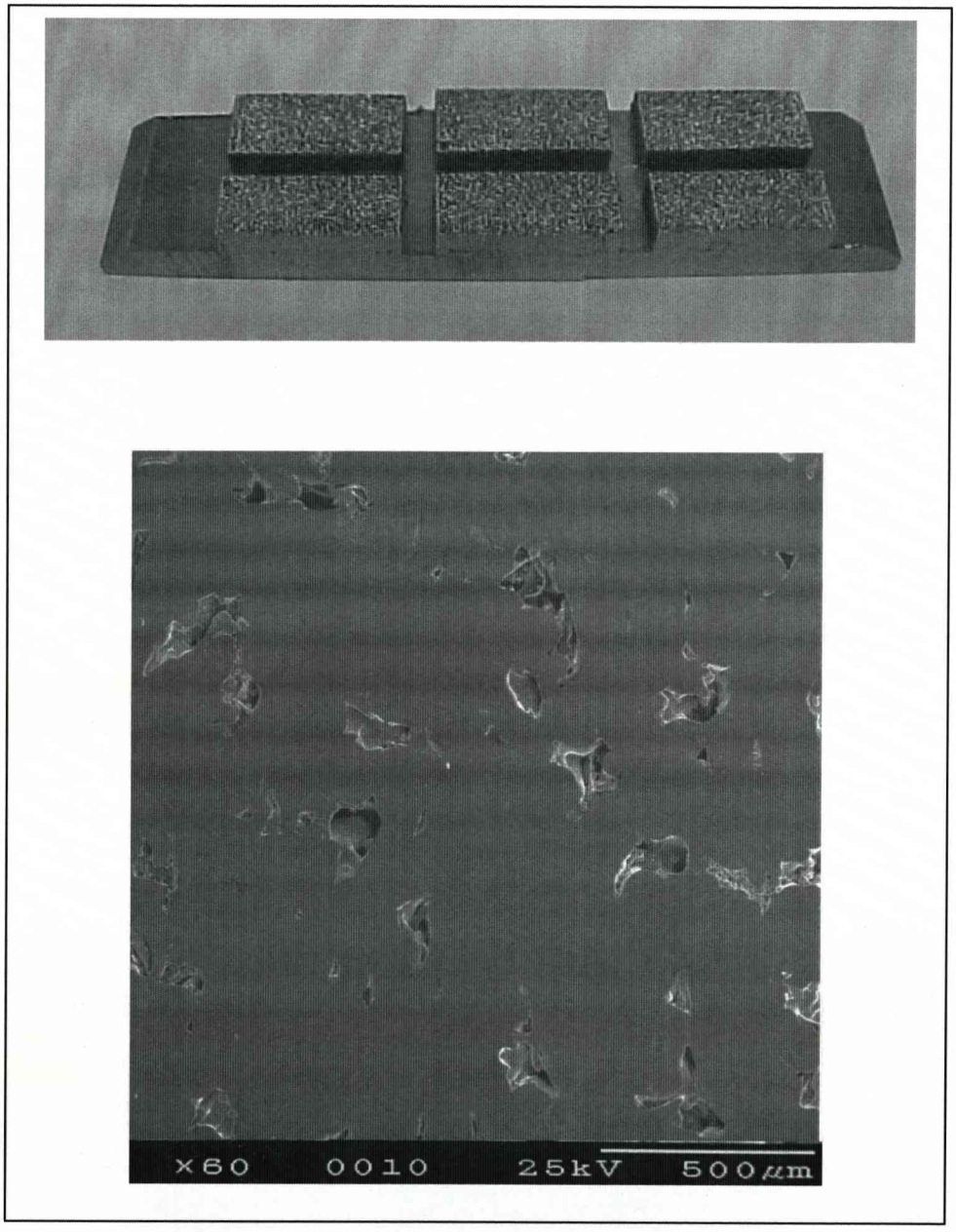

Figure 4.6 Digital photograph and SEM micrograph of a sectioned H13 build produced with laser scanning speed of 240mm.s^{-1}, laser power of 82W at a frequency of 30kHz and a beam overlap of 50%

The microstructure of the DMLR processed H13 was martensitic, even though it was formed directly from the melt (Figure 4.7 shows part of the sample shown in Figure 4.6

after tint etching [potassium metabisulphate, H_20 and HCl]), and was therefore suitable for use in tooling.

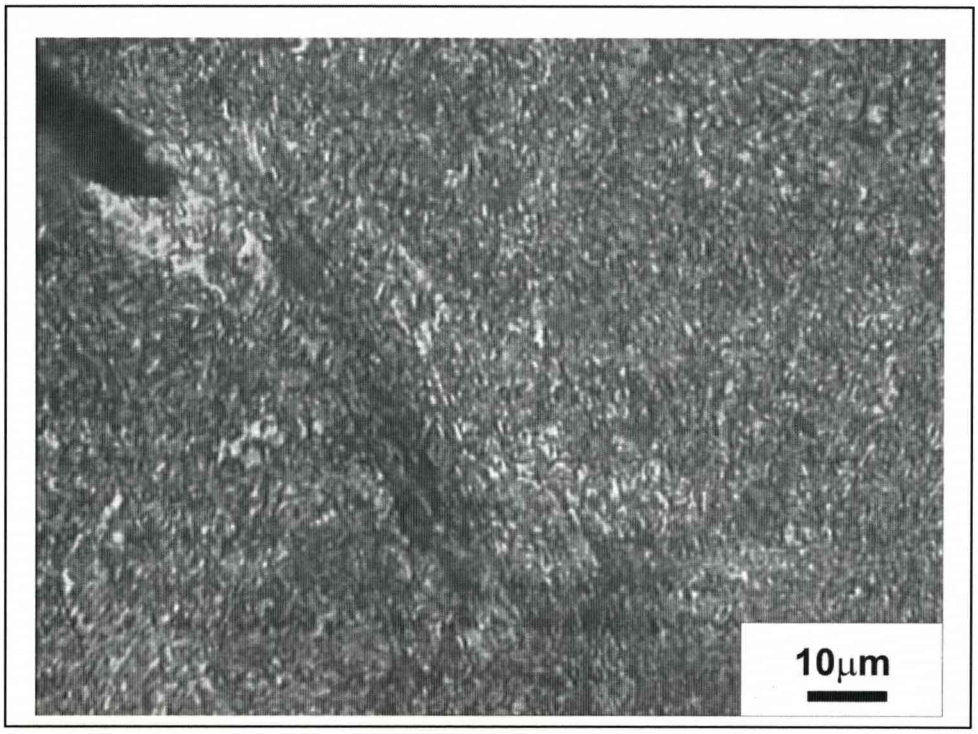

Figure 4.7 Optical micrograph showing cast microstructure within DMLR processed H13 produced with laser scanning speed of 240mm.s^{-1}, laser power of 82W at a frequency of 30kHz and a beam overlap of 50%

4.2.2 Cu/H13 Pre-placed Powder Bed (Single Layer Coupons)

The processing of mixed H13 and copper as thick beds produced coupons free from surface cracks, but in each case, the top surface was copper coloured, while the bottom was silver. This was an early indication of one of the problems that would occur when processing this system; the copper segregates to the top of the melt pool on freezing. Figure 4.8 shows a photograph of the 50% copper, 50% H13 powder bed following the laser scanning of the coupons. When producing graded structures, this would be problematic as the desire would be to melt the materials without them mixing; if the copper were pushed to the surface of the melt pool on freezing, it would not be possible to have sufficient control over the final structure.

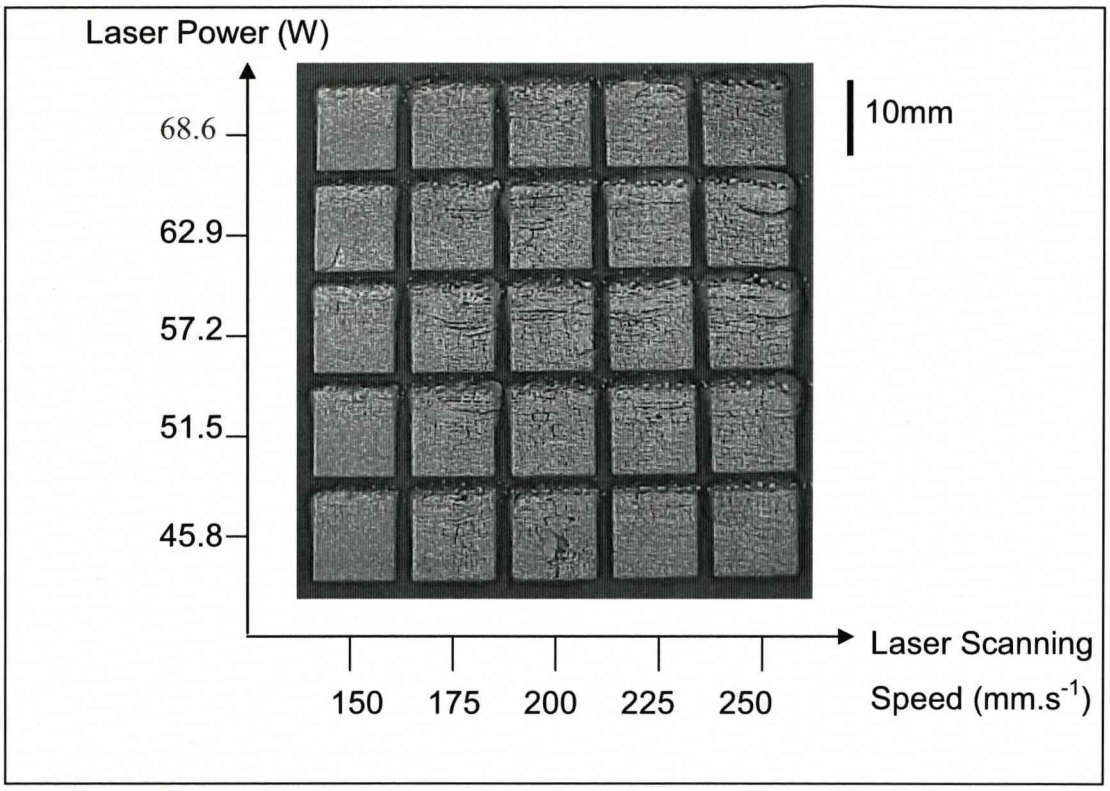

Figure 4.8 First array of dissimilar metal coupons showing the relationship between laser power and laser scan speed; this experiment used a fixed Ø100μm laser spot, laser frequency of 0Hz (CW) and a beam overlap of 25%

SEM micrographs (Figure 4.9) of the samples showed that two surface morphologies formed; the 50%Cu, 50%H13 and the 75%Cu, 25%H13 samples showed evidence of balling (albeit with finer melt-beads than for the H13 alone), while the 25%Cu,75%H13 samples were fairly flat. When balling occurred there was no obvious alignment between surface features and the laser beam scans, however with the flatter samples surface lines formed parallel to the laser scan. The difference in behaviour of the different powder mixtures was unaffected by the processing parameters used and therefore must be a feature of the 'alloy' composition.

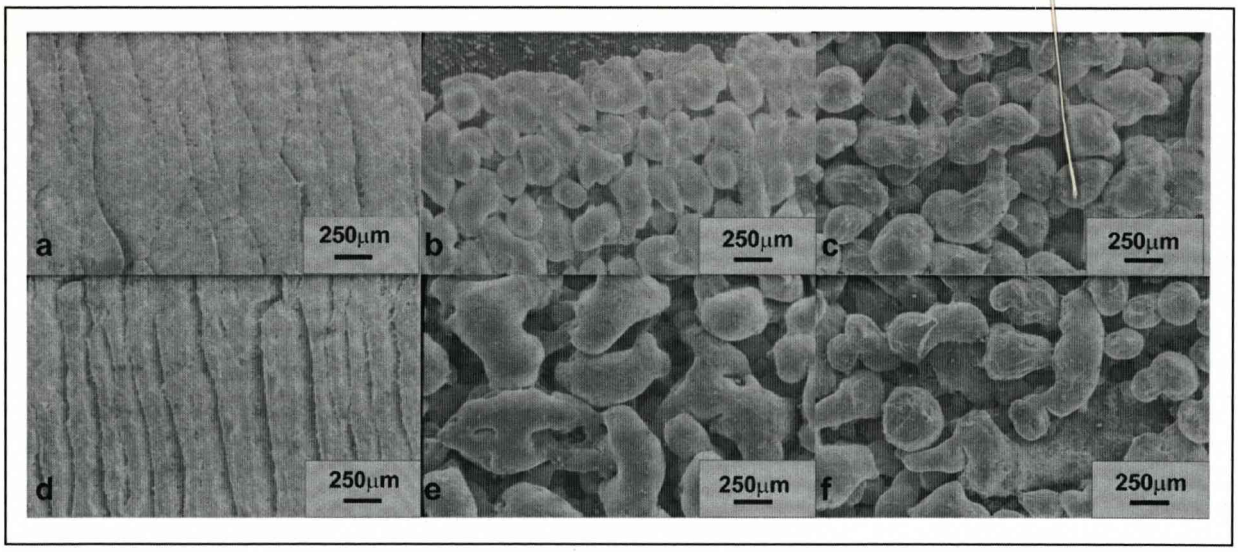

Figure 4.9 SEM Micrographs showing the surfaces of six selected coupons with a) 25% Cu, 75% H13; b) 50% Cu, 50% H13; c) 75% Cu, 25% H13 composition produced with a 250mm.s^{-1} laser scanning speed and 57.2W CW laser power; and d) 25% Cu, 75% H13; e) 50% Cu, 50% H13; f) 75% Cu, 25% H13 composition produced with a 175mm.s^{-1} laser scanning speed and 51.5W CW laser power

Cross-sectioning revealed (Figure 4.10) the microstructural differences between the samples. The 50%Cu, 50%H13 and 75%Cu, 25%H13 samples were similar, while the 25%Cu, 75%H13 samples were very different. The 50%Cu, 50%H13 and 75%Cu, 25%H13 samples, which showed balling, consisted of two distinct regions, one iron-rich and the other copper-rich. The iron-rich regions were present as spheres (of a range of sizes) within a copper-rich matrix (Figure 4.10c) with each copper-rich region containing one or two large iron-rich regions and many smaller ones (Figure 4.10e). The iron-rich regions had a needle-like microstructure and sometimes also contained copper-rich precipitates (Figure 4.11). The copper-rich regions appeared to have a fine cast structure but the microstructure was less distinct. The 25%Cu, 75%Fe samples, with the flatter morphology, had a very fine structure that made the microstructure difficult to determine, e.g. it was difficult to analyse specific regions using EDS.

EDS analysis was conducted on each of the samples to ascertain the variation in iron, copper and chromium with increasing distance from the upper surface. The variation in the composition was determined by comparing the intensity of the Fe, Cu and Cr kα peaks,

which were then used to provide the differing proportions of each metal within the regions. It was found from this that the relative peak heights varied only slightly from place to place (Figure 4.12). SEM/EDS also confirmed that the upper surfaces of the 25%Cu, 75% Fe samples were copper-rich and contained significant numbers of voids.

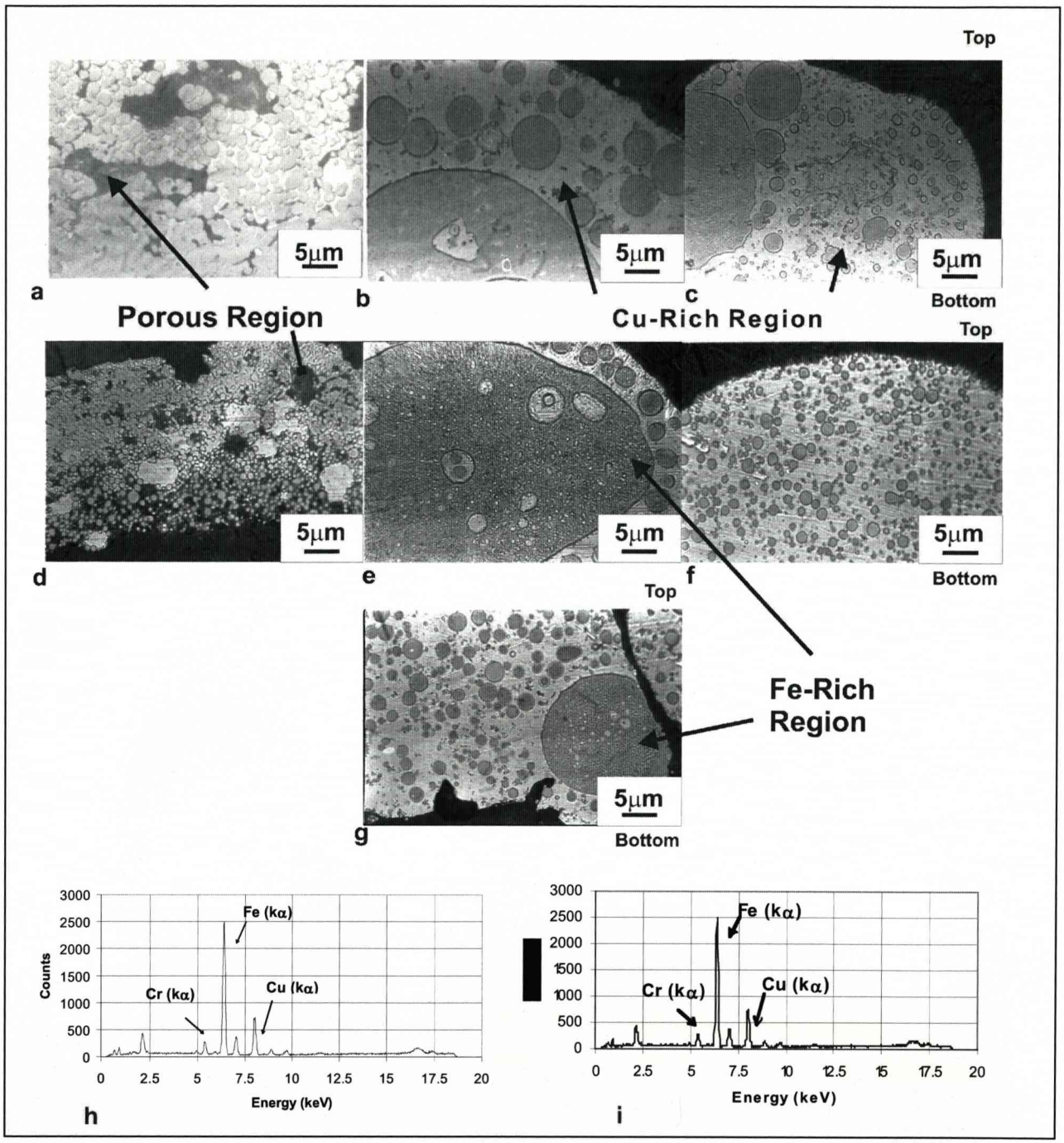

Figure 4.10 SEM micrographs showing sections of the coupons with compositions: a) 25% Cu, 75% H13; b) 50% Cu, 50% H13; c) 75% Cu, 25% H13 produced using v = 250mm.s^{-1}, P = 57.2W CW and d) 25%Cu, 75% H13; e) 50% Cu, 50% H13; f) 75% Cu, 25% H13; g) 75% Cu, 25% H13 (alternative view) using v = 175mm.s^{-1} and P = 51.5W CW. EDS spectra highlighting g) Fe-rich region (0.12mm from upper surface); h) Cu-rich region at upper surface, for specimens produced with a 50%Cu, 50% H13 composition, and parameters v = 175mm.s^{-1} and P = 51.5W CW

Microhardness results (Table 4.4) revealed that the hardness of the iron-rich regions varied significantly between regions, while the hardness of the copper-rich regions showed little variability. Figure 4.13 shows a plot of the data from Table 4.4, showing the variations in microhardness between each of the six coupons at the upper surface.

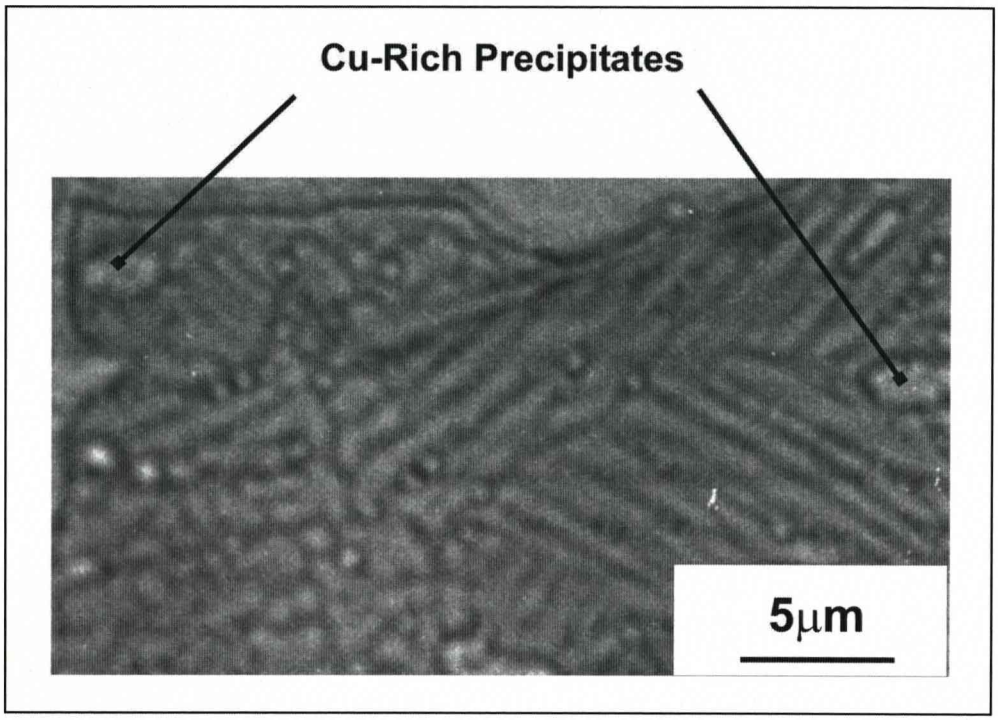

Figure 4.11 Optical micrograph showing Fe-rich region on a coupon produced with a 75% Fe, 25% Cu composition produced using laser scanning speed of 250mm.s^{-1} and laser power of 57.2W CW

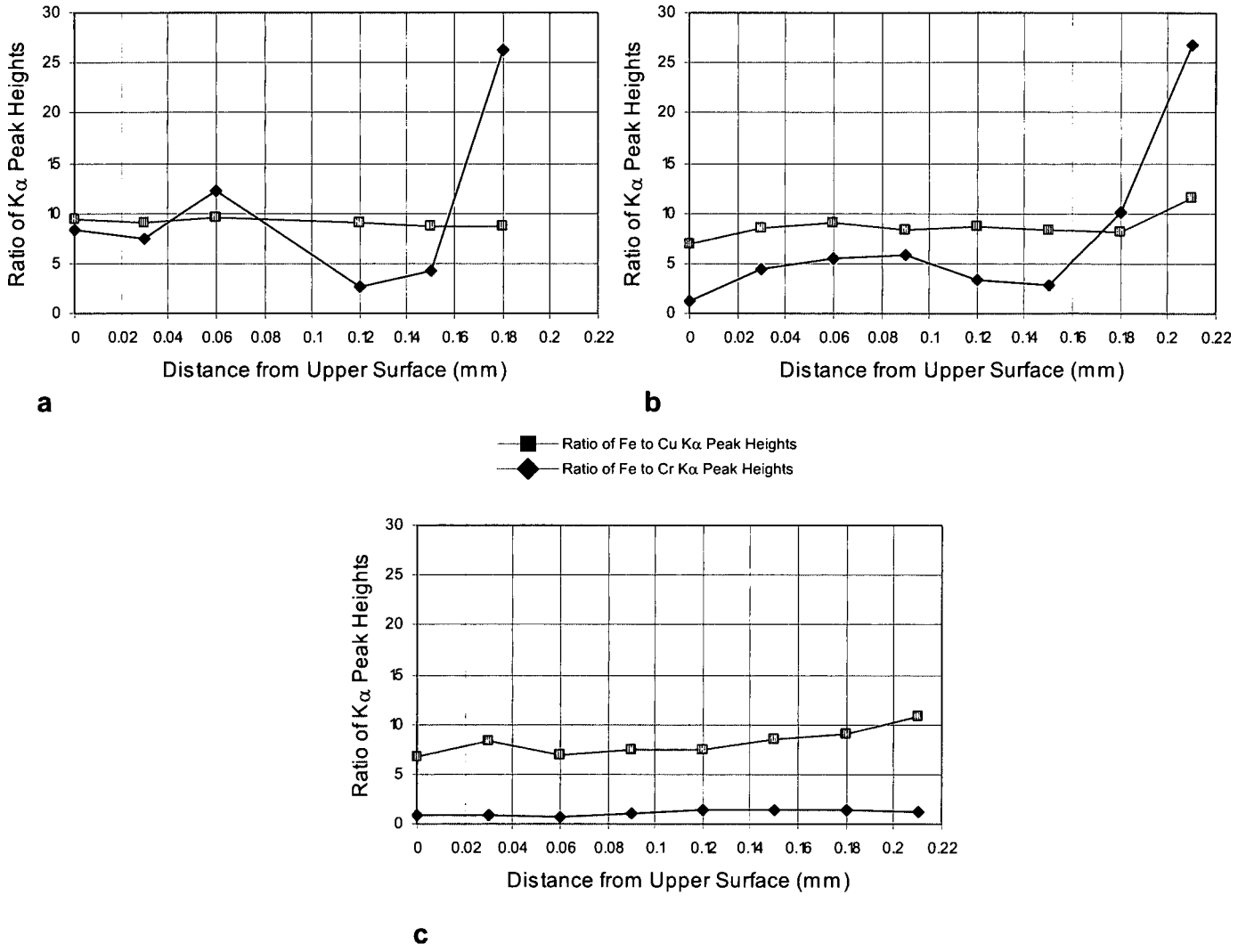

Figure 4.12 Plot showing ratio of kα peak heights (Fe:Cu and Fe:Cr) with distance from sample upper surface. This data has been derived from the EDS spectra for coupons with a) 25% Cu, 75% H13; b) 50% Cu, 50% H13; c) 75% Cu, 25% H13 compositions for the three coupons produced with laser scanning speed of 175mm.s^{-1} and laser power of 51.5W CW

Coupon	Parameters	VICKERS HARDNESS No.	
		Fe-Rich Region (Avg. of 10 Readings)	Cu-Rich Region (Avg. of 10 Readings)
A	25% Cu, 75% H13. $v = 250mm.s^{-1}$, P = 57.2W	321.7	70.7
B	50% Cu, 50% H13. $v = 250mm.s^{-1}$, P = 57.2W	349.9	101.7
C	75% Cu, 25% H13. $v = 250mm.s^{-1}$, P = 57.2W	343.2	105.1
D	25% Cu, 75% H13. $v = 175mm.s^{-1}$, P = 51.5W	330.5	54.7
E	50% Cu, 50% H13. $v = 175mm.s^{-1}$, P = 51.5W	390.4	99.4
F	75% Cu, 25% H13. $v = 175mm.s^{-1}$, P = 51.5W	428.6	84.7

Table 4.4 Table showing results of micro-hardness measurements (Vickers Hardness No.) across discrete Fe-rich and Cu-rich regions of the six selected coupons

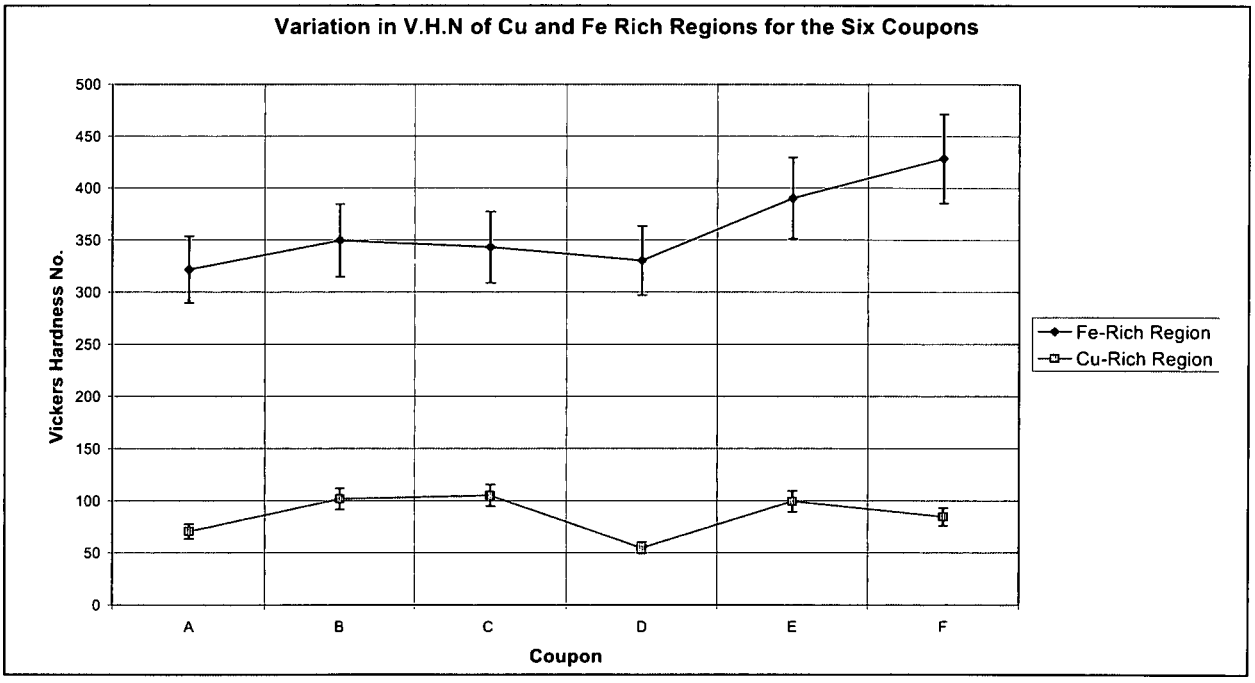

Figure 4.13 Plot showing variation in microhardness, for the six coupons listed in Table 4.4, at the upper surface (VHN values mean of 10 readings)

4.2.3 Cu/H13 Multi-Layer Coupons

With the multilayer builds, greater porosity was observed when processing mixed H13/copper powders than with H13 alone and although the simple line scan strategy used tends to lead to high porosity, the same strategy was used in both sets of experiments. Although the resultant porosity of the samples is not a paramount issue here (the samples were produced to investigate the material interactions and not to create densified, functional, parts), the high levels of porosity point to the wettability and the flowability of the molten metal being significantly different between the mixed powders and pure H13. The mixed powders produced melt beads with two distinct regions with different microstructures (Figure 4.14). As with the thick single layer coupons described earlier, one region was found to be copper-rich while the other iron-rich.

At lower laser scanning speeds, with the 25%Cu-75%H13 material, the copper-rich regions formed a thin layer around the melt beads. This region diminished as the laser scanning speed was increased to 400mm.s^{-1} (Figure 4.15) when the copper-rich material became trapped within the iron-rich regions. At the higher copper contents (75%Cu-25%H13), where the copper-rich phase dominated, the iron-rich regions were not displaced to the outside of the melt bead; instead they formed discrete regions within the copper-rich matrix, at all scanning speeds.

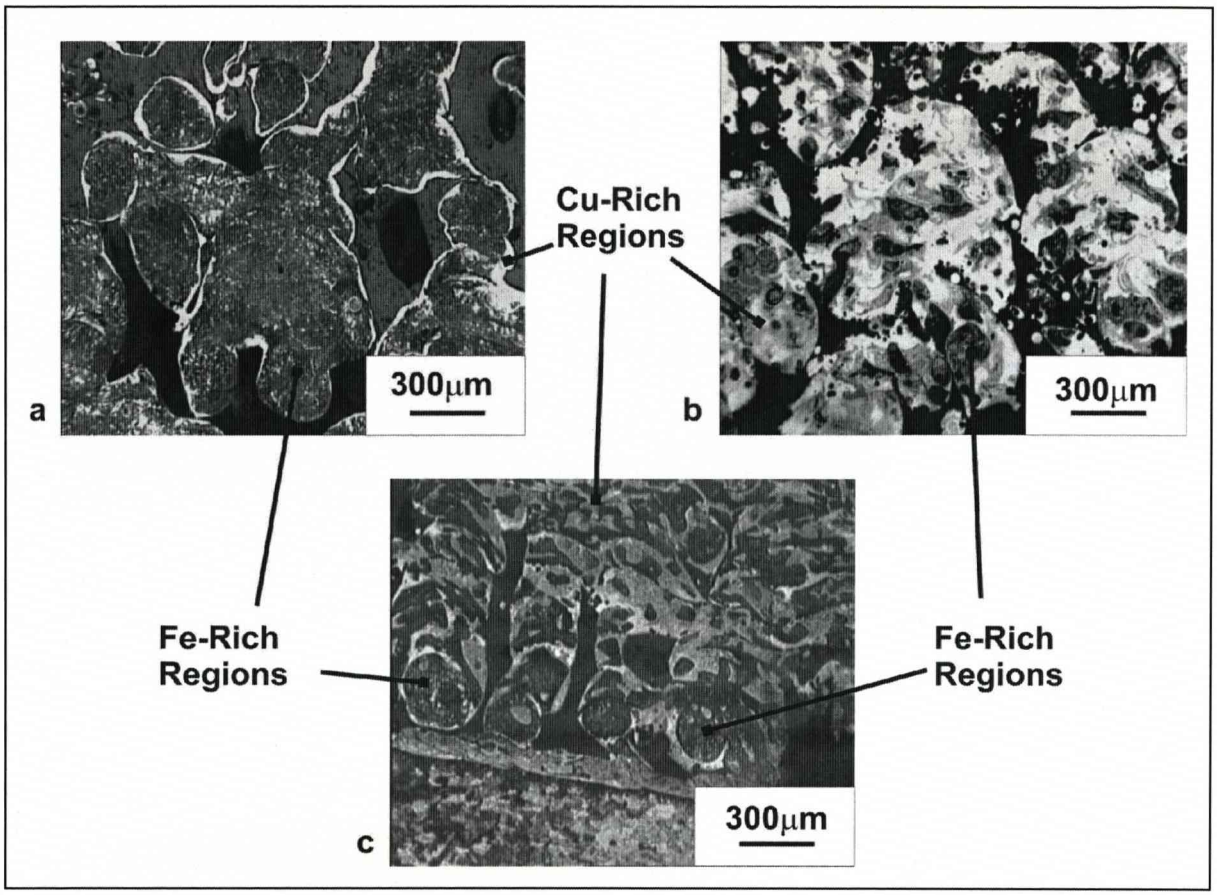

Figure 4.14 Optical images showing section views of samples produced with a laser scanning speed of 175mm.s^{-1}, laser power of 51.5W CW and compositions of: a) 25%Cu, 75%H13; b) 50%Cu, 50%H13 and c) 75%Cu, 25%H13

4.2.4 Cu/H13 Optimised Processing Parameters

When the scanning speed was increased to 400mm.s^{-1} (the laser power being increased to 82W CW to compensate for the reduction in specific energy density), in an attempt to optimise the processing conditions, a similar structure to that at lower speeds was observed (Figure 4.15), except that for the 25%Cu-75%H13 sample, copper-rich regions were observed trapped within the iron-rich regions. Although the higher scan speed leads to a reduction in the time the powders are molten, significant mixing could not be avoided.

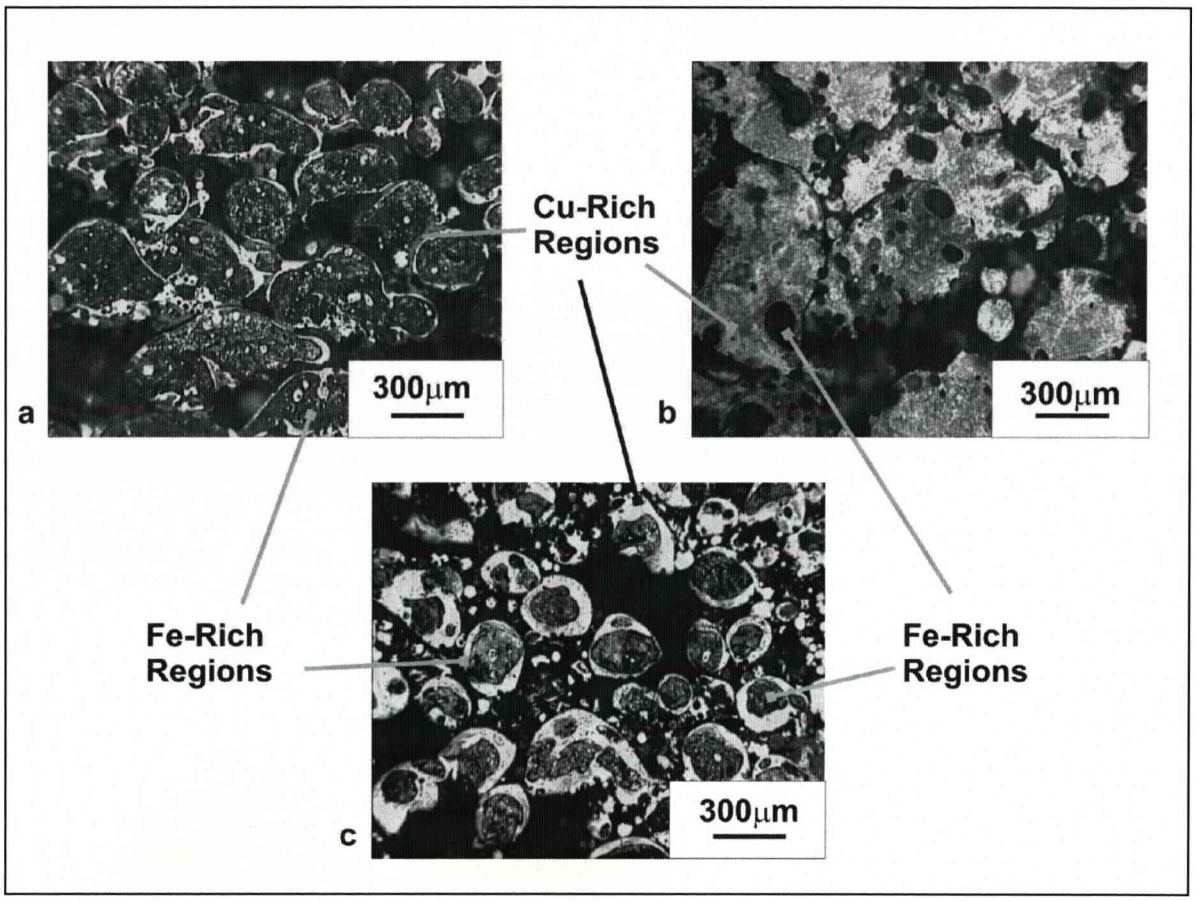

Figure 4.15 Optical images showing section views of samples produced with a laser scanning speed of 400mm.s^{-1}, laser power of 82W CW and compositions of: a) 25%Cu, 75%H13; b) 50%Cu, 50%H13 and c) 75%Cu, 25%H13

Significant cracking was observed in the coupons produced with the mixed H13/copper powders (Figure 4.16) that was not observed with H13. This may be due to the difference in microstructural morphology. Figure 4.17 shows optical micrographs taken from the three Cu/H13 compositions in section. Observed here is a microstructure within the H13 with a different morphology from the martensitic microstructure observed within the samples produced from H13 alone (Figure 4.7). The microstructure seen was needle-like, but it was not possible to confirm whether it was martensite.

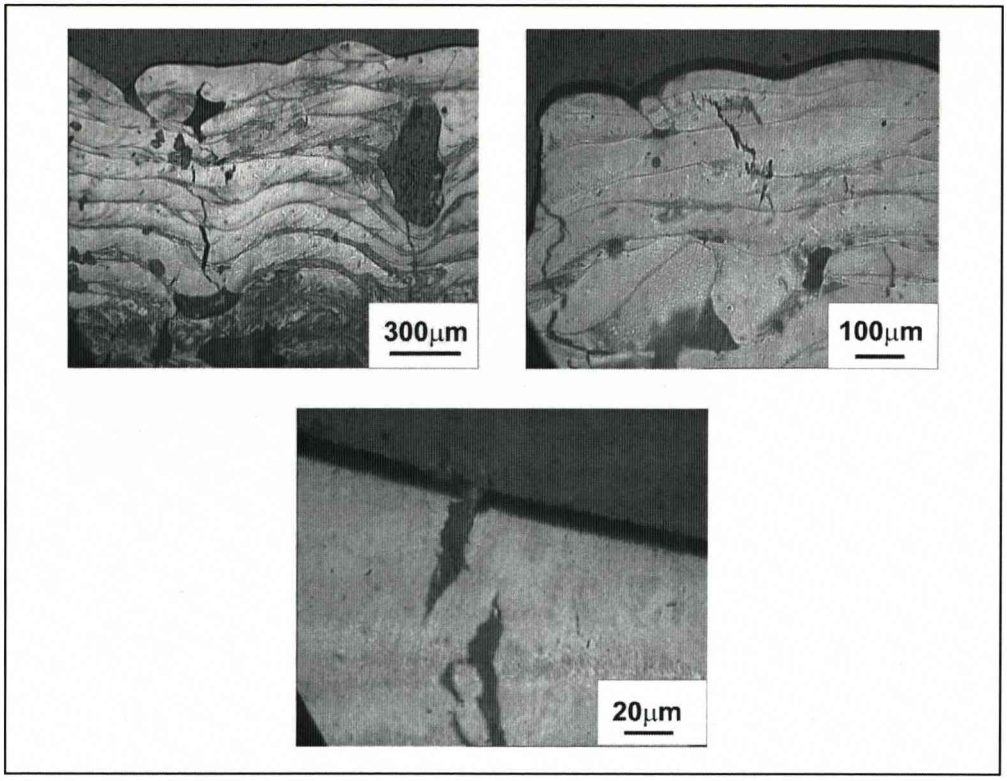

Figure 4.16 Optical images showing appearance of cracks in the structure produced with a 25% Cu, 75% H13 composition, laser scanning speed of 175mm.s^{-1}and laser power of 51.5W CW

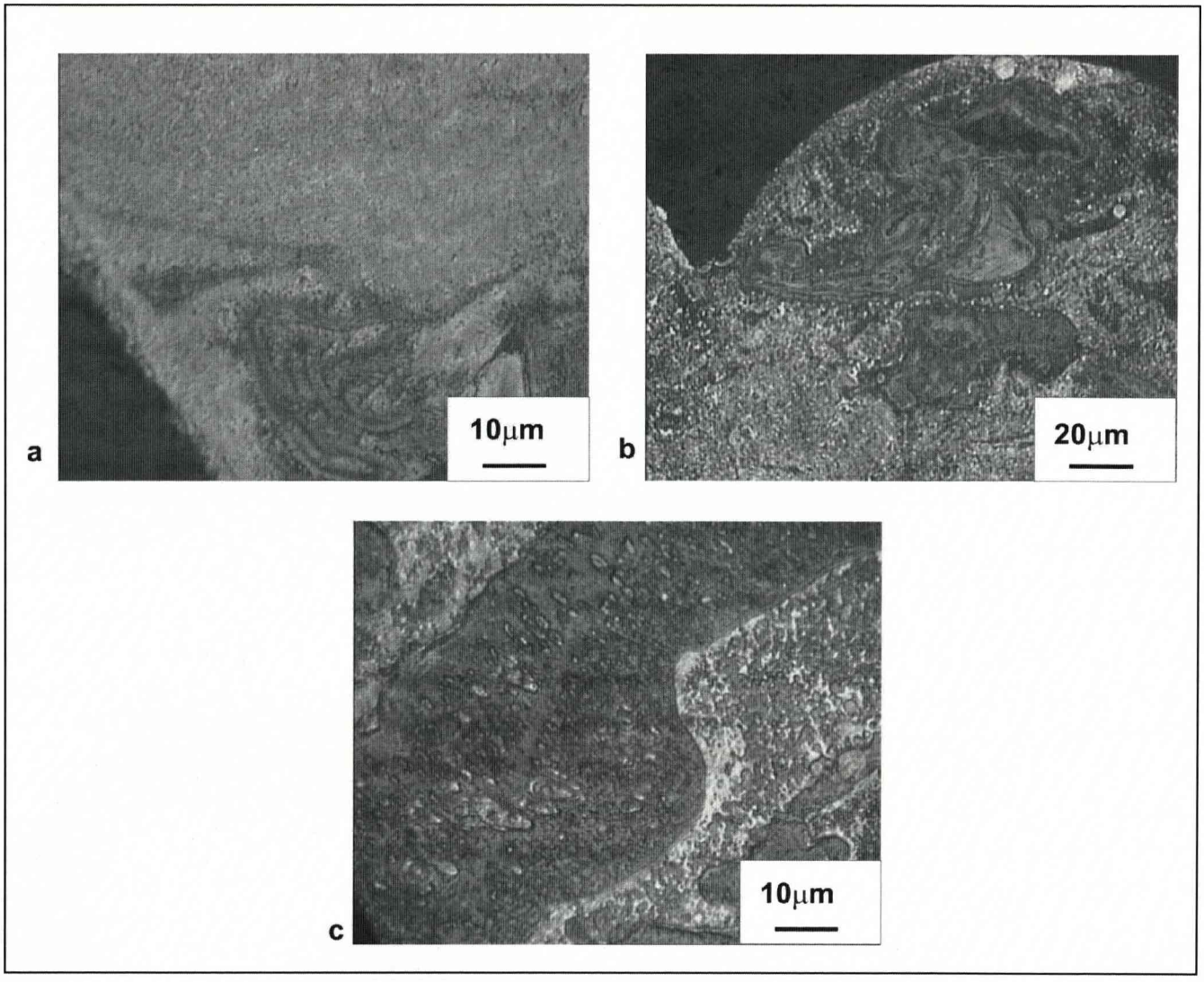

Figure 4.17 Higher magnification optical images showing section views of samples produced with a laser scanning speed of 175mm.s^{-1} laser power of 51.5W CW and compositions of: a) 25%Cu, 75%H13; b) 50%Cu, 50%H13 and c) 75%Cu, 25%H13

A comparison of the XRD data for H13 and the H13/copper processed materials showed that the lattice parameters of the iron phase did not change significantly between the samples and therefore there was little or no dissolution of copper within the room temperature iron-rich phase (Figure 4.18). The only other phase observed was copper.

From identification of the respective peaks, Figure 4.18 shows that martensite is formed in both the H13 and H13/Cu samples. The plot also shows significant amounts of copper with the 50/50 composition.

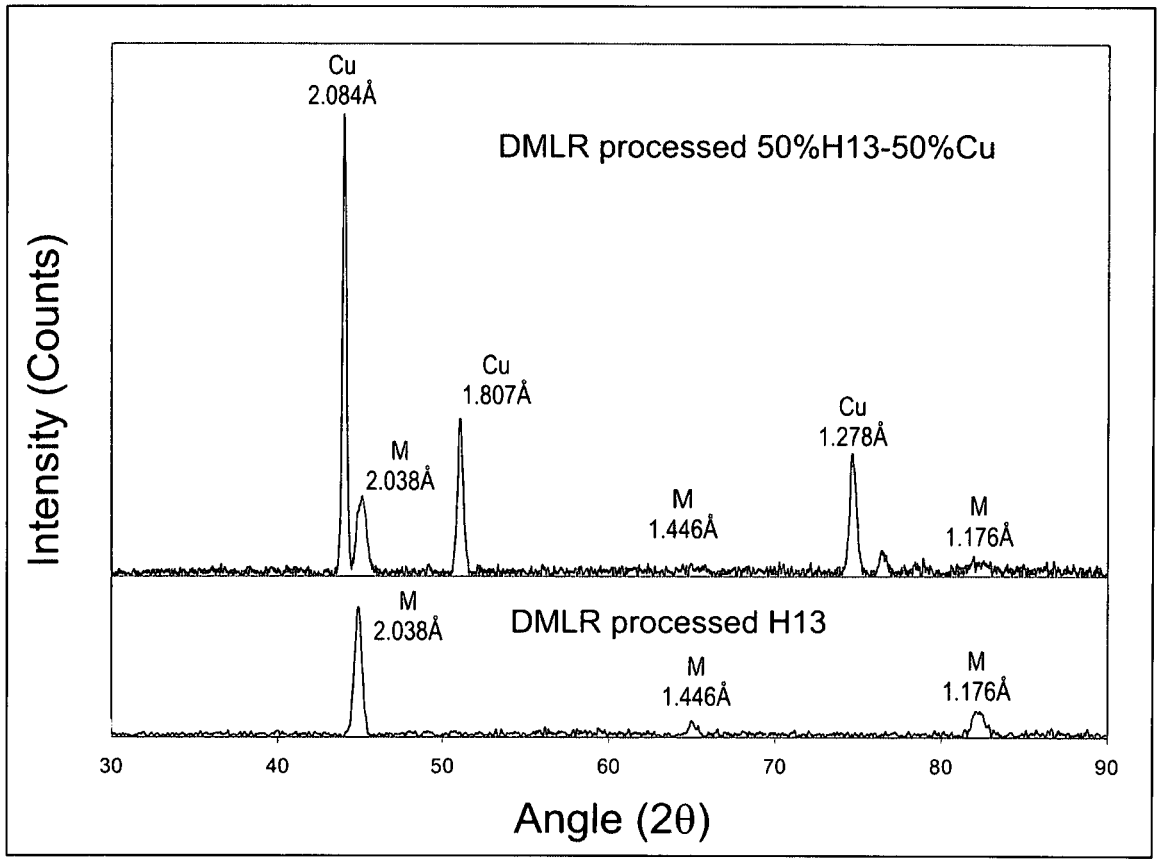

Figure 4.18 Plot of the XRD data for DMLR processed H13 and 50% Cu, 50% H13

Figure 4.19 shows optical micrographs of the samples produced using an increased scanning speed of 400mm.s^{-1} (by increasing the heating and cooling rates of the melt-pool, the intention of this experiment was to give the two powders less time to flow in their molten state and subsequently mix together). These samples showed reduced formation of copper regions within the iron, but discrete copper-rich regions within the iron-rich regions could still be seen.

The previous experiments used variations in the processing conditions to modify the structures formed but with limited success. Therefore, the use of different sized powders was investigated. By using the larger copper particle size (Figure 4.20; 212+65μm Cu, 80%<22μm H13), the time to melting of the two different powders could be modified. Again, it was found that the iron-rich regions contained copper and the copper-rich regions contained areas that were iron-rich. The extremely fragile nature of the 75% Cu, 25% H13

samples showed that changing the relative particle sizes was modifying the powder melting but that the powders were not fusing together.

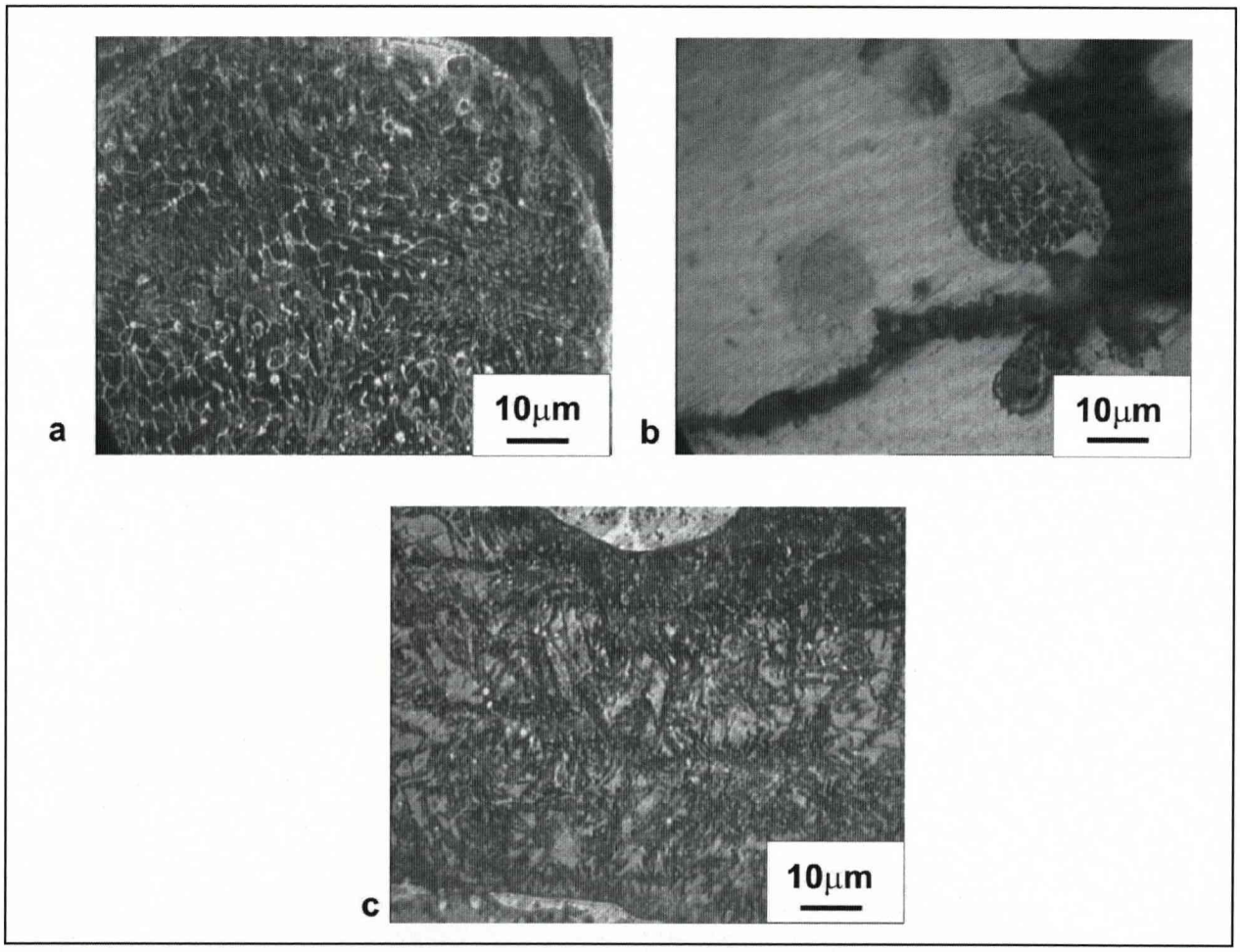

Figure 4.19 Higher magnification optical images showing section views of the samples produced with a laser scanning speed of 400mm.s^{-1}, laser power of 82W CW, beam overlap of 25% and compositions of: a) 25%Cu, 50%H13; b) 50%Cu, 50%H13 and c) 75%Cu, 25%H13

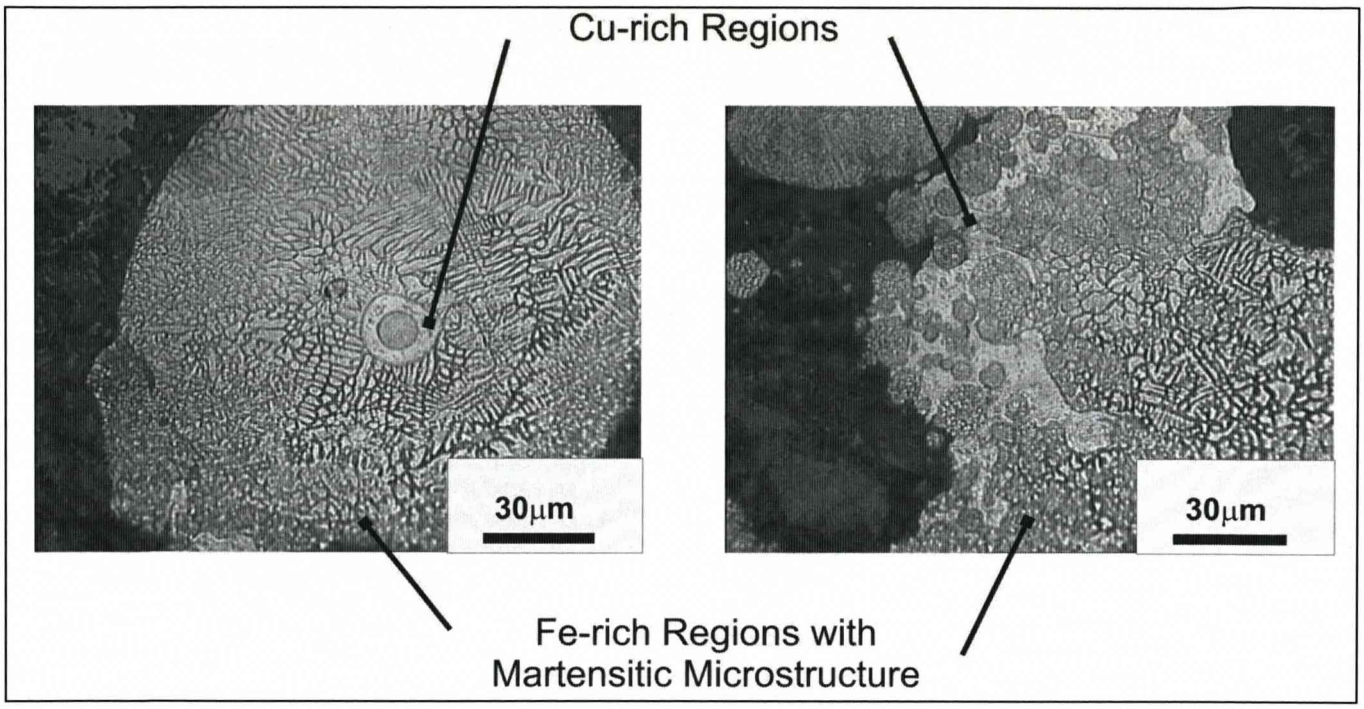

Figure 4.20 Optical image of sample produced with 25% 212μm+65μm Cu, 75 % 80%<22μm H13 with a laser scanning speed of 250mm.s^{-1}, laser power of 82W CW and beam overlap of 25%

4.3 Discussion

The initial work on H13 showed that DMLR processing is dominated by the behaviour of the molten metal and how it interacts with the processing conditions. It is the behaviour of the melt pool and whether it flattens out or balls up that dominates the process. If the balling is too severe, it can lead to the component building above the powder bed and the jamming of the powder spreading roller. Although balling has been observed when processing aluminium and stainless steel (Abe *et al*, 2003), it was less of a problem, both because these materials do not build significantly above the powder bed and because they are relatively soft and so do less damage to the powder spreading system. As would be expected, the problem only occurred with multilayer builds and as the build height increased with each added layer, the more likely the system was to jam.

The morphology of the melt bead has been commented on by other workers looking at a range of materials (e.g., iron and copper [Zhu *et al*, 2003] and a nickel-alloy [Tolochko *et al*, 2004]), while other work explained the material behaviour in terms of Marangoni forces generated by temperature gradients within the melt pool that develop because the laser beam is moving (Simchi *et al* 2001). Other forces acting upon the melt pool are due to the Rayleigh instability acting to break up the cylinder of liquid (the melted scan-track) into spheres, and the effects of reductions in surface energy due to the wetting of any underlying material.

Two groups of researchers discussed the role of Rayleigh instability during SLS/SLM processing where, as the laser beam moves across the powder the melt pool is elongated in one direction, making it long and thin (Simchi *et al* 2001 and Hauser *et al* 2003). This long thin cylinder has a higher surface area to volume ratio than a series of spheres and so it is possible for this cylinder of molten material to reduce its surface energy by forming a row of spheres. If the spheres are large enough, they will protrude above the surface of the powder, interfering with the powder spreading mechanism. The effect was shown to be greater at slower scan speeds and higher specific energy densities where the volume of molten material was greater. This is confirmed by the work here, where it was found that increasing the scanning speed reduced the tendency for the melt pool to ball-up.

There are several factors indirectly controlled by the laser scanning speed that affect the behaviour of the melt pool, of which a number will be important. These include the reduction in the specific energy density at higher scan speeds, which would reduce the superheating of the molten metal. This would make the melt pool narrower by reducing the melting of powder not directly under the laser beam and also allowing the melt pool to freeze more rapidly as there is less heat to diffuse away. However, the faster moving laser beam will also tend to elongate the melt pool, altering the temperature gradients along it and therefore the Marangoni forces that will lead to liquid movement within the melt. Although the scan speed can be used to control the behaviour of the melt pool, there are limitations because at higher speeds the power density may drop below that needed to melt the powder, while if the laser power is increased to counteract the drop in energy density, the high instantaneous powers may lead to the vaporisation of the surface rather than the melting of the powder layer. This was observed when the laser was used in pulsed mode, when the vaporised material produced shock waves that displaced the powder bed.

A second method of increasing part density and reducing balling was proposed by one group of researchers who developed scanning patterns that allowed fully dense parts to be produced with 316L stainless steel (Morgan *et al*, 2001). However, when the same strategy was tried with H13 it had a more harmful effect. The scanning patterns were designed to fill voids in the previous layer and also help the new material wet and spread across the previous layer, producing a flat surface. However, with H13, although the new powder filled any voids, it did not flow out to wet the previous layer but instead remained balled up. This increased the rate at which the component grew above the nominal powder bed height and subsequently jammed the powder spreader. This effect appears to be controlled by the surface energies of the solid/gas, liquid/gas and solid/liquid interfaces as these affect the wetting angle.

From the single-track and multi-track builds, it was seen that the former required much slower laser scanning speeds (10 to 30mm.s^{-1}) to successfully fuse samples, when compared to the latter (300 to 500mm.s^{-1}). This occurs because the use of overlapping laser tracks increases the specific energy density (consider the relationship in Eqn. (8) in Section 3.1), and the surrounding material is preheated by the earlier tracks, reducing the

temperature gradient and therefore slowing the diffusion of heat from the melt pool. Thus, less energy is required from the laser to melt the powder and so higher scanning speeds can be used. The increased laser scanning speed not only reduced processing time but also reduced the overall size of the melt pool as there was likelihood of melting and drawing into the melt pool material that was not directly under the laser beam. If the scanning speed had been increased further (which was not possible with the laser system used) then problems would have occurred with achieving high enough power input without vaporising some of the powder, generating shock waves and a plasma above the melt pool. In comparison, when processing H13 using Electron Beam Melting (EBM), Cormier *et al*, 2004 used ten preheating scans of 10,000mm.s^{-1} prior to the main scan (500mm.s^{-1}). The authors considered this necessary for two key reasons. Firstly, to preheat the substrate, gently raising the temperature so as to reduce the temperature difference between the melted layer and the rest of the part and secondly, to lightly sinter the powder together so that it was not disturbed during the main scan. Although this technique is different to DMLR, the best results were still obtained at speeds similar to those used here and very much higher than those used by many other researchers (e.g. Abe, 2000, Das, 2001).

If the scan speed was increased without increasing the energy density then the powder would sinter rather than fully melt, as was observed in previous work on copper (Pogson *et al*, 2003). The copper liquid phase sintered because of the powder particle size distribution within the bed: the smallest particles melting while the large particles did not as the smaller particles require less energy to melt them (as described in Section 2.3.1). With pure copper, the processing is made more difficult by the high conductivity of copper and the high reflectivity of the metal once frozen, which reduced the effectiveness of beam overlap.

For H13, the best results were achieved by following the original series of high power (82W) parallel X-direction scan tracks with a lower powered 45W, parallel Y-direction scan. The second scan putting additional energy into the remelted powder layer, which provided sufficient energy to melt the rough surface left after the first pass of the laser beam, leaving a finer surface. Even so, 6% porosity still remained in the finished components, which is somewhat high. As well as porosity, it is also important that the component has the correct microstructure as without it, the mechanical properties would be different to

those of the conventionally produced components. With DMLR processed H13, the final room temperature microstructure was of fine needles of martensite. This is the microstructure used in conventionally processed H13 tools.

The phase changes that occur during the DMLR processing of H13 are complex, as unlike with conventional tool steel manufacturing, the component is produced directly from the melt and the material behaviour is more like that achieved during welding than during normal heat treatment, which starts in the austenitic phase. Also, as each new layer is produced by partially remelting the previous layer, it is likely that the material refreezes by growth of the grains in the previous layer, rather than by nucleation of new grains. These grains are likely to be austenite rather than δ-ferrite and it is the austenite that transforms to martensite on cooling if the cooling rate is sufficiently rapid. With alloy steels, martensite is formed at reasonably slow cooling rates as can be seen from the CCT diagram for H13 (Figure 4.21). The microstructure will be further modified by the subsequent passes of the laser beam nearby, which will lead to the tempering of the martensite structure and possibly the formation of fine carbides, although a tempering process would also be undertaken during conventional processing.

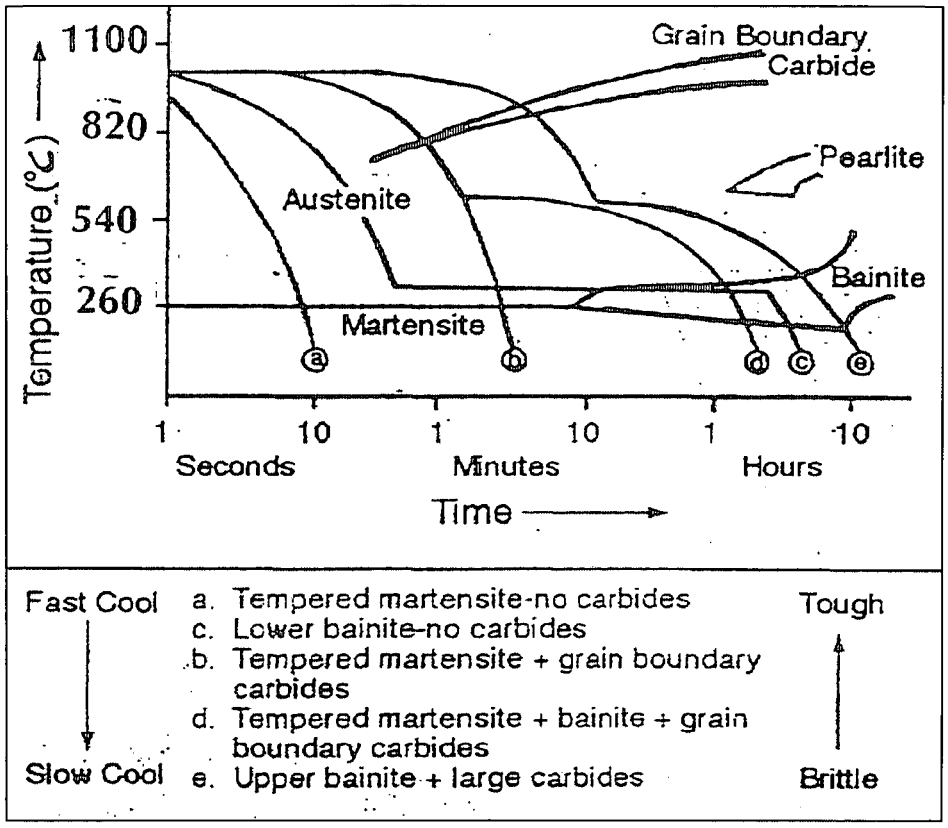

Figure 4.21 CCT diagram for H13 Tool Steel austenised at 1020°C *(reproduced courtesy of Jacques, P. and Doyle, E.D., 1997)*

Although the behaviour of H13 during DMLR processing appears complex, it is relatively simple compared to the behaviour of the mixed powders of H13 and copper. When H13 is processed alone, only one liquid is formed, while the mixture of H13 and copper forms a melt pool that contains two liquids that are only partially soluble and whose solubility will vary with temperature. The powder bed initially consists of a mixture of the two powders (H13 and copper) and while the powders are solid, little interaction will occur as the rapid heating by the fast moving laser beam will leave little time for solid state diffusion. Which powder melts first will not be purely determined by their relative melting points as the rate of heating of the powder particles will also be affected by the relative particle sizes and the efficiency with which the different powders absorb the laser energy. Also, although copper melts at a single temperature (1083°C), H13 melts over a range of temperatures (1370 to 1450°C). If the initial formation of the melt pool at the start of a scan line is ignored, the system can be simplified and considered as a melt pool that moves across the surface

following the laser beam, into which powder is drawn at one end and solid is frozen out at the other. The composition of the melt pool is considered to remain fairly constant with time; if it did not the phases formed would vary from place to place. When processing copper and H13, the melt pool will contain two immiscible liquids (see Section 2.4.4 in the literature review) and this appears in the final microstructure as the copper- and iron-rich regions (Figures 4.14 and 4.15).

Thermodynamically, the two liquids should adjust their compositions to bring them into equilibrium. However, given the short time the material is molten there will be insufficient time for equilibrium to be reached. The two powders will be incorporated into the melt pool, producing liquid spheres of one molten powder within a liquid matrix of the other, but initially, they will not have the equilibrium composition so diffusion will occur. If there is sufficient turbulence, then the small spheres will meet and conglomerate to form larger particles, while if there is little turbulence, the liquids will tend to separate vertically, as they will have different densities. At the trailing end of the melt pool the temperature falls and freezing will start. The equilibrium reaction between these two liquids is the monotectic ($L_1 \leftrightarrow L_2 + \gamma$; Raghavan, 2002). For the alloys being considered, L_1 will be the high carbon liquid rich in iron while L_2 will be a low carbon liquid rich in copper but still containing a significant concentration of iron. This reaction will continue as the temperature falls, with L_1 becoming richer in copper. This reaction will lead to the formation of austenite (with a significant copper content) probably by the continued growth of the grains in the underlying layer rather than by the nucleation of new grains if the powder mixture is H13-rich. This growth of the austenite from the substrate will form a copper-rich region at the top of the track. Subsequent remelting when the next layer is deposited will lead to this copper-rich region being incorporated into the new melt pool and will again freeze out at the top of the track. This will make producing discrete regions of copper within the tool steel difficult as it will tend to be 'swept up' the block as the part is grown.

On further cooling, the solubility of copper in austenite reduces (Larsson, 1975), leading to its rejection and the formation of a copper-rich phase at the austenite grain boundaries. It is the formation of these copper-rich regions that will most likely lead to embrittlement and the consequential tearing and cracking, as at higher temperatures they will be very weak compared to the surrounding H13. On further cooling, the diffusion rate of copper within

the iron-rich phase will slow and it is likely that fine precipitates will form within the austenite; these precipitates would likely be the ε-phase intermetallic suggested by Larsson, 1975. On cooling to room temperature, the austenite will transform into martensite, producing the microstructure observed in these experiments. This is confirmed by the XRD data (Figure 4.18) where copper and martensite were detected. It is not possible to say if there is any retained austenite, as any small peaks would be hidden by the copper peaks. These results differ from those of other research work who reported the formation of ferrite and an intermetallic phase Fe_4Cu_3 when direct laser sintering iron and copper powders (Zhu *et al*, 2003). The presence of carbon within H13 will lead to the formation of martensite rather than ferrite, but with Fe_4Cu_3, no crystal data could be found for this phase and it is not present on the iron-copper binary phase diagram.

The detrimental effect of this intermixing between copper and H13 is seen in Figure 4.16 (25%Cu, 75%H13, laser scanning speed 175mm.s^{-1}), where the component has cracked on cooling, an effect not seen when processing either H13 or copper alone. These cracks may be due to hot tearing, where at temperature the copper-rich regions are much weaker than the iron-rich regions and so cannot withstand the stresses that occur on cooling. Even if cracking was avoided during manufacture, the presence of copper on the steel grain boundaries would significantly increase the risk of cracking during use.

Comparison of the iron-rich regions produced within the copper/H13 mix (Figure 4.17) with the microstructure of the sample produced with H13 (Figure 4.7) alone revealed significant differences in microstructure. The samples produced using H13 powder alone showed only martensite, the low carbon content avoiding the formation of large carbide networks (unlike M2, a high carbon tool steel; Niu and Chang, 2000). The microstructure of the Cu/H13 materials was modified by the copper on the prior austenite boundaries within the iron-rich regions. Thus the iron-rich regions appear mainly martensite, but with copper in solid solution and/or as fine precipitates within them. Although copper is likely to stabilise austenite, austenite could not be detected.

As stated at the start of this thesis, the ability to build tool steel moulds that include copper cooling channels would increase the usefulness of the DMLR process. This appears, however, to be a more complex problem than was first envisaged as the interactions within

the melt pool were not considered. With conventional sintering, the inclusion of copper or the use of bronze to fill porosity is not a problem as mixing is not significant during sintering or during post-sintering infiltration. This is not true with DMLR where the components strongly interact in the melt pool. These experiments show that increasing the laser scanning speed reduces the material interactions but it cannot stop them, and increasing the laser scanning speed much further would not be an option as the low energy densities would be unable to completely melt the powders. Limited success was also achieved by controlling the relative powder sizes; copper still being observed in the iron-rich regions but to a lesser extent. Again, there are limits to this strategy as it becomes difficult to spread the powders as the particles sizes become very different. An initial literature survey on the use of an intermediate material was conducted, but the concept was not investigated experimentally due to the project ending. It is likely that a suitable material would melt before copper and have a high solubility in it, but be insoluble in steel. To be useful, the intermediate material would have to possess a high thermal conductivity, otherwise the cooling of the mould would be impeded. The actual strength of the layer would be less important. One possible material is silver, which is soluble in copper, has superior thermal conductivity to copper (429W/m.K compared to 401W/m.K for copper at room temperature), a similar melting point (962°C compared to 1083°C for copper) and is nearly completely immiscible in iron.

4.5 Summary

Before DMLR can be used to produce tool steel components with copper sections, a number of metallurgical challenges will have to be overcome. The incorporation of copper into the tool steel during processing leads to the formation of a copper-rich region around the austenite grain boundaries. This increases the risk of hot tearing and significantly weakens the material. If these materials were actually used in the production of an FGS such as a mould tool, as discussed at the beginning of this chapter, the integrity of the final part would be compromised. This problem can be reduced by the careful control of the processing conditions, so as to limit the time the materials are molten; it cannot however be avoided completely. A second problem with this system is due to the first phase to freeze out being austenite. This will lead to the top of the processed layer being copper-rich and this region tending to be incorporated into the next layer, sweeping the copper up the block in a way similar to zone refining. Seemingly, the only possible solution to this problem would be to use an intermediate material that would keep the copper and H13 apart. This must therefore be considered a major limitation of this process as the mixing of materials can lead to unwanted effects.

5.0 Investigation into the Production of Structures with a Controlled Variation in Porosity

The development of techniques for producing materials with controlled porosity is mainly driven by the orthopaedic implant industry, where there is a need for materials into which bone can grow. Conventional orthopaedic implants are bonded to the bone using bone cement (Oliveira *et al*, 2002), but this fixation method is a major cause of implant loosening and failure (Laberge *et al*, 1999). Therefore, recent research (Oliveira *et al*, 2002 and Akin *et al*, 2001) has investigated the use of porous coatings on implants to allow bone ingrowth to give a direct mechanical attachment. To this end, a number of techniques, including sintered metal, polymeric (Pompe *et al*, 2003) and ceramic coatings (Akin *et al*) have been investigated (refer to Section 2.5.2 of this thesis).

A further development of this work has been into materials where the pore shape and size is controlled so as to produce a gradual change from solid to highly porous material. This interest comes from an observation that human bone varies from a dense, stiff external structure (the cortical bone) to a porous internal structure (the cancellous bone), and to the improvement in fatigue resistance if there is a gradual change from porous to solid rather than a sharp interface (Pompe *et al*, 2003).

The aim of the research discussed in this chapter was to show that DMLR has the potential to produce porous coatings with a three-dimensional array of interconnected pores, where the coating becomes less porous towards the substrate/coating interface. It has already been shown that for some materials DMLR is capable of producing fully dense structures (Morgan *et al*, 2001), but it is in the production of controlled porosity materials where DMLR is most likely to be useful, as these structures are difficult to produce by conventional manufacturing techniques. For the sponsor of the work (Stryker Howmedica Osteonics), it was important that this initial work demonstrated the level of control over the pore size that could be achieved, before greater investment was made in this technology. A sign of the success of this project has been the subsequent investment by Stryker Howmedica Osteonics at The University of Liverpool with the purchase of a MCP "Realizer".

The first phase of the project involved a full parametric investigation of the processing variables for a range of bio-implant materials so as to characterise the material transformations and to identify the optimum processing parameters for producing porous materials. The second phase investigated the production of porous coatings on substrates where the coating has a porosity gradient (varying density). The final part of the research was to tensile test the coated substrates so as to demonstrate the strength of the coatings and the coating/substrate interface, to show that the coatings produced were reliable and reproducible.

5.1 Experimental Procedure

As a number of studies (see Section 2.5.2 of this thesis) have identified different optimum pore structures for bone in-growth, the pores produced in this work were designed to meet the size range used by Stryker Howmedica Osteonics (Table 5.1).

Optimum porosity:	20 - 40%,
Pore shape:	Irregular and inter-connective
Minimum pore size:	200 - 300 μm
Maximum pore size:	600 - 800 μm
Structured thickness:	140 - 160μm

Table 5.1 Stryker specifications for porosity of structured components

5.1.1 Initial Process Characterisation

Initial experiments were carried out using a range of powders of metals commonly used for bio-implants. These included titanium, cobalt-chrome, niobium and tantalum. Stryker Howmedica Osteonics requested that for this initial process characterisation, each of these materials was to be built on both titanium alloy and cobalt-chrome alloy substrates. From a marketing point of view, they were only interested in either titanium or cobalt-chrome

coatings but wished to find out whether coherent structured coatings with a controlled morphology could be produced using all four materials.

The cobalt-chrome alloy powder was spherical, gas atomised Co212-e obtained from Osprey Metals (particle size distribution 90%<22μm, composition Table 5.2). The niobium and tantalum both had a purity of 99.85% and a particle size distribution of 80%<75μm. As biomedical grade titanium powders were not available, commercially pure (CP) titanium (nominal composition Table 5.3) was used. The particle size distribution of the spherical titanium powder was 80%<45μm with a purity of 99.5%. Also used was titanium sponge powder which had a very different particle morphology (Figure 5.1) and had a particle size of <45μm.

Element	**Cr**	**Mo**	**Si**	**Fe**	**Mn**	**Ni**	**N**	**C**	**Co**
wt %	27.1	5.9	0.84	0.55	0.21	0.20	0.16	0.050	Balance

Table 5.2 Composition of Co212-e cobalt-chrome alloy

Element	**Ti**	**O**	**H**	**N**	**C**	**Si**	**Fe**	**Cl**
wt %	99.47 min	0.20 max	0.01 max	0.04 max	0.04 max	0.04 max	0.10 max	0.08 max

Table 5.3 Composition of CP titanium powder

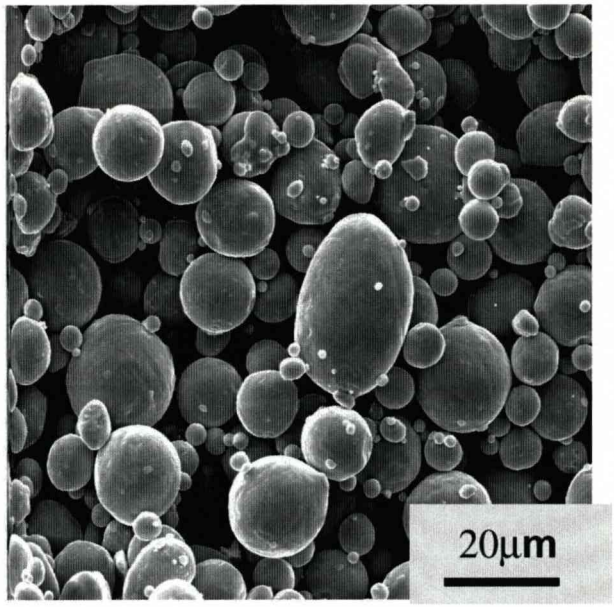

a

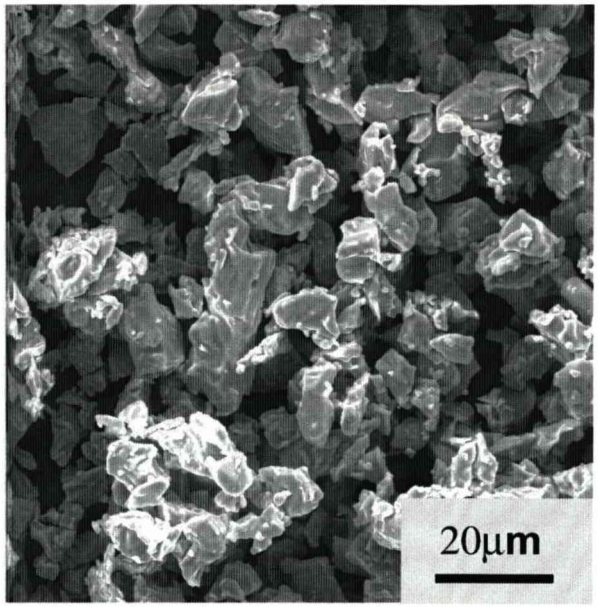

b

Figure 5.1 SEM micrographs showing: a) spherical 'solid' titanium powder; b) irregular 'sponge' titanium powder

The materials used in this work are highly reactive and therefore the protective gas used during laser-processing was changed from nitrogen to argon so as to prevent the formation of nitrides. To avoid increasing the oxygen content of the material, Arcella *et al*, 1998 recommended that a gas oxygen content of less than 150ppm be used, as a greater oxygen concentration would change the mechanical properties of the solid titanium, and the formation of oxides would alter the wettability and fluidity of the melt with all the metals.

To begin this work, a relatively large quantity (5kg) of cobalt-chrome powder was obtained from Osprey Powders and as no work had been undertaken with this material previously, a large range of parameter sets were considered. Therefore to reduce the cost, the cobalt-chrome coupons were built on stainless steel substrates with each build being part of an array of nine samples (Figure 5.2). A maximum laser power of 82W CW was used, with the laser scanning speed being varied between 100 and 260mm.s^{-1}. A linear X-direction laser scan was used, simplifying the experimental procedure and allowing the processing parameter 'beam overlap' ('line-spacing') to be used to control the space between scan lines, for example, with a 100μm laser spot size, an overlap of –200% produced a 300μm gap between the scan lines. This allowed the pore size to be increased or decreased in an

easily controllable manner, but meant that the scan speed alone had to be used to control the specific energy density. For most of the experiments, the laser power was held constant at 82W CW (pulsing was avoided at this stage to aid in the production of unbroken scan tracks and to make the thermal history of the build simpler to predict; i.e. delivering a constant stream of laser energy to the powder bed rather than instantaneous pulses) and the layer thickness at 100μm, while the other parameters were modified. Once the most suitable parameter ranges had been identified, the experiments were repeated using the more expensive ∅59mm titanium alloy substrates (Ti, 12%Mo, 6%Zr, 2%Fe; ASTM Standard F1813-97) and ∅72mm cobalt-chrome alloy substrates (Co, 28%Cr, 6%Mo; ASTM F75-98). The complete set of process parameters examined for this initial work is given in Table 5.4.

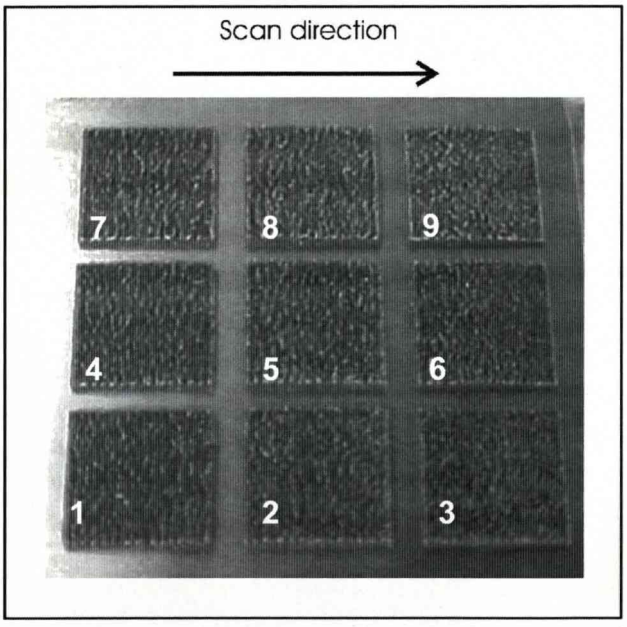

Figure 5.2 3 x 3 Array of 1.6mm thick cobalt-chrome coupons on stainless steel substrate produced with a laser power of 82W, beam overlap of 25% and laser scanning speeds of: 1) 100mm.s^{-1}, 2) 120mm.s^{-1}, 3) 140mm.s^{-1}, 4) 160mm.s^{-1}, 5) 180mm.s^{-1}, 6) 200mm.s^{-1}, 7) 220mm.s^{-1}, 8) 240mm.s^{-1}and 9) 260mm.s^{-1}

Metal Powder	Beam Overlap (%):	-500									-250									-60									
	Laser Scanning Speed (mms^{-1}):	100	120	140	160	180	200	220	240	260	100	120	140	160	180	200	220	240	260	75	85	95	105	115	125	135	145	155	
	Substrate																												
CoCr	Ti Alloy																			√	√	√	√	√	√	√	√	√	
	CoCr																			√	√	√	√	√	√	√	√	√	
	Stainless Steel	√	√	√	√	√	√	√	√	√	√	√	√	√	√	√	√	√	√	√	√	√	√	√	√	√	√	√	
Nb	Ti Alloy																												
	CoCr																												
	Stainless Steel																												
Ta	Ti Alloy																												
	CoCr																												
Ti	Ti Alloy																												
	CoCr																												

Metal Powder	Beam Overlap (%):	-40									-25									40									
	Laser Scanning Speed (mms^{-1}):	160	170	180	190	200	210	220	230	240	100	120	140	160	180	200	220	240	260	100	120	140	160	180	200	220	240	260	
	Substrate																												
CoCr	Ti Alloy										√	√	√	√	√	√	√	√	√										
	CoCr										√	√	√	√	√	√	√	√	√										
	Stainless Steel										√	√	√	√	√	√	√	√	√	√	√	√	√	√	√	√	√	√	√
Nb	Ti Alloy	√	√	√	√	√	√	√	√	√																			
	CoCr	√	√	√	√	√	√	√	√	√																			
	Stainless Steel	√	√	√	√	√	√	√	√	√										√	√	√	√	√	√	√	√	√	
Ta	Ti Alloy	√	√	√	√	√	√	√	√	√																			
	CoCr	√	√	√	√	√	√	√	√	√																			
Ti	Ti Alloy	√	√	√	√	√	√	√	√	√																			
	CoCr	√	√	√	√	√	√	√	√	√																			

Metal Powder	Beam Overlap (%):	50									50									75									
	Laser Scanning Speed (mms^{-1}):	100	120	140	160	180	200	220	240	260	280	300	320	340	360	380	400	420	440	280	300	320	340	360	380	400	420	440	
	Substrate																												
CoCr	Ti Alloy																												
	CoCr																												
	Stainless Steel	√	√	√	√	√	√	√	√	√	√	√	√	√	√	√	√	√	√	√	√	√	√	√	√	√	√	√	
Nb	Ti Alloy																												
	CoCr																												
	Stainless Steel	√	√	√	√	√	√	√	√	√																			
Ta	Ti Alloy																												
	CoCr																												
Ti	Ti Alloy																												
	CoCr																												

√ = Most Satisfactory Parameter Set

Table 5.4 Complete parameter set for initial process work on porous structures

The prime objective of the first part of this porosity work was to investigate whether the materials listed in Table 5.4 could be processed using DMLR and what control over the final part morphology was possible; the ability to meet the Stryker Howmedica Osteonics' specification shown in Table 5.1 was not critical at this stage. For this reason, the beam overlap used in the scanning patterns was much less than that used in later experiments and the scan pattern was only a simple 'raster-scan' (i.e. series of parallel lines) rather than the preferred hatched pattern (or 'waffle' due to its resemblance to the lattice shaped food product; Figure 3.4) used later.

After the initial experiments using cobalt-chrome powder, it was not necessary to examine such a large process range for the other powders. Further, due to their high costs and difficulty obtaining supplies, only much smaller quantities (around 0.5kg) of the other powders could be obtained. Whilst it was appreciated that there were significant differences in the melting temperatures (cobalt-chrome [1383°C], titanium [1668°C], niobium [2468°C], and tantalum [3017°C]] and thermal conductivity of the different

materials, the range of parameters used was considered large enough to explore the interactions of the different powders with the laser beam. A scanning speed ranging from 160 to 240mm.s^{-1} was used and the laser power was maintained at 82W CW; pulsing the beam was avoided at this stage to aid in the production of unbroken scan tracks and to make the thermal history of the build simpler to predict.

Following the completion of the multi-layer coupons, a series of 20mm x 20mm structures was built from titanium using an X and Y-direction 'hatched' scanning pattern (beam overlap –400% to –700%) to demonstrate that DMLR could produce parts with controlled porosity (channels 500μm to 800μm across). On successful completion of these builds, surface analysis was conducted using optical and scanning electron microscopy. Normally, the xylene impregnation technique (Arthur, 1954-55) is used to measure porosity but this technique requires large samples so it was not used here. Therefore, approximate part porosities were determined from the photographs using the process considered in Chapter 4.

5.1.1.1 Z-Growth Investigations

The earlier work on H13/copper showed that 'overbuilding' (which is referred to as 'Z-growth' due to the build growing proud of the surface of the powder bed in the Z-direction [using the Cartesian co-ordinate system]) produced problems with build quality and therefore the behaviour of these new coating materials was investigated, initially with titanium. It was important for the tensile tests that were to be carried out that the coating surfaces were flat (±50μm); the ASTM standard F1147-99 ("Test Method for Tension Testing of Calcium Phosphate Coatings and Metallic Coatings") requires the adhesive bonding of a platen to the top surface of the coating. Any unevenness in this surface leads to poor bonding and failure at the glue-line rather than in the coating. This tolerance can only be achieved with DMLR if Z-growth is controlled. A series of experiments was therefore conducted to determine the extent of this undesirable Z-growth and to investigate methods to control it so flat, uniform, samples could be produced.

5.1.1.2 Substrate Preparation and Optimised Cleaning Procedure

The effectiveness of different substrate cleaning methods was also investigated at this stage using Secondary Ion Mass Spectrometry (SIMS) analysis. It was found that both the ultrasonic and laser cleaning methods were not fully effective as they left contaminants on the surfaces, if organic solvents were used. The most effective cleaning method was to ultrasonically clean the substrates in a dilute detergent solution for 20 minutes followed by 20 minutes in distilled water, in the same bath. This method was used to clean all the substrates used just prior to depositing the coating.

5.1.2 Development of Titanium Coatings

After the initial process characterisation, only the porous titanium coatings were developed further with samples for tensile testing being produced on both titanium alloy bars (either ∅20mm or ∅25mm, cut to 25mm and 10mm lengths respectively with the bar ends being machined to be parallel and square with the sides) and cobalt-chrome. The cobalt-chrome substrates were cast items specifically designed for tensile testing with the surface on which the porous coating was built being ∅25.4mm (Figure 5.3). The coatings were produced using the parameters in Table 5.4. To achieve reasonable bonding between the coating and the substrate, the initial layer of the coating was produced with a -25% beam overlap and the subsequent eight layers were produced with a -1000% beam overlap (1100μm line-spacing).

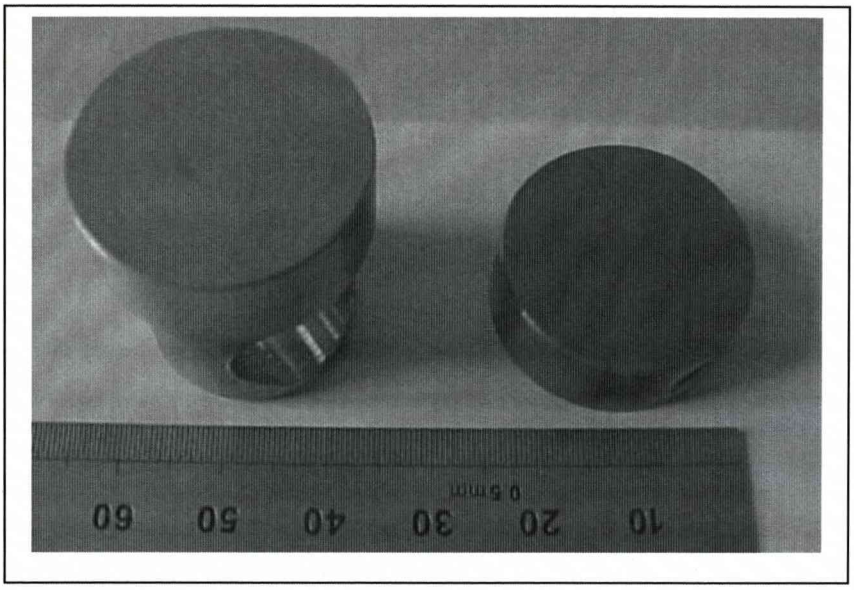

Figure 5.3 Uncoated cobalt-chrome (left) and titanium alloy (right) substrates

Samples were produced using both the spherical and sponge titanium to see if the cheaper sponge powder produced reasonable coatings. However, the coatings produced with the sponge powder were fragile and poorly bonded, as the powder did not spread evenly across the bed because of its irregular shape.

The samples for tensile testing were produced with nine porous layers (Table 5.5), on top of three layers created with a positive beam overlap (the higher energy density being required to bond the coating/substrate interface). The first layer of the coating was deposited and scanned twice before lowering the build chamber to spread the next layer of powder. The porous section of the coating was created as 3 sets of 3 layers of the trellis or 'waffle' pattern (a series of X and Y-direction scan lines with 1100μm line-spacing/-1000% Beam Overlap) being rotated by 45° between each set. The scan line-spacing was reduced for some samples to reduce the pore size and improve structural integrity.

Pattern	Beam Overlap (% of laser beam diameter)
Parallel X-Direction Scan Lines	50
Parallel X-Direction Scan Lines	25
Parallel X-Direction Scan Lines	0
Hatched Parallel X and Y-Direction Scan Lines (Referred to as a 'Waffle')	-1000
Waffle Pattern Rotated 45°	-1000
Hatched Parallel X and Y-Direction Scan Lines	-1000

Each Repeated 3 Times in Sequence

Table 5.5 Initial scan strategy for production of structured coatings

5.1.3 Titanium Coated Cobalt-Chrome Alloy Substrates

Initial work conducted with titanium coated cobalt-chrome samples showed failure of the samples occurring during handling (e.g. during removal of the builds from the chamber; see Section 5.2.3). These failures indicated that the coating/substrate interface was significantly weaker than that of titanium on titanium and that a different strategy was required to produce this coating/substrate combination. The use of an intermediate layer was therefore investigated using three 50μm layers of either tantalum or niobium. The parameters used for these layers were:

$P = 82W$

$Qs = 30kHz$

$v = 60mm.s^{-1}$

$E_d = 27.333J.mm^{-2}$ (calculated using. Eqn (8))

5.1.4 Mechanical Testing of Porous Titanium Coatings

Tensile tests were performed to measure the strength of the coating and the coating/substrate interface and to determine the mechanism of failure. The minimum tensile strength aimed for was 24.1MPa (the minimum value set by Stryker for other porous coatings). The tests were carried out using the jig shown (Figure 5.4), which allowed the samples to self-align with the load axis so as to avoid non-axial stresses that may have led to the coating peeling. To test the samples, the outer surface was attached to an uncoated substrate that had been grit blasted to roughen the adhered surface, using two pieces of adhesive sheet. The glue joint was clamped together at temperature while the glue cured.

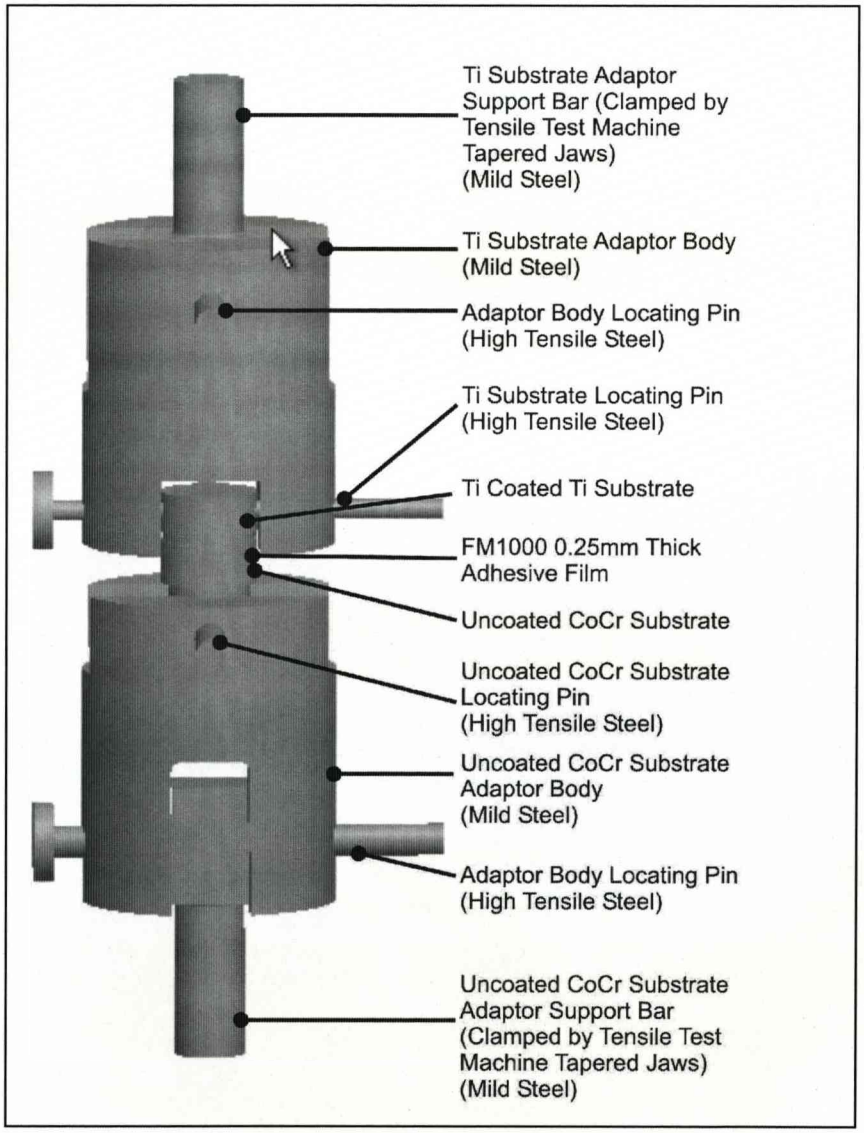

Figure 5.4 Tensile test assembly

The tensile tests were performed initially on titanium coated titanium samples to adjudge whether they could meet the Stryker requirements. Following this, tests were also conducted on titanium coated cobalt-chrome samples without the application of an intermediate coating and then with the application of an intermediate layer. To complete this series of experiments, tensile tests were also conducted on the intermediate coating materials when applied directly to the cobalt-chrome substrates, i.e. with no final titanium coating.

5.1.4.1 Pore Size Optimisation

After resolving the repeatability, flatness and concentricity issues, it was found that some tensile tests showed that the coating failed to meet the required standard, requiring the investigation of a method to strengthen them. Two possible solutions to this problem were investigated, one of reducing the pore size and the other of reducing the layer thickness. The latter is to some extent limited by the powder size and layers thinner than 100μm have tended to be avoided, except with the work in Section 5.2.1.1 where three 50μm initial layers were used to improve the bond to the substrate. To investigate the effects of layer thickness, titanium on titanium samples with layers thicknesses of 100, 75 and 50μm were produced with different scan line-spacing. Nine experiments were conducted using three different values for both the layer thickness and scan line-spacing for the waffle layers.

5.1.4.2 Random Scan Generation

This work considered how the essentially ordered structures produced by DMLR could be made to look random or more disordered, so as to produce structures similar to conventionally sintered porous structures (Figure 5.5). This morphology was thought by Stryker Howmedica Osteonics, the commissioners of this work, to be preferred by the medical industry and is likely to lead to greater bone ingrowth (Hofmann *et al*, 1997). The creation of more "disordered" structures was achieved by using "randomly-generated" line scans or by manually defining the scan patterns. This produced structures that appeared less ordered than the simple X and Y-direction 'waffle' structures (see Figure 3.4) produced by the bi-directional scanning strategy (as shown in Figure 5.11) and created a wider range of pore sizes.

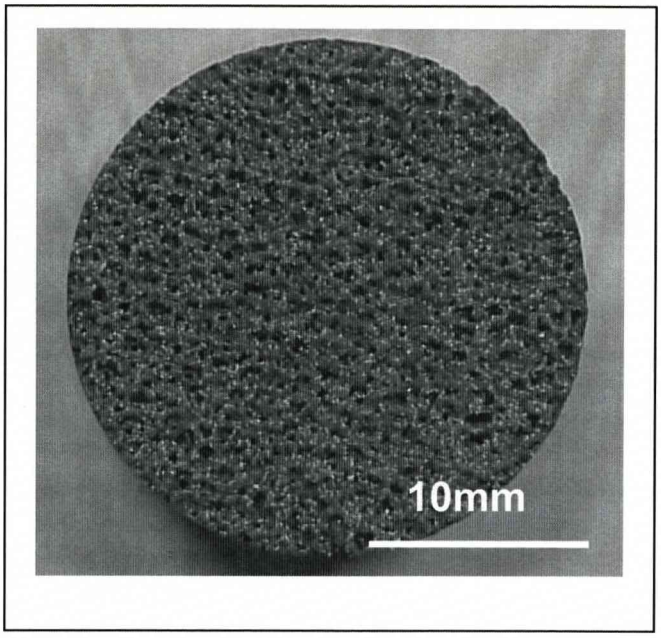

Figure 5.5 Porous titanium structure produced using sintering *(sample provided by Stryker Howmedica Osteonics for comparison purposes)*

It is not within the remit of this thesis to show whether ordered or disordered structures produced the greatest bone ingrowth, only to show that both structures could be created. Consequently, more intricate scanning arrangements were developed and used in the production of titanium coated titanium substrate samples (the cobalt-chrome substrates were not used in these experiments because of the more complex metallurgy associated with the titanium/cobalt-chrome interface). The laser parameters used for these experiments are shown in Table 5.6.

Layer	Laser Power	Line-spacing	Scanning Speed	Pulse Repetition Rate
Interface Scan:	82W	-50μm (50% beam overlap)	60mm.s^{-1}	10kHz
1st 3 Layers:	75W	1st Layer = 50μm (50% BO) 2nd Layer = 75μm (25% BO) 3rd Layer = 100μm (0% BO)	500mm.s^{-1}	30kHz
Coating Scan:	82W	700μm (-600% beam overlap)	160mm.s^{-1}	0kHz

Table 5.6 Laser parameters used for 'random scan' experiments

To achieve the random structures, a more flexible software package (that allowed the user more control over the laser scanning) was needed for the control of the laser, than the one used previously. The laser used on this system was originally designed to laser-mark components and so features a graphics-based program, requiring the individual scan-patterns to be either drawn in or to follow a regular arrangement. The only other control that was possible with this software was the distance between patterned lines and the direction in which they are scanned, so with "Unidirectional" the lines are all scanned in the same direction, while with "Bi-directional", the odd and even scans are in different directions (Figure 5.6).

The limited control available made the graphics-based software package unsuitable for the next stage of the work and therefore it was replaced by a command-line driven package, where the type of line (e.g. straight, circle, arc etc..), start point, length and direction were specified either directly or from a text file. With this system, scan patterns were generated in Microsoft "Excel", imported as a text file, which was then used to control the laser. Initial experiments investigated random scan patterns derived from trigonometrical relationships, with each scan line beginning at a random point on the perimeter of a ∅24mm circle and finishing at a second random point, again on the perimeter. Two patterns were produced, one with 32 lines and the other with 54, with each line beginning at the finish point of the previous line (Figures 5.7a and 5.7b). These showed that because of the truly random nature of the patterns there are areas with a high density of scan lines and others with none.

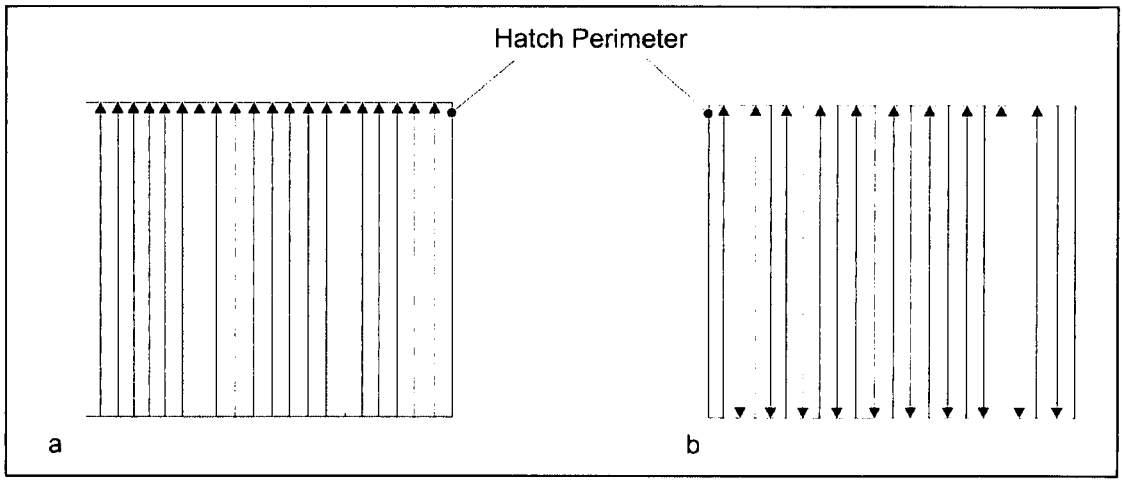

Figure 5.6 Diagram showing use of: a) Unidirectional and b) Bidirectional hatch lines used by graphics-based laser-marking software

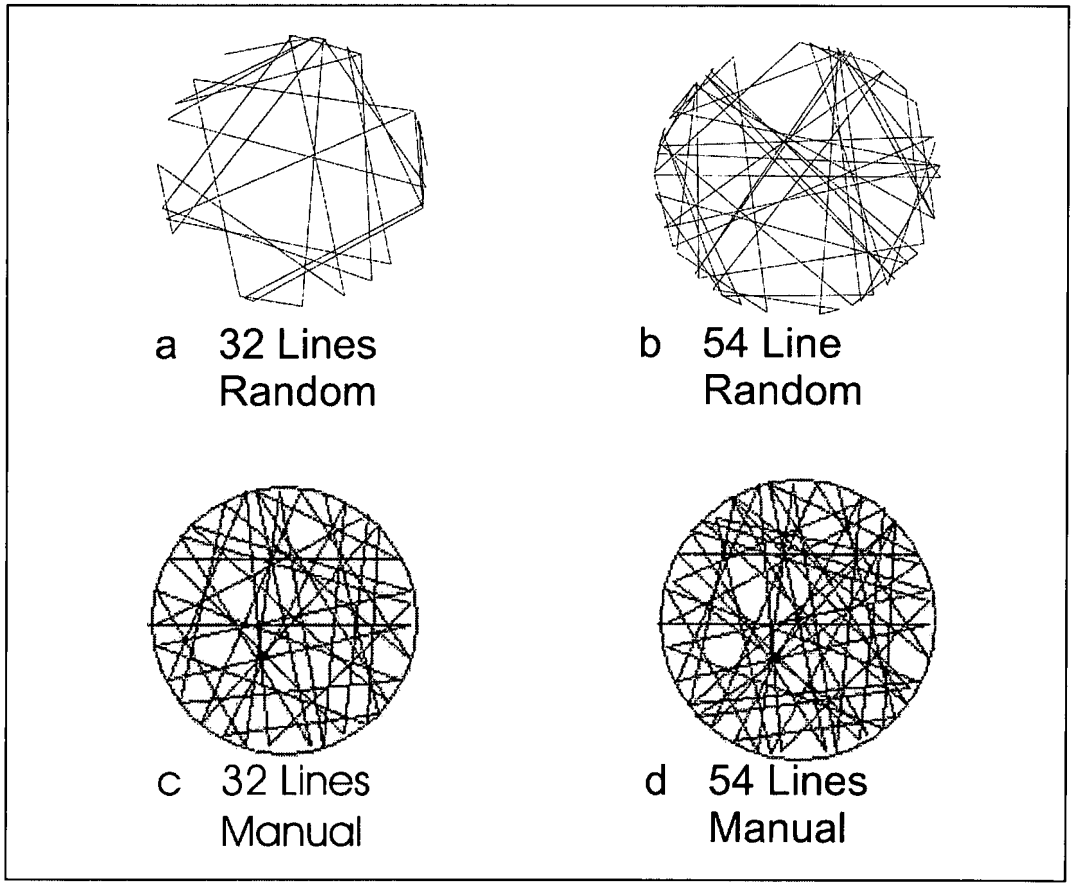

Figure 5.7 Graphical representations of initial "random" scans

Although these patterns were random (which was what was requested) they were not the type of structure that was needed (the project specification required a more evenly distributed pore network). Therefore the patterns were manually drawn to give a uniform distribution that looked fairly random (manually drawn referring to the operator defining the start and end-points of each line, using PC mouse movements, rather than the computer generating these points automatically from a line in a program; Figures 5.7c and 5.7d). These two patterns were used to create samples by replacing the final three hatched 'waffle' scans used in previous structures. A second attempt to computer-generate disordered patterns with an even distribution of lines was produced by creating randomly generated co-ordinates with endpoints at random points within a circle. The definition of the diameter of this circle allowed the user to have some control over the spacing of the lines, e.g. a small diameter would increase the density of lines near the centre of the pattern but a larger diameter would reduce this. Again, this scan pattern was used for the last three layers of the build (Figure 5.8a 50 lines, Figure 5.8b 100 lines).

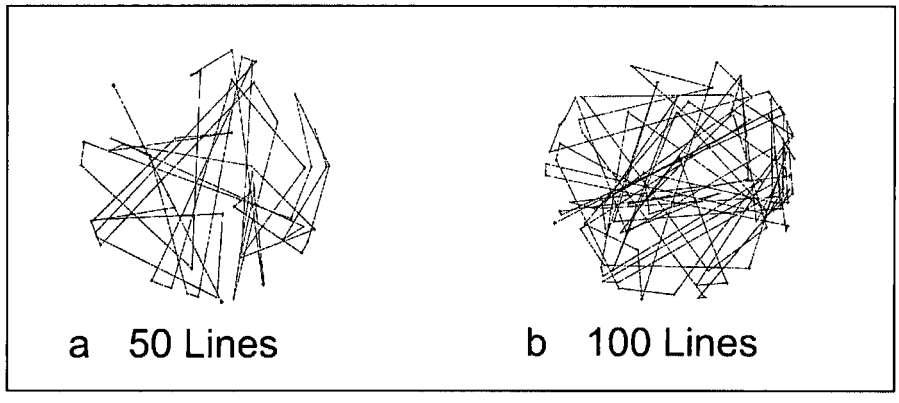

Figure 5.8 Graphical representations of revised random scan patterns

Although the distribution of lines was more uniform with this latest scanning arrangement, there was still a higher density of scan line intersections in the centre of the circle with fewer towards the perimeter (which would result in a reduced pore density towards the middle of the sample and subsequently compromise any bone/porous coating interface). The program was further revised by this time introducing numerical data based on the definition of a number of incrementally smaller, concentric, circles; the largest diameter being 24mm and smallest being 4mm. Lines were drawn from a point on one circle to a

point on another (e.g. to begin, a line was drawn from a random point on the ∅24mm circle to a random point on the ∅23mm circle, a second line was drawn from this point to a random point on a Ø22mm circle, continuing until a continuous polyline had been drawn between each circle to the smallest Ø4mm circle). This pattern could be further revised to alter the density of lines by changing the number of circles in the pattern and the diameter of each.

Modifying the sizes of the circles, within the limits of the outer and inner circles, was found to alter the distribution of scan lines across the area of the scan. Figure 5.9 shows three scans produced using this method to show how the number and diameter of these circles varied the spread of the scan line vertices. Each of these scans was then run for the last three layers of a build cycle instead of the previously used waffle arrangement described earlier.

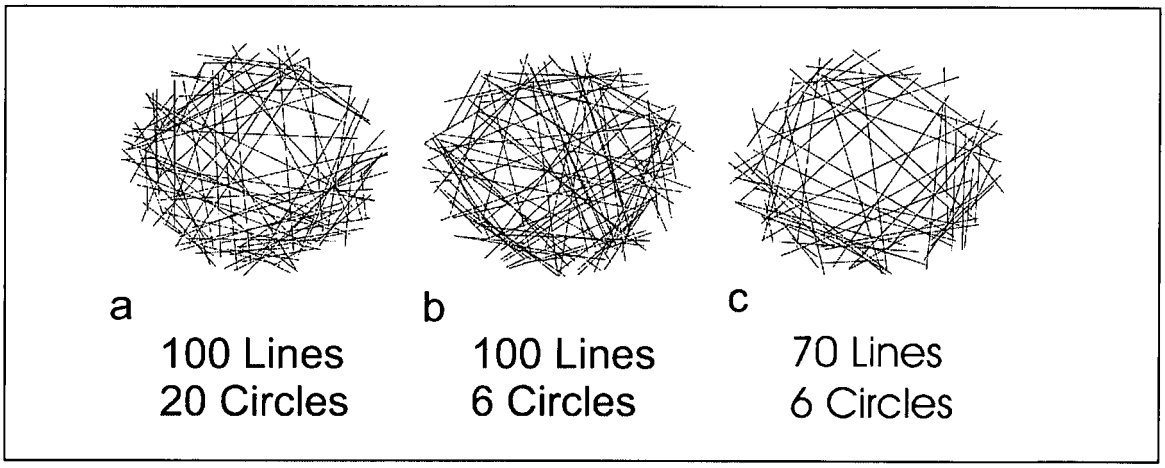

Figure 5.9 Further revised random scan patterns used to enable more even distribution of scan lines

5.2 Results

5.2.1 Initial Process Characterisation

The initial process characterisation was carried out on a range of bio-compatible materials, with process maps being developed so that the parameters that allowed successful coatings to be produced could be identified, e.g. it was found that a laser power of 82W CW, -40% beam overlap and scanning speeds varying from 160mm.s^{-1} to 240mm.s^{-1} provided the best results. It also identified the candidate materials which were easiest to process (coherent titanium structures could be produced using a wider range of parameters than structures made using the other materials). After the initial work on stainless steel substrates, coatings were produced on both cobalt-chrome alloy and titanium alloy substrates.

When cobalt-chrome coatings were produced on titanium substrates (laser power 82W CW, -25% beam overlap and scanning speeds varying from 100 to 260mm.s^{-1}; Figure 5.10), the parameters used produced layers of incomplete scan-tracks that created a network of interconnected pores throughout the coating. The coating/substrate interface consisted of a patchwork of fused points that bonded the coating to the substrate, producing a weak interface. Similar macrostructures were seen with niobium (Figure 5.11) and tantalum (Figure 5.12) on titanium substrates even though the laser parameters (laser power of 82W CW; –40% beam overlap; laser scanning speeds varying from 160 to 240mm.s^{-1}) were somewhat different as the melting points are higher.

Only when titanium was deposited on titanium (Figure 5.13) and cobalt-chrome substrates (Figure 5.14) was a significant difference seen. Here, the titanium on titanium morphology was similar to that seen before, but the titanium on cobalt-chrome was very different as in this case, the scan lines can be clearly see and the tracks have spread out on the substrate surface. This indicated very strong wetting, with the lines only beginning to break up at higher scanning speeds.

Note: Although all the material combinations shown in Table 5.4 were used in this initial series of experiments, images of the cobalt-chrome, niobium and tantalum on cobalt-

chrome substrates are not reproduced here as the morphology of these coupons appeared identical to the samples produced on titanium substrates. As such, in the interests of saving space, only one set of results is shown in its entirety, i.e. the titanium substrates samples.

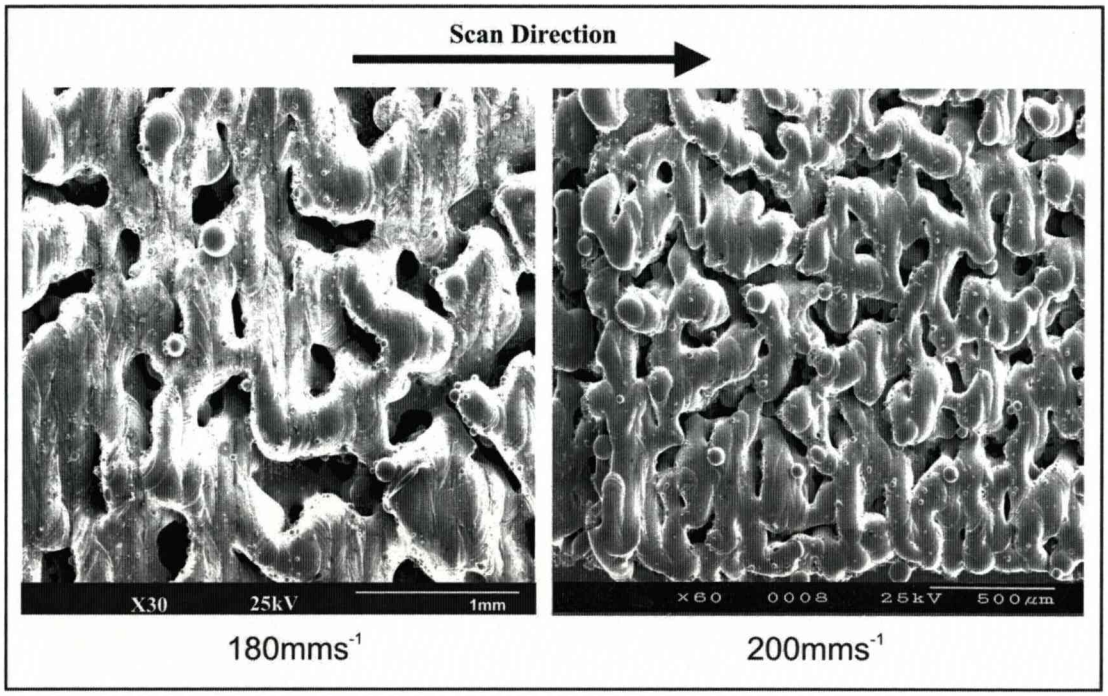

Figure 5.10 SEM micrographs of the surface structure of cobalt-chrome on titanium alloy substrate produced with a laser power of 82W CW, -25% beam overlap and laser scanning speeds of 180 and 200mm.s^{-1}

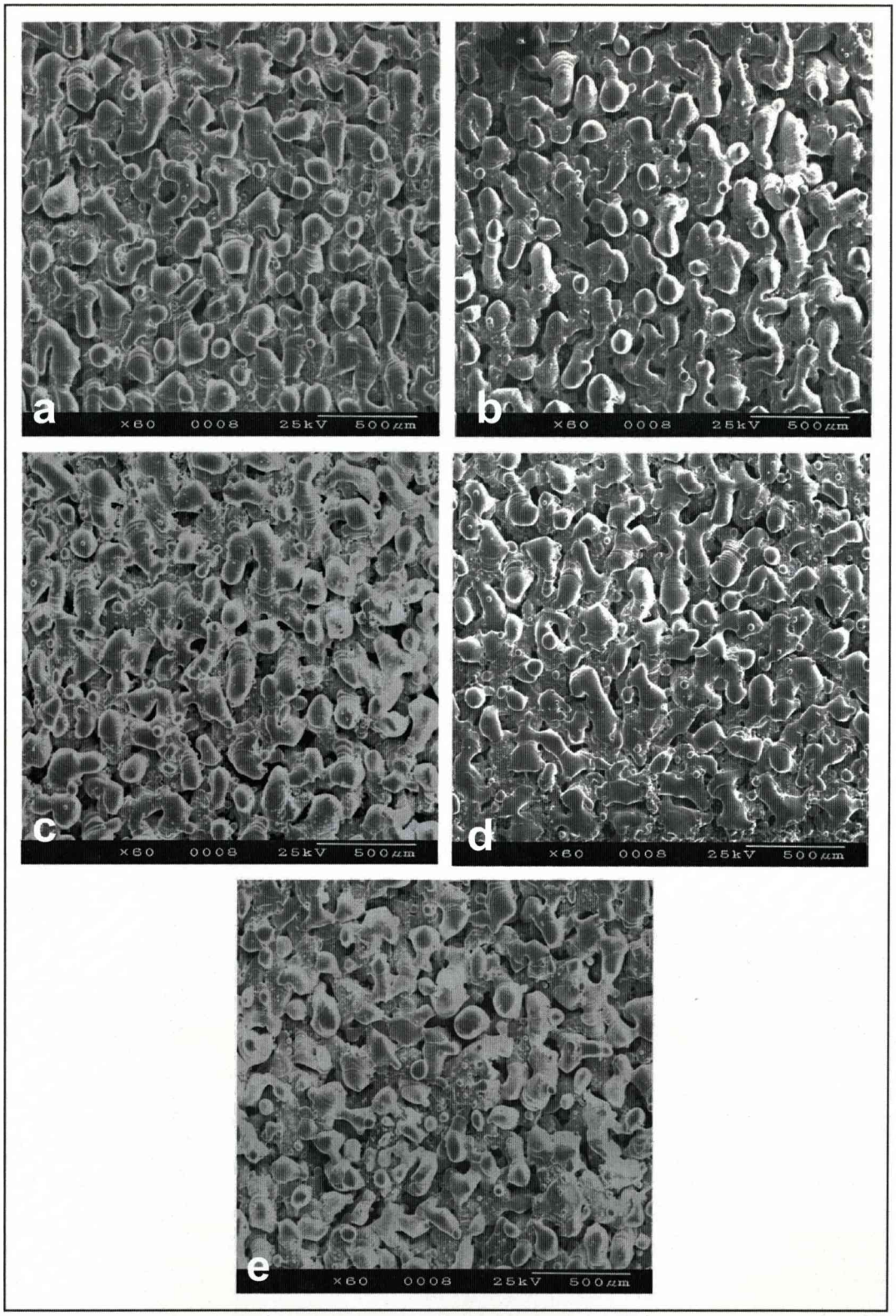

Figure 5.11 SEM micrographs of the surface structure of niobium on titanium alloy substrate produced with a laser power of 82W CW, -40% beam overlap at scanning speeds of: a) 160mm.s^{-1}, b) 190mm.s^{-1}, c) 200mm.s^{-1}, d) 210mm.s^{-1} and e) 240mm.s^{-1}

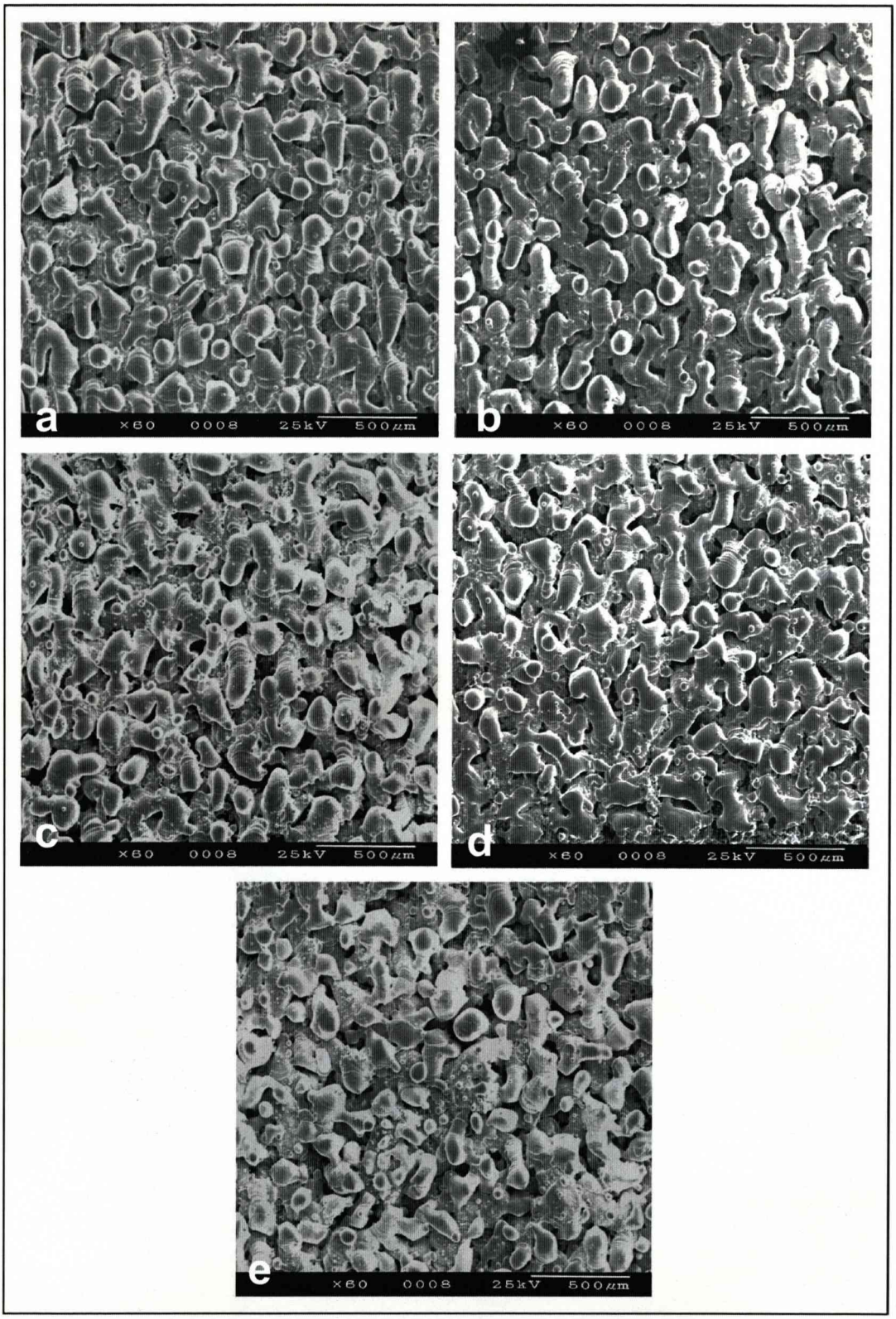

Figure 5.12 SEM micrographs of the surface structure of tantalum on titanium alloy substrate produced with a laser power of 82W CW, -40% beam overlap and laser scanning speeds of: a) and b) 160mm.s^{-1}, c) and d) 200mm.s^{-1} and e) 240mm.s^{-1}

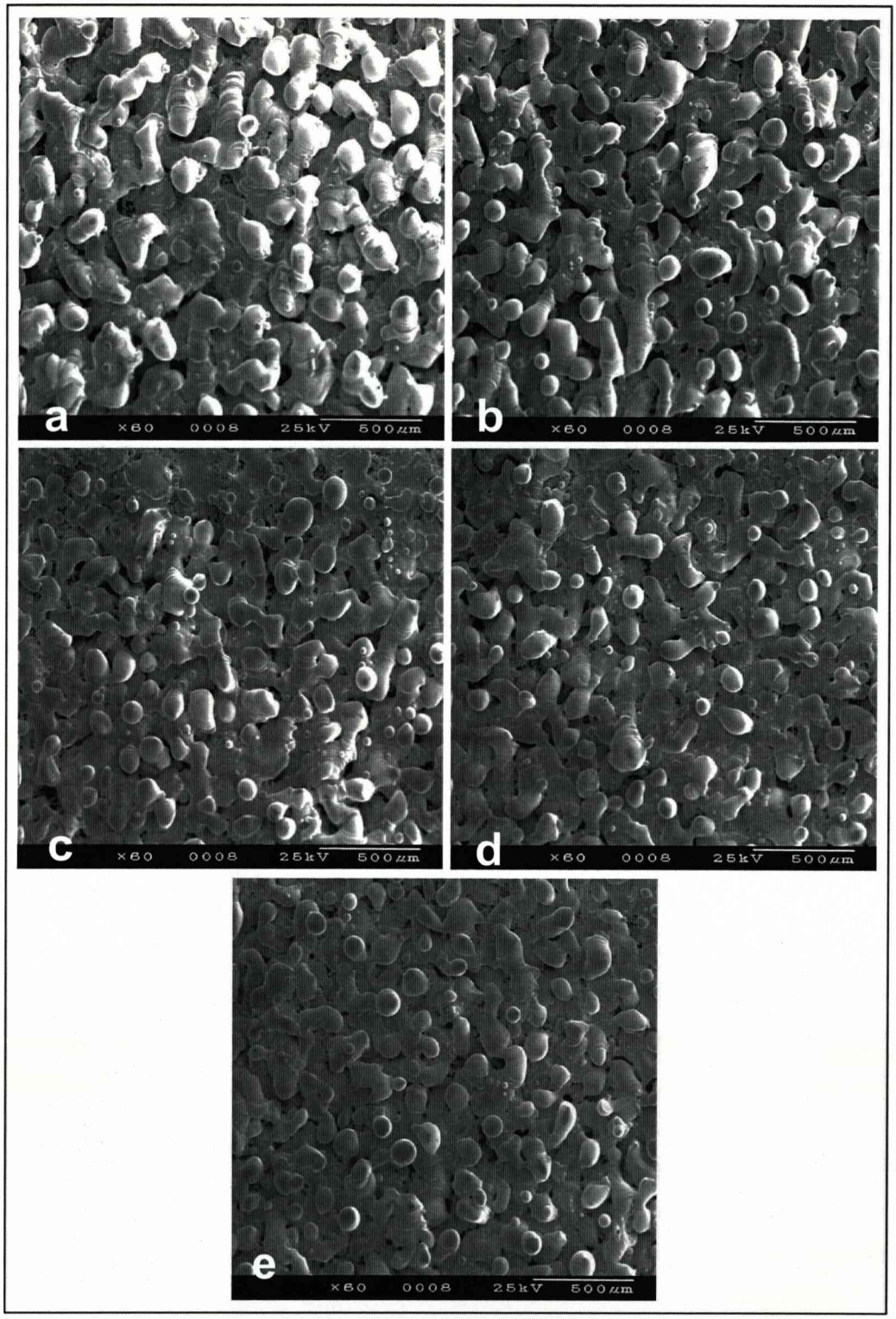

Figure 5.13 SEM micrographs of the surface structure of titanium on titanium alloy substrate produced with a laser power of 82W CW, -40% beam overlap and scanning speeds of: a) 160mm.s^{-1}, b) 170mm.s^{-1}, c) 200mm.s^{-1}, d) 230mm.s^{-1} and e) 240mm.s^{-1}

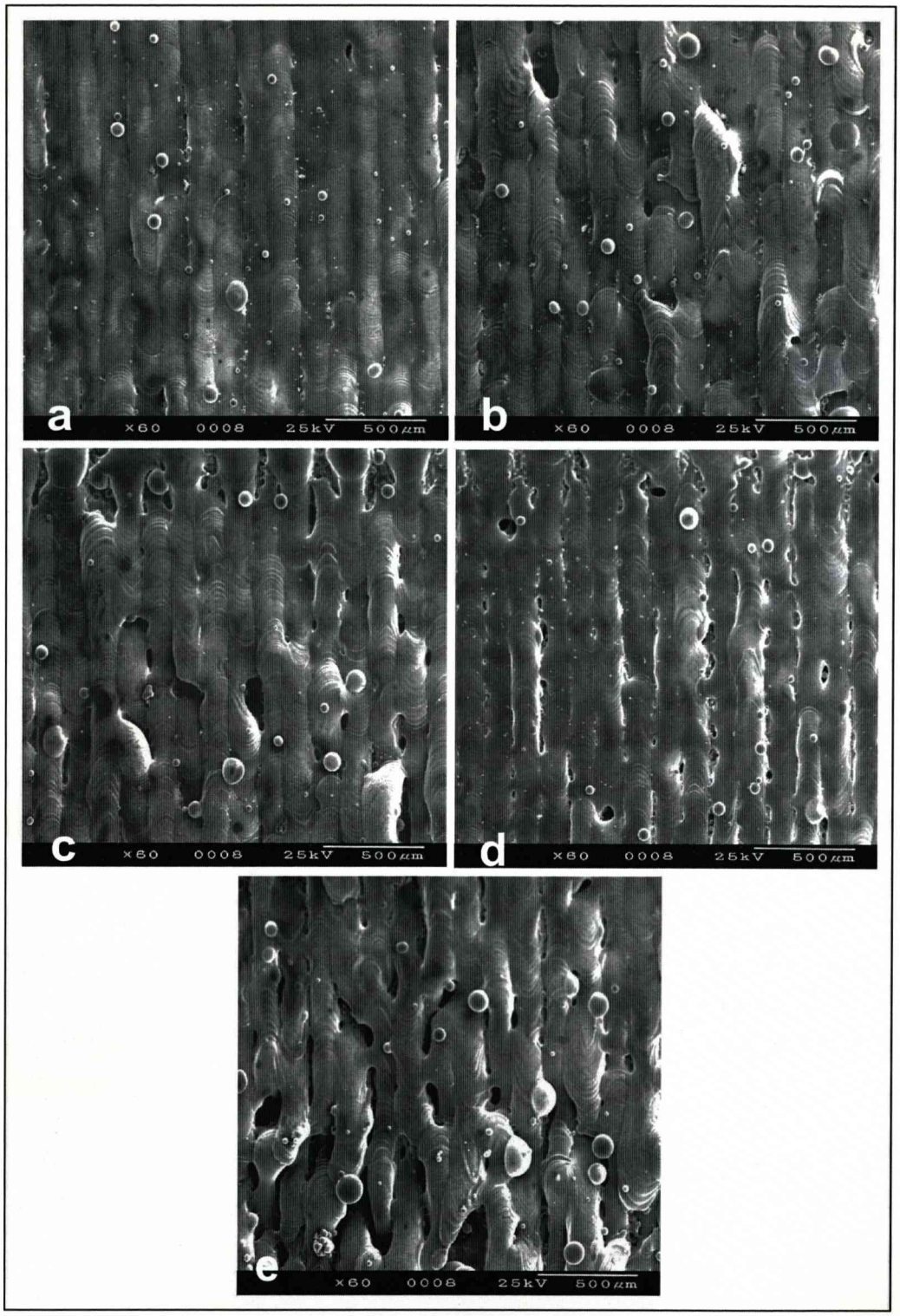

Figure 5.14 SEM micrographs of the surface structure of titanium on cobalt-chrome substrate produced with a laser power of 82W CW, -40% beam overlap and laser scanning speeds of: a) 160mm.s^{-1}, b) 170mm.s^{-1}, c) 200mm.s^{-1}, d) 230mm.s^{-1} and e) 240mm.s^{-1}

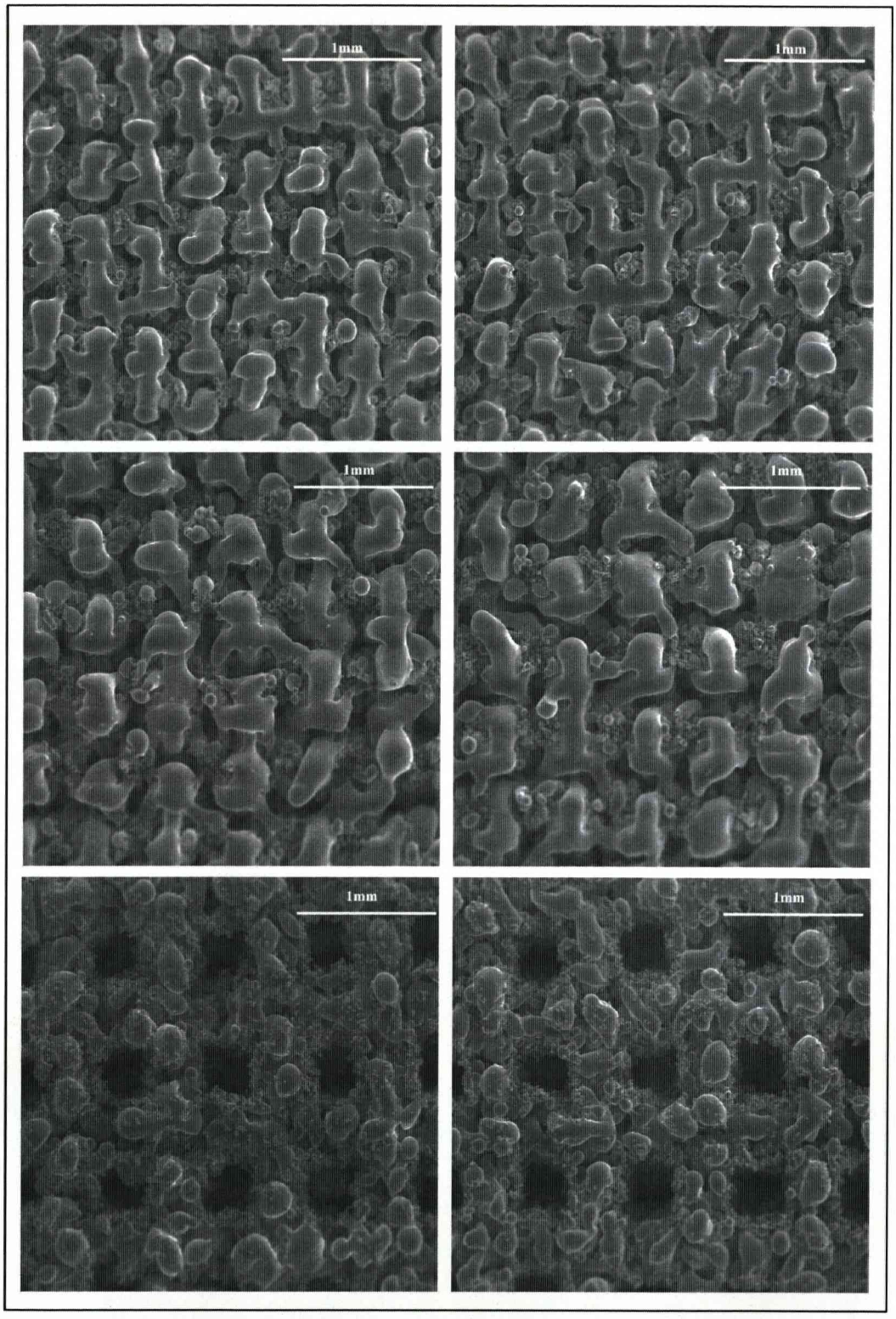

Figure 5.15 SEM micrographs showing titanium builds on titanium alloy substrates produced with a waffle scanning format, scanning speed of 160mm.s^{-1}, laser power of 72W CW and beam overlaps of: -400% (top row), -500% (middle row) and -600% (bottom row)

Although the coatings produced with a basic single direction scan showed porosity, it was controlled by the incomplete wetting of the melt pools in the different line scans. As a more controllable method of producing porosity was required, samples were produced with the hatched X and Y-direction scan pattern; this produced interconnected pores of a controllable morphology (Figure 5.15). These structures compare favourably with the porous coatings that are produced by sintering (Figure 5.16). Although the DMLR samples are more regular, they show similar interconnected pores

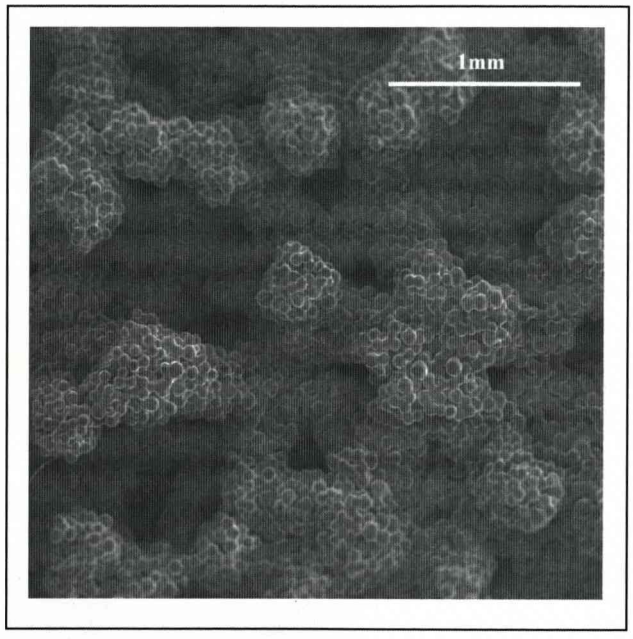

Figure 5.16 SEM surface micrograph of porous structure made from sintered titanium sponge *(from sample shown in Figure 5.5, provided by Stryker Howmedica Osteonics)*

Following the initial trials on flat, square, substrates, samples were then produced using the supplied titanium and cobalt-chrome substrates shown in Figure 5.3. A new problem was seen with these circular specimens, that of accurately positioning the specimens so as to centre the coating on the substrate. As the entire surface had to be coated, the coatings were built oversize (the coating scan area being larger than the substrate diameter), but this meant that post-process machining was required to remove the excess material. If this was not carried out with sufficient care then part of the porous coating detached (Figure 5.17), the loss predominantly occurring at the coating perimeter.

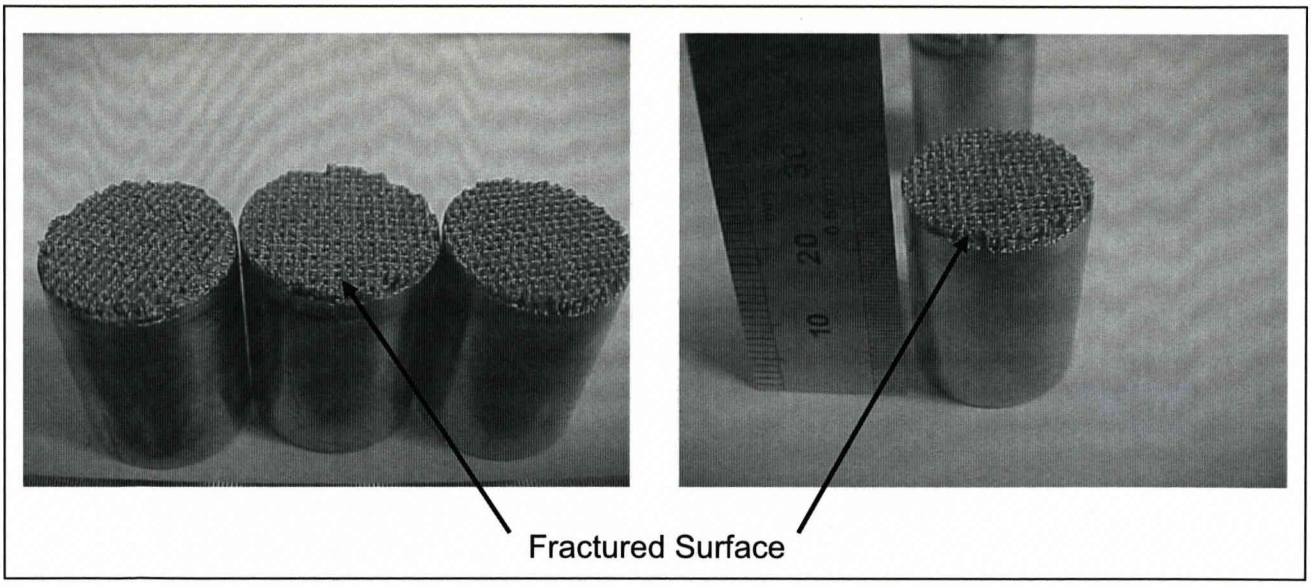

Figure 5.17 Failed samples produced using titanium sponge coating on Ø20mm titanium alloy substrates (samples produced using v = 120mm.s^{-1}, P = 82W, Qs = 30kHz and BO = 0% for the first three layers followed by v = 200mm.s^{-1}, P = 82W CW and BO = -1000% for the hatched layers)

The loss of coating during machining was found to be even worse with titanium on the cobalt-chrome alloy as they were poorly bonded. Some improvement was achieved by depositing three dense titanium layers at the interface before gradually increasing the scan line-spacing to produce the porous structure but the greatest improvement was achieved by increasing the specific energy density by reducing the scanning speed to 180mm.s^{-1}and using a 30kHz pulse frequency.

5.2.1.1 Z-Growth Investigations

From experiments conducted with titanium coated titanium samples, it was seen that several of the samples possessed curved upper surfaces, similar to what was seen with the earlier H13 experiments shown in Section 4.2.1. The degree of curvature also varied according to which parameter set was used. Figure 5.18 shows evidence of this Z-growth, with a distinct ridge which had been formed in the build chamber about the specimen in the centre of the powder bed. With H13 the laser parameters (scan speed in particular) had a significant effect on Z-growth and so the consequences of these parameters was investigated. However, to obtain a reasonable bond to the substrate, a high energy scan was needed for the first three layers, followed by three 'solid' scans and only during the building of the waffle structure above this were the parameters altered (Table 5.7).

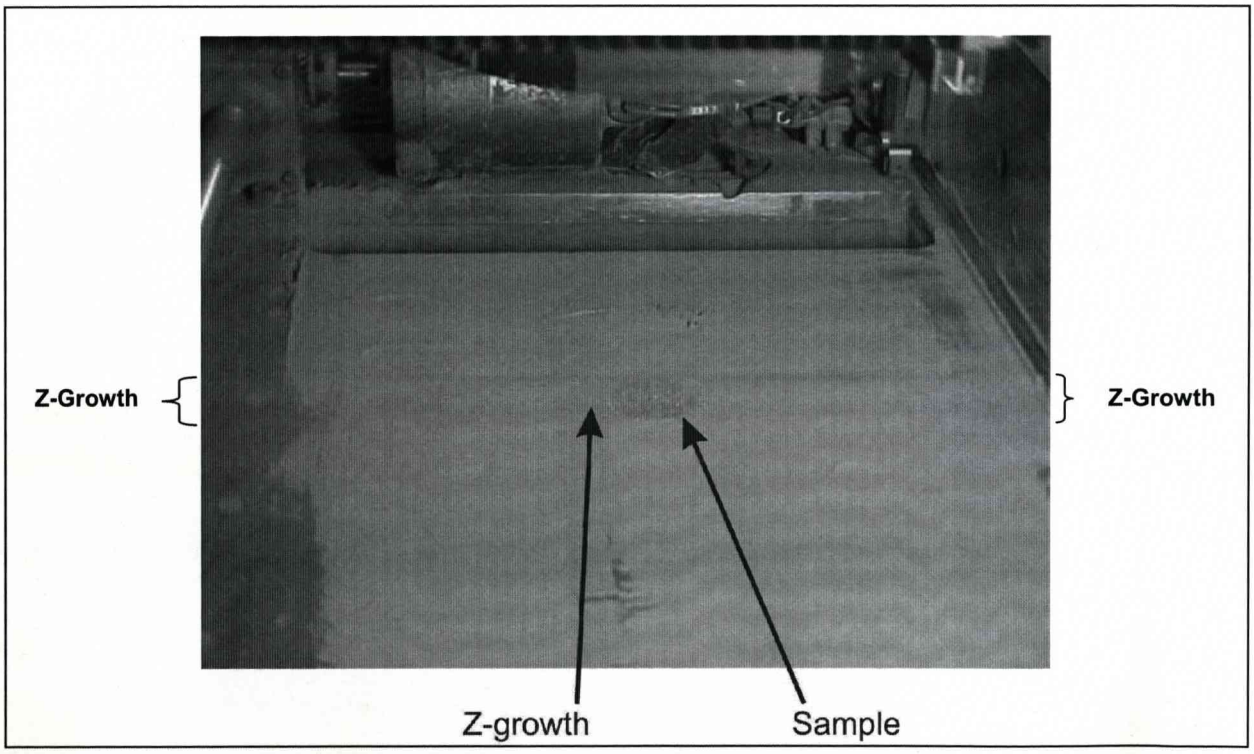

Figure 5.18 Photograph showing Z-growth (identified by a ridge in the surface of the spread powder layer) during a 15 layer build where the resultant coating measured 2mm thick

Experiment No.	Laser Scanning Speed ($mm.s^{-1}$)	Leading Edge (mm)	Middle (mm)	Trailing Edge (mm)	Substrate Thickness (mm)	% of Total Build Height (-)
1	180	10.40	10.60	10.40	10	19.048
2	200	10.20	10.35	10.20	10	14.286
3	220	10.10	10.22	10.08	10	12.381
4	240	10.05	10.05	10.10	10	9.048

Table 5.7 Variations in coating thickness, expressed as a proportion of total build height, relative to laser scanning speed; a laser power of 82W CW was used for each sample

The results from these experiments have been plotted on Figure 5.19 below.

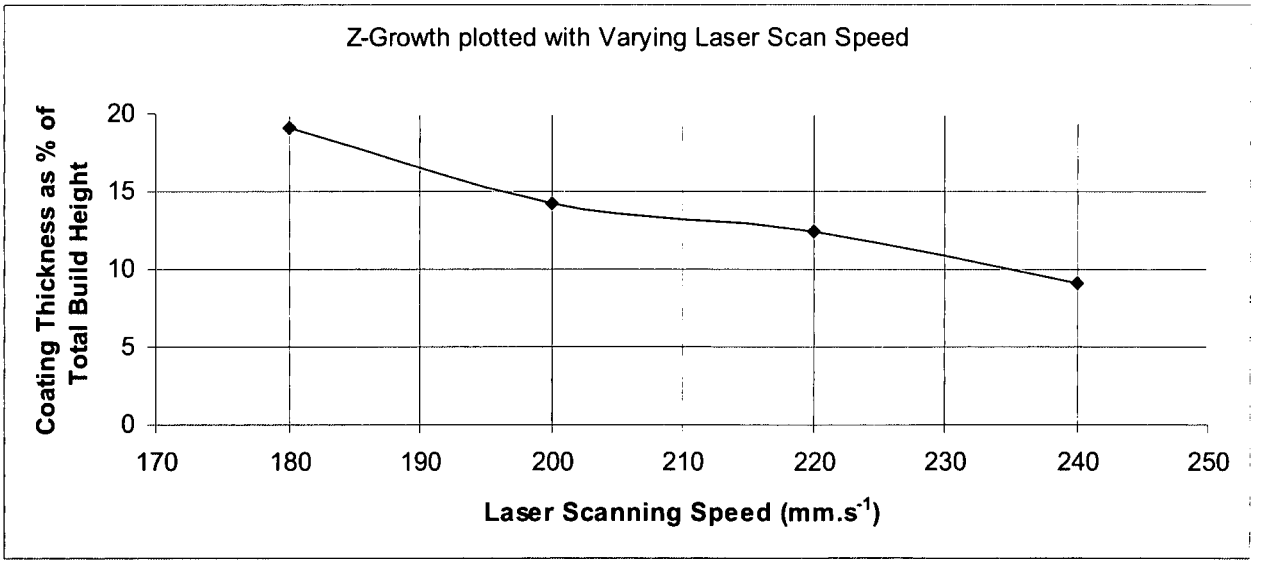

Figure 5.19 Plot of degree of excess vertical growth ("Z-growth"), for titanium powder on titanium substrates, relative to variation in scanning speed

The Z-growth that was observed during the production of these initial titanium coated titanium substrates indicated that the titanium behaved in a similar way to H13 in the experiments described in Section 4.1.1. That is, the molten metal "balls-up" and draws in material from surrounding regions. As with the H13 experiments, this overbuilding eventually restricted movement of the powder spreading roller, lifting it over the surface of the build, which hindered the distribution of a flat, uniform, layer of powder and resulted in the curvature seen in Figure 5.20. The problem was partially solved by reducing the specific energy density applied to the powder bed, e.g. the laser scanning speed was increased (Table 5.7), but if the speed was increased too much, insufficient energy was available to melt the powder. Only by experimentation and careful selection of processing parameters was it possible to find the right balance.

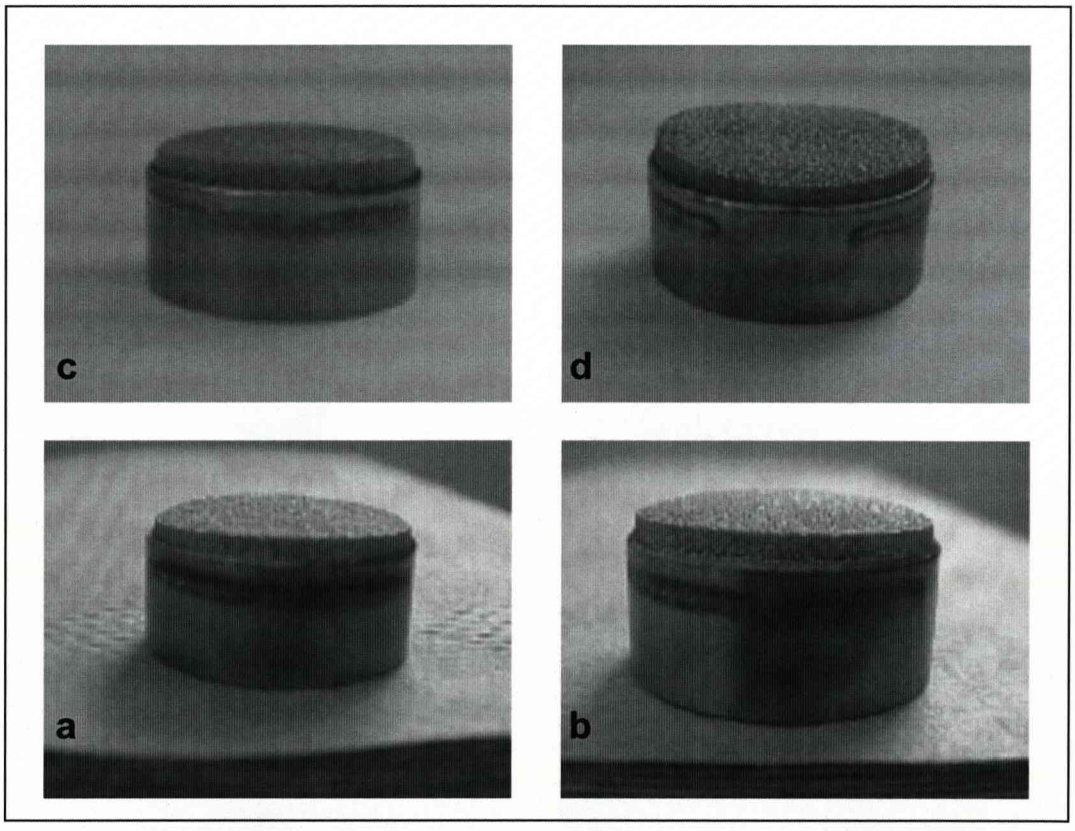

Figure 5.20 Photographs showing evidence of Z-growth and curvature on top surface showing samples (from Table 5.7): a) Experiment 1, b) Experiment 2, c) Experiment 3 and d) Experiment 4

5.2.2 Titanium Coated Titanium Substrates

Metallographic sections (Figure 5.21) of the titanium on titanium samples (etched with 100ml H_20, 5ml NH_4FHF and $2cm^3$ HCl for 30 seconds) showed the structure of both the coating and the substrate. The coating shows a fine needle structure because of the rapid cooling of the material which leads to the formation of a needle-like morphology as the ßTi transforms to αTi by a shear mechanism, rather than by the growth of grain boundary allotriomorphs. The material does not form a martensitic Ti structure as the alloy is commercially pure titanium. This contrasts with the large equiaxed grains of the substrate and shows clearly the limit of penetration of the melt pool. This difference in microstructure makes the coating substrate easy to identify and a degree of substrate melting can be identified.

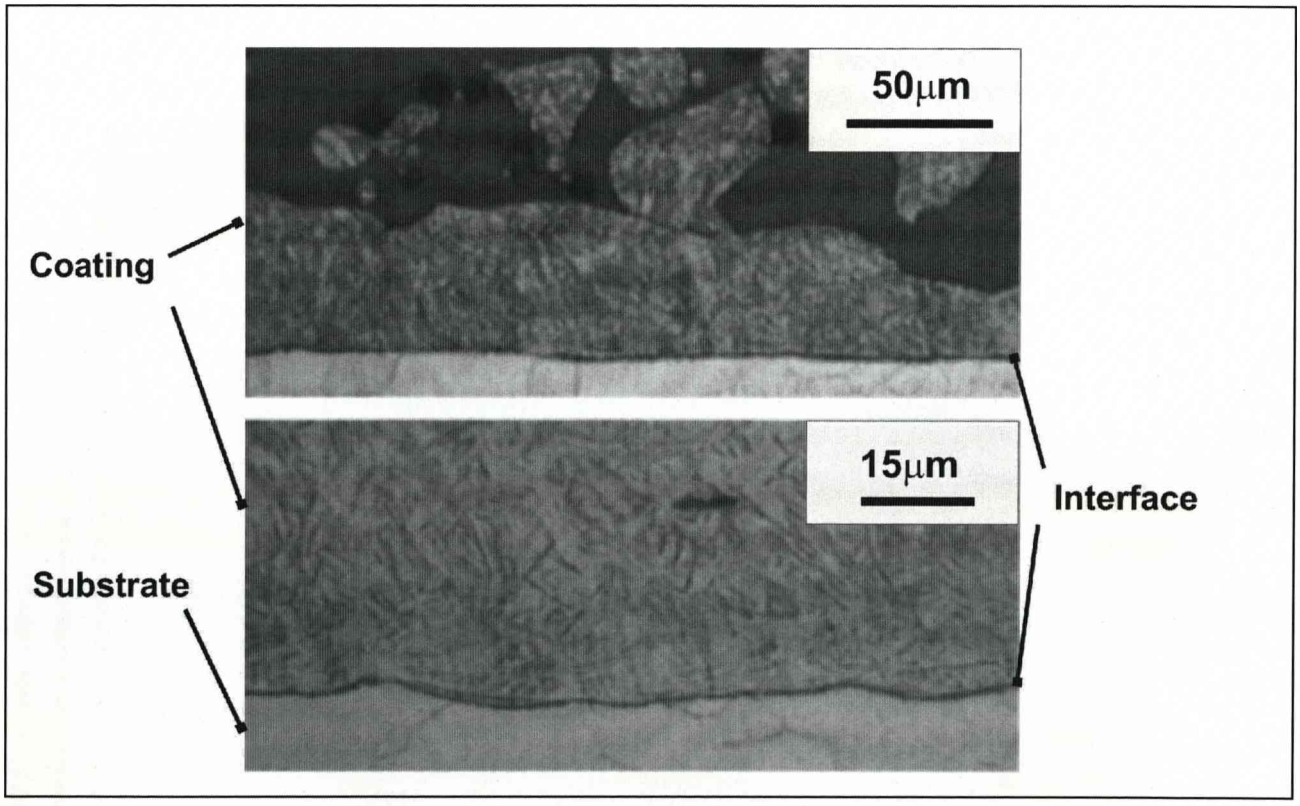

Figure 5.21 Optical micrographs showing the interface interaction of a titanium structure and titanium alloy substrate produced with a laser scanning speed of 180mm.s^{-1}, laser power of 82W CW and beam overlap of –40% (laser scanning direction from left to right)

5.2.3 Titanium Coated Cobalt-Chrome Substrates

The production of titanium coatings on the cobalt-chrome alloy was investigated further as it behaved very differently to the other combinations of coating and substrate. Only with titanium on cobalt-chrome was there a strong tendency for the coating material to wet the substrate, an effect that should produce a strong substrate/coating interface and yet this interface was very weak. When the coating was detached from the substrate and the surface examined (Figures 5.22 and 5.23) a highly fractured region was seen, which is the source of the weak interface. The same cracked region can be seen in section (Figure 5.24), the cracks spreading both along the interface and across the thin layer at the coating/substrate interface. By multiple etching, the microstructure of the different regions was revealed (Figure 5.25). As expected, the titanium coating away from the interface had an acicular αTi structure, a morphology observed in titanium on the other substrates, because of the rapid cooling from the high temperature β phase. The substrate away from the interface was unchanged by the coating production, but where the coating/substrate had successfully fused there was a thin layer with a very different morphology and it was within this layer that the cracks were observed. The restriction of the cracks to this layer may imply that it is much more brittle than the surrounding material.

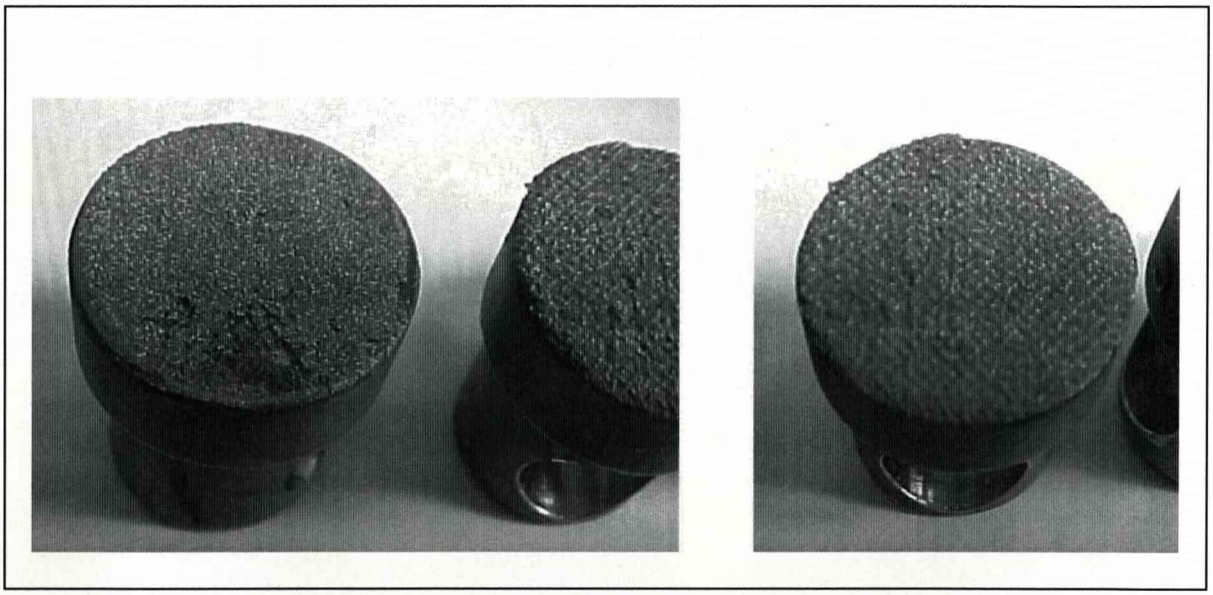

Figure 5.22 Failed samples produced using titanium sponge coating on cobalt-chrome substrates with a laser scanning speed of 120mm.s^{-1}, laser power of 82W, frequency of 30kHz and beam overlap of BO = 0%)

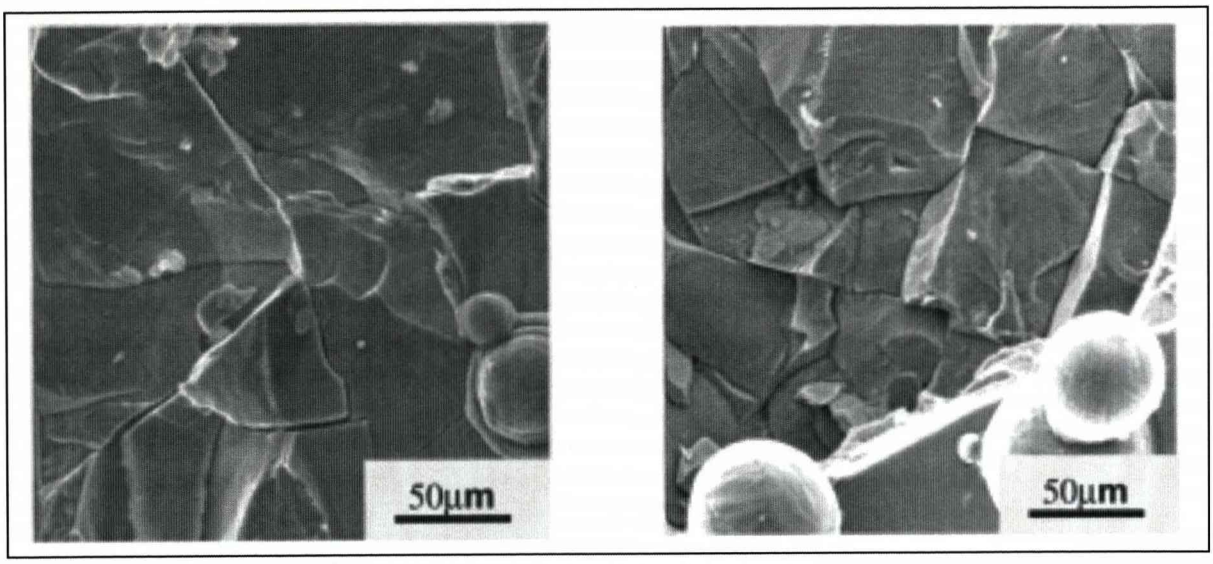

Figure 5.23 SEM micrographs of fractured titanium on cobalt-chrome interface produced with a laser scanning speed of 180mm.s^{-1}, laser power of 82W CW and beam overlap of –40%

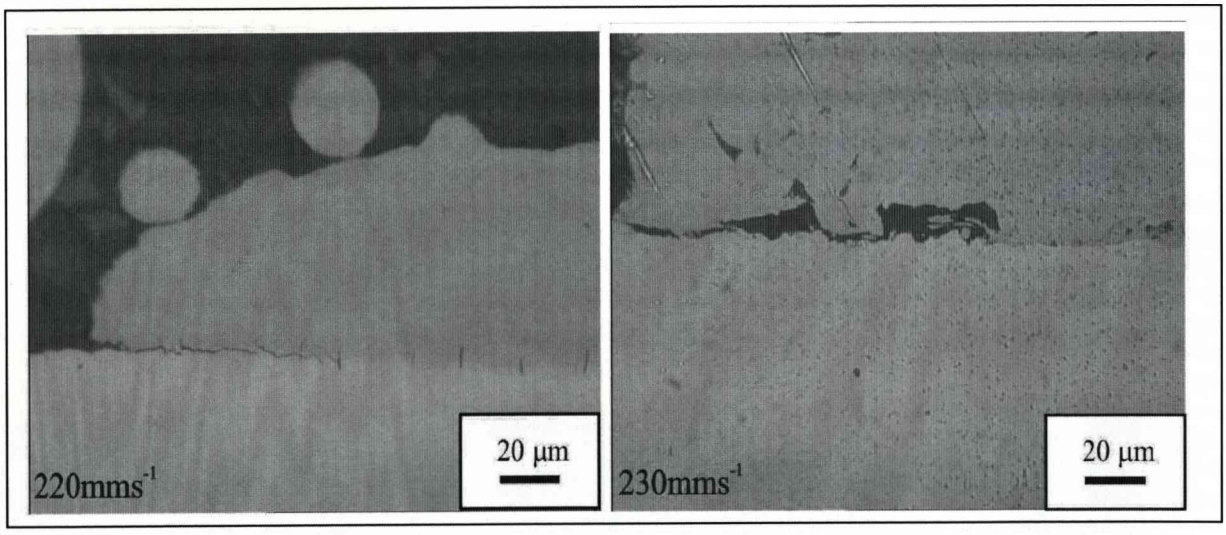

Figure 5.24 Optical images showing micro-fractures along cobalt-chrome substrate/ titanium coating interface produced with laser power of 82W CW, beam overlap of -40% and laser scanning speed of: 220mm.s-1 (left image) and 230mm.s-1 (right image)

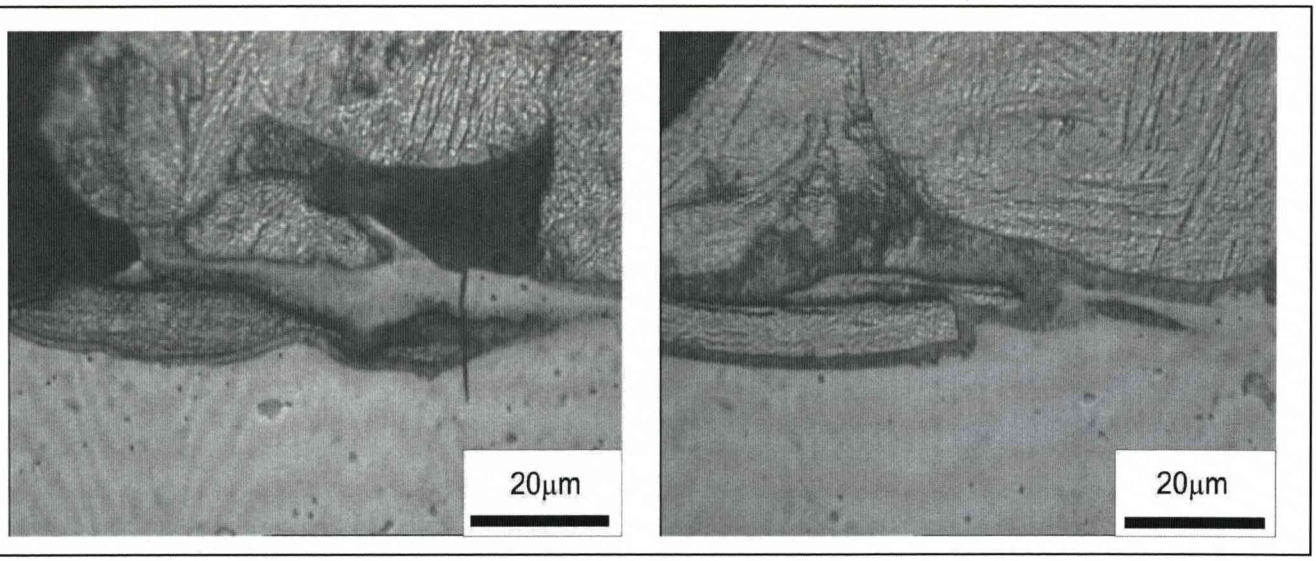

Figure 5.25 Optical micrographs of sectioned Ti/CoCr interface (v = 220mm.s^{-1}, P = 82W CW and BO = –40%). Etchants: 5g NH_4FHF 100ml Distilled H_20, + 5ml HCl (titanium coating); 5% Nital solution (interface); 50% vol. HCl, 50% H_20 heated to 80°C: (cobalt-chrome alloy)

SEM analysis (Figure 5.26) of heavily etched cross-sections allowed the coating and substrate microstructural morphology to be observed, although it did etch away the interface layer. Within the substrate, close (5 to 10μm) to the coating/substrate interface, a phase rich in molybdenum was observed (Figure 5.27). It is likely that these regions are either small carbides in the original alloy or the effect of small $M_{23}C_6$ carbides decomposing. XRD analysis of the surface of the titanium coating identified only αTi. However, as the coating was ground away and the sample reanalysed, a number of other phases were detected (Figure 5.28), until the substrate was reached. It should be noted that the phase identified as βTi in Figure 5.28 can also be identified as the intermetallic TiCo. EDS analysis (Figure 5.29) of the cracked layer at the interface showed it to be titanium-rich but containing cobalt and chromium. However, with thin layers, some of the X-rays detected may come from the surrounding phases, the volume from which the X-rays are generated being much larger than the electron beam diameter. Microhardness tests of the sections showed that the substrate (410Hv) was somewhat softer than the first layer (520Hv) of the titanium coating and that the hardness dropped with each subsequent

layer to about 200Hv at the outer edge, the hardness dropping rapidly within the first few layers of the coating.

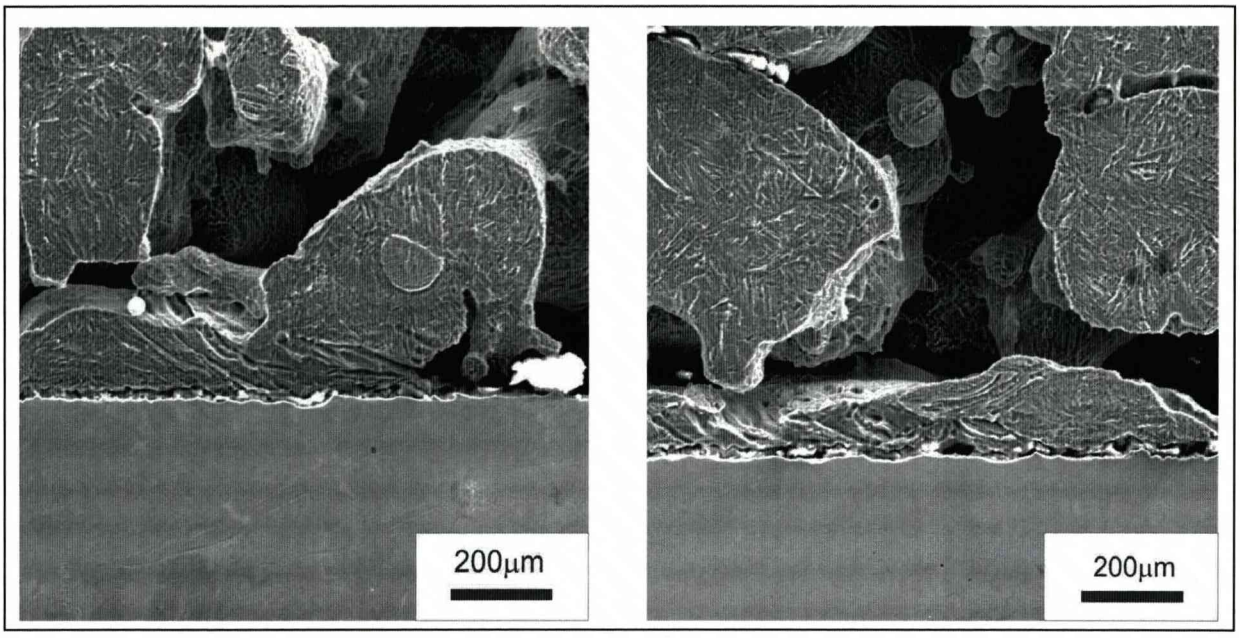

Figure 5.26 SEM micrographs of sectioned titanium/cobalt-chrome samples produced with parameters v = 190mm.s^{-1}, P = 82W CW and BO = –40%

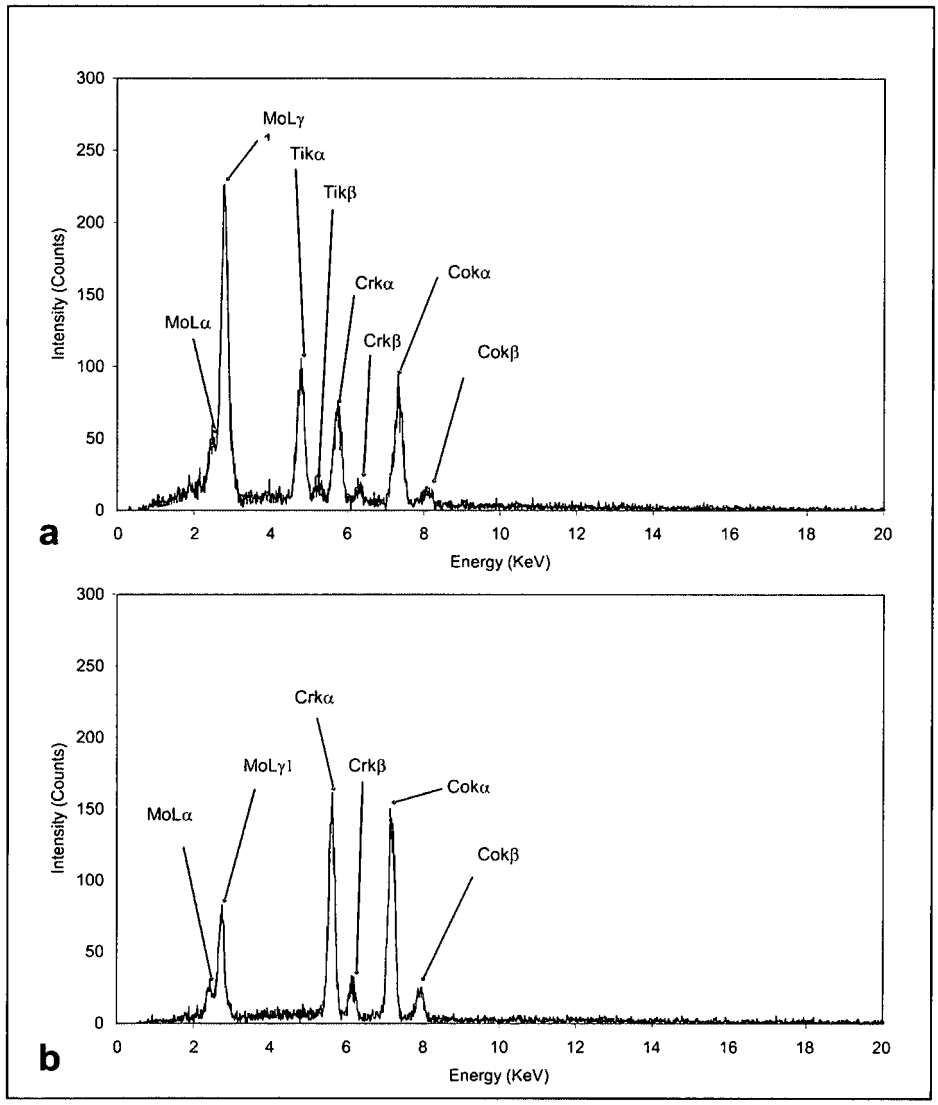

Figure 5.27 EDS spectra of two regions within interface of a sectioned titanium/cobalt-chrome sample showing variation in molybdenum content between phases

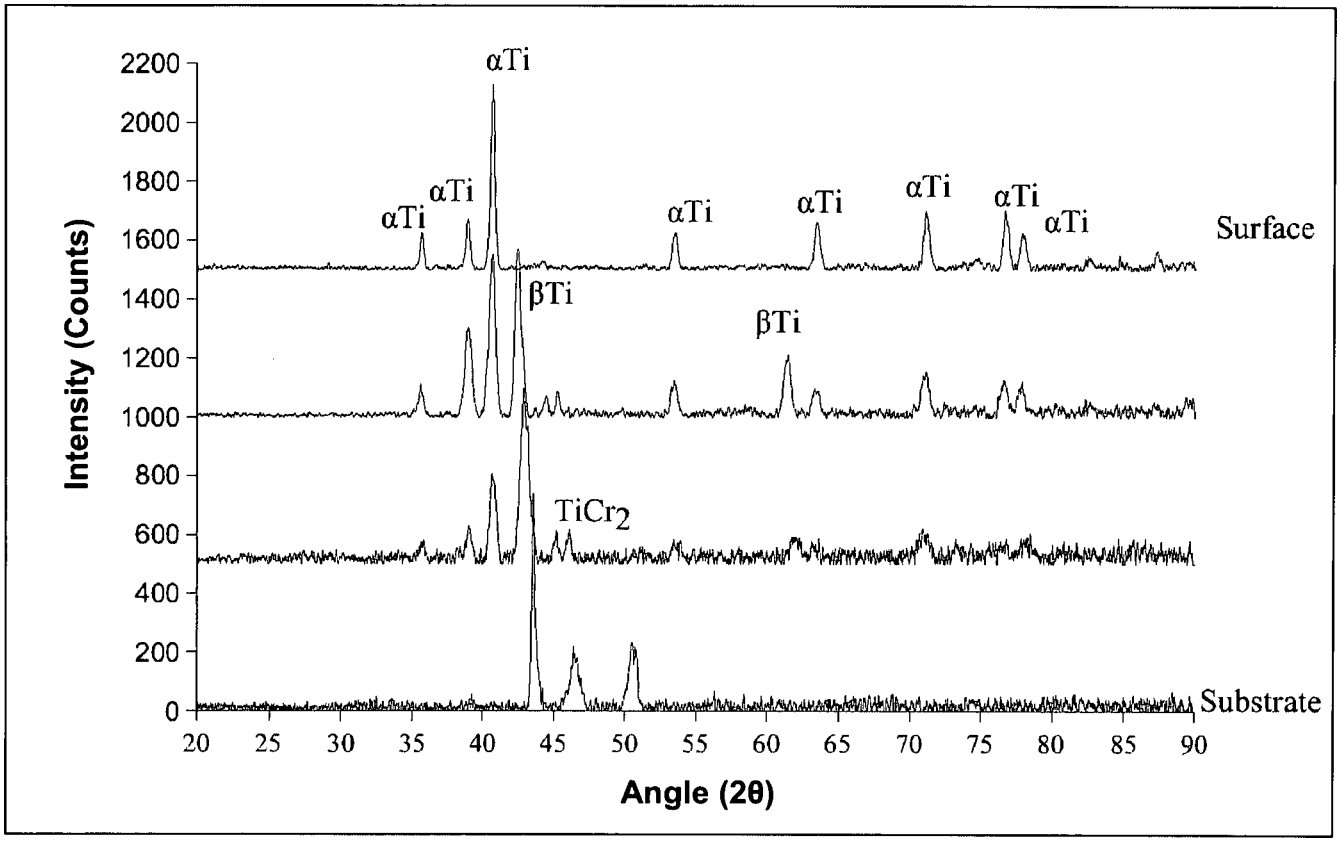

Figure 5.28 XRD spectra of titanium/cobalt-chrome interface

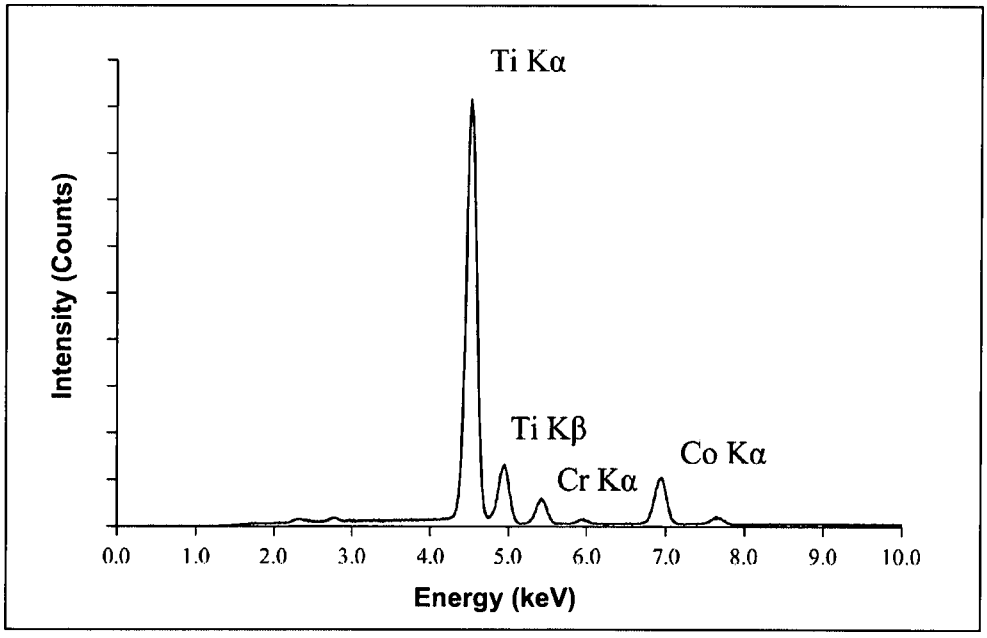

Figure 5.29 EDS spectra of the cracked layer within a titanium/cobalt-chrome alloy interface

5.2.3.1 Application of Intermediate Tantalum Coating

It was known, from the initial experiments, that tantalum could be successfully deposited on to a cobalt-chrome alloy and therefore the use of a tantalum interface layer was investigated. The samples produced showed significantly better bonding between the coating and the substrate than when titanium was applied directly onto cobalt-chrome, and suppressed the formation of cracks at the interface (Figure 5.30). EDS analysis (Figure 5.31) shows some dissolution of the substrate (5.31c) and coating (5.31a) with possibly some intermetallics forming within the first layer. XRD analysis of sections through the tantalum/substrate interface revealed only one peak which was not from either tantalum or from the substrate (Figure 5.32). The phase that produced this peak could not be identified as insufficient peaks were detected. As with the titanium coatings, microhardness tests were carried out, revealing that the tantalum at the interface was harder (600Hv) than the titanium layer that cracked, which may indicate that the cracks at the Ti/CoCr interface are not simply the result of the formation of a hard phase.

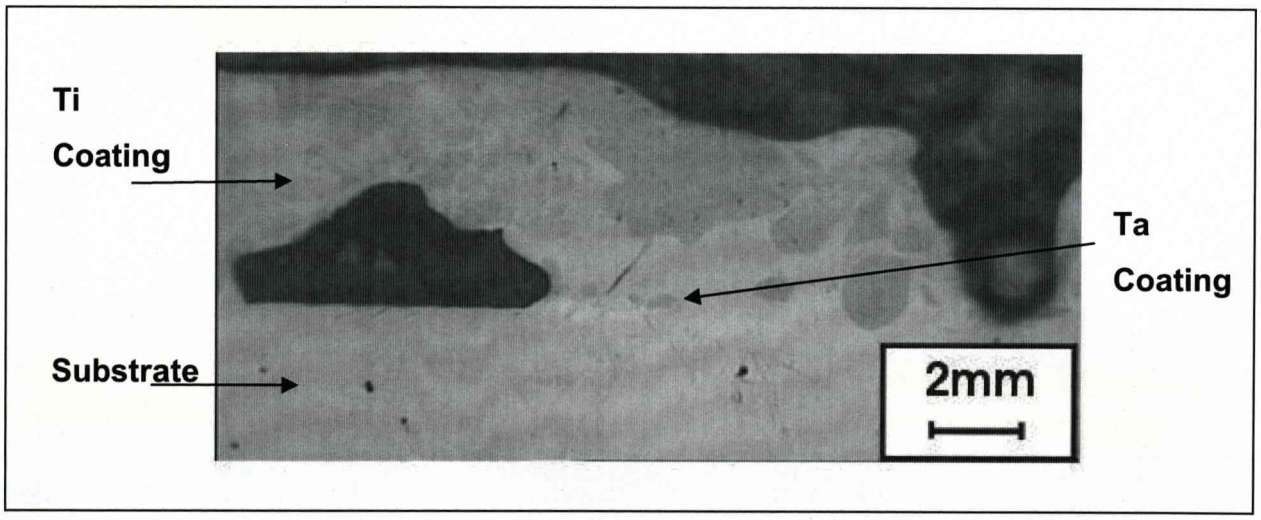

Figure 5.30 Optical micrograph of tantalum/cobalt-chrome interface

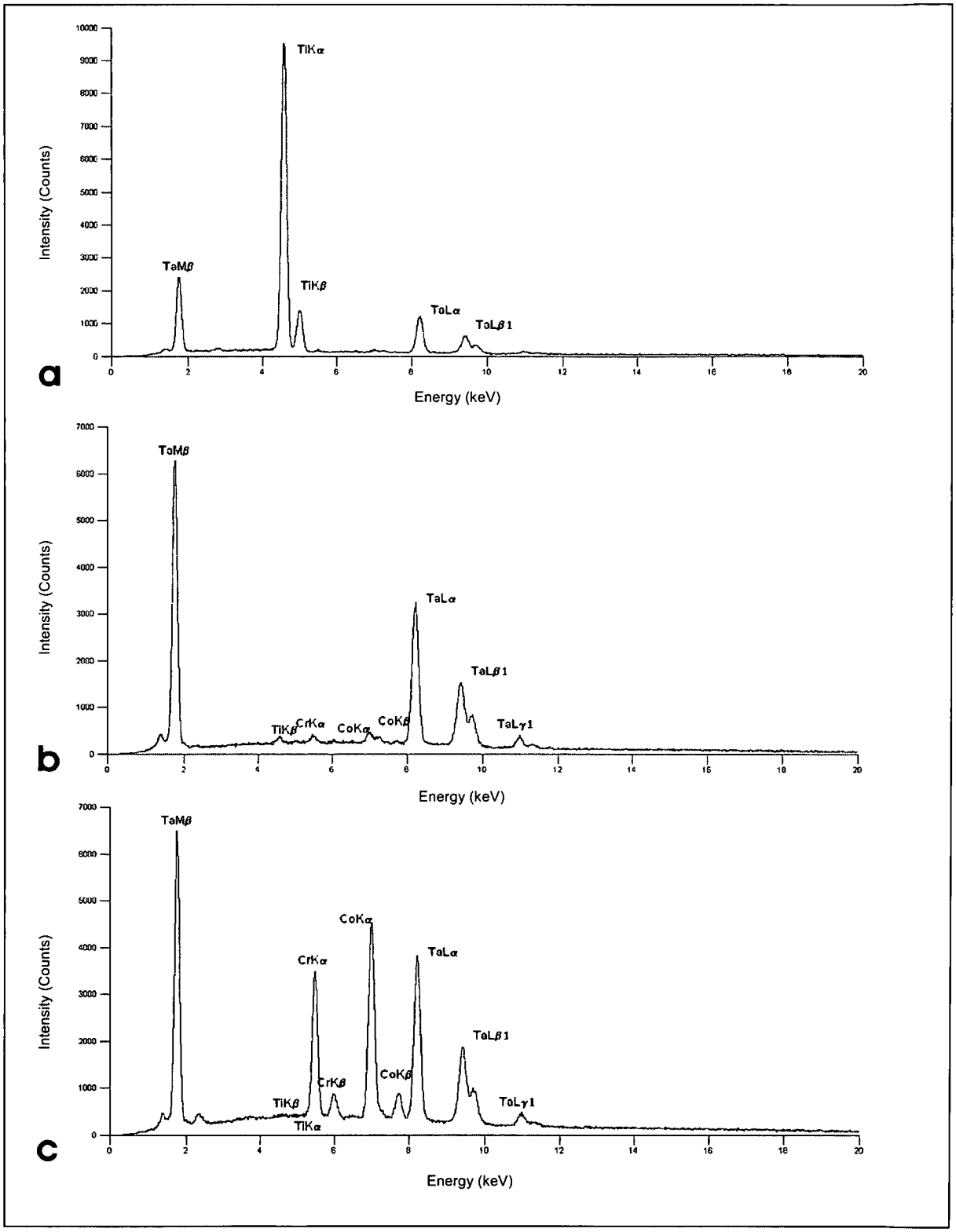

Figure 5.31 EDS spectra obtained across the interface of tantalum bond-coated titanium on cobalt-chrome sample showing: a) coating, b) interface and c) substrate

The EDS (Figures 5.31) showed that some alloying of the titanium with tantalum occurred within the first few layers of the final coating, while XRD analysis (Figure 5.32) of the tantalum-rich region contained some alloying elements from the cobalt-chrome alloy and close to the tantalum/cobalt-chrome interface there was some mixing. It appears therefore that mixing occurs within the melt pool between the different layers as Marangoni forces, produced by the temperature gradient, stir the melt pool.

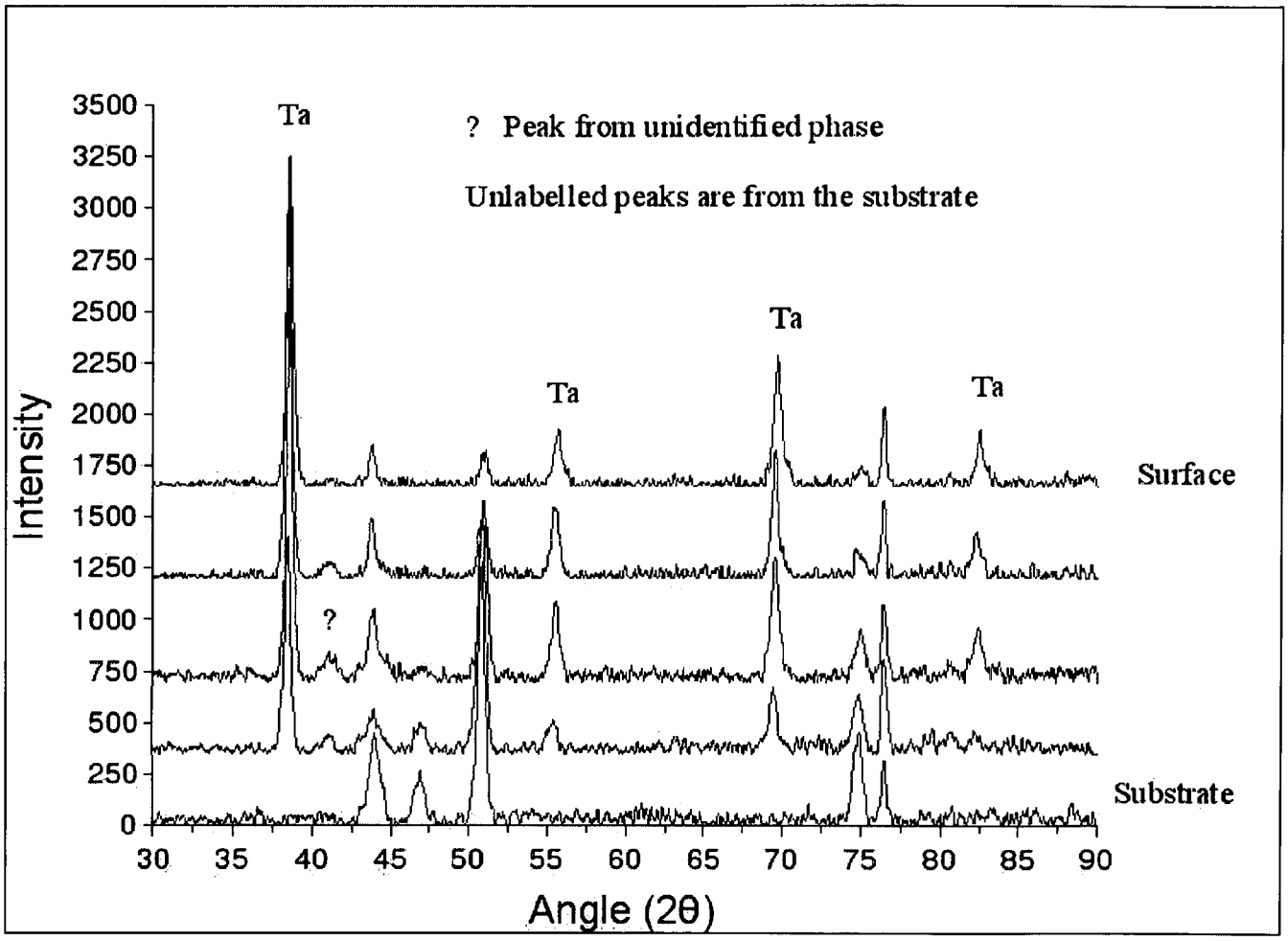

Figure 5.32 XRD analysis through the tantalum/cobalt-chrome substrate interface

5.2.4 Mechanical Testing of Porous Titanium Coatings

5.2.4.1 Mechanical Testing of Coated Titanium Substrates

Tensile tests (Table 5.8) showed that for the titanium coated titanium substrates the initial processing conditions (Table 5.9) led to most samples failing below the minimum required

tensile force. The majority of these samples failed at the interface between the coating and substrate (Figure 5.33) although for two samples there were regions where the interface was stronger than the coating. A second set of tensile tests was therefore carried out with samples produced with a different set of process conditions (Table 5.11). These changes produced a small increase in the average tensile force, such that three out of the five samples exceeded the required load. However, the greatest change was that the failure was now located within the coating rather than at the interface (Figure 5.34).

The laser parameters for the first set of samples (Table 5.9) were revised to reduce the specific energy density applied to the three layers of the coating scan. It was considered that excessive energy applied to these layers (resulting from a combination of a pulsed beam applying a large instantaneous surge of power to the powder bed and a reduced scanning speed) resulted in failure to create a flat, uniform layer. This was seen in earlier experiments (Figure 3.5) where powder had been blasted from the substrate around the edge of the scan and resulted in 'bowing' of the top surface. During the tensile testing, this inability to create a flat, satisfactorily bonded, structure resulted in the tensile force effectively being applied over a smaller area.

The first three solid layers following the interface scan were introduced to provide a "bond coat" (using a similar principle to the application of an undercoat during automobile painting) for the subsequently produced porous layers to fuse with. Parameters that provided a higher specific energy density were initially considered to be the best way to allow these layers to fuse with the substrate. Repeated experimental iterations, however, showed that it was more important to achieve a flat, uniform layer to provide a larger area of material for the porous coat to bond to. To achieve this, the laser scanning speed was increased to the limits of the system ($500mm.s^{-1}$; Table 5.11) to reduce the energy that was applied to the powder to prevent it from being blasted from the substrate, but still being high enough to melt the powder. Unfortunately, it was not possible to increase it further to test the limits of this theory.

Sample No.	Figure	Tensile Strength (MPa)	% Required Strength	Failure Mode
(Uncoated Substrate)	5.33a	32.2		100% Adhesive
1	5.33b	22.3	92.5	Interface
2	5.33c	21.0	87.2	Interface
3	5.33d	21.3	88.3	Interface 90%, Coating 10%
4	5.33e	20.9	86.8	Interface
5	5.33f	24.2	100.4	Interface 90%, Coating 10%

Table 5.8 First series of titanium on titanium tensile test results

Layer	Laser Power	Line-spacing	Scanning Speed	Pulse Repetition Rate
Interface Scan:	82W	-50μm (50% beam overlap)	60mm.s^{-1}	10kHz
1st 3 Layers:	75W	1st Layer = 50μm (50% BO) 2nd Layer = 75μm (25% BO) 3rd Layer = 100μm (0% BO)	300mm.s^{-1}	30kHz
Coating Scan:	82W	700μm (-600% beam overlap)	240mm.s^{-1}	0kHz

Table 5.9 Laser parameters of Samples 1 to 5 in Table 5.8

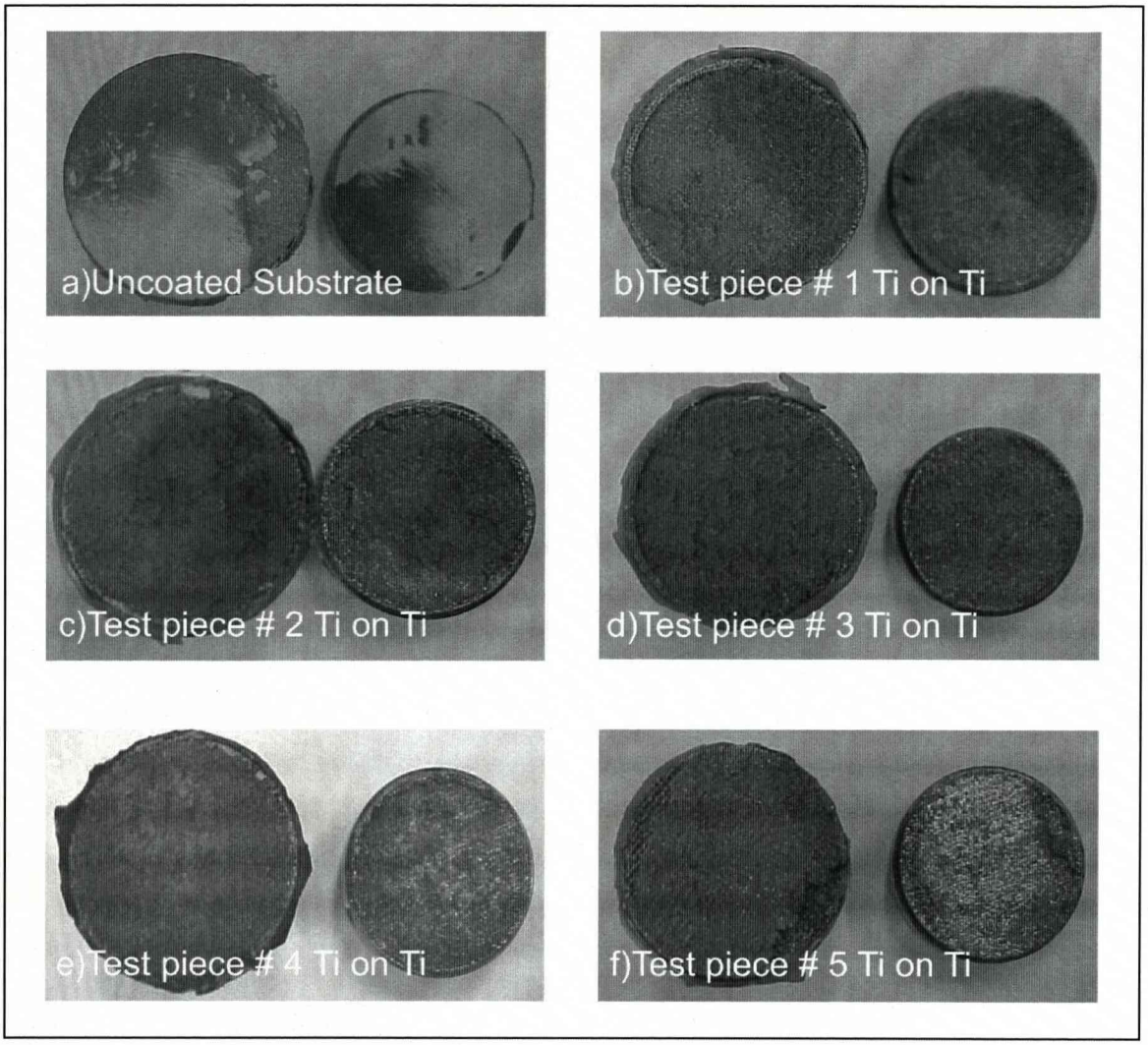

Figure 5.33 First series of tensile test failures, produced with laser parameters shown in Table 5.9

Sample No.	Figure	Tensile Strength (MPa)	% of Required Strength	Failure Mode
6	5.34a	22.1	91.7	90% Coating solid layers, 10% Webbing.
7	5.34b	24.2	100.3	90% Coating solid layers, 10% Webbing.
8	5.34c	25.1	104.3	90% Coating solid layers, 10% Webbing.
9	5.34d	21.6	89.5	90% Coating solid layers, 10% Webbing.
10	5.34e	24.9	103.2	90% Coating solid layers, 10% Webbing.

Table 5.10 Second series of titanium coated titanium tensile test results

Layer	Laser Power	Line-spacing	Scanning Speed	Pulse Repetition Rate
Interface Scan:	82W	-50µm (50% beam overlap)	60mm.s^{-1}	10kHz
1st 3 Layers:	75W	1st Layer = 50µm (50% BO) 2nd Layer = 75µm (25% BO) 3rd Layer = 100µm (0% BO)	500mm.s^{-1}	30kHz
Coating Scan:	82W	700µm (-600% beam overlap)	160mm.s^{-1}	0kHz

Table 5.11 Laser parameters of samples 6 to 10 in Table 5.10

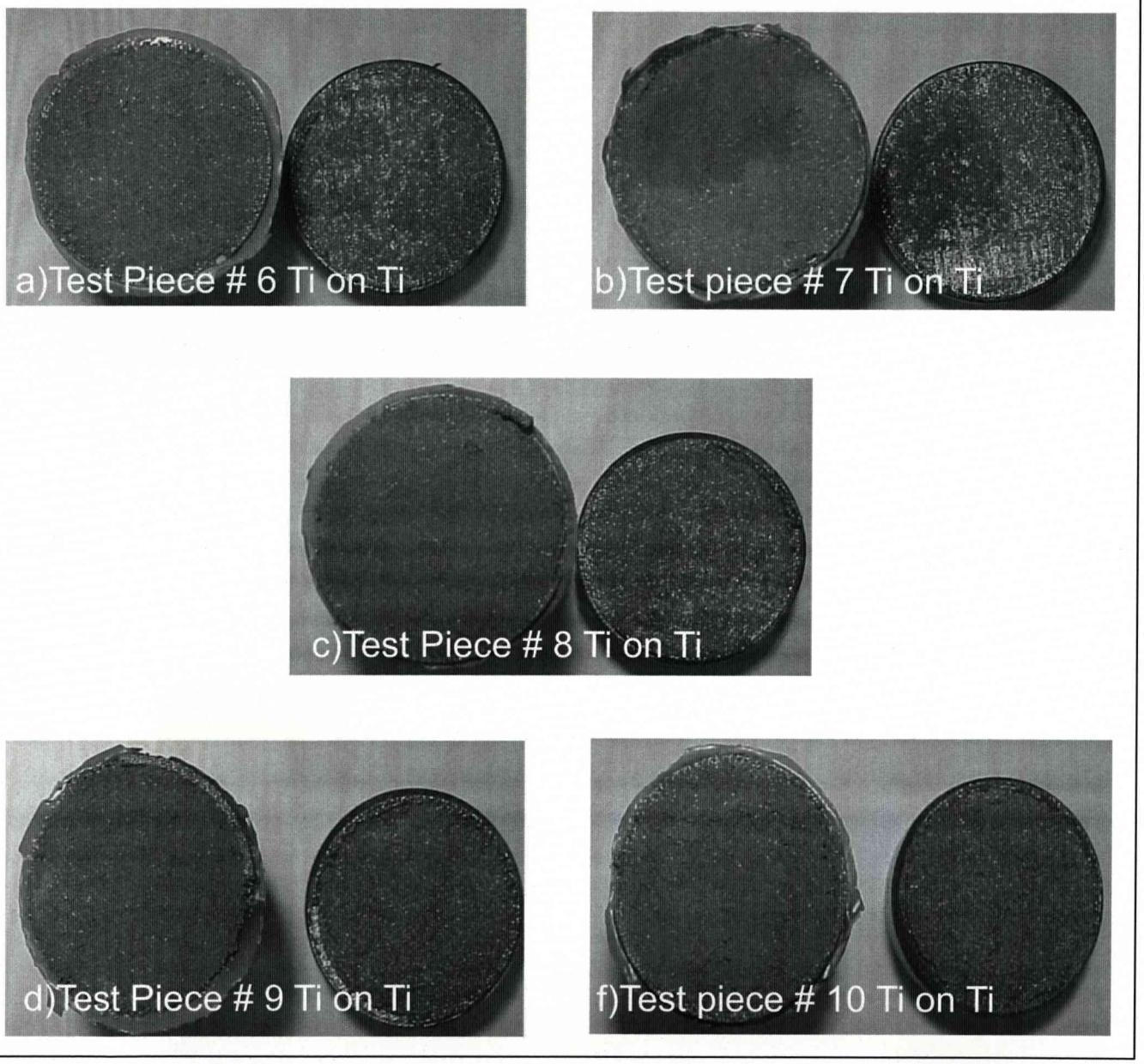

Figure 5.34 Second series of tensile test failures, produced with laser parameters shown in Table 5.11

5.2.4.2 Mechanical Testing of Coated Cobalt-Chrome Substrates

Although it was already known that the titanium on cobalt-chrome substrate samples were very weak, tensile tests were carried out to quantify their behaviour, allowing comparison with the other coatings/substrate combinations. The results (Table 5.12) clearly show that the titanium/cobalt-chrome alloy interface is significantly weaker than the other coating/substrate combinations, some of which failed at the adhesive (Figure 5.35) and

therefore the measured value is less than the maximum strength of the coating/substrate combination. The adhesive failure is likely due to curvature of the top surface of the coating leading to peeling of the adhesive.

Sample No.	Figure	Tensile Strength (MPa)	% of Required Strength	Failure mode (%; (Estimate Only))
1 (Nb on CoCr)	5.35a	26.18	109	65% adhesive, 35% bond interface
2 (Ti on CoCr)	Not shown	5.00	21	Interface
3 (Ti on CoCr)	Not shown	6.20	26	Interface
4 (Ti on Nb on CoCr)	5.35b	15.62	65	Mostly bond coat interface
5 (Ti on Nb on CoCr)	5.35c	18.53	77	20% adhesive, 40% bond coat, 40% porous Ti
6 (Ti on Ta on CoCr)	5.35d	23.33	97	Mostly adhesive with discrete webbing weakness
7 (Ti on Ta on CoCr)	Not shown	22.57	94	100% porous Ti
8 (Ta on CoCr)	5.35e	27.92	116	60% adhesive, 40% interface
9 (Ti on Ta on CoCr)	5.35f	13.62	57	100% bond interface

Table 5.12 Tensile testing results of coated cobalt-chrome substrates

To allow for comparison with the titanium on titanium samples, the parameters used for the coated cobalt-chrome samples were the same as those used for the second series of titanium coated titanium samples. These are shown in Table 5.13.

Layer	Laser Power	Line-spacing	Scanning Speed	Pulse Repetition Rate
Interface Scan:	82W	-50μm (50% beam overlap)	60mm.s-1	10kHz
1st 3 Layers:	75W	1st Layer = 50μm (50% BO) 2nd Layer = 75μm (25% BO) 3rd Layer = 100μm (0% BO)	500mm.s-1	30kHz
Coating Scan:	82W	(dictated by scanning pattern)	160mm.s-1	0kHz

Table 5.13 Laser parameters of samples 1 to 9 in Table 5.12

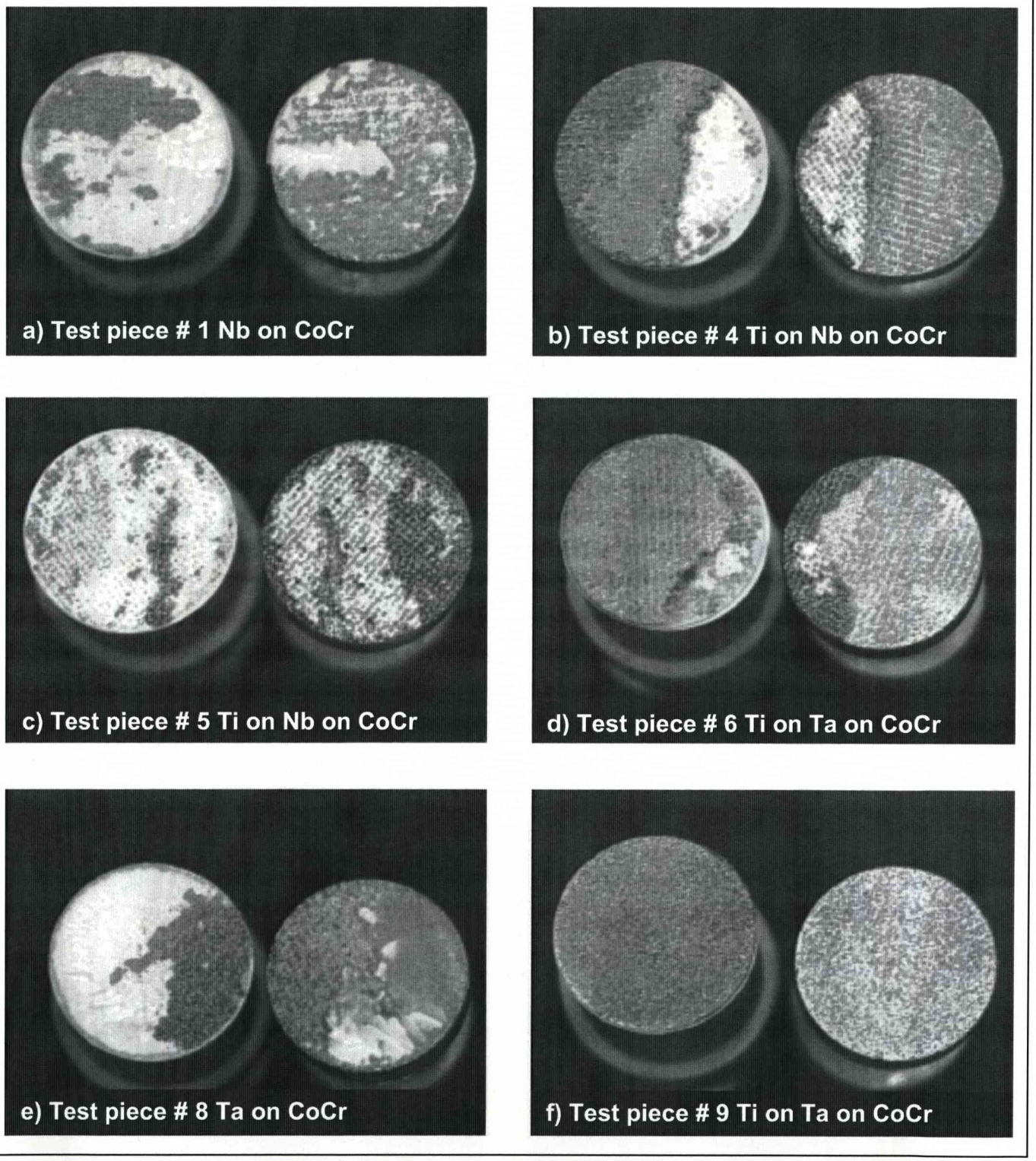

Figure 5.35 Coated cobalt-chrome tensile test pieces after fracture for the results shown on Table 5.12, produced with the laser processing parameters shown in Table 5.13

5.2.5 Pore Size Optimisation

The experiments to initially characterise the DMLR process, presented earlier, showed that the laser scan line-spacing was an effective way of controlling the coating porosity, but further experiments were required to determine if the relationship between pore size and line-spacing was linear for the pore sizes that were required. Non-linear behaviour may occur if powder not directly under the laser beam is incorporated into the melt pool, which is more likely to occur when the laser scans slowly. To evaluate this, the relationship between pore size and line-spacing was determined.

Using a calibrated Carl Zeiss "Travelling Microscope," eight pore sizes were measured for each of nine titanium coated titanium samples. In each case, the average pore size was calculated to allow the variation in pore size to be determined (Figure 5.36 and Figure 5.37).

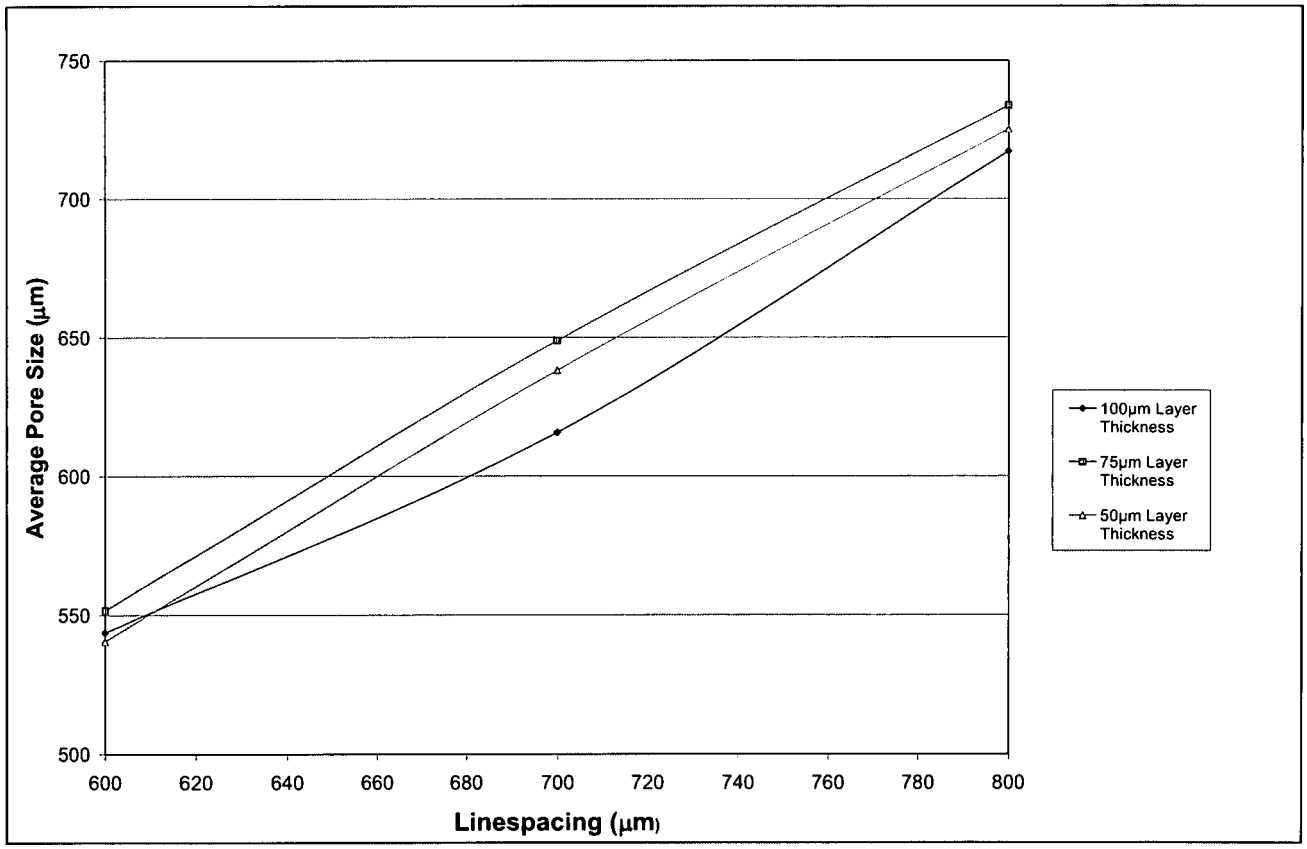

Figure 5.36 Pore size characteristics for typical layer thicknesses for solid titanium coated titanium samples with laser scanning speed of 180mm.s^{-1} and laser power of 82W CW

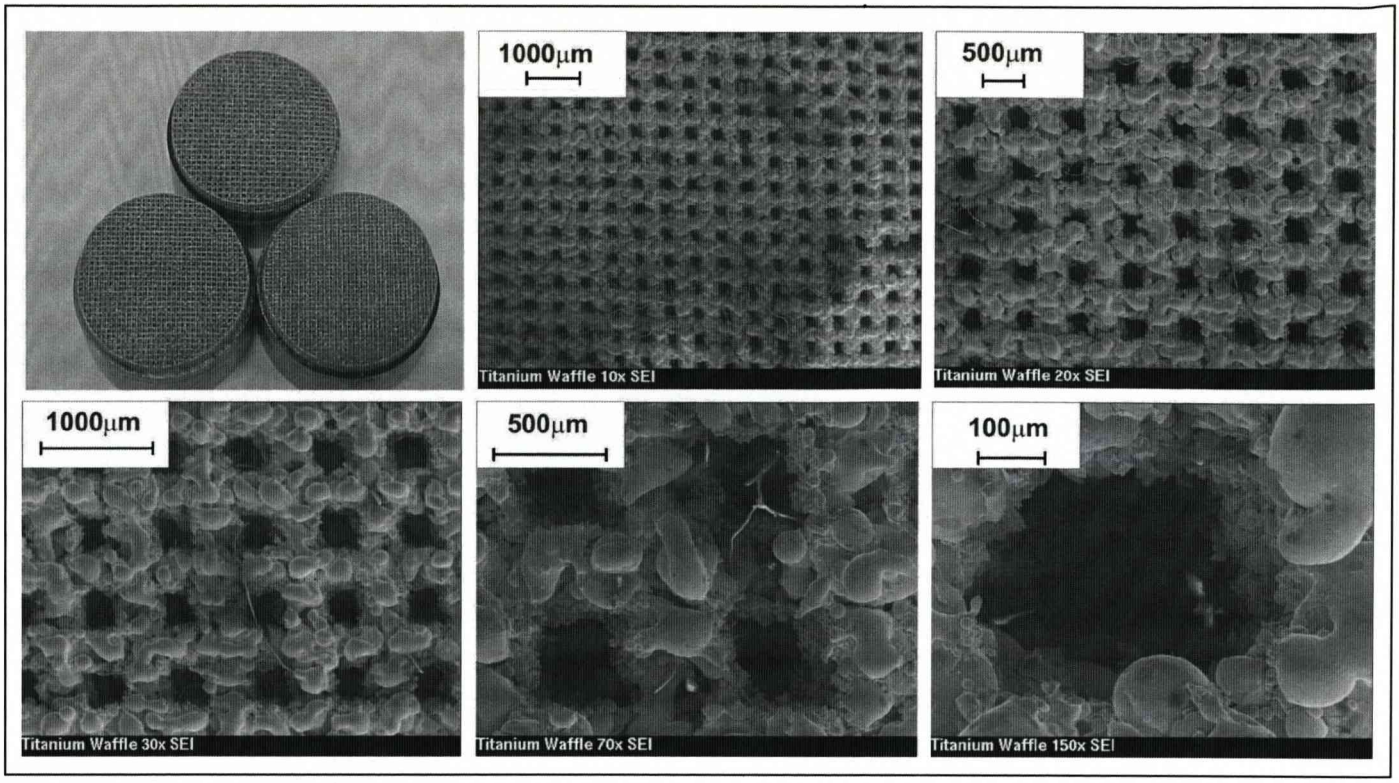

Figure 5.37 Clockwise from top left, array of three samples, solid titanium on titanium waffle structure at increasing magnification, showing the regular pore size achievable by DMLR processing; these samples were produced with laser scanning speed of 180mm.s^{-1}, laser power of 82W CW and beam overlap of 500%

The plot of line-spacing against pore size (Figure 5.36) shows a reasonably linear relationship for all three layer thicknesses. However, for any given line-spacing, the effect of coating thickness is less certain as the largest pores for a given line-spacing are produced with the intermediate layer thickness. This may be due to the thinner layers being more sensitive to over-building as the roller/sample clearance is reduced, making the production of uniform layers more difficult. Confirmation that this effect may dominate behaviour with the 50μm layer thickness comes from the greater curvature of the top surface.

After successful production of the regular structures, the random and apparently disordered structures (Section 5.1.4.2) were manufactured. The scan patterns (Figure 5.7) were produced on top of a conventional waffle structure, with initial work being with the 32 line scan pattern (Figure 5.38a), where the subsequently produced pore size was

measured and the process adjusted accordingly. Manually drawn 54 line-segments (Figure 5.38b) were produced, as were the 50 line and 100 line patterns (Figures 5.39a and 5.39b). In each case the structure produced was very similar to the computer simulation, showing that the process was controllable. To improve the structures further, samples were produced where the scan line start and end points were based on the definition of a number of circles within the scan-pattern (Figure 5.9). Figure 5.40a shows a build produced with a scan distributed on one of twenty virtual circles whose diameters varied from 24mm to 10mm; Figure 5.40b used a scan based on six circles whose diameters varied from 24mm to 18mm; Figure 5.40c shows 70 scanning lines on six circles, whose diameters varied from 24mm to 18mm. The final stage of this work was to confirm that the structures produced were reasonably cross-linked, which was confirmed by optical microscopy (Figure 5.41). This work confirmed that DMLR was able to produce structures that were not regular and gave Stryker Howmedica Osteonics confidence to continue the work.

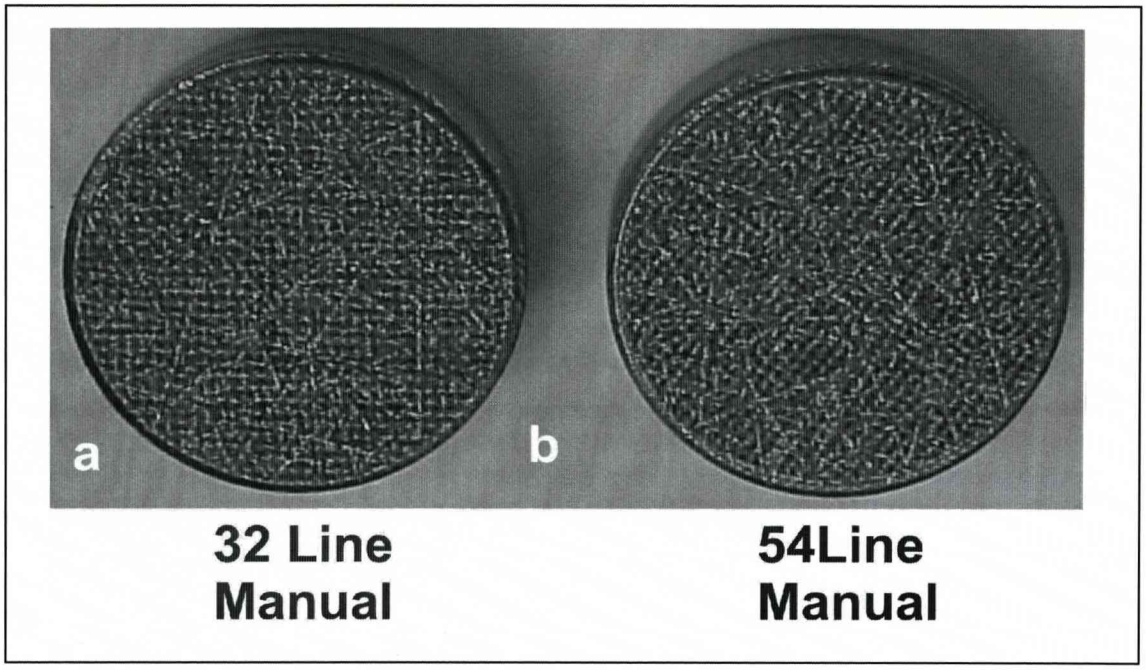

Figure 5.38 Photograph showing 32 line and 54 line manually drawn interpretations of random scan used during the production of solid titanium on titanium samples, produced with the parameters shown in Table 5.6

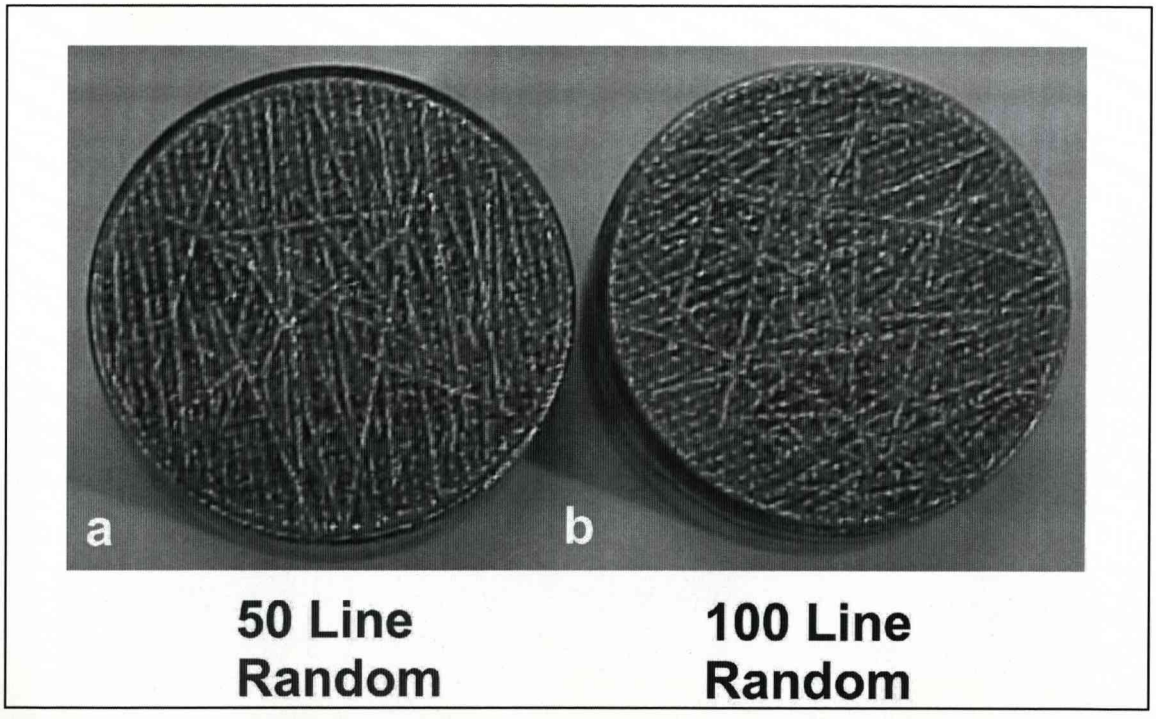

Figure 5.39 Photograph showing solid titanium on titanium structures produced using a 50 line and a 100 line scan, using revised computer generated data, and the parameters shown in Table 5.6

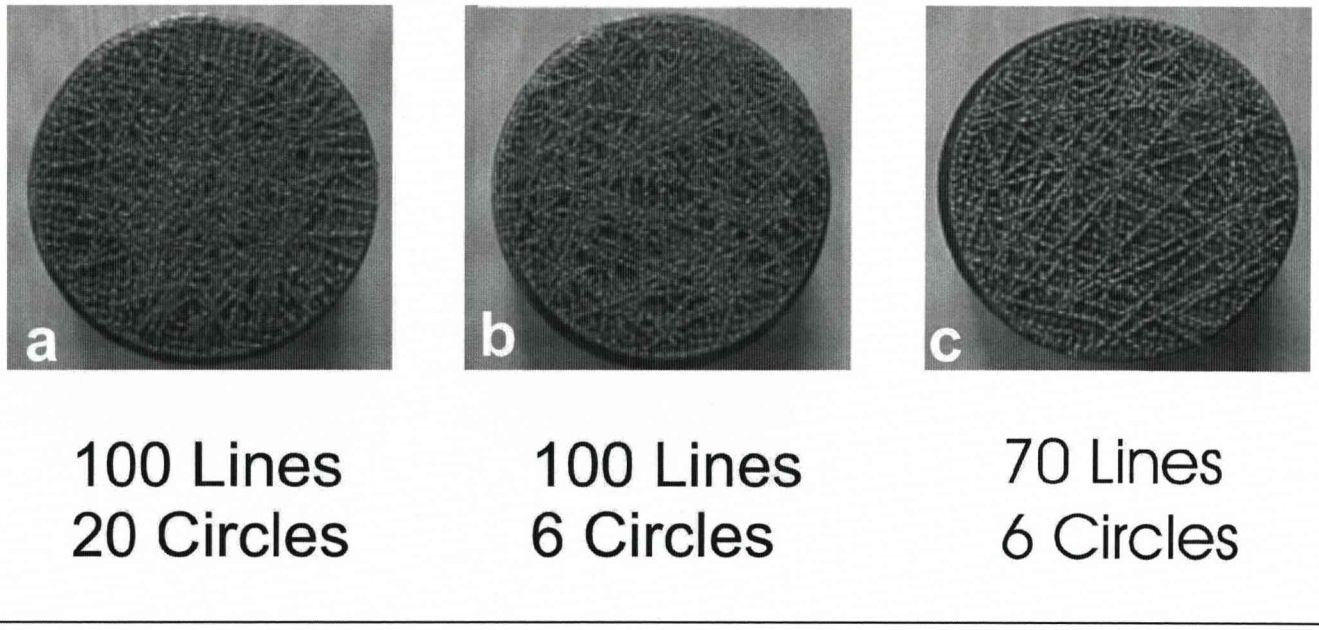

Figure 5.40 Photograph showing solid titanium on titanium structures produced using random scans with scan pattern based on a varying number of scan lines whose vertices are based on the perimeter of a varying number of circles (Figure 5.9). The laser parameters used are shown in Table 5.6

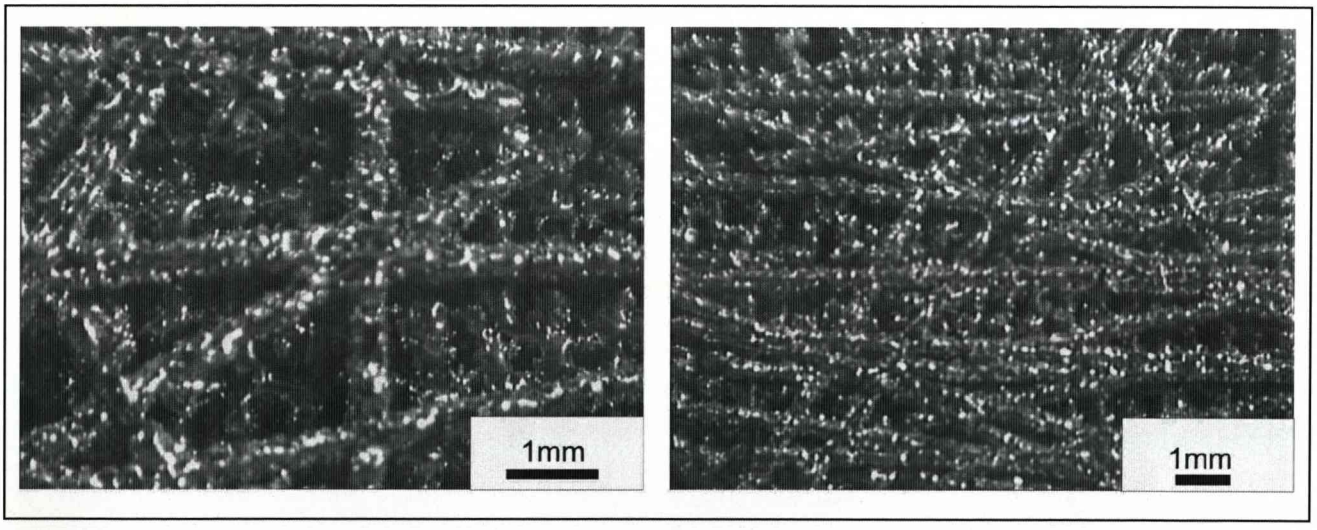

Figure 5.41 Optical micrographs of solid titanium on titanium specimen produced with 50 line random scan and laser parameters shown in Table 5.6

The final section of this work was to examine these latest samples in section (Figure 5.42). These showed a structure at the coating/substrate interface similar to those observed with welding, with what appears to be the regrowth of the underlying grains. Further into the

coating, where the structure is porous, the regrowth of existing grains does not occur and the rapid cooling produces an acicular microstructure.

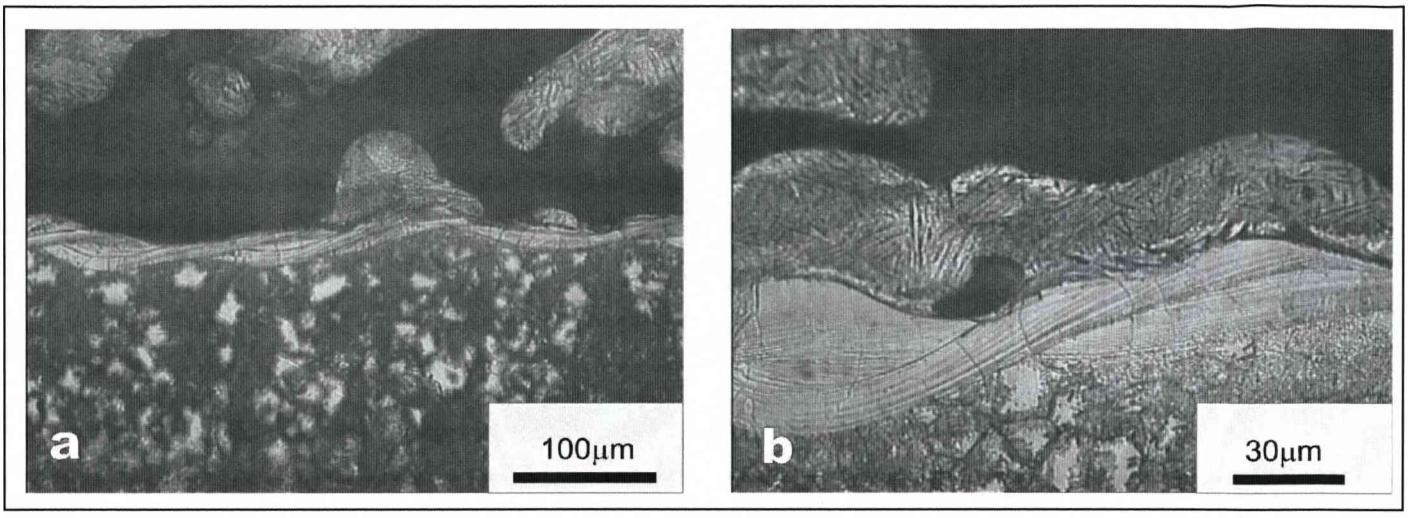

Figure 5.42 Optical micrographs of the sectioned sample shown in Figure 5.41

5.3 Discussion

In a similar way to the research on H13-copper, this work again encountered one of the limitations of melt-processing materials; the unsuitable phases and microstructures that can form as the melt pool freezes. The production of titanium coatings on titanium was fairly trivial compared to the other systems where alloying occurred between the coating and substrate. The greatest problems were seen with the titanium on cobalt-chrome system (although not with cobalt-chrome on titanium; Figure 5.10) where severe cracking was observed at the coating/substrate interface. Also observed were differences in the wetting of the substrate by the coating; again, with titanium on cobalt-chrome behaving very differently to cobalt-chrome on titanium.

5.3.1 Titanium on Cobalt-Chrome

The binary Ti-Co phase diagram (American Society of Materials, 1997; see Figure A3.4 in Appendix 3.0) shows complete liquid solubility but only limited solid solubility, with the formation of a number of intermetallics. In titanium-rich alloys, cobalt acts as a β stabiliser

with β stable down to 685°C. The maximum solubility of cobalt in the β phase is 15wt% Co which occurs at 1020°C. In the αTi phase, the solubility of Co is much lower (1wt %). With increased Co there is a rapid lowering of the liquidus until a eutectic (L → ßTi + Ti_2Co) is reached at 1020°C (26wt%Co). At the cobalt-rich end of the diagram, Ti dissolves into Co to an appreciable degree (10wt%Ti at 1190°C), before forming a range of intermetallics at higher concentrations. The highest melting point intermetallic is TiCo at 1335°C; still appreciably lower than the pure elements.

In contrast, the Ti-Cr binary phase diagram (American Society of Materials, 1997; see Figure A3.5 in Appendix 3.0) shows complete solubility both in the liquid and in the solid, but only at high temperatures (above 1370°C). Below this temperature an intermetallic, $TiCr_2$, can form. In titanium-rich alloys, chromium acts as a β stabiliser with βTi being stabilised down to 667°C, below which a eutectoid (βTi → αTi + $TiCr_2$) occurs. Also present within the cobalt-chrome alloy are molybdenum and carbon, both of which will interact with the titanium in the melt pool. Molybdenum and titanium (American Society of Materials, 1997; see Figure A3.6 in Appendix 3.0) show complete solid solubility at higher temperatures (above 882°C), with Mo also stabilising the βTi phase to lower temperatures. The solubility of Mo in αTi is much lower than that in βTi with a eutectoid reaction (βTi → αTi + βMo (Ti)). Carbon, in comparison, reacts strongly with titanium to form the carbide TiC. Little data has been published for the Co-Cr-Ti ternary system, with what has been published being reviewed by Gupta, 2001 (see Figures A3.7 to A3.11 in Appendix 3.0). This paper concentrates on the cobalt rich corner of the diagram, which shows three binary eutectic and three ternary eutectic reactions occurring in this section of the diagram.

The application of phase diagrams to DMLR must be carried out with caution as the cooling rates during DMLR processing are fast. The cooling rates for laser melted 321 stainless steel have been calculated to be in excess of 10^6 Ks^{-1} (Yilbas and Aleem, 1999), whilst the cooling rate of Laser Engineered Net Shaping (LENS) has been measured to be in the range 100 to 1000Ks^{-1} (Hofmeister *et al*, 1999). This rapid cooling may lead to the formation of metastable phases and the suppression of slow phase changes, such as peritectic or solid state reactions that occur by solid state diffusion.

The XRD analysis of the titanium on cobalt-chrome alloy samples showed the presence of a bcc phase that could be identified either as βTi or the intermetallic TiCo, although the lattice parameter is similar to that of TiCo. TiCo is an ordered version of the high temperature β phase of titanium and the only observable difference between the two XRD plots would be the presence of small peaks which are not allowed in the disordered structure. These peaks are not visible within the XRD data but this may be due either to the structure being disordered or that they are hidden by peak overlaps and noise in the data. SEM/EDS analysis of the region near to the interface did not identify compositions similar to that of TiCo unless very close to the interface, where it is likely that the underlying substrate is being detected as well as the interface layer. It is therefore reasonable to assume that the phase is the metastable βTi, with a lattice parameter similar to the intermetallic but without any ordering. This also fits with the data from the phase diagrams as Co, Cr and Mo are all stabilisers of βTi. It is likely that the alloy concentrations are high enough to lower the martensite Ms temperature below room temperature.

What appears to be the most important feature of the Ti-Co system is the very deep eutectic valley on the titanium-rich side of the diagram where the eutectic melting point is 1020°C (significantly below the melting point of either titanium (1668°C) or cobalt (1495°C)). When the thin layer of titanium on the cobalt-chrome alloy is laser melted the powder melts, forming a melt pool, but as it forms the underlying substrate begins to dissolve into it rapidly suppressing the freezing point. As the laser is not stationary but moves across the surface, unmelted titanium is added to the front of the melt pool, while at the tail material freezes. As the melt pool is moving rapidly it is likely that the front of the melt pool will contain material that melts at a temperature close to that of titanium (1668°C) while the tail will be highly alloyed, lowering the freezing point close to 1020°C. This produces an extended melt pool and extreme superheating of the molten material, which accounts for the increased wetting/fluidity that was observed with this alloy combination. The presence of the alloying additions not only suppresses the melting point but also stabilises the ßTi phase and hardens it by solid solution hardening.

After the first layer has been deposited, a second layer of powder is applied and this powder is melted by the scanning laser beam. The titanium powder in this second layer now has a significantly higher melting point than the underlying layer. This will allow the

melt pool to melt a significant part of the previous layer but probably not through to the underlying substrate. As the layers mix, the concentration of alloying additions will reduce and there will be an increase in the freezing point. A similar effect will occur with each subsequent layer, but with each layer, the concentration of alloying additions from the substrate will reduce until the layer composition is almost the same as the original powder. Associated with this change in composition will be a reduction in hardness and a change in microstructure as the βTi phase is no longer stabilised at room temperature. The βTi layer near the coating/substrate interface probably cracks under the applied thermal stresses (different thermal expansion coefficients) as it has a lower melting point and is likely to be weaker at high temperatures. The effect is probably not observed when the system is reversed (cobalt-chrome coatings on titanium) because the melt pool is richer in Co and Cr, and the Co-rich end of the Co-Ti system does not show a deep eutectic.

5.3.2 Tantalum on Cobalt-Chrome

The behaviour of tantalum when coating cobalt-chrome is complicated by the large difference in melting temperatures (Ta (3017°C), Co (1495°C) and Cr (1907°C)) of the different elements. Also, the temperature required to melt tantalum is sufficient to vaporise cobalt (2927°C) and chromium (2671°C). It is unlikely that when forming the first layer of the coating that the tantalum melts first. The interface layer will probably be formed by the laser melting the substrate rather than the tantalum powder, with each powder layer being only 50μm thick. The alloying of the tantalum by the substrate material will reduce the melting point, producing a melt pool containing significant levels of elements from the substrate along with tantalum. However, in this case the freezing point of the liquid will vary less from one end of the melt pool to the other. When the titanium is deposited onto the tantalum, the melting point of the powder is significantly below that of the tantalum and so the melt pool will initially be titanium rich. It will then alloy to some extent with tantalum, as titanium and tantalum show complete liquid solubility. The alloying raises the freezing temperature of the melt pool, thus avoiding a layer of material which melts at a much lower temperature than the surrounding layers.

5.3.3 Pore Size

In the initial process characterisation of DMLR, it was demonstrated that intentionally porous materials could be produced with the pore size being controlled mainly by the line-spacing. However, the pore size is also affected by the laser energy density as this affects the size of the melt bead. The energy density is chosen to produce a uniform melt bead and then the line-spacing can be used to control the pore size. Less control is possible over the bead thickness as although the energy density gives some control, it is limited as high power densities lead to overbuilding; if it is too low, it does not melt the material. At slower scanning speeds and with increased laser power, the beads formed are more circular in cross-section as well as having greater width (Hauser *et al*, 2004), as the increased power density produces a hotter, larger, melt bead which takes longer to cool and freeze. The larger track cross-sections result in improved mechanical performance but reduced pore size and also increase the risk of the powder delivery system jamming.

The use of hatched scanning allowed samples with channels of controlled size to be produced, while rotating the pattern produced pores rather than channels. However, to get sufficient interface strength, it was necessary to create a porosity gradient in the intermediate layer between the solid substrate and the coating (thereby reducing the stress concentration that would result from a sharp interface between the porous coating and the flat substrate). The interface between the coating and the substrate was formed by a scan pattern that was repeated three times, giving the best combination of porosity and strength. This meant that these first three layers were fairly solid and produced a strong interface. It was also found necessary to use a profile scan around the perimeter to avoid "end-effects" (i.e. increased energy at the beginning of a scan, resulting from the First Pulse effect, blasting powder from the substrate) on the scan-tracks. Further revisions of the process delivered an increased specific energy to the powder bed for the first layer, but reduced it for the next three so as to minimise Z-growth and upper surface bowing. Reduction of the layer thickness below that normally used (nominal 100□m) provided some improvement in bonding between successive layers but did increase the risk of the roller jamming as the clearance between the top of the specimen and the roller was reduced.

5.3.4 Random Patterns

From the photographs shown in Figures 5.38 to 5.41 inclusive, it can be seen how the specification of the random scan, that is, the definition of the trigonometrical formulae, alters the distribution of scan lines across the surface of the coating. A more dense distribution of these lines would result in the pore size being smaller than that specified for this work, which stated a required 200μm minimum pore size, an optimum porosity of 20 to 40% and a mean volume percent of voids of 70%. To satisfy these, a degree of control over the scanning arrangement was required. Images shown in Figures 5.38 and 5.41 show how an increased density of scan line vertices can affect the distribution of pores.

The ability to produce either regular or non-regular structures using DMLR has been demonstrated, but also demonstrated was that although the medical industry believed it required random structures produced by randomly scanning lines, what was actually required was a structure that 'looked random'. A number of strategies were experimented with to produce suitable morphologies, from manually drawn lines to complex, mathematically derived, patterns. In all these cases, it was not possible to recreate the porous structures seen in sintered materials, mainly because the structures produced by the DMLR system are derived from multiple straight lines. Therefore, if structures like those seen in sintering are to be produced, then the structures will have to be built point by point rather than as lines. However, building as a series of points is not possible with this system as energy builds up in the laser cavity whenever the laser is turned off. What is required is a system that is capable of dissipating this excess energy whenever the laser cavity is 'shuttered'.

5.3.5 Tensile Tests

The tensile tests on the initial design of coating/substrate showed failure at the coating/substrate interface as there was insufficient fusion between the coating and the surface. The samples produced with the later strategy instead failed both at the interface and within the solid layers of the coating, except for the titanium on cobalt-chrome alloy samples which were dominated by the cracking in the interface layer. A serious problem with these tests is the lack of repeatability in the tensile behaviour of the samples. This

unpredictability indicates that with the experimental system used here, the build conditions are varying significantly from build to build, possibly from problems controlling the atmosphere in the build chamber or in achieving a uniform powder layer. Some of the samples did exceed the requirements of Stryker Howmedica Osteonics, therefore achieving the objective of showing that suitable coatings could be produced using DMLR. A better engineered system would, however, be required to more fully explore the development of these porous coated samples.

5.3.6 Laser System

The choice of laser system for this work was critical in controlling the quality of the materials produced. The Nd:YAG laser used here had been identified in previous research work as being superior to other laser types (e.g. CO_2) for processing metal powders (Xie *et al*, 1997). The Rofin-Sinar (RS) laser marking system used had the further advantages of a relatively small spot size of ∅100μm, relatively high maximum scanning speed of 500mm.s^{-1} and reasonable maximum laser power of 82W continuous wave, which could be increased by pulsing the laser to give high peak powers of up to 10kW for pulse durations of the order of a few nanoseconds. Although these parameters enabled satisfactory components to be produced from the materials investigated during this work, the laser power may be insufficient to process materials with both very high melting point and high thermal conductivity. When the laser was pulsed to increase the instantaneous heat output, especially at low frequencies of <10kHz, shock waves were induced that disrupted the powder bed.

A further limitation of this laser system was the inability to dissipate the laser energy stored within the cavity when it was pulsed. Although this system was suitable for producing the melt beads as a series of lines, assuming that the first pulse could be successfully suppressed, it was not suitable for producing the melt pool as a series of spots. The production of spots instead of lines would have produced significantly different melt pool morphology and may have produced some interesting effects by limiting the size of the melt pool.

The laser spot size, which controls, to some extent, both the minimum width of any feature that can be produced and the pore size in porous structures, is also important, although the melt pool is often wider than the beam size and is dependent upon many other parameters, including laser scan speed and power.

5.3.7 Processing Chamber

The design of the process chamber is critical in controlling not only powder deposition but also the integrity of the finished parts. The production of good quality, functional components is related to the wetting of the molten and solid materials, which is affected by any oxide layers that form either on the surface of the solid or on the melt pool. To reduce oxidation, the build chamber was evacuated/refilled with a protective gas a number of times. This process relies on there being no significant leaks and there being no regions which leak air out slowly. This requires the careful design of the seals and feed-throughs and the removal of areas within the build chamber that are connected together by small orifices. The most obvious problem is between the region below the pistons and the main build chamber and inside both the rollers and electrical motors.

With some materials, such as copper, small amounts of oxygen of the order of several hundred parts per million in the atmosphere is not a serious issue because reducing gases such as a hydrogen/nitrogen mix can be used. With other materials that have a greater propensity for oxide formation, such as H13 tool steel and titanium, it is a greater problem. With H13, the hydrogen will not stop the alloying additions in the steel oxidising and with titanium alloys, detrimental hydrides would form. Although increasing the gas flow rate through the chamber would seem a logical method for diluting the oxygen in the atmosphere, it is likely to have the opposite effect. The oxygen within the build chamber is used up by reacting with the molten powder and if the chamber is under a positive pressure no more oxygen enters the system. Moreover, even reasonably pure gases contain some oxygen and so a high flow rate of protective gas actually provides a constant oxygen supply to the build chamber.

5.4 Summary

From the optical and SEM analysis conducted, it was apparent that the DMLR process is capable of producing porous structures where the pore size, interconnectivity and pore density can be controlled; the line scan spacing being used to control the pore size and the laser power density being used to produce strong, fully melted, material. It was determined that DMLR could be used to produce structures on substrates even where the coating and substrate materials have significantly different melting points.

Consideration of the metallurgical interactions in the more complex systems (e.g. titanium-cobalt-chrome) allowed the behaviour of the systems to be understood and problems avoided.

This work confirms that although DMLR is capable of producing the structures required by industry, the system used to produce them needs further refinement to improve repeatability.

6.0 Conclusions

This thesis has considered some of the problems associated with the production of functional gradients in components produced by DMLR. Microstructural and process factors that limit this technology have been identified and, where possible, methods have been devised to overcome these problems. This chapter will summarise the key issues affecting satisfactory component production for both compositional and porosity graded materials and conclude the important features of the work.

6.1 Production of Structures with Graded Composition

- The optimal processing conditions for a single component powder bed tend to be sub-optimal for processing multi-component systems, even if they contain a significant amount of the same powder. For example, with the copper/H13 system, reducing the scanning speed to increase the specific energy density may work with a single powder system (the optimal speed for copper was found to be <100mm.s^{-1}; Pogson *et al*, 2003), but it will tend to be detrimental to a mixed powder system (where the best results were obtained with a scanning speed of 400mm.s^{-1}) because it will increase the size of the melt pool and the time the material is molten.
- A complete process parameter characterisation is required for the full composition range of any multi-component powder bed.
- With materials where it is not desirable that the components mix (e.g. copper and H13), controlling the time at temperature is unlikely to be a suitable method to avoid mixing as the materials must be molten for a sufficient time to form a suitable melt pool. In these cases, the use of an intermediate material (e.g. tantalum in the titanium/cobalt-chrome system) may be the optimum route to avoid undesirable material interactions.
- The mixing of materials makes the formation of sharp interfaces difficult for some materials with appreciably different melting points (e.g. copper at 1083°C and H13 at 1450°C, due to embrittlement of the higher melting point material in this case), while for others the system metallurgy makes forming gradients complex (e.g. cobalt-chrome/tantalum/titanium).

- If composition gradients are to be produced, then a method of selectively depositing the powder is required, with a spatial resolution similar to the melt pool diameter. With a conventional DMLR layout, this is likely to be a slow process. It would thus be necessary to consider a multiple hopper "blown powder" system such as that used with LENS (Section 2.2.1.3) or an "Ink-Jet Printing" system (Section 2.2.4.6) that has the potential to accurately control where each powder is placed.
- Although this work showed it was possible to produce structures using dissimilar materials (e.g. titanium coated cobalt-chrome with intermediate tantalum layers), certain difficulties are associated with their production, and given the possible galvanic corrosion problems that may occur with dissimilar metals (especially when immersed in a corrosive or conductive solution [Fontana, 1987] such as human blood), the advantages of using different coating and substrate materials is debatable.

6.2 Production of Structures with Graded Porosity

- The DMLR system appears to be more suited to producing materials that vary their mechanical properties by means of structural variation rather than gradation of the composition. The work concerned with the production of porous materials investigated the application of porous coatings to a solid substrate. However, there is no reason why the whole structure cannot be produced with the DMLR system. Where coatings were produced, it was seen to be best to use the same material for the coating and substrate, e.g. the titanium powder wetted and fused well with the titanium substrates and had superior mechanical strength. Any variations in the mechanical properties observed between samples were due to the purely research nature of the experimental apparatus used and that it was never intended to produce identical parts on a production line basis.
- The work on structures with a graded porosity showed that with DMLR it is possible to produce parts, repeatedly, with a porosity of the range 600 to 800μm using the hatched "waffle" scanning arrangement. It was also possible to modify the density of the pores by the use of a more "random" scan pattern (Section 5.2.5). The ability of the DMLR process in producing parts with a structured surface satisfied the

sponsor, Stryker Howmedica Osteonics, such that they agreed to fund continuing work on bio-implants at The University of Liverpool after this project ended, including the purchase of MCP "Realizer" Selective Laser Melting machines.

- The size of the pores could be controlled and changed, subject to the limitations of the software, both between and within the layers, showing that property gradients could easily be produced. However, it was observed during the mechanical testing of the titanium coated titanium samples that the use of a gradual porosity variation at the coating/substrate interface was preferable to a sharp interface between the porous and solid regions so as to reduce the stress concentrations between coating and interface.

6.3 General

- The key parameters for the DMLR process are laser scanning speed, laser power, pulse repetition rate and beam overlap/line-spacing. Unless these are carefully controlled, suitable microstructural or structural gradation cannot be obtained. It was found necessary for the composition work to use a high scanning speed in conjunction with a high laser power to ensure sufficient energy density (a scanning of 400mm.s^{-1} in conjunction with a maximum power of 82W CW were used for the copper/H13 work). The limitations of the laser system used here (maximum scanning speed of 500mm.s^{-1}, laser power of 82W CW) restricted the experiments that could be conducted for this work.
- Scanning patterns have a significant effect on the integrity of the components produced. The lay-up and laser scanning of a new powder layer affects the morphology and composition of previously processed layers, which limits the type of structures that can be produced.
- In DMLR, the powder bed heats and cools relatively quickly with the material only molten for a short time. This, along with minimising the size of the melt pool, leads to the production of finer micro or macrostructures and a more controllable melt pool.
- Many problems, associated with DMLR when producing functionally graded components, were identified. Some of these problems are limitations of the specific

laser system used (e.g. spot size, laser parameters), while others are due to the fundamental process (the restrictive nature of a roller/platform build chamber). It appears that in the short term, porosity gradients are more achievable (depending more on controlling the processing conditions than any subsequent microstructural interactions) than compositional gradients. The production of structures with composition gradation may become possible as understanding of melt pool dynamics improves.

- Although this work has shown the limitations of the DMLR process when handling mixed powders, it has also shown that the technique does have far reaching potential, both within the fields of rapid prototyping and manufacturing where novel structures with a designed porosity are required.

7.0 Future Work

The work presented in this thesis has started to understand the subtle interactions of materials under the laser beam during the DMLR process. It has been shown that controlled porosity gradients can be achieved but that the problems associated with compositional changes are much more complex than first expected and, consequently, require a detailed understanding of both the process and metallurgy.

This chapter proposes an outline of the future work that should be undertaken in order to bring the work described in this thesis to a satisfactory conclusion.

7.1 Basic Process Metallurgy

Future work should include a detailed study of the dynamics of melt pool formation and the processes that occur as the melt pool traverses the surface of the powder bed, following the laser. Little is known of how the powder enters the melt pool or of the freezing process that occurs at the other end of the melt pool. This latter problem is further affected by various phenomena such as melt pool stirring, caused by Marangoni forces, which make it difficult to accurately predict the exact melt pool composition.

There is also little understanding of how the aspect ratio of the melt pool affects behaviour and whether short sections of melt pool behave differently to long lines. This work needs to be carried out on single element powders before considering mixed powders so that the basic behaviour of the melt pool can be understood.

7.2 Porous Materials

The development of porous materials has continued at Liverpool University since the end of the work reported here. The research has concentrated on improving the control of the position of the laser and using a system incorporating a different type of laser, which is easier to control, and also using a better controlled atmosphere. For the graded porosity work, it is the laser control system that is fundamental. The ability to place the melt pools

in each layer in the correct place is vital in order to have sufficient control over the structure that is produced. This work has developed rapidly, unlike some of the other sections of the future work considered here.

7.3 Powder Placement for Composition Gradients

The development of a fast method of accurately positioning the powders is required if parts exhibiting composition variation are to be produced. Ink-jet printing based powder delivery systems are the most obvious method for positioning powders. The problem is that ink-jets are not designed to deliver fairly coarse powders (i.e. >10μm) and they usually require a fluid to deliver the powder (powders in fluid suspension can be delivered rapidly and in a controlled way). The use of a fluid has several key disadvantages: -

a) The fluid must evaporate, leaving the dried powder in place on the powder bed, prior to processing.
b) A water-based system would corrode some powders, while under the laser it may lead to oxidation or the incorporation of hydrogen into the alloy.
c) Alcohol-based systems have the added disadvantage of adding carbon to the melt pool.

It therefore appears that a dry system is required, although it is difficult to see how a dry system would produce the same spatial resolution.

7.4 Automatic Control of Laser Parameters

One of the main difficulties in selecting the appropriate laser parameters for a multi-component powder bed is determining how the behaviour of these mixed powders will differ from when the individual components are processed separately. This makes processing of powder beds of varying compositions difficult.

The work described in this thesis has shown that a large series of experiments would be required to identify the correct processing parameters for any point on the build. This tends to suggest that there is a better way of obtaining this information. It may be possible to control the system by analysing the melt point during processing, so as to control the

system by a feed-back loop, as the composition of the melt pool may not remain uniform during its passage over the entire powder bed. However, if it were possible to detect in real time when the melt pool forms under the laser, then it would be possible to decrease or increase the laser power sufficiently to give the correct level of melting required by the material directly beneath it.

Having the ability to continually monitor melt pool development would also remove the need for a large data set to set up the machine. If continuous monitoring were not used, then the data set that determines each layer would have to contain, for each point, information about the melt pool composition so the laser parameters can be modified accordingly. At present, the only way that this can be achieved is using experimental data but if more accurate computer-based models of the melt pool could be produced, these could be used to predict the correct settings.

7.5 Composition Gradients

The metallurgy of a graded composition will be complex as the melt pool is subjected to both composition and temperature gradients. To some extent, the behaviour of a multi-component powder bed can be predicted by using both binary and ternary phase diagrams. However, due to the high heating and cooling rates associated with laser processing, equilibrium conditions do not exist, so these diagrams can only be used as a guide. The presence of further alloying components such as carbon, silicon and molybdenum, as found in this work, can further complicate the interactions. It is therefore necessary for any further work in this area to carry out a detailed study of the materials to be used. This will include both research into the theoretical interactions between the materials (software programs are now becoming available that would allow for the prediction of complete Cu/H13 phase diagrams) and experimental investigations into the interactions of the materials under a laser beam.

References

Abbott, D. H. and Arcella, F.G. (1998). "Aeromet Implementing Novel Ti Process." Metal Powder Report. **53**(2): pp24-26.

Abe, F., Costa Santos, E., Kitamura, Y., Osakada, K. and Shiomi, M. (2003). "Influence of Forming Conditions on the Titanium Model in Rapid Prototyping with the Selective Laser Melting Process." Proceedings of the Institute of Mechanical Engineers. **217**(Part C.): pp119-126.

Abe, F., Osakada, K., Kitamura, Y., Matsumoto, M. and Shiomi, M. (2000). "Manufacturing of Titanium Parts for Medical Purposes by Selective Laser Melting". Rapid Prototyping & Manufacturing 3D Scanning Applications, Tokyo, Japan.

Abe, F., Osakada, K., Shiomi, M., Uematsu, K. and Matsumoto, M. (2001). "The Manufacturing of Hard Tools from Metallic Powders by Selective Laser Melting." Journal of Materials Processing Technology **111**(1-3): pp210-213.

Akin, F. A., Zreiqat, H., Jordan, S., Wijasundara, M., Hanley, L. (2001). "Preparation and Analysis of Macroporous TiO_2 Films on Ti Surfaces for Bone-Tissue Implants." Journal of Biomedical Materials Research **57**: pp588-596.

American Society of Materials (1997). ASM Handbook. Volume 3: Alloy Phase Diagrams. Ohio, ASM International. **3**.

American Society of Materials (2003). "Handbook of Materials for Medical Devices" (2003). Coatings for Medical Devices. Chapter 9, Ed. J. R. Davis, ASM International: pp179-194.

American Society of the Testing of Materials (2000). Annual Book of ASTM Standards. (2000). Section 13: Medical Devices & Services. West Conshohocken, Pennsylvania. ASTM. **13**.

Amon, C., Beuth, J., Kirchner, H., Merz, R., Prinz, F., Schmaltz, K. and Weiss, L. (1993). "Material Issues in Layered Forming." Proceedings of the Solid Freeform Fabrication Symposium, The University of Texas at Austin. pp1-11.

Arcella, F. G., Abbott, D.H. and House, M.A. (1998). "Rapid Laser Forming of Titanium Structures". Metallurgy World Conference, Grenada, Spain.

Arthur, G. (1954-55). "Porosity & Permeability Changes during the Sintering of Copper Powder." Journal of the Institute of Metals: pp329-336.

Bobyn, J. D., Pilliar, R.M., Cameron, H.U. and Weatherley, G.C. (1980). "The Optimum Pore Size for the Fixation of Porous-Surfaced Metal Implants by the Ingrowth of Bone." Clinical Orthopaedics and Related Research. **150**: pp263-270.

Bourell, D. L., Marcus, H. L., Barlow, J. W. and Beaman, J. J. (1992). "Selective Laser Sintering of Metals and Ceramics." The International Journal of Powder Metallurgy **28**(4): pp369-380.

Brooks, J., Robino, C., Headley, T., Goods, S. and Griffith, M. (1999). "Microstructure and Property Optimization of LENS Deposited H13 Tool Steel". Solid Freeform Fabrication Symposium, The University of Texas at Austin.

Cardonne, S. M., Kumar, P., Michaluk, C.A. and Schwartz, H.D. (1995). "Tantalum and its Alloys." International Journal of Refractory Metals & Hard Materials. **13**: pp187-194.

Carslaw, H. S. and Jaeger, J.C. (1959). Conduction of Heat in Solids. Oxford, Oxford University Press.

Carter Jr., W. T. and Jones, M.G. (1993). "Direct Laser Sintering of Metals." Solid Freeform Fabrication Proceedings: pp54-60.

Collins, P. C., Banerjee, R., Banerjee, S., Fraser, H.L. (2002). "Laser Deposition of Compositionally Graded Titanium-Vanadium and Titanium-Molybdenum Alloys." 352.

Cormier, D., Harrysson, O., and West, H. (2004). "Characterisation of H13 Steel Produced by Electron Beam Melting." Rapid Prototyping Journal **1**: pp35-41.

Das, S. (2001). "On Some Physical Aspects of Process Control in Direct Selective Laser Sintering of Metals - Part 1." Solid Freeform Fabrication Symposium Proceedings, 2001: pp85-93.

Deckard, C. and Miller, D. (1995). "Improved Energy Delivery for Selective Laser Sintering." SFF Symposium Proceedings, 1995: pp151-158.

Eurolaser Academy (1998) "Handbook of the Eurolaser Academy". London, Chapman & Hall.

Evans, T. and Strezov, L. (2000). "Interfacial Heat Transfer and Nucleation of Steel on Metallic Substrates." Metallurgical and Materials Transactions B: Process Metallurgy and Materials Processing Science **31**(5): pp1081-1089.

Fessler, J.R., Nickel, A.H., Link, G., Prinz, F.B. and Fussel, P. (1997). Functional Gradient Metallic Prototypes Through Shape Deposition Manufacturing. Solid Freeform Fabrication Symposium, The University of Texas at Austin.

Fischer, P., Romano, V., Weber, H.P., Karapatis, N.P., Boillat, E. and Glardon, R. (2003). "Sintering of Commercially Pure Titanium Powder with a Nd:YAG Laser Source." Acta Materialia **51**(6): pp1651-1662.

Fontana, M. G. (1998) "Corrosion Engineering International Engineering". London, McGraw-Hill Book Company.

Gasik, M. M. (1998). "Micromechanical Modelling of Functionally Graded Materials." Computational Materials Science **13**(1-3): pp42-55.

German, R. M. (1996). "Sintering Theory and Practice". New York, Wiley.

German, R. M. (2003). "An Update on the Theory of Supersolidus Liquid Phase Sintering". International Conference on the Science, Technology & Applications of Sintering, Penn State University, Pennsylvania.

Gupta, K. P. (2001). "The Co-Cr-Ti System (Cobalt-Chromium-Titanium)." Journal of Phase Equilibria **22**(1): pp52-60.

Hacking, S. A., Bobyn, J.D., Toh, K.K., Tanzer, M. and Krygier, J.J. (2000). "Fibrous Tissue Ingrowth and Attachment to Porous Tantalum." Journal of Biomedical Materials Research **52**(4): pp631-638.

Handbook of Biomaterials Evaluation: Scientific, Technical & Clinical Testing of Implant Materials. (1999). Philadelphia, Taylor & Francis.

Hansen, M. (1958). Cu-Fe Phase Diagram. Constitution of Binary Alloys. New York, McGraw Hill: pp580-582.

Hauser, C., Childs, T. and Badrossamay, M. (2004). "Further Developments in Process Mapping and Modelling in Direct Metal Selective Laser Sintering". 15th Solid Freeform Fabrication Symposium, Austin, Texas.

Hauser, C., Childs, T. and Dalgarno, K. W. (2003). "Direct Selective Laser Sintering of Tool Steel Powders to High Density. Part A: Effects of Laser Beam Width and Scan Strategy". 14th Solid Freeform Fabrication Symposium, Austin, Texas.

Hauser, C., Childs, T., Taylor, C. and Badrossamay, M. (1999). "Selective Laser Sintering of Stainless Steel 314S HC Process using Room Temperature Powder Beds." Proc. 10th SFFF Symposium, University of Texas at Austin: pp273-280.

Henc-Bartolic, V., Andreic, Z., Stubicar, M. and Kunze, H. J. (1998). "Nitrogen Laser Beam Interaction with Copper Surface." FIZIKA A **4**: pp205-212.

Ho, H. C. H., Gibson, I. and Cheung, W. L. (1999). "Effects of Energy Density on Morphology and Properties of Selective Laser Sintered Polycarbonate." Journal of Materials Processing Technology **89-90**: pp204-210.

Hofmann, A. A., Bloebaum, R.D. and Bachus, K.N. (1997). "Progression of Human Bone Ingrowth into Porous-Coated Implants." Acta Orthop Scand **68**(2): pp161-166.

Hofmeister, W., Wert, M., Smugeresky, J., Philliber, J.A., Griffith, M. and Ensz, M. (1999). "Investigating Solidification with the Laser-Engineered Net Shaping (LENS) Process." Journal of Materials **51**(7): pp1-5.

Jackson, T. R., Liu, H., Patrikalakis, N.M., Sachs, E.M. and Cima, M.J. (1999). "Modelling and Designing Functionally Graded Material Components for Fabrication with Local Composition Control." Materials and Design **20**(2-3): pp63-75.

Jacques, P. and Doyle, E.D. (1997). Vacuum Heat Treatment of Large Die Blocks. Die Casting & Technology Conference, Melbourne.

Karapatis, N. P., Egger, G., Gygax, P. E. and Glardon, R. (1999). "Optimisation of Powder Layer Density in Selective Laser Sintering." Solid Freeform Fabrication Proceedings, 1999: pp255-264.

Kou, S. (1981). "Simulation of Heat Flow during the Welding of Thin Plates." Metallurgical Transactions A (Physical Metallurgy and Materials Science) **12A**: pp2025-2030.

Laberge, M., J. B. Medley, et al. (1999). Friction & Wear. Handbook of Biomaterials Evaluation: Scientific, Technical & Clinical Testing of Implant Materials. Ed. A. F. von Recum. Philadelphia, Taylor & Francis: pp. 171-195.

Larsson, L. E. (1975). "On the Effect of Copper on the Iron-Carbon Diagram." Zeitschrift fuer Metallkunde **66**(4): pp220-223.

Laser Institute of America (2001). "LIA Handbook of Laser Materials Processing". Orlando.

Lide, D. R. (2002-2003). CRC Handbook of Chemistry and Physics. Handbook of Chemistry and Physics. Florida, CRC Press LLC: 12-232.

Majumdar, J. D. and Manna, I. (1999a). "Laser Surface Alloying of Copper with Chromium II. Improvement in Mechanical Properties." Materials Science and Engineering A: Structural Materials: Properties, Microstructure and Processing **A268**(1-2): pp227-235.

Majumdar, J. D. and Manna, I. (1999b). "Laser Surface Alloying of Copper with Chromium I. Microstructural Evolution." Materials Science and Engineering A: Structural Materials: Properties, Microstructure and Processing **A268**(1-2): pp216-226.

Maziasz, P. J., Payzant, E.A., Schlienger, M.E. and McHugh, K.M. (1998). "Residual Stresses and Microstructure of H13 Steel Formed by Combining Two Different Direct Fabrication Methods." Scripta Materialia **39**(10): pp1471-1476.

McQuillan, A. D. and McQuillan, M.K. (1956). Constitution of Titanium Alloys. Titanium. London, Butterworths Scientific Publications.

Mohebi, M. M. and Evans, J. (2001). "A Drop-on-Demand Ink-Jet Printer for Combinatorial Libraries and Functionally Graded Ceramics." J. Comb. Chem. **4**: pp267-274.

Morgan, R. H., Papworth, A.J., Sutcliffe, C.J., Fox, P. and O'Neill, W. (2001). "High Density Net Shape Components by Direct Laser Remelting of Single-Phase Powders." Journal of Material Science **37**: pp3093-3100.

Morgan, R. H. (2003). Direct Metal Laser Remelting of 316L Stainless Steel with an Nd:YAG Laser. Engineering. Liverpool, The University of Liverpool: 250.

Mott, M. and Evans, J. (1999). "Zirconia/alumina Functionally Graded Material Made by Ceramic Ink Jet Printing." Materials Science & Engineering A **271**: pp344-352.

Niu, H. J. and Chang I. T. H. (1998). "Liquid Phase Sintering of M3/2 High Speed Steel by Selective Laser Sintering." Scripta Materialia **39**(1): pp67-72.

Niu, H. J. and Chang, I. T. H. (1999). "Instability of Scan Tracks of Selective Laser Sintering of High Speed Steel Powder." Scripta Materialia **41**(11): pp1229-1234.

Niu, H. J. and Chang, I. T. H. (2000). "Selective Laser Sintering of Gas Atomized M2 High Speed Steel Powder." Journal of Materials Science **35**: pp31-38.

Oliveria, M. V., Pereira, L.C., Cairo, C.A.A. (2002). "Porous Structure Characterization in Titanium Coating for Surgical Implants." Materials Research **5**(3): pp 269-2002.

Pei, Y. T. and De Hosson, J. T. M. (2002). "Producing Functionally Graded Coatings by Laser-Powder Cladding." Journal of Materials: pp1-9.

Pei, Y. T., Ocelik, V. and De Hosson, J.Th.M. (2002). "SiCp/Ti6Al4V Functionally Graded Materials Produced by Laser Melt Injection." Acta Materialia **50**: pp 2035-2051.

Perrie, W., Rushton, A., Gill, M., Fox, P. and O'Neill, W. (2005). "Femtosecond Laser Micro-Structuring of Alumina Ceramic." Applied Surface Science. **248**(1-4): pp213-217.

Pogson, S.R., Fox, P., Sutcliffe, C.J. and O'Neill, W. (2003). "The Production of Copper Parts Using DMLR." Rapid Prototyping Journal **9**(5): pp334-343.

Pogson, S.R., Fox, P., Sutcliffe, C.J. and O'Neill, W. (2004). "The Direct Metal Laser Remelting of Copper and Tool Steel Powders." Materials Science & Engineering A **386**: pp453-459.

Pompe, W., Worch, H., Epple, M., Friess, W., Gelinsky, M., Greil, P., Hempel, U., Schamweber, D. and Schulte, K. (2003). "Functionally Graded Materials for Biomedical Applications." Materials Science & Engineering A **A362**: pp 40-60.

Raghavan, V. (2002). "C-Cu-Fe (Carbon-Copper-Iron)." Journal of Phase Equilibria **23**(3): pp251-252.

Santos, E. C., Osakada, K., Shiomi, M., Kitamura, Y. and Abe, F. (2004). "Microstructure and Mechanical Properties of Pure Titanium Models Fabricated by Selective Laser Melting." Proceedings of the Institute of Mechanical Engineers. 218 (Part C): Journal of Mechanical Engineering Science: pp711-719.

Shen, Z. H., Zhang, S.Y., Lu, J. and Ni, X.W. (2001). "Mathematical Modelling of Laser Induced Heating and Melting in Solids." Optics & Laser Technology **33**: pp533-537.

Simchi, A., Petzoldt, F. and Haiko, P. (2001). "Direct Metal Laser Sintering: Material Considerations and Mechanisms of Particle Bonding." The International Journal of Advanced Powder Metallurgy **37**(2): pp49-60.

Simchi, A. and Pohl, H. (2003). "Effects of Laser Sintering Processing Parameters on the Microstructure and Densification of Iron Powder." Materials Science & Engineering A **359**: pp119-128.

Steen, W. M. (1998). Laser Material Processing. London, Springer-Verlag.

Su, W.-N., Erasenthiran, P. and Dickens, P.M. (2003). "Investigation of Fully Dense Laser Sintering of Tool Steel Powder using a Pulsed Nd:YAG Laser." Proceedings of the Institute of Mechanical Engineers. **217** Part C: J. Mechanical Engineering Science. pp127-138.

Tolochko, N. K., Arshinov, M.K., Gusarov, A.V., Titov, V.I., Laoui, T. and Froyen, L. (2003). "Mechanisms of Selective Laser Sintering and Heat Transfer in Ti Powder." Rapid Prototyping Journal **9**(5): pp314-326.

Tolochko, N. K., Mozzharov, S. E., Yadroitsev, I. A., Laoui, T., Froyen, L., Titov, V. I. and Ignatiev, M. B. (2004). "Balling Processes during Selective Laser Treatment of Powders." Rapid Prototyping Journal **10**(2): pp78-87.

Ward, L. P., Strafford, K.N., Wilks, T.P. and Subramanian, C. (1996). "The Role of Refractory Element Based Coatings on the Tribological and Biological Behaviour of Orthopaedic Implants." Journal of Materials Processing Technology **56**: pp364-374.

Williams, J. D. and Deckard, C.R. (1998). "Advances in Modelling the Effects of Selected Parameters on the SLS Process." Rapid Prototyping Journal **4**(2): pp90-100.

Xie, J., Kar, A., Rothenflue, A. and Latham, W. P. (1997). "Temperature-Dependent Absorptivity and Cutting Capability of CO_2, Nd:YAG and Chemical Oxygen-Iodine Lasers." Journal of Laser Applications **9**: pp77-85.

Yevko, V., Park, C. B., Zak, G., Coyle, T. W. and Benhabib, B. (1998). "Cladding Formation in Laser-Beam Fusion of Metal Powder." Rapid Prototyping Journal **4**(4): pp168-184.

Yilbas, B. S. (1993). "Analytical Solution for Heat Conduction Mechanism Appropriate to the Laser Heating Process." Int. Commun. Heat Mass Transfer **20**: pp545-555.

Yilbas, B. S. and Aleem, B. J. A. (1999). "Theoretical and Experimental Investigation into Laser Surface Melting of 321 Austenitic Stainless Steel." Lasers in Engineering **9**(2): pp111-125.

Zhu, H. H., Fuh, J.Y.H. and Lu, L. (2003). "Formation of Fe-Cu Metal Parts Using Direct Laser Sintering." Proceedings of the Institute of Mechanical Engineers. **217**(Part C.): pp139-147.

Zhu, H. H., Lu, L. and Fuh, J.Y.H. (2003). "Development and Characterisation of Direct Laser Sintering Cu-based Metal Powder." Journal of Materials Processing Technology **140**: pp314-317.

Appendix 1.0 Example Calculation of Peak Power from a Pulsed Laser Beam

Peak laser power (W) can be defined as:

$$P_{peak} = \frac{\frac{P_n}{Q_s}}{n}$$

Where P_{peak} is the peak laser power (W) delivered during laser pulsing, P_n is the nominal laser power (W) available in continuous wave operation of the laser and n is the pulse width (ns).

From the Rofin Sinar laser manual, at a maximum laser power of 82W available in CW mode and a pulse repetition rate (frequency) of 40kHz, the pulse width is 120ns and the peak laser power would be:

$$P_{peak} = \frac{\frac{82}{40{,}000}}{200 \times 10^{-9}} = 10.250\text{kW}$$

From this, it can be seen that the power available during laser pulsing is 125 times that that can be available during normal CW operation, if only for a fraction of a second.

Appendix 2.0 Theoretical Temperature Profile from Surface of Powder Bed

Plot generated using Microsoft "Excel" using Steen, 1998 and Carslaw and Jaeger, 1959 analytical solutions (Eqns. (4) & (5)) to describe the conduction of heat through a semi-infinite body as outlined in Section 2.3.2 of this thesis and using sample data for H13 tool steel:

Thermal conductivity	= 28.7W/m.K @ 605°C	(source, Efunda.com)
Specific heat	= 2081K/kg.k:	(source, Efunda.com)

and typical data from a DMLR processed powder bed:

Layer thickness	= 100μm
Laser Power	= 82W,
Beam Diameter	= 100μm
Absorptance	= 0.4

The calculated temperature profile, Figure A2.1, shows a peak temperature approaching 1900K at the surface, which gradually reduces to 293K at a depth of 2mm below the surface. The predicted temperature indicates that there is likely to be significant superheating of the melt pool as the melting point of H13 tool steel is 1450°C.

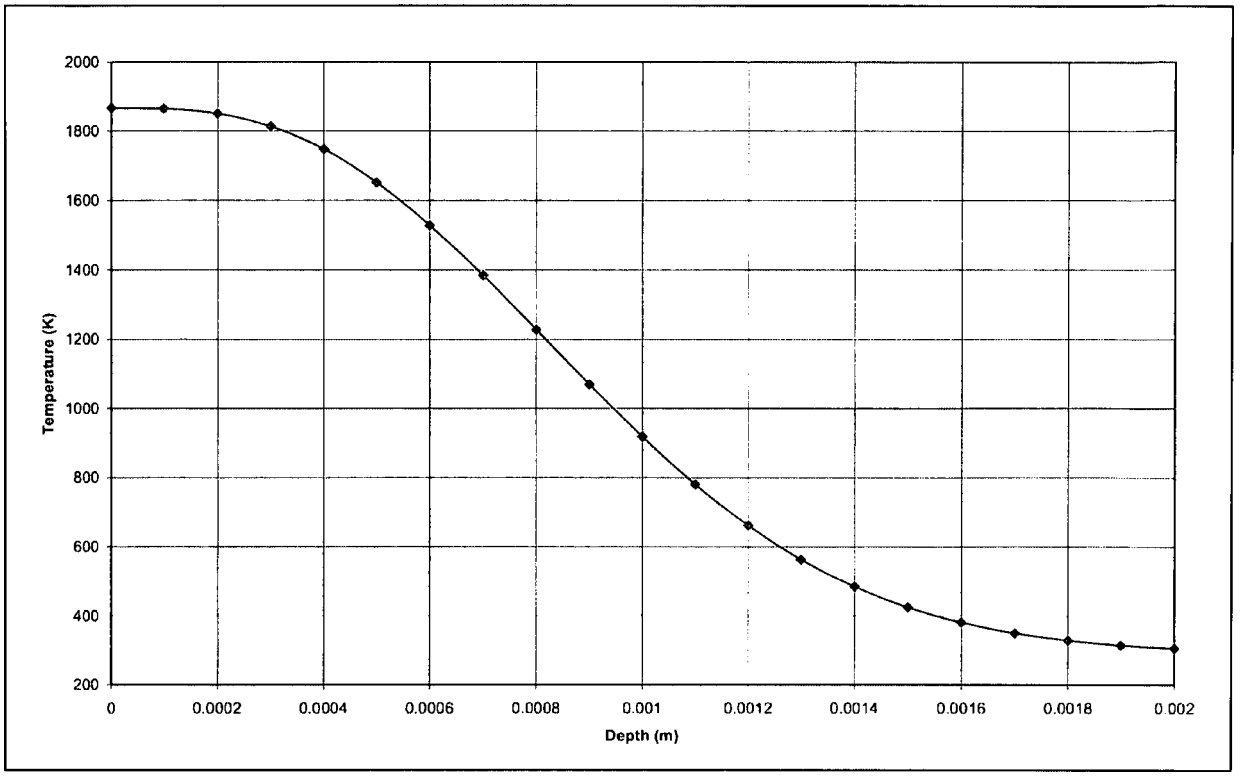

Figure A2.1 Theoretical temperature profile from surface of powder bed derived using analytical solution provided by Steen, 1998

Appendix 3.0 Referenced Phase Diagrams

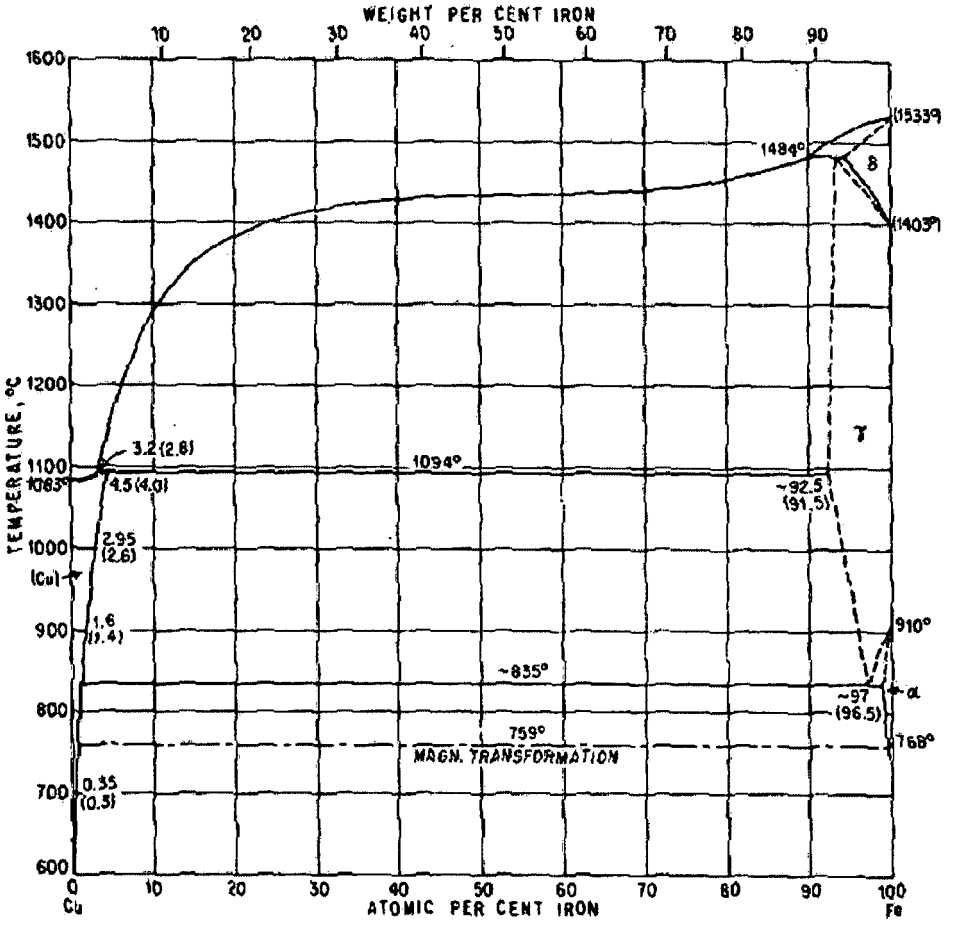

Figure A3.1 Cu-Fe binary phase diagram *(reproduced courtesy of Hansen, 1958)*

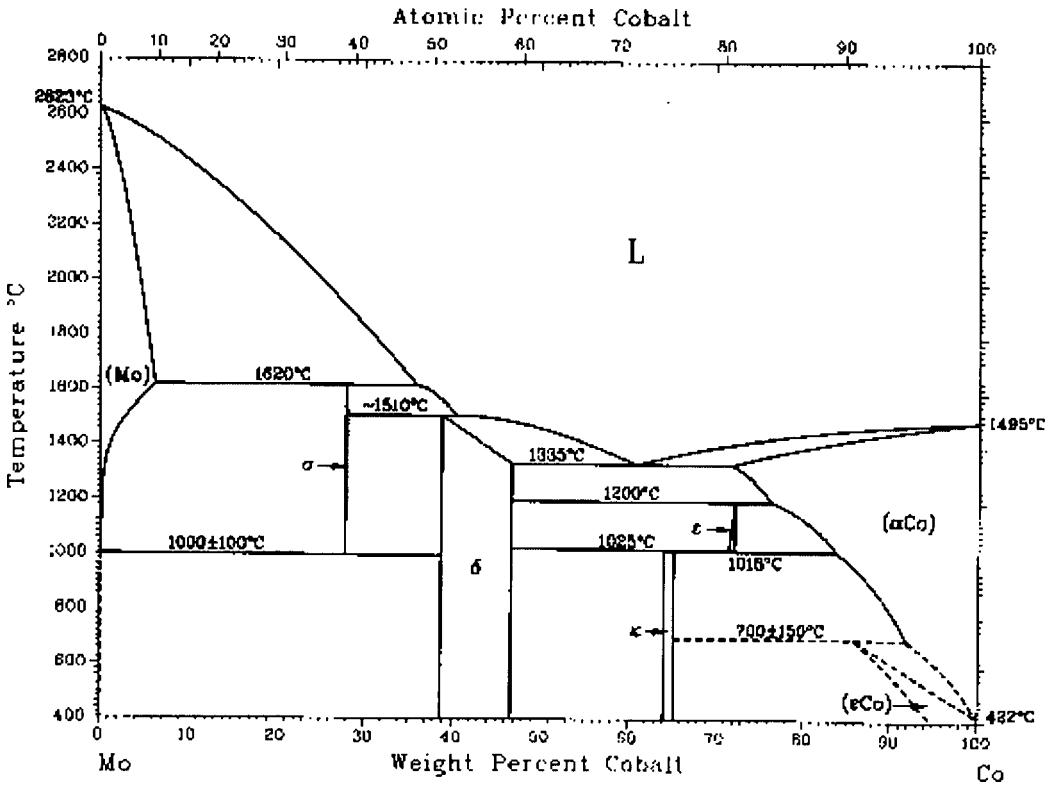

Figure A3.2 Mo-Co binary phase diagram *(reproduced courtesy of ASM International)*

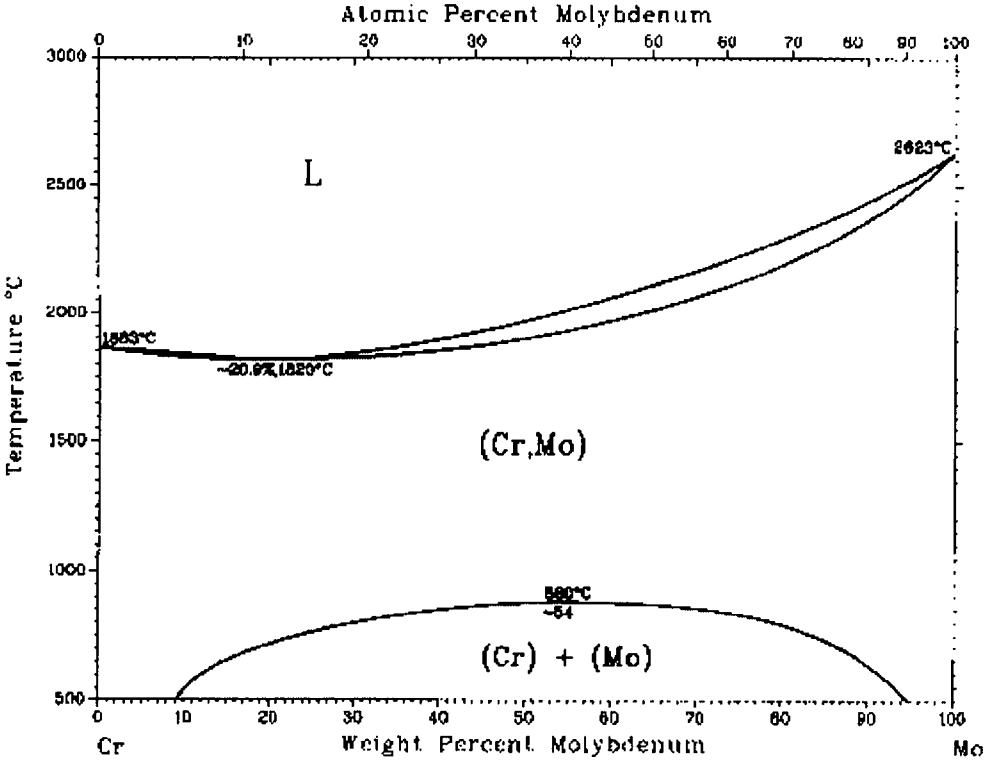

Figure A3.3 Mo-Cr binary phase diagram *(reproduced courtesy of ASM International)*

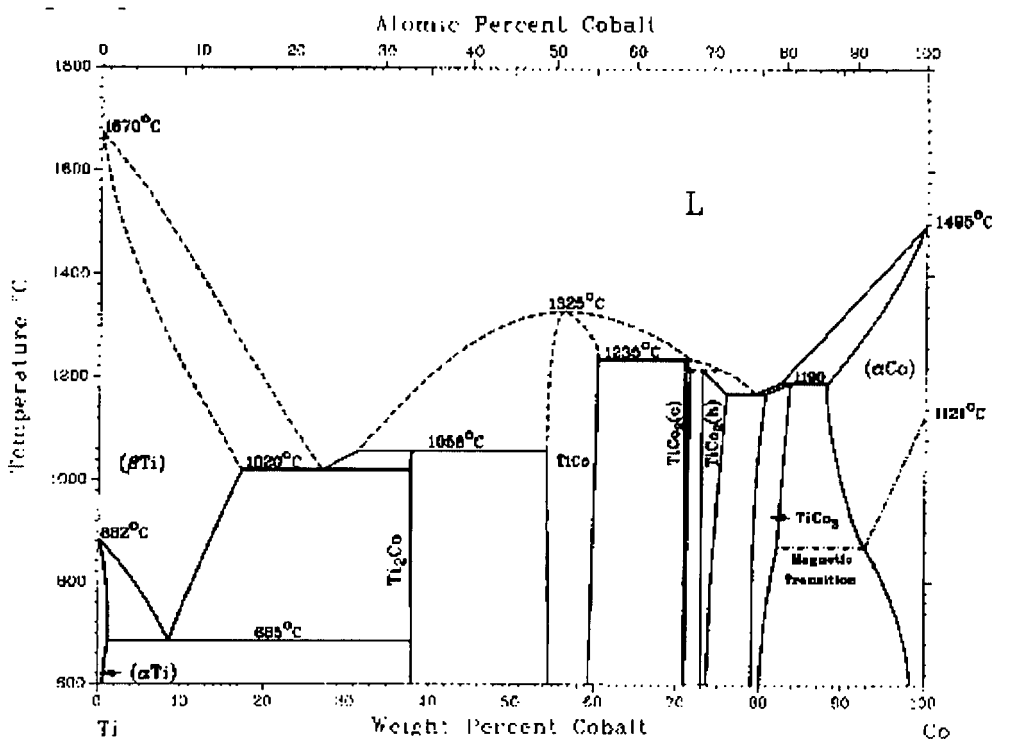

Figure A3.4 Ti-Co binary phase diagram *(reproduced courtesy of ASM International)*

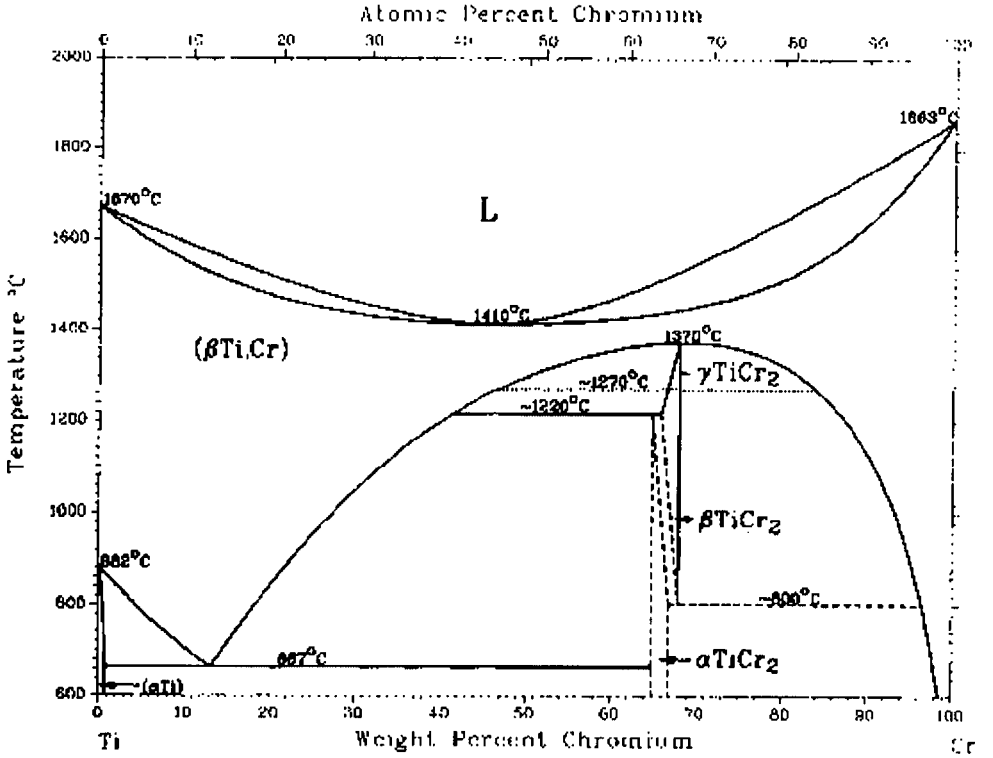

Figure A3.5 Ti-Cr binary phase diagram *(reproduced courtesy of ASM International)*

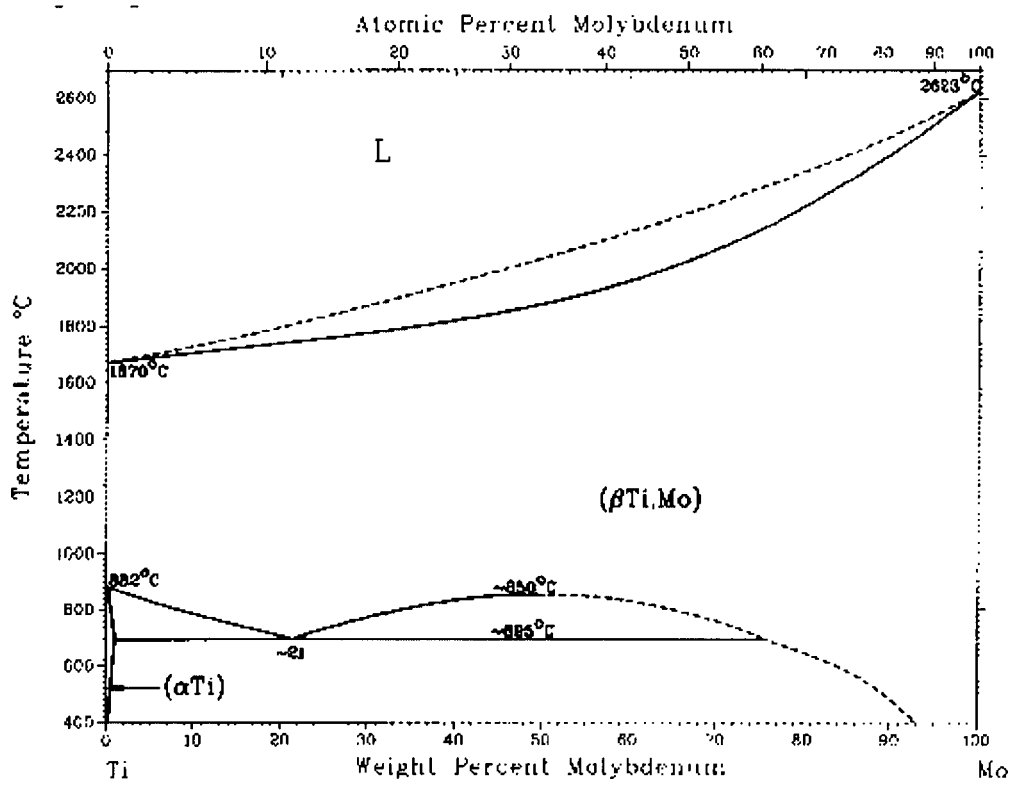

Figure A3.6 Ti-Mo binary phase diagram *(reproduced courtesy of ASM International)*

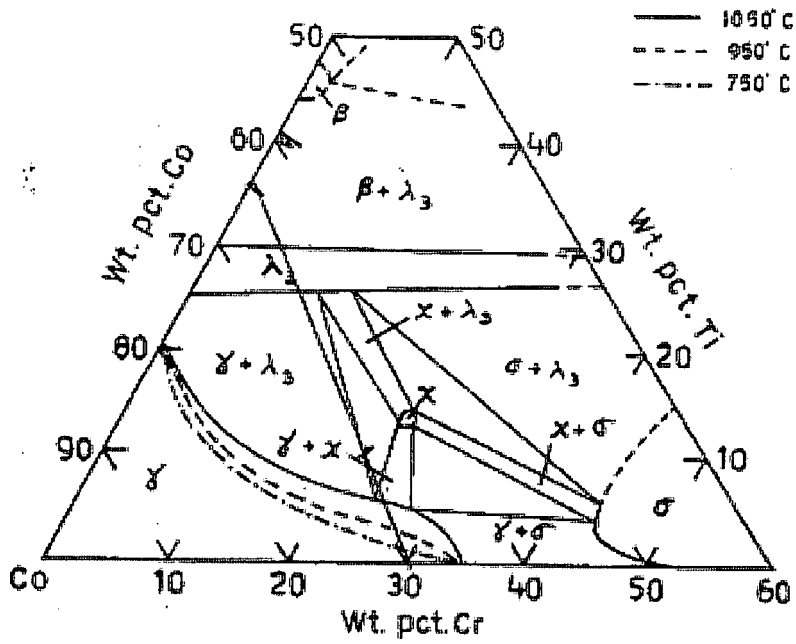

Figure A3.7 A 1050°C partial isothermal section of Co-Cr-Ti system with the FCC γ phase boundary at 950°C shown by a dashed line and at 750°C by a dash-dot line *(reproduced courtesy of Gupta, 2001)*

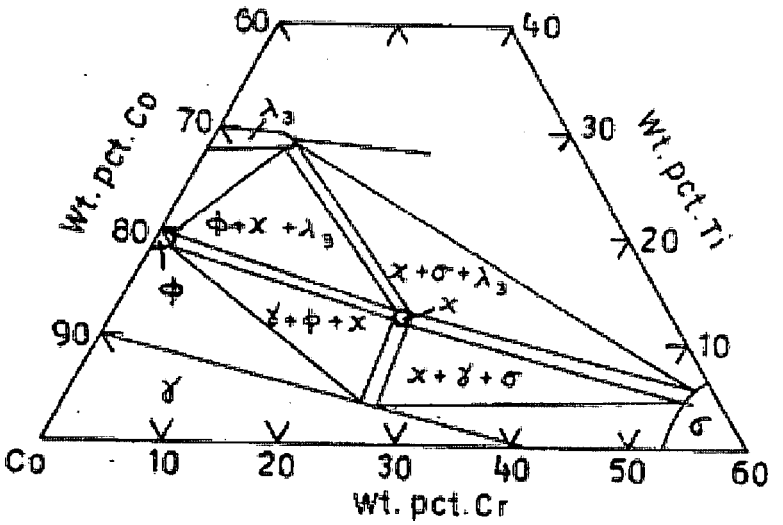

Figure A3.8 A 1000°C partial isothermal section of Co-Cr-Ti system *(reproduced courtesy of Gupta, 2001)*

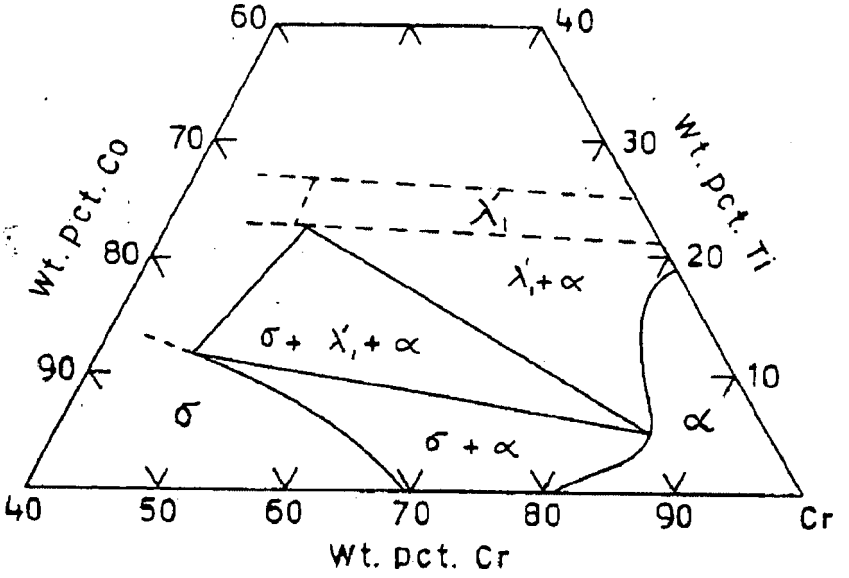

Figure A3.9 A 20°C partial isothermal section of Co-Cr-Ti system *(reproduced courtesy of Gupta, 2001)*

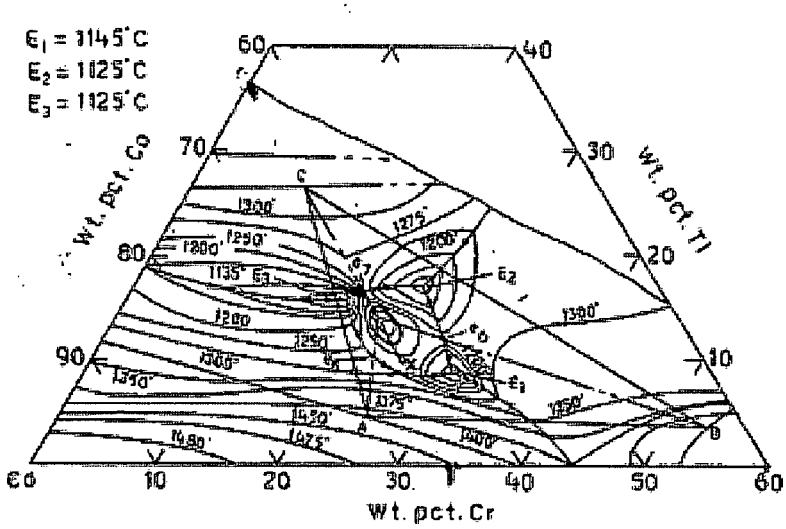

Figure A3.10 A liquidus projection at the Co corner of Co-Cr-Ti system showing liquidus isotherms and three binary eutectic reactions (e) and three ternary eutectic reactions (E). (*Reproduced courtesy of Gupta, 2001)*

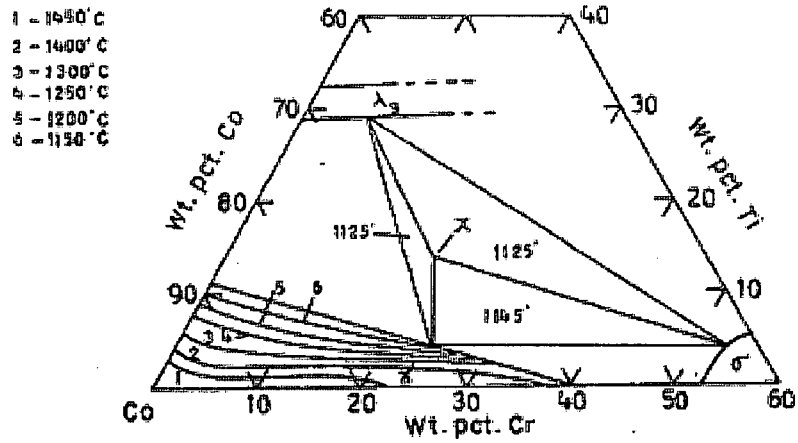

Figure A3.11 A solidus projection at the Co corner of Co-Cr-Ti system showing solidus isotherms *(reproduced courtesy of Gupta, 2001)*